ALMA MATER STUDIORUM
UNIVERSITÀ DEGLI STUDI DI BOLOGNA

Dipartimento di Fisica e Astronomia

DOTTORATO DI RICERCA IN
ASTROFISICA

Ciclo XXXI

Tesi di Dottorato

STUDYING THE FINAL STAGES OF GALAXY EVOLUTION ACROSS COSMIC TIME

Presentata da: Salvatore Quai

Coordinatore Dottorato:
Francesco Rosario Ferraro

Supervisore:
Prof. Andrea Cimatti

Co-supervisori:
Dott. Lucia Pozzetti
Dott. Michele Moresco

Collaboratore:
Prof. Jarle Brinchmann

Esame finale anno 2019

Settore Concorsuale: 02/C1 – Astronomia, Astrofisica, Fisica della Terra e dei Pianeti
Settore Scientifico Disciplinare: FIS/05 – Astronomia e Astrofisica

Abstract

One of the key open questions of galaxy evolution is to understand when, how and where the star formation ceases (the so called star formation quenching). It is well known that galaxies have pronounced bimodal distributions of their main properties, and that they are segregated into the two populations of blue star-forming (spiral and irregular) and red passive (elliptical and lenticular) galaxies. There is a general consensus on a scenario in which blue/star-forming galaxies quench their star formation transforming into red passive systems. However, the processes which drive this change in galaxy properties and structure are still unclear. The main goal of this Thesis work is twofold. On the one hand, we aim at defining new methods to select galaxies that are in the critical phase of quenching, or that have recently (e.g. within 0.5 Gyr) terminated their star formation. On the other hand, the final goal is to study the physical properties of the selected galaxies in order to investigate the origin of the quenching, place constraints on how and where (within the galaxies) star formation terminates and understand the possible evolutionary links with the population of E/S0 galaxies. Our main results can be summarised as follows:

1. In Citro et al. (2017), we proved that [O III]/Hα ratio is a very sensitive tracer of the ongoing quenching as it drops by a factor ~ 10 within ~ 10 Myr from the quenching, assuming a sharp interruption of the star formation, and even for a smoother and slower star formation decline (i.e. an exponential declining star formation history with e-folding time $\tau = 200$ Myr) the [O III]/Hα decreases by a factor ~ 2 within ~ 80 Myr from the quenching.

2. Detecting galaxies when their star-formation is being quenched is crucial to understand the mechanisms driving their evolution. We identify for the first time a sample of quenching galaxies selected just after the interruption of their star formation by exploiting the [O III] $\lambda5007$/Hα ratio and searching for galaxies with undetected [O III]. Using a sample of ~ 174000 star-forming galaxies extracted from the SDSS-DR8 at $0.04 \leq z < 0.21$, we identify the ~ 300 quenching galaxy best candidates with low [O III]/Hα, out of $\sim 26\,000$ galaxies without [O III] emission. They have masses between $10^{9.7}$ and $10^{10.8}$ $M_{\odot}$, consistently with the corresponding growth of the quiescent population at these redshifts. Their main properties (i.e. star-formation rate, colours and metallicities) are comparable to those of the star-forming population, coherently with the hypothesis of recent quenching, but preferably reside in higher-density environments.

   Most candidates have morphologies similar to star-forming galaxies, suggesting that no morphological transformation has occurred yet. From a survival analysis we find a low fraction of candidates ($\sim 0.58\%$ of the star-forming population), leading to a short quenching timescale of $t_Q \sim 50$ Myr and an

e-folding time for the quenching history of $\tau_Q \sim 90$ Myr, and their upper limits of $t_Q < 0.76$ Gyr and τ_Q <1.5 Gyr, assuming as quenching galaxies 50% of objects without [O III] ($\sim 7.5\%$).

Our results are compatible with a 'rapid' quenching scenario of satellites galaxies due to the final phase of strangulation or ram-pressure stripping. This approach represents a robust alternative to methods used so far to select quenched galaxies (e.g. colours, specific star-formation rate, or post-starburst spectra). *These results have been published in Quai et al. (2018, MNRAS, 478, 3335).*

3. In chapter 4, we extend our method to IFU data from the SDSS-IV MaNGA survey, data release 14 (Bundy et al., 2015; Blanton et al., 2017; Abolfathi et al., 2018) in order to derive spatial information about the quenching process within the selected galaxies. To this aim, we analyse 12 SDSS-IV MaNGA galaxies that show regions with low [O III]/Ha compatible with a recent quenching of the star formation. We compare the properties of these 12 galaxies with those of a control sample of 10 MaNGA galaxies with ongoing star formation at same stellar mass, redshift and gas-phase metallicity range. The quenching regions are located between 0.5 and 1.1 effective radii from the centre. This result is supported by their average radial profile of the ionisation parameter, that reaches a minimum at the same radii, while that of the star-forming sample shows an almost flat trend. Moreover, the average radial profile of the star formation rate surface density of our sample is lower than that of the control sample, at any radii, suggesting a sharp decline in their star-formation rate. Finally, the radial profile of gas-phase metallicity of the two samples have a similar slope and normalisation, therefore, our results cannot be ascribed to a difference in the intrinsic properties of the analysed galaxies. *These results are being presented in a paper (Quai et al.) submitted to MNRAS.*

4. In chapter 5, we analyse galaxies in an advanced quenching phase, whose star formation was quenched less than 1 Gyr ago. To this purpose, we search for galaxies with strong Balmer absorption lines (Hδ with equivalent width $> 4-5$ Å, in particular) because these lines are strongest for stellar populations dominated by A-type stars with ages between 300 Myr and 1 Gyr after the interruption of the star-formation. In the literature, these systems have been called Hδ-strong galaxies, and they differ from the classical post-starburst galaxies for the presence of emission lines in their optical spectra. It has been found that their number density decreases with redshift (e.g. Le Borgne et al., 2006; Wild et al., 2009). In this work we will exploit very deep MUSE spectra (>10 hours of exposure time) to study the recent star formation activity, and cessation thereof, in low mass galaxies (i.e. $\log(\mathrm{M}/\mathrm{M}_\odot) \lesssim 10.2$) at $0.3 < z < 1.24$. We selected about 115 Hδ-strong galaxies from a parent sample of about 400 galaxies in the MUSE Hubble Ultra Deep Field (MHUDF Bacon et al., 2017) and we estimated their mass function in three redshift bins by using the $1/\mathrm{V}_{\mathrm{max}}$ technique, also taking into account a correction due to the effects of the radial variation in the large-scale structure. The results are in agreement with the redshift evolution of more massive Hδ-strong galaxies. At fixed mass, the number density

of Hδ-strong with log(M/M$_{\odot}$) $\lesssim 10$ increases from redshift z~ 1.1 to z~ 0.8 and then, it decreases weakly around z ~ 0.45. This behaviour is in contrast with the trend of Hδ-strong in the recent Eagle cosmological simulation, that predicts a decrement in the number density of low mass Hδ-strong from high redshift towards the local Universe. The final steps of this work are ongoing and consist of the general interpretation of the results to understand how these low-mass galaxies evolve (e.g. passive evolution, bursty SFH, etc.). *T*he results will be presented in a paper (Quai et al. in preparation).

CONTENTS

1. INTRODUCTION

1.1 Galaxy formation and evolution in the cosmological context

This PhD Thesis is devoted to giving a contribution to our understanding of when and how the star formation ceases in galaxies, the so-called quenching of the star formation (or quenching). In chapter 2 we illustrate a comprehensive introduction to the quenching. Before diving into this fundamental open question in galaxy evolution, in this Chapter, we frame galaxies in the cosmological context in which they formed and evolve and we provide a useful overview of the main observational and general properties of the star-forming galaxies representing the precursors of the quenching phase.

1.2 The standard ΛCDM model of cosmology

Modern cosmology is rooted in a spatially homogeneous and isotropic Universe on large scales (the cosmological principle), and in the theory of General Relativity, that predicts the structure of space-time according to the mass distribution in the Universe. This theoretical basement and the observational efforts in the last decades, have led to the current standard cosmological model, referred to as ΛCDM (Λ cold dark matter), in which a flat (Euclidean), expanding Universe is dominated by the dark energy (referred to as the cosmological constant Λ) for about 75% and by a cold (non-relativistic) dark matter for $\sim 21\%$. Only the remaining 4% is due to baryons[1] that constitute the visible Universe. Despite dark matter accounts for about 85% of the entire mass in the Universe, its nature is still elusive, due to its inability to interact electromagnetically. However, the existence of dark matter is supported by several observational results, such as evidence of galactic rotation curves that remain flat at large radii (e.g. Roberts and Rots, 1973; Rubin, Ford, and Thonnard, 1978; Rubin, Ford, and Thonnard, 1980), the high dynamic mass in cluster of galaxies and gravitational lensing of background galaxies (Zwicky, 1933). Dark energy, that takes the form of a constant vacuum energy density, is instead responsible for the accelerated expansion of the Universe, as revealed by the distances of standard candles Type Ia supernovae up to z $\sim 1.5 - 2$ (e.g. Riess et al., 1998; Perlmutter et al., 1999).

[1]Cosmologists refer to baryons as all the particles in the Standard Model of atomic physics that interacts electromagnetically, including electrons and the other leptons. In other word, baryons are the components of the ordinary matter that forms galaxies, stars, men, etc.

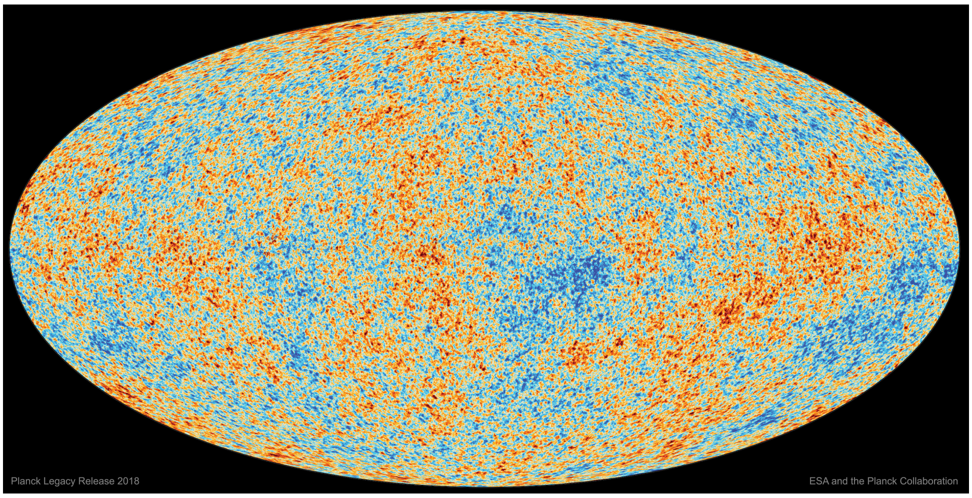

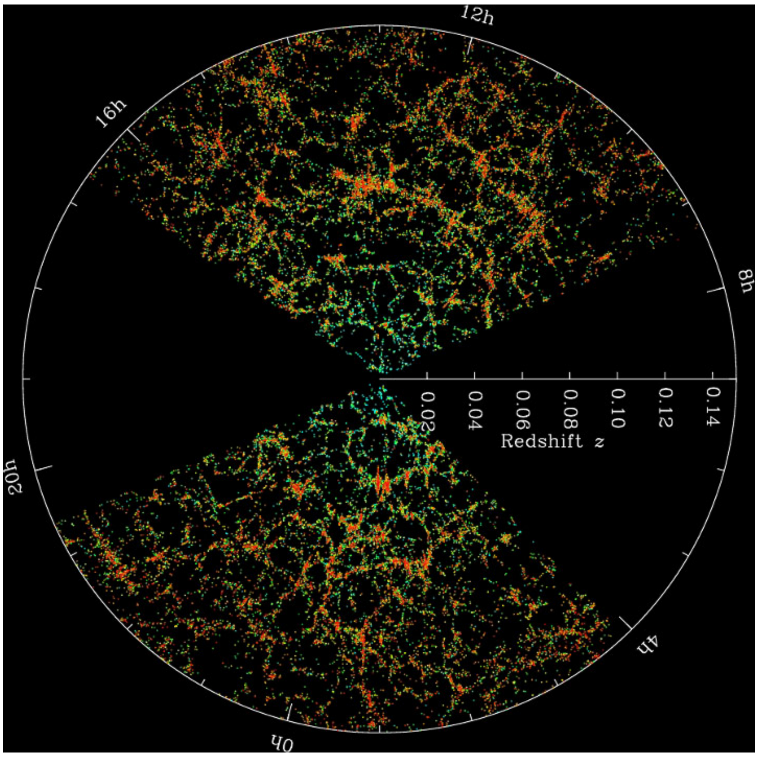

FIGURE 1.1: *Top:* the map of the anisotropies of the Cosmic microwave background (CMB) with the highest angular resolution so far, as observed by Planck mission. Image credit: ESA and the Planck Collaboration. *Bottom:* the local large-scale structure (LSS) from the SDSS 3-dimensional map of the distribution of galaxies. Earth is at the centre, and each point represents a galaxy, that is coloured according to its average stellar population age: redder implies older ages. Image credit: M. Blanton and SDSS.

In this scenario, the primordial seeds of structures observed in the local Universe are Gaussian-distributed adiabatic fluctuations with an almost scale-invariant spectrum. The most accepted theory predicts that these energy density perturbations may arise from quantum processes in the early phases of the Universe, during an exponential expansion (called inflation) driven by the vacuum energy (Guth, 1981; Guth, Kaiser, and Nomura, 2014). The discovery of the cosmic microwave background (CMB) by Penzias and Wilson (1965), a snapshot of the Universe about 380.000 years after the Big Bang (corresponding to a redshift z $\sim$ 1100), playes a primary role in constraining the fundamental of the standard cosmology. Temperature anisotropies and polarisation (see Figure 1.1) in the CMB represent one of the most powerful probes of cosmology and early-Universe evolution, because they are due to primordial signatures of the fluctuations that grew up to form all the structures that we see today (e.g. Smoot, Gorenstein, and Muller, 1977; Smoot et al., 1992; Bennett et al., 2003; Hinshaw et al., 2003; Spergel et al., 2003; Planck Collaboration et al., 2014; Planck Collaboration et al., 2018). On the other hand, the complexity of the spatial density distribution of structures on scales larger than that of a galaxy (the so-called large-scale structure, LSS) depends both on cosmological parameters (e.g. dark matter and dark energy densities) and on the physics of galaxy formation and evolution. Therefore, the analysis of the LSS helps in placing tight constraints on the theoretical stage of the growth of initial energy density fluctuations of the early Universe via gravitational instability. At present, the largest survey of galaxies is the Sloan Digital Sky Survey (SDSS York et al., 2000), a map that covers about 12000 degrees of the sky in the local Universe (z $\sim$ 0.2) with position and distances of a million of galaxies. The SDSS and other similar surveys (e.g. 2dFGRS, Colless et al., 2001) reveal a LSS with galaxies distributed following a Swiss cheese pattern (see Figure 1.1), where huge voids of $10-100$ Mpc in diameter (containing a few, or no galaxies) are surrounded by low-density filaments which, in turn, intersect in high-density clusters (containing thousands of galaxies) or in smaller groups (containing up to a dozen of galaxies). Another step forward in this direction will be done in the coming five years with the new surveys generation such as ESA-Euclid, NASA-WFIRST, DESI, 4MOST and LSST, among many others. These missions are aimed at mapping the LSS and the evolution of cosmic structures out to redshift z $\sim$ 2 (or about 10 billion years in look-back time).

1.3 Structure formation in the ΛCDM context

The formation of galaxies represents one of the main open questions. As mentioned earlier, observations suggest that galaxies reside in extended halos of dark matte. Dark matter, for instance, is thought to be responsible to keep flat the rotation curves of spiral galaxies at distances at which there are no stars and gas anymore. According to the cosmological framework, these halos result from the linear growth of the density fluctuations that follows the early expansion of the Universe. When the perturbations reach a critical density, they decouple from the expansion and collapse to form virialised dark matter halos. These halos continue to grow hierarchically, both in mass and size, by accreting material from the surrounding medium or by the coalescence (merging) with other halos (bottom-up growth scenario). In this scenario, baryons are bound to follow the collapsing collision-less dark matter halos. This inward motion generates shocks in the collisional baryons which are heated to the virial temperature of host halos. Later, if cooling is inefficient (slow cooling), the baryonic gas can settle into a quasi-hydrostatic equilibrium in the potential well of the dark matter halo (White and Rees, 1978). When the cooling gas accumulates enough to be supported by self-gravitation it can collapse catastrophically, increasing the density and temperature and reducing the cooling time and forming clouds of cold gas. The gas clouds may then fragment into small cool clumps of neutral atomic and molecular gas that may form the first generation of stars in galaxies. It must be clear, however, that galaxy formation is far from being completely understood. For instance, White and Rees (1978) already pointed out the role of negative stellar feedback, predicted by Larson (1974), to explain the low efficiency of galaxies formation. Several processes involve baryonic physics in the formation and evolution of galaxies, including but not limited to (i) the AGN formation, accretion and feedbacks, (ii) the rate and mechanism of cosmological gas accretion, (iii) the interplay between star formation and rate of supernovae which, in turn, is related to the problem of the universality of the initial mass function that rules the initial distribution of stellar masses. Understanding these various mechanisms and their coaction is one of the most important and difficult issues in the global comprehension of the formation and evolution of galaxies.

1.4 The *inside-out* growth scenario for disc galaxies

The Thesis project deals with galaxy quenching of the star formation. It is therefore important to provide a general description of star-forming galaxies.

The formation of galaxy discs within the bottom up growth scenario was proposed by Fall and Efstathiou (1980). In a hierarchical evolution of the primordial fluctuations, the angular momentum in disc galaxies is produced by cosmological tidal torques acting at early times (Peebles, 1969). Therefore, Fall and Efstathiou (1980) predicted that starting from these initial conditions, disc galaxies formed from collapsing gas in extended massive halos (or coronae).

The theory of cosmological tidal torques (Peebles, 1969), predicts also that mean specific angular momentum of galaxies (i.e. angular momentum per unit mass) must increase with time. This results lead to a scenario for the evolution of disc galaxies in which the outskirts should form later than the inner part, by acquiring gas at higher angular momenta from the surrounding corona (the so-called *inside-out* growth Larson, 1976). Inside-out growth is also predicted by hydrodynamical simulations (e.g. Pichon et al., 2011; Stewart et al., 2013) and it is supported by chemical evolution models (e.g. Boissier and Prantzos, 1999; Chiappini, Matteucci, and Romano, 2001).

This scenario is in agreement with numbers of observational evidences (e.g. Prantzos and Boissier, 2000; Gogarten et al., 2010; Spindler et al., 2018). Indeed, a natural consequence of inside-out growth is that central regions of galactic discs are, on average, older and more metal-rich than the outskirts (e.g. Zaritsky, Kennicutt, and Huchra, 1994; Rosales-Ortega et al., 2011; Sánchez-Blázquez et al., 2014; González Delgado et al., 2014b; González Delgado et al., 2015; González Delgado et al., 2016; Goddard et al., 2017b; Goddard et al., 2017a). These observational results showed even more intriguing aspects when it turned out that almost every isolated galaxy in the local universe exhibits similar strong negative radial profiles of oxygen abundance (e.g. Vila-Costas and Edmunds, 1992; Zaritsky, Kennicutt, and Huchra, 1994; Sánchez et al., 2012; Sánchez et al., 2014; Carton et al., 2015; Carton et al., 2018). Moreover, once negative gradients are normalized to the effective radius (r_e), they systematically show similar slopes (-0.12 dex/r_e) (Boissier and Prantzos, 1999; Boissier and Prantzos, 2000; Sánchez et al., 2014; Ho et al., 2015). Discs show, in addition, remarkably dust-corrected colour gradients (e.g. de Jong and Lacey, 2000; Muñoz-Mateos et al., 2007; Wang et al., 2011), with outskirts becoming bluer with increasing galactocentric distance and this behaviour is observed also in the Milky Way disc (Portinari and Chiosi, 1999). This almost ubiquitous behaviour can be explained by a common evolution of gas, chemical history and stars (Ho et al., 2015), bearing in mind that without a continuous replenishing of fresh gas, galaxies would have fuel to sustain at most ~ 1 Gyr of star formation (Tacconi et al., 2013). In other words, the star-forming galaxies need for a systematic supply of new gas and, together with evidence that inside-out growth is still active in outer part of most local star-forming galaxies (e.g. Wang et al., 2011; Muñoz-Mateos et al., 2011; Pezzulli et al., 2015), it suggests that galactic halos are still providing high angular momentum gas to assemble the outskirts of galaxies. Bouché et al. (e.g. 2010) model predicts a co-evolution of accretion rate from surrounding halo, star formation and outflows (see also Lilly et al., 2013; Peng and Maiolino, 2014). However, starting from the evidence that hot coronae must rotate more slowly than the disc (i.e. pressure gradients provide support against gravity) Pezzulli and Fraternali (2016) discussed that a misalignment between disc and halo velocity implies a systematic radial gas flow towards the inner parts of galaxies. Taking into account this effect and disentangling it from the contribution of inside-out growth in their models, these flows show a strong impact on the structural and chemical evolution of galaxies, naturally creating strong steep abundance gradient. Those models predict, for instance, that $70-80\%$ of disc velocity is required to match observations in a galaxy like Milky Way.

1.5 Main scaling relations of star-forming galaxies

In this section, we present an overview (not exhaustive) of the main scaling relation of star-forming galaxies, which represent the obvious precursors of the quenching galaxies.

Our understanding of the formation and evolution of galaxies is hampered by the complexity of baryon cycle in the interstellar medium. Direct observations of gas flows would give constraints on the dynamics of the accretion process in star-forming galaxies, however, they are very challenging to observe and indirect methods are therefore necessary to study the whole history of galaxies. Fundamental indirect tracer, such as the gas-phase metallicity, the stellar mass and the star-formation rate (SFR), can help to unravel this evolution. It has been suggested that galaxies grow in a regulated fashion which maintains an equilibrium between cosmological accretion rate, star formation, gas-phase metallicity and outflow rate (e.g. Erb, 2008; Bouché et al., 2010; Peeples and Shankar, 2011; Davé, Finlator, and Oppenheimer, 2012; Lilly et al., 2013; Peng and Maiolino, 2014). In the previous section, we have already mentioned how chemical evolution history can support an inside-out growth scenario. In the following, we focus on other fundamental relation that can help in building a comprehensive global picture in galaxy evolution.

1.5.1 The Schmidt-Kennicutt law

To push forward our understanding of galaxy evolution is needed a solid understanding of the link between the star formation activity and the physical condition (both dynamical and chemical) of the interstellar medium (ISM) that fuels the SFR. To this topic are related all the others evolutionary studies, with implications for the gas cycle and chemical enrichment, kinematics and dynamic of gas and stars, assembly of stellar mass and evolution of stellar populations and star formation quenching among other crucial subjects. Schmidt (1959) was the first to argue that there should be a scaling relation between gas density ($\rho_{\rm gas}$) and star formation rate density ($\rho_{\rm SFR}$) and introduced a power law relation of the form

$$\rho_{\rm SFR} = \frac{\epsilon_{\rm SF}}{t_{\rm SF}} \times \rho_{\rm gas}, \tag{1.1}$$

in which the coefficient $\epsilon_{\rm SF}$ is the efficiency at which gas is converted into stars over the time scale $t_{\rm sf}$ and it is related to the micro-physics of conversion gas content into stars (e.g. Cen and Ostriker, 1992). Different assumptions on this efficiency lead to significant variation of equation (1.1). The most common choice is to opt for $t_{\rm sf} = t_{\rm ff}$, where $t_{\rm ff}$ is the free-fall time, defined as $t_{\rm ff} = \sqrt{3\pi/32G\rho}$. In this case, $\epsilon_{\rm SF} = \epsilon_{\rm ff}$ assumes the meaning of a star formation efficiency (SFE) per free-fall time and the (1.1) becomes $\rho_{\rm SFR} \propto \rho_{\rm gas}^{1.5}$.

Since most observations of external galaxies can only measure two-dimensional projected observables, integrated along the line of sight, in literature is commonly used the version of (1.1) in terms of surface densities[2], that was proposed in the seminal work of Kennicutt (1998b):

$$\Sigma_{\rm SFR} = A \times \Sigma_{\rm gas}^{\rm N}, \tag{1.2}$$

that is known as the Kennicutt law or Schmidt-Kennicutt (SK) law . The term $\Sigma_{\rm gas}$ comprehends both atomic ($\Sigma_{\rm HI}$) and molecular ($\Sigma_{\rm H_2}$) hydrogen and the precise form of 1.2 changes with different chosen assumptions for deriving $\Sigma_{\rm gas}$ from the observables. In Figure 1.2 is shown an updated version of the global SK relation in local galaxies (z < 0.3), in which different symbols represents individual galaxies from different dataset (see legend in the figure). A constant X(CO) factor (i.e. the conversion factor from CO luminosity to H_2 mass, with no correction for helium) of 2.3×10^{20} cm^{-2} (K km s^{-1})$^{-1}$ is applied. A strong correlation is clearly present, with a slope N $= 1.4 - 1.5$ (Kennicutt, 1998b). However, three distinctly different regimes can be observed (see vertical lines in Figure 1.2): (i) a low-density regime

[2]Bacchini et al. (in preparation) are investigating a tridimensional version of the SK relation.

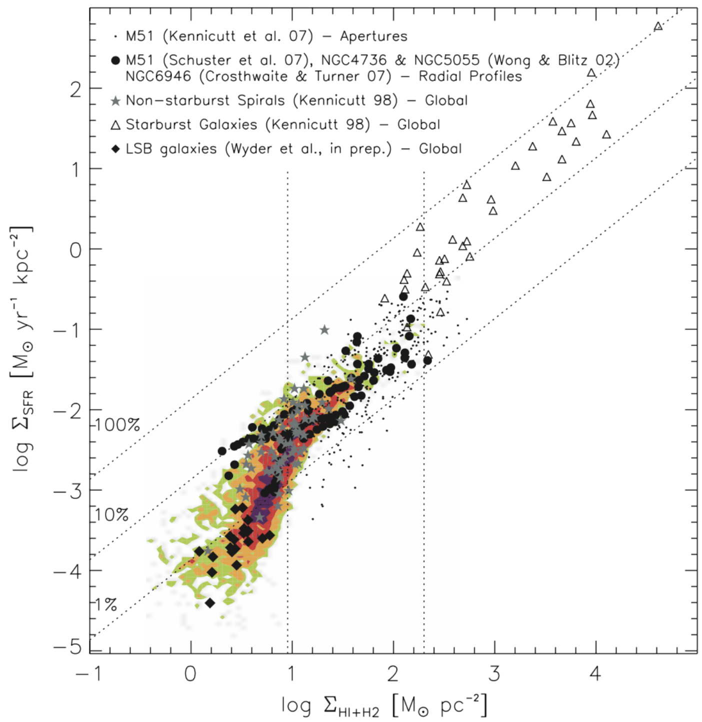

FIGURE 1.2: The relation between $\Sigma_{\rm SFR}$ and total (atomic + molecular) gas surface densities $\Sigma_{\rm gas}$. The diagonal dotted lines and all other plot parameters are the same as in Figure 4. Superimposed as black dots are data from measurements in individual apertures in M51 (Kennicutt et al., 2007). Data points from radial profiles from M51 (Schuster et al., 2007), NGC4736, and NGC5055 (Wong and Blitz, 2002) and from NGC 6946 (Crosthwaite and Turner, 2007) are shown as black filled circles. Furthermore, are shown disk-averaged measurements from 61 normal spiral galaxies (filled gray stars) and 36 starburst galaxies (triangles) from K98. The black filled diamonds show global measurements from 20 low surface brightness galaxies (Wyder et al., 2009). Data from other authors were adjusted to match the assumptions on the underlying IMF, X(CO) and galaxy inclinations. One finds good qualitative agreement between our data and the measurements from other studies despite a variety of applied SFR tracers. From Bigiel et al. (2008) and Kennicutt and Evans (2012).

at 10 $M_\odot$ pc^{-2}, with gas dominated by HI and without a clear correlation with the SFR density (typically dwarf galaxies), (ii) an intermediate regime characterised by a tight correlation (normal star-forming galaxies) and (iii) a higher-density regime at $\Sigma_{\rm gas} > 100$ $M_\odot$ pc^{-2}, with a slightly shift above the normal star-forming relation (typically starburst systems). Most normal galaxies follow a tight relation with a dispersion of about ± 0.30 dex, that is considerably higher than what can be attributed to observational uncertainties, which suggests that much of the dispersion is physical. The SK relation is strongly affected by the assumptions made about the choice of X(CO). Different studies showed that high-redshift starburst systems, for which a typical Milky Way X(CO) was applied, tend to follow the local SK relation. Instead, if a lower X(CO) factor is applied (as suggested by many independent analyses of X(CO), e.g. Leroy et al., 2013), the SK relation of these starbursts is shifted above the local relation, forming a parallel relation (e.g. Bouché et al., 2007; Daddi et al., 2010;

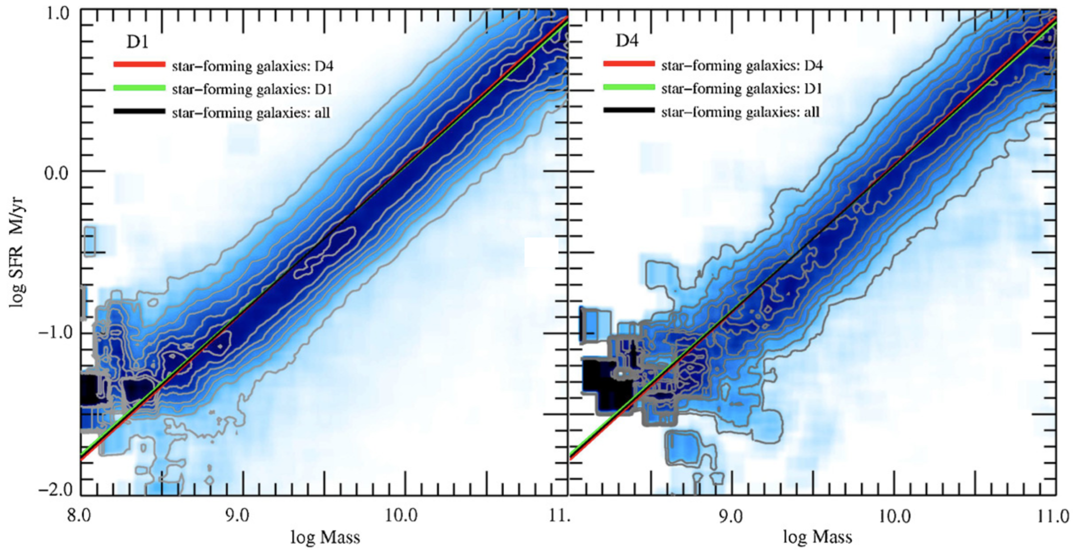

FIGURE 1.3: The SFR-stellar mass relation for star-forming SDSS galaxies in low-density environments D1 (left) and high-density environments D4 (right). The three coloured straight lines represent the fitted relation for all galaxies (black), and for those in D1 and D4 (green and red, respectively) From Peng et al. (2010) .

Genzel et al., 2010).

1.5.2 The star formation rate-mass relation

The star formation in galaxies is tightly correlated to the stellar mass (e.g. Brinchmann et al., 2004) and many authors described, almost simultaneously, a linear relation which connects the SFR of star-forming galaxies with their stellar mass (e.g. Daddi et al., 2007; Elbaz et al., 2007; Noeske et al., 2007b, see Figure 1.3). Noeske et al. (2007b) defined this relation the main sequence (MS) of the star-forming galaxies, though there is no evidence of precise tracks along which galaxies move in a SFR-Mass plane.

The existence of this SFR-Mass relation is linked to the physical processes regulating galaxy formation and evolution (Dutton, van den Bosch, and Dekel, 2010; Hopkins et al., 2010; Leitner, 2012). The correlation has been firmly established from the local to the earliest Universe out to z $\sim$ 7 (e.g. Brinchmann et al., 2004; Noeske et al., 2007b; Elbaz et al., 2007; Daddi et al., 2007; Pannella et al., 2009; Stark et al., 2009; Magdis et al., 2010; González et al., 2010; Peng et al., 2010; Rodighiero et al., 2010; Oliver et al., 2010; Karim et al., 2011; Papovich et al., 2011; Lee et al., 2012; Reddy et al., 2012; Whitaker et al., 2012; Salmon et al., 2015). A strong correlation between SFR and stellar mass throughout the cosmic epochs and its tightness (e.g. $0.25 - 0.3$ dex Noeske et al., 2007b; Rodighiero et al., 2011; Sargent et al., 2012; Whitaker et al., 2012) imply a high degree of homogeneity suggesting that some kind of self-regulation mechanism may be at work among the most of star-forming galaxies (e.g. Noeske et al., 2007b; Bouché et al., 2010; Peng et al., 2010; Leitner, 2012; Behroozi, Wechsler, and Conroy, 2013). The few outliers in the SFR-Mass relation are shifted above the MS, showing higher SFRs with respect to normal star-forming of similar mass and, for this reason, are called starburst systems. These galaxies are linked to a highly efficient mode of the star-formation, that is triggered by major mergers (Rodighiero et al., 2011). However, they account for only about the 2% of mass-selected star-forming galaxies, suggesting that major mergers are not the main mechanism for forming stars in star-forming galaxies.

It is common to express the relation in terms of SFR per unit galaxy mass, or specific-SFR (sSFR). The inverse of the sSFR is proportional to the timescale with which a galaxy assemblies its stellar content[3] and thus it is useful to characterise the star formation history of a galaxy. Using sSFR, the SFR-Mass relation is parametrised as:

$$\log(\mathrm{sSFR})\ [\mathrm{yr}^{-1}] = \alpha \times \log(\mathrm{M}/\mathrm{M}_{\odot}) + \beta. \tag{1.3}$$

The slope α is negative, with the sSFR clearly decreasing towards the more massive galaxies. The slope slightly varies in different studies between $\sim -0.4, -0.2$ due to effects of different sampling (e.g. Stringer et al., 2011; Salmi et al., 2012) and observational (e.g. extinction correction to SFR indicator; Wuyts et al., 2011) biases and it is still unclear if the slope changes with redshift (e.g. Pannella et al., 2009; Rodighiero et al., 2010; Karim et al., 2011; Whitaker et al., 2012; Rodighiero et al., 2014). A negative slope suggests that the downsizing scenario (see section 1.6) should be responsible for the evolution of star-forming galaxies, where low massive galaxies are forming a high fraction of their stellar content today, while the more massive ones must have formed their stars much earlier. Instead, it is observed an evolution of the normalisation β in equation (1.3) over cosmic time: in the distant universe galaxies were more active in building their stellar content relative to today (e.g. Madau et al., 1996). For a given mass, the SFR is stayed roughly constant from z $\sim$ 7 to z $\sim$ 2 (González et al., 2010; Karim et al., 2011) when the cosmic-SFR density peaks (Wilkins, Trentham, and Hopkins, 2008; Madau and Dickinson, 2014) and then it is decreased by a factor of about 30 from z$\sim$ 2 to z$=0$ (Daddi et al. 2007). The elevated rates of star formation observed in the early Universe can be explained by a larger reservoir of cold gas in galaxies that was continuously replenished by higher accretion rate (Bouché et al., 2010). The rapid decline of the normalization from z $\sim$ 2 to now, instead, is mostly due to gas exhaustion (e.g. Noeske et al., 2007a; Daddi et al., 2007; Magdis et al., 2012; Tacconi et al., 2013).

An overview on the sSFR-Mass evolution is given in Sargent et al. (2014) in which they collected the results of several studies from z $= 0$ out to z $\sim$ 7 to show the redshift dependence of the sSFR of star-forming galaxies with stellar mass. In Figure 1.4 is reported their study for two different stellar scales: $\mathrm{M}_*/\mathrm{M}_{\odot} \approx 5 \times 10^9$ and 5×10^{10}. From the direct comparison of the two trends, they obtained a slope $\alpha \sim -0.2$ for the relation 1.3. Moreover, it appears clear the steep rise of sSFR in star-forming galaxies out to z $\sim$ 3. At z > 4 samples do not contain enough high-mass galaxies to probe their evolution, while the sSFR of galaxies with $\mathrm{M}_*/\mathrm{M}_{\odot} \approx 5 \times 10^9$ flattens or increases slowly. Moreover, also the lower normalisation of the two sSFR in the more

[3]The sSFR scales directly with the parameter b (the stellar *birthrate*), defined as the ratio between the current and the average SFR in the past: b = SFR/ $<$ SFR $>$. Since / $<$ SFR $>$=$\mathrm{M}_*/\mathrm{t}_0$, with M_* the stellar mass of the galaxy and $\mathrm{t}_0 \sim 10^{10}$ yr the age of the Universe. Hence b = SSFR $\times$ t_0.

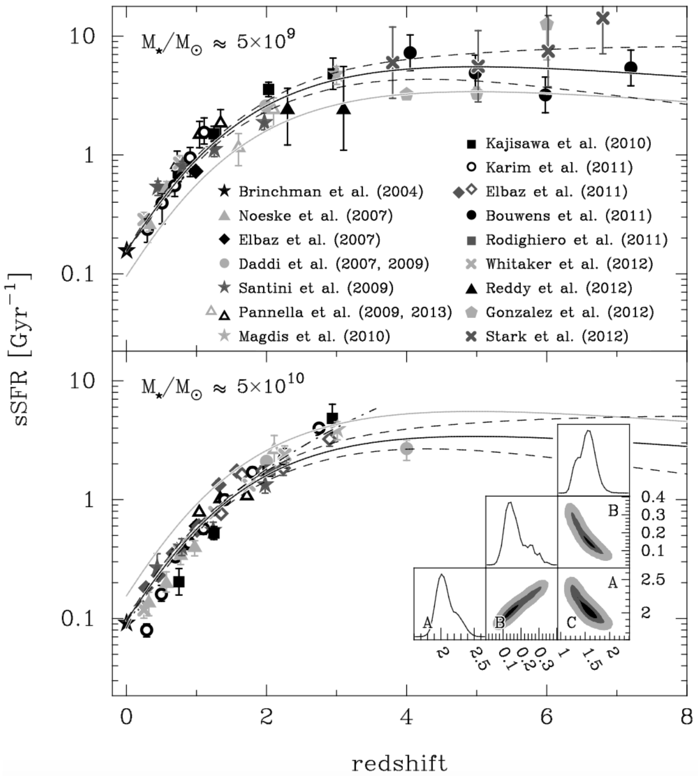

FIGURE 1.4: Redshift dependence of the sSFR of star-forming galaxies with stellar mass $M_*/M_\odot \approx 5\times10^9$ (top) and 5×10^{10} (bottom) draw from a collection of recent results (see legend. Measurements derived based on image-stacking are indicated with open symbols and error bars denote the uncertainty on the sSFR-average rather than the sSFR-scatter in the population. Solid/dashed black lines (the best-fit evolution of the sSFR) and associated 2σ limits; light gray lines indicate the sSFR evolution in the other stellar mass bins, for comparison; dot-dashed line represents the evolution according to $(1+z)^{2.8}$. From Sargent et al. (2014).

massive mass bin, that indicates a shorter birthrate, suggests a downsizing scenario (see section 1.6) for the assembly of the stellar content.

Recently, it emerged that the MS tends to bend at stellar masses larger than $\log(M/M_\odot) > 10.5$ requiring to be fitted by a double power law, one for the highest masses and the other one for lower masses. A suggested possibility for the flattening of the high-mass tail of the MS is that galaxies above the turnover mass have gradually reduced the star formation efficiency and are experiencing a slow quenching of the star formation due, for example, to the growth of bulges (e.g. Salmon et al., 2015; Lee et al., 2015; Schreiber et al., 2015).

1.5.3 The mass-metallicity relation

It is well known that star-forming galaxies present a strong correlation between gas-phase metallicity and stellar mass (M-Z relation, Lequeux et al., 1979), being massive galaxies more metal-rich. A similar relation has been also found for the stellar metallicity (e.g. Gallazzi et al., 2005; Mendel et al., 2009; González Delgado et al., 2014a),

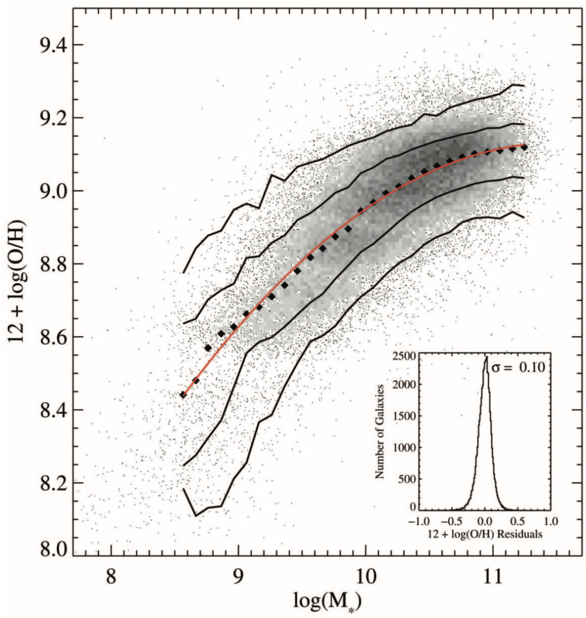

FIGURE 1.5: Relation between gas-phase oxygen abundance and stellar mass for a sample of star-forming galaxies in the SDSS. The large black filled diamonds represent the median in bins of 0.1 dex in mass that includes at least 100 data points. The solid lines are the contours that enclose 68% and 95% of the data. The red line shows a polynomial fit to the data. The inset plot shows the residuals of the fit. From Tremonti et al. (2004).

but with a larger scatter at low-masses. Using a large sample of local (z $\sim$ 0.1) star-forming galaxies extracted from the Sloan Digital Sky Survey (SDSS), Tremonti et al. (2004) found that this correlation spans over about three orders of magnitude in stellar mass and a factor of 10 in gas-phase oxygen abundance and it shows a small dispersion ($\sim$ 0.1 dex), though it presents a clear flattening above $\sim 10^{10.5}$ $M_\odot$ (see Figure 1.5). Kewley and Ellison (2008) found that this bending depends on the aperture covering fraction. Moreover, they argued that the M-Z relation can vary significantly when different metallicity calibrations are used, thus requiring the need to compare different works only when similar metallicity calibrations are assumed (see also Foster et al., 2012). The M-Z correlation has been confirmed also at higher redshift, where it shows a clear evolution. At redshifts $0.4 < z < 1$ the evolution have been confirmed by several groups (Lara-López et al., 2009a; Lara-López et al., 2009b; Savaglio et al., 2005; Kobulnicky and Kewley, 2004; Mouhcine et al., 2006; Rodrigues et al., 2008), though Carollo and Lilly (2001) did not find significative differences between a sample of galaxies at $0.5 < z < 0.7$ and a local one. However, other studies at higher redshift have confirmed clear evidences of the evolution up to z$\sim$ 4 (e.g. Savaglio et al., 2005; Erb et al., 2006; Maiolino et al., 2008; Mannucci et al., 2009; Henry et al., 2013; Maier et al., 2014; Maier et al., 2015; Salim et al., 2015) and even at $3 < z \lesssim 5$ Laskar, Berger, and Chary (2011) have found an offset of the relation towards lower metallicities.

With the advent of integral field spectroscopy, it became possible to investigate the spatially resolved M-Z relation. Moran et al. (2012) and Rosales-Ortega et al. (2012), independently found a correlation between the local stellar mass density and the metallicity, as a scaled version of the total M-Z relation. This result suggests that the M-Z relation is stable when using single aperture spectroscopic (and the obvious inconvenient of aperture effects) or spatially resolved data (e.g. Sánchez et al., 2014; Sánchez et al., 2017).

Several mechanisms have been proposed to explain the origins of the M-Z relation, including: (i) higher capability of massive galaxies (i.e. deeper potential well) to retain enriched gas ejected by stellar feedback, or in other words that outflows are more effective at expelling rich-gas from less massive galaxies (e.g. Larson, 1974; Edmunds, 1990; Tremonti et al., 2004; Kobayashi, Springel, and White, 2007; Scannapieco et al., 2008; Spitoni et al., 2010); (ii) the accretion of pristine gas by inflows from the inter-galactic medium and the coaction with outflows of enriched gas (e.g. Finlator and Davé, 2008; Davé et al., 2010; Mannucci et al., 2010); (iii) an IMF that varies with galaxy mass (e.g. Köppen, Weidner, and Kroupa, 2007; Wilkins, Trentham, and Hopkins, 2008; Spitoni et al., 2010; Gunawardhana et al., 2011; Ferreras et al., 2012); (iv) the downsizing (e.g. Maier et al., 2006; Brooks et al., 2007; Maiolino et al., 2008; Mouhcine et al., 2008; Calura et al., 2009; Vale Asari et al., 2009; Zahid, Kewley, and Bresolin, 2011), or a combination of them. The downsizing scenario (see section 1.6) naturally leads to an M-Z relation: a lower α-elements abundance ratio in less massive local galaxies suggests that they are forming slowly over longer timescales (e.g. Cowie et al., 1996; Kodama et al., 2004; Thomas et al., 2010). Moreover, Nagao, Maiolino, and Grazian (2008) found that the evolution of the M-Z relation is stronger in less massive galaxies, because more massive galaxies assemble their stars and consequently reach their final chemical state earlier than less massive ones. This is also in agreement with Garnett (2002) who suggested that less massive galaxies have higher gas fractions than more massive ones, and therefore they are still converting gas into stars. Moreover, Rodrigues et al. (2012) showed that gas fraction increases with redshift, leading to a natural evolution of the M-Z relation in a downsizing scenario. On the other hand, other studies (e.g. Erb et al., 2006; Erb, 2008; Mannucci et al., 2009) suggest that a high gas fraction (and its relation with chemical evolution) in high redshift galaxies indicates the infall of pristine gas as the dominant mechanism for the M-Z relation (e.g. Agertz, Teyssier, and Moore, 2009; Bournaud and Elmegreen, 2009; Brooks et al., 2009; Dekel et al., 2009). Moreover, the evidence of positive metallicity gradients in disc galaxies at z~ 3.5 can be also explained by accretion of low-metallicity gas.

1.5.4 The Fundamental metallicity relation

Metallicity in galaxies is, at a basic level, the result of the action of (i) inflows, that dilute the ISM with almost pristine low-metallicity gas, (ii) star formation, that is fuelled by the in-falling gas and that generates an increment of the metallicity and (iii) outflows, that eject metals produced by supernovae (i.e. a product of the star formation). Therefore, a relation between metallicity and SFR is expected to exist. Mannucci et al. (2010) have reported a secondary correlation of the M-Z relation with the SFR in SDSS local galaxies: the so-called fundamental metallicity relation (FMR). The FMR is an anti-correlation of metallicity with the SFR, i.e at a fixed stellar

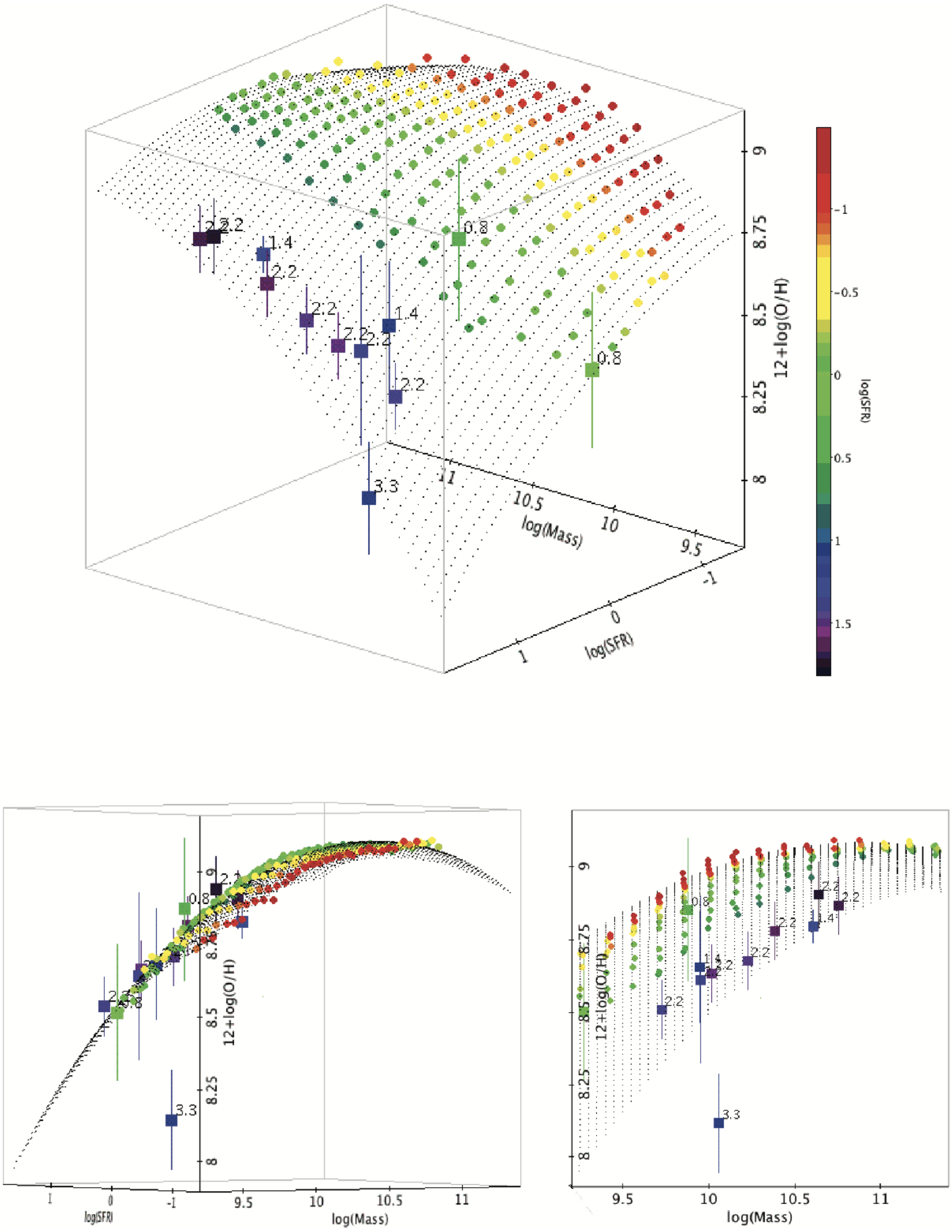

FIGURE 1.6: The surface generates by the FMR (Mannucci et al., 2010) in the plane M_*, SFR and gas-phase metallicity. Circles without error bars are the median values of the metallicity of local SDSS galaxies in bins of M_* and SFR, colour-coded with SFR. The dispersion of single galaxies around this surface is about 0.05 dex. The black dots show a second-order fit to these SDSS data, extrapolated towards higher SFR. Square dots with error bars are the median values of high-redshift galaxies. Labels show the corresponding redshifts. The projection in the lower left-hand panel shows that most high-redshift data fall in the same surface defined by low-redshift data. emphasising the absence of a redshift evolution for the FMR. The projection in the lower right-hand panel suggests that the origin of the observed evolution in metallicity up to z = 2.5 can be due to the progressively increasing SFR. From Mannucci et al. (2010).

mass, galaxies with higher SFR have lower gas-phase metallicity, though the effect is more pronounced in less massive galaxies, while in massive galaxies the metallicity does not depend on SFR (see Figure 1.6). Ellison et al. (2008) had already found a weak dependence of metallicity on specific-SFR and also Lara-López et al. (2010) presented a relation almost identical (just with a different functional form) to the FMR.

Mannucci et al. (2010) found also that the FMR does not show any evolution up to z ~ 2.5, suggesting that the same physical process drives galaxy evolution on a long interval of cosmic time. On the contrary, more recent studies (e.g. Cullen et al., 2014; Maier et al., 2014; Zahid et al., 2014) argued that FMR evolves towards higher redshift, since galaxies at z ~ 2 does not lie on the local FMR relation.

However, the FMR is not without tension, with an intense debate over its origin or existence. For example, Andrews and Martini (2013) found a discrepancy with the result of Mannucci et al. (2010), arguing that the secondary correlation does not change towards higher masses and Yates, Kauffmann, and Guo (2012) found that in massive galaxies the metallicity increases towards increasing SFR. Other authors observed that a secondary dependence on SFR could be spurious, and plausibly due to selection effects (e.g. Juneau et al., 2014) or to systematic errors in metallicities estimation (e.g. Yates, Kauffmann, and Guo, 2012) or to bias introduced by the fiber aperture covering (e.g. Sánchez et al., 2013; Sánchez et al., 2017).

1.6 The downsizing scenario

Since the late nineties, it started to emerge a discrepancy between the stellar assembly history of galaxies traced by observations and the hierarchical assembly of structures predicted by cosmology. Empirically, there are several proofs suggesting that more massive galaxies have formed their stellar content earlier and on shorter timescales than less massive ones (see Figure 1.7). Typically, one refers to this scenario as *Downsizing* (Cowie et al., 1996). Among the evidences, the most compelling ones are that more massive galaxies: (i) host older stellar populations than lower mass galaxies, both in high-density (e.g. Nelan et al., 2005; Thomas et al., 2005; Thomas et al., 2010) and in low-density environments (e.g. Trager et al., 2000; Heavens et al., 2004; Gallazzi et al., 2005; Panter et al., 2007; Thomas et al., 2010); (ii) are more metal rich (see subsection 1.5.3), (iii) have (in the case of early-types galaxies) enhanced [α/Fe] ratio (e.g. Carollo, Danziger, and Buson, 1993; Davies, Sadler, and Peletier, 1993; Trager et al., 2000; Kuntschner et al., 2001; Bernardi et al., 2006; Thomas et al., 2010) indicating a shorter timescale of the star formation that leads to high rates of Type II Supernovae explosions of massive stars, thus an enhanced production of α-elements (*archeological downsizing* Thomas et al., 2010); (iv) have (in the case of star-forming galaxies) lower specific-SFR, implying that they were forming the most of their stars earlier and at higher rates (see subsection 1.5.2).

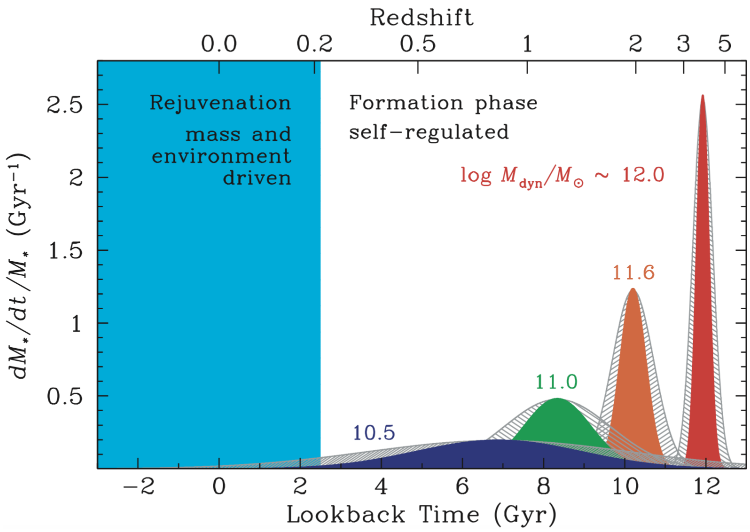

FIGURE 1.7: Specific-SFR as a function of look-back time for early-type galaxies of various masses (see labels).The grey hatched curves indicate the range of possible variation in the formation time-scales that are allowed within the intrinsic scatter of the [α/Fe] ratios derived. These star formation histories are meant to sketch the typical formation history averaged over the entire galaxy population (at a given mass), while real star formation histories of individual objects are expected to be more irregular. No dependence on environmental density is found. From Thomas et al. (2010).

Moreover, the high-mass end of the stellar mass function[4] (SMF) and the corresponding high-luminosity end of the luminosity function (LF) evolve more slowly than the low-mass end(see Figure 1.8), indicating that massive galaxies were assembled earlier than less massive ones (e.g. Drory et al., 2004; Drory et al., 2005; Cimatti, Daddi, and Renzini, 2006; Borch et al., 2006; Bundy et al., 2006; Fontana et al., 2006; Conselice et al., 2007; Pozzetti et al., 2007; Pérez-González et al., 2008; Pozzetti et al., 2010; Ilbert et al., 2010; Ilbert et al., 2013).

At a first order, this behaviour can be considered ‘antihierarchical. The ΛCDM theory may nevertheless be reconciled with the observational downsizing if the epoch of stellar assembly within a galaxy does not coincide with the epoch of the galaxy assembly (Baugh, Cole, and Frenk, 1996; Kauffmann, 1996). However, several authors (Cimatti, Daddi, and Renzini, 2006; Fontana et al., 2006; Fontanot et al., 2006; Cirasuolo and Dunlop, 2008) argued that downsizing can be extended to the mass assembly in galaxies, representing a challenge for hierarchical galaxy formation models.

[4]The stellar mass function (SMF) and the luminosity function (LF) represent the number density of galaxies within a mass and luminosity bin, respectively. From comparison of SMF (or LF) at different epochs it is possible to infer statistically the evolution of galaxy populations.

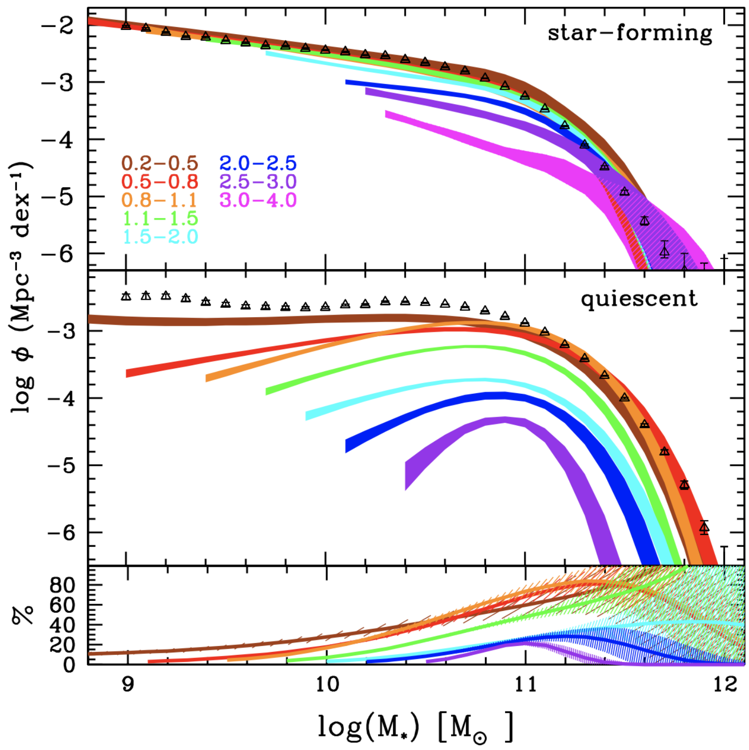

FIGURE 1.8: Galaxy stellar mass function up to $z = 4$ for the star-forming population (top sub-panel) and for the quiescent population (middle sub-panel), while the bottom sub-panel shows the percentage of quiescent galaxies as a function of stellar mass in the same redshift bins. It clearly appears that the high-mass end of quiescent galaxies does not evolve with redshift, while low-massive galaxies are continuously rising the low-mass end profile from $z \sim 4$ to $z \sim 0.2$. From Ilbert et al. (2013).

2. A NEW APPROACH TO SELECT GALAXIES JUST AFTER THE QUENCHING OF STAR FORMATION

2.1 The quenching of the star-formation

Since the pioneering work of Hubble (Hubble, 1926), galaxies have been divided into two broad populations: blue star-forming spirals (late-type galaxies) and red ellipticals and lenticulars (early-type galaxies) with weak or absent star formation. The advent of massive surveys, such as the Sloan Digital Sky Survey (SDSS, York et al., 2000; Strauss et al., 2002), provided very large samples of all galaxy types and allowed to study their general properties with unprecedented statistics.

At low redshifts (z $\sim$ 0.1), galaxies show a bimodal distribution of their colours (Strateva et al., 2001; Blanton et al., 2003; Hogg et al., 2003; Balogh et al., 2004; Baldry et al., 2004) and structural properties (Kauffmann et al., 2003; Bell et al., 2012). In a colour-magnitude (CMD) diagram or in a colour-mass diagram, early-type and bulge-dominated galaxies occupy a tight 'red sequence'. Instead, late-type, disk-dominated systems are spread in the so-called 'blue cloud' region. At higher redshifts, this bimodality has been clearly observed up to at least z $\sim$ 2 (e.g. Willmer et al., 2006; Cucciati et al., 2006; Cirasuolo et al., 2007; Cassata et al., 2008; Kriek et al., 2008; Williams et al., 2009; Brammer et al., 2009; Muzzin et al., 2013). The increase of the number density and the stellar mass growth of the red population from $z \sim 1-2$ to the present (e.g. Bell et al., 2004; Blanton, 2006; Bundy et al., 2006; Faber et al., 2007; Mortlock et al., 2011; Ilbert et al., 2013; Moustakas et al., 2013) suggests that a fraction of blue galaxies migrates from the blue cloud to the red sequence, together with a transformation of their morphologies and the suppression of the star formation (quenching) (e.g. Pozzetti et al., 2010; Peng et al., 2010). An interesting possibility is that both galaxy bimodality and the growth of the red population with cosmic time are due to a migration of the disk-dominated galaxies from the blue cloud to the red sequence when they experience the interruption (quenching) of the star formation while, at the same time, there is a continued assembly of massive (near L*), red spheroidal galaxies through dry merging along the red sequence (Faber et al., 2007; Ilbert et al., 2013). It is also thought that these transitional scenarios depend on the environment where galaxies are located (e.g. Goto et al., 2003; Balogh et al., 2004; Peng et al., 2010).

Interestingly, the CMD region between the blue and the red populations is underpopulated (e.g. Balogh et al., 2004). In particular, the distribution of optical colours, at fixed magnitude, can be fitted by the sum of two separate Gaussian distributions (Baldry et al., 2004), without the need for an intermediate galaxy population. This suggests that the transition timescale from star-forming to passive galaxies must be rather short (e.g. Martin et al., 2007; Mendez et al., 2011; Mendel et al., 2013; Salim, 2014). By considering also ultraviolet data, it has been possible to better explore the CMD at $z \sim 0.1$ thanks to colours more sensitive to young stellar populations (lifetimes < 100 Myr) with respect to the standard optical CMD (Wyder et al., 2007; Martin et al., 2007; Salim et al., 2007; Schiminovich et al., 2007). This showed that there is an excess of galaxies in a wide region between the red sequence and the blue cloud that is not easily explained with a simple superposition of the two populations. This intermediate region has been named 'green valley' and it should be populated by galaxies just in the process of interrupting their star formation (quenching).

The physical origin of the star formation quenching is still unclear, and many mechanisms have been proposed (see Somerville and Davé, 2015). The most appealing options include (i) the radiative and mechanical processes due to AGN activity (e.g. Fabian, 2012), (ii) the quenching due to the gravitational energy of cosmological gas accretion delivered to the inner-halo hot gas by cold flows via ram-pressure drag and local shocks (*gravitational quenching*, Dekel and Birnboim, 2008), (iii) the suppression of star formation when a disk becomes stable against fragmentation to bound clumps without requiring gas consumption, the removal or termination of gas supply (*morphological quenching*, Martig et al., 2009), and (iv) the processes due to the interaction between the galaxy gas with the intracluster medium in high density environments (*environmental or satellite quenching*, Gunn and Gott, 1972; Larson, Tinsley, and Caldwell, 1980; Moore et al., 1998; Balogh, Navarro, and Morris, 2000; Bekki, 2009; Peng et al., 2010; Peng et al., 2012). The quenching processes are also termed internal or environmental depending on whether they are originated within a galaxy or if they are triggered by the influence of the environment (e.g. the intracluster medium). These processes are not mutually exclusive, and they could in principle take place together on different timescales. For instance, the environmental quenching (e.g. gas stripping) is expected to be dominant only in dense groups and clusters. The internal AGN feedback and gravitational heating quenching are thought to be limited to halos with masses higher than 10^{12} $M_{\odot}$, whereas morphological quenching can play an important role also in less massive halos and in field galaxies.

Despite the importance and necessity of quenching, the actual identification of galaxies where the suppression of the star formation is taking place remains very challenging. Several approaches have been exploited so far to find galaxies in the quenching phase. In particular, most studies focused on galaxies migrating from the blue cloud to the red sequence. For instance, green valley galaxies show varied morphologies (Schawinski et al., 2010), with a predominance of bulge-dominated disk shapes (Salim, 2014). Furthermore, there is a consensus in interpreting the decreasing of the specific Star Formation Rate (sSFR) with redder colours (e.g. Salim et al., 2007; Salim et al., 2009; Schawinski et al., 2014) as an indicator of recent quenching or rapid decrease of the star formation. However, Schawinski et al., 2014 argue that, despite the lower sSFR, the green valley is constituted by a superposition of two populations that share the same intermediate optical colours: the green tail of the blue late-type galaxies with no sign of rapid transition towards the red sequence (quenching timescale of several Gyr) and a small population of blue early-type galaxies which are quickly transiting across the green valley (timescale ~ 1 Gyr) as a result of major mergers of late-type galaxies. The connection between quenching, red sequence and mergers has been investigated by studying the so called post-starburst (E+A or K+A) galaxies. These galaxies have morphological disturbances associated with gas-rich mergers and are spectroscopically characterized by strong Balmer absorptions (i.e. dominated by A type stars), although they do not show emission lines due to ongoing star-formation (e.g. Quintero et al., 2004; Goto, 2005; Poggianti et al., 2004; Poggianti et al., 2008). The strong Balmer absorption of post-starburst galaxies suggest that their star formation terminated 0.5-1 Gyr ago. Other interesting cases are represented by early-type galaxies with recently quenched blue stellar populations, or where star formation is occurring at low level and likely going to terminate soon (e.g. Thomas et al., 2010; Kaviraj, 2010; McIntosh et al., 2014). Some recent results suggest that quenching may also occur with longer timescales during the inside-out evolution of disks and the formation of massive bulges via secular evolution (e.g. Tacchella et al., 2015; Belfiore et al., 2017b), or through the so called strangulation process (Peng, Maiolino, and Cochrane, 2015). In addition to normal galaxies, many studies have been focused on systems hosting AGN activity in order to understand whether the released radiative and/or mechanical energy is sufficient to suppress star formation (e.g. Fabian, 2012). Several results indicate that AGN feedback can indeed play a key role in the rapid quenching of star formation (e.g. Smethurst et al., 2016; Baron et al., 2017) and references therein). In the case of massive galaxies, the indirect evidence of a past rapid quenching (< 0.5 Gyr) of the star formation is also provided by the super-solar [α/Fe] and the star formation histories (SFHs) derived for the massive early-type galaxies (e.g. Thomas et al., 2010; McIntosh et al., 2014; Conroy and van Dokkum, 2016; Citro et al., 2016).

To summarise, the results obtained so far identified galaxies some time *after* (e.g. post starbursts) or *before* (e.g. AGN hosts) the quenching of the star formation. Star-forming galaxies *during* the quenching phase have not been securely identified. In this Thesis work, we present a new method aimed at selecting galaxies when their star formation is being quenched. Our search is based on the use of emission line ratios between lines requiring high- (i.e. [O III] λ5007, hereafter [O III]) and lower- (mainly Hα) energetic photons. The theoretical basis and modelling of the method have been presented in *Citro, Pozzetti, Quai et al., 2017; Montly Notices of the Royal Astronomical Society, Volume 469, Issue 3, p3108-3124* (hereafter C17). We apply this new approach at low redshift (0.04<z<0.2) within the SDSS main galaxy sample (see chapter 3).

2.2 A new approach to the quenching of the star formation

The novel approach proposed in C17 is based upon a straightforward fundamental principle. After a few Myr from the interruption of star formation, the shortest-lived (i.e. most massive) O stars and their hard UV photons rapidly disappear, and this causes a fast decrease of the luminosity of lines requiring high-energetic photons. However, emission lines with lower ionisation should be observable as long as late

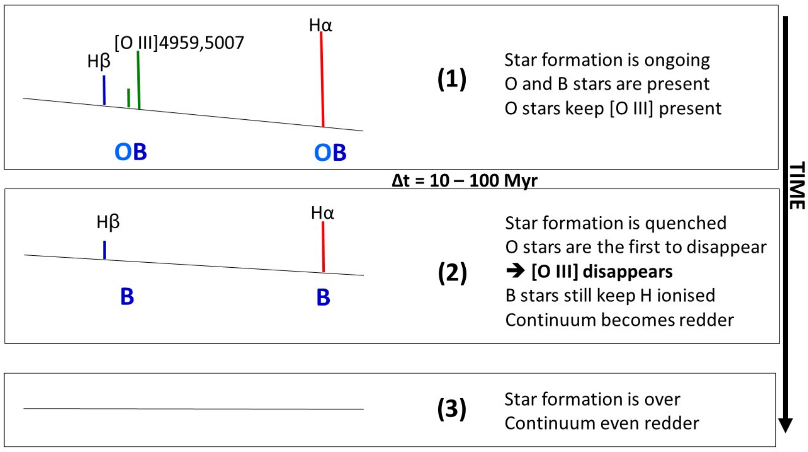

FIGURE 2.1: Scheme of the spectral evolution just after the quenching (from Quai et al. (2018)). By assuming a sharp quenching model by C17 the delay between phase (1) and (2) is ∼10 Myr and become ∼100 Myr by assuming a smoother and slower star formation decline (with a smoother exponential decline of the star-formation with e-folding time $\tau = 200$ Myr).

O and early B stars are still present before they abandon the main sequence (see Figure 2.1). Consequently, quenching galaxy candidates can be selected based on the high-to-low ionisation emission line ratios.

2.3 H II regions

Being responsible for most of the optical emission lines in star-forming galaxies spectra, although they are mainly constituted by hydrogen, the H II regions spectra reflect the evolution of stellar populations and gas in galaxies. Therefore, they contain a wealth of information also about dramatic phenomena like the interruption of the star-formation.

A stellar type O8 V (19 $M_\odot$), with a surface temperature of about 35.000 K, emits $\sim$ 32% of its radiation at hν $>$ 13.6 eV (wavelength shorter than 912 Å). These photons can ionise a substantial fraction of the surrounding inter-stellar medium, creating an almost spherical ionised region (Stromgrën Sphere). The photoionised gas surrounding massive O- or B- stars is referred to as an H II region. These regions have typical dimension of a few pc and they have lifetimes of about $3-10$ Myr (i.e. the lifetime of the ionising stars). Hydrogen in H II regions is rapidly thermalised by collisions with electrons and heavy ions, thus its distribution can be described by a Maxwellian (see Dopita et al., 2015) with temperatures in the range 7000 - 20.000 K (depending on the metallicity of the gas and the temperature of the exciting star). The physics within the Stromgrën Sphere is basically governed by photo-ionisation equilibrium in a thermal balance condition. The photo-ionisation equilibrium in a H II region is supported by recombination events. Assuming the simplified case of a pure-hydrogen nebula, if an electron of kinetic energy E recombines into an excited level *nl* of the hydrogen atom, it will emit a photon of energy $h\nu$ = E + ΔE, where ΔE represents the binding energy of an electron in level *nl*. Therefore, when recombination takes place directly to the ground state ($n = 1$), the resulting Lyman photon will have sufficient energy to ionise hydrogen. This photon will travel only a short distance before being re-absorbed by a close neutral hydrogen atom, with creation of a hydrogen ion. However, this is true only in an extreme limit, called Case B (Baker and Menzel, 1938; Osterbrock, 1989): the nebula is optically thick to radiation more energetic than 13.6 eV, therefore, ionising photons emitted during recombination to the ground level are immediately reabsorbed, creating another ion and free electron by photo-ionisation, leaving no net effect on the overall ionisation balance. This process will cyclically repeat until a decay takes the atom to an energetic level higher than 1, that will leave the photon free to escape from the nebula. Case B[1] is an excellent approximation of H II regions, where there is plenty of neutral hydrogen and photons with h$\nu > 13.6$ have a very small probability of escaping from the nebula. Real nebulae, however, contain helium and metals. In the optical domain, heavy elements undergo forbidden transitions of a few eV, mostly due to collisional recombination, that cannot be re-absorbed within the nebula and leave, producing prominent emission lines (e.g. [O II] $\lambda\lambda$3726-29, [O III] $\lambda\lambda$4959-5007, [N II] $\lambda\lambda$6548-84 and S II$\lambda\lambda$6717-31) in the spectra. This effect, in presence of high metallicity regime and at typical nebular temperature, dominates the cooling rate and it lowers the nebular temperature. Finally, the effect of dust cannot be neglected. Dust grains heavily compromise the ionisation radiation field, because they can absorbe a substantial amount of the radiation with $h\nu > 13.6$ eV, redistributing the photons at longer wavelengths.

2.4 Citro et al. (2017) models of the quenching phase

In order to investigate the behaviour of the proposed emission line ratios during the quenching phase, C17 simulated star-forming regions until their quiescent phase. Here we describe the main ingredients of these photo-ionisation models. They considered a star-forming region as formed by a central source of energy, with a given spectral energy distribution (SED) and intensity, surrounded by a spherical cloud and simulated its final spectrum by means of the photo-ionisation code CLOUDY (Version 13.03 Ferland et al., 1998; Ferland et al., 2013), adopting a plane-parallel geometry (i.e. the simplest geometry allowed by the code), in which the thickness of the photoionised nebula is very small compared to the distance to the photoionising source.

A fundamental parameter that helps to parametrize the starting ionization state of a H II region at the inner shell of the nebula is the adimensional ionisation parameter U, which is defined as the ratio between the mean intensity of the radiation field and the density of the ionized gas. In the plane parallel case, U can be written as Tielens (2010), $U = F_0/n_H c$, where n_H is the hydrogen number density of the photoionised gas, c is the speed of light and F_0 is the flux of the UV ionising photons

[1]The opposite extreme limit is the so-called Case-A, in which the nebula is optically-thin to ionising radiation. Therefore, a ionising photons emitted during the recombination to the ground level escapes, contributing to cooling the nebula and to the observed spectrum.

($\lambda < 912$ Å) striking the photoionised cloud. F_0 is proportional to the number of UV hydrogen ionising photons Q(H), which in turns depends on the stellar metallicity, the stellar mass, the star-formation rate, the age and the initial mass function (IMF) of the ionising central source. For instance, higher masses, higher star formation rates (SFRs), younger ages, top-heavy IMFs or lower metallicities, which all imply an higher number of massive stars, lead Q(H) to increase. Moreover, F_0 depends on the proximity of the central stars to the photoionised nebula. When a galaxy quenches its star formation, Q(H) declines due to the aging and the softening of the SED. As a consequence, F_0 decreases and so does the ionization parameter.

C17 assumed a sharp quenching of the star formation as extreme case. This is in agreement with recent studies arguing that quenching processes occurring on 100 - 200 Myr time-scales can be modelled by a sudden interruption of the star formation (e.g. Schawinski et al., 2014; Ciesla et al., 2016; Schaefer et al., 2017). Then, we will illustrate the C17 results obtained if a more realistic, smoother but still short decline of the star formation is adopted.

The shape of the ionising source is simulated by means of different stellar synthetic spectra, such as the Leitherer et al. (1999) (Starburst99) and Bruzual and Charlot (2003) (BC03) models. The adopted Starburst99 synthetic spectra are simple stellar populations (SSPs) with a fixed mass of $M = 10^6$ $M_\odot$, metallicities Z = 0.004, 0.008, 0.02, 0.04 and a Salpeter IMF (with $m_{\rm low} = 1$ and $m_{\rm up} = 100$ $M_\odot$). They are computed using Lejeune – Schmutz stellar atmospheres (Lejeune, Cuisinier, and Buser, 1997; Schmutz, Leitherer, and Gruenwald, 1992) and Geneva-HIGH 1994 evolutionary tracks (Meynet et al., 1994; Leitherer et al., 1999). This set of ingredients is in agreement with the ones generally used in the literature (e.g. Levesque, Kewley, and Larson, 2010; Kewley et al., 2001; Dopita et al., 2006). For BC03 synthetic spectra, C17 adopt SSPs with metallicities Z = 0.004, 0.008, 0.02, 0.04. In particular, since the default BC03 highest metallicity is Z = 0.05, C17 interpolate the metallicities to create BC03 models with Z = 0.04, in order to be consistent with the Starburst99 results. These models are normalized to $M = 1$ $M_\odot$ and assume a Chabrier IMF with $m_{\rm low} = 0.1$ and $m_{\rm up} = 100$ $M_\odot$.

C17 parametrized the intensity of the ionising source by means of the ionization parameter. They adopted two different kind of models, which account for the decrease of the ionization parameter and the decline of the number of ionising photons due to the quenching process:

1. *Fixed-age models*. To fit with the majority of the literature studies (e.g. Dopita et al., 2006; Levesque, Kewley, and Larson, 2010; Kashino et al., 2017), C17 assumed the central source to be an SSP with a given metallicity (Z = 0.004, 0.008, 0.02, 0.04) and a fixed age of 0.01 Myr. Moreover, they adopted a grid of decreasing ionization parameters in order to simulate different ionization levels. They assumed a grid of fixed-age ionization parameters $\log(U)_0$ going from -3.6 to -2.5 with steps of 0.1 dex, to be consistent with the observations of unresolved star-forming H II regions (log(U) $lowsim - 2.3$, see Yeh and Matzner, 2012), local H II regions ($-3.2 <$ log(U) < -2.9, see Dopita et al., 2000) and star-forming galaxies (see Moustakas, Kennicutt, and Tremonti, 2006; Moustakas et al., 2010). In these models, given a metallicity, the shape of the ionising source is fixed, regardless of the ionization parameter, and models with the lowest

log(U)$_0$ can describe star-forming regions, but with very low densities of ionising photons.

2. *Evolving-age models*. C17 also built models which take account of the shape variation of the ionising SED as a function of time after star formation is stopped. The UV ionising flux decreases as a function of time, with harder energies disappearing first, due to the sudden disappearance of the most massive O stars able to produce them. This behaviour is also visible in Figure 2.2, which shows the time evolution of the number of ionising photons below different energy thresholds (i.e. the ones relative to the emission lines studied in this Chapter: H and O^+, 13.6 eV; O^{++}, 35 eV and Ne^{++}, 41 eV) and for different metallicities. The number of ionising photons decreases with time, and its decline is more pronounced for harder energies and higher metallicities. Moreover, the effect of the increased metallicity is more visible at the harder energies, which are more absorbed due to the larger stellar opacities. To account for the softening of the UV ionising spectrum as a function of time after the SF quenching, in these models C17 simulated the central ionising source using an SSP with given metallicity (Z = 0.004, 0.008, 0.02, 0.04) and age going from 0.01 to 10 Myr. In particular, the youngest SSP of 0.01 Myr is taken as representative of a still star-forming region (this kind of assumption is often used in literature, e.g. Kewley et al., 2001; Dopita et al., 2006; Levesque, Kewley, and Larson, 2010), while older SSPs are used to describe the epochs subsequent to the star formation quenching. The still star-forming region can have a ionization state described by one of the fixed-age ionization parameters log(U)$_0$ defined before, which then evolves with time according to the Q(H) time evolution (Rigby and Rieke, 2004, see). Since Q(H) decreases after the SF quenching, the ionization parameter is expected to get lower as a function of time. For this reason, each model with a given age will be characterized by an evolving-age ionization parameter log(U)$_t$.

For the ionized nebula, C17 adopted an hydrogen density $n_H = 100$ cm^{-3}, which is in agreement with the typical densities in observed star-forming regions (Dopita et al., 2000; Kewley et al., 2001; Dopita et al., 2006), and the solar chemical composition by Asplund, Grevesse, and Sauval (2005). In particular, C17 match the metallicity of the ionised nebula with the metallicity of the ionising stellar population. For non-solar metallicities, they linearly rescaled the abundance of each element, except for He, C and N, for which they assumed the metallicity dependences reported in Dopita et al. (2006). Depletion factors are fixed at the same values regardless of metallicity (e.g. Dopita et al., 2006; Nakajima and Ouchi, 2014). This implies that the dust-to-metal ratio is fixed regardless of metallicity, and that the dust-to-gas ratio is proportional to metallicity (e.g. Issa, MacLaren, and Wolfendale, 1990; Lisenfeld and Ferrara, 1998; Draine et al., 2007). To account for the presence of dust, C17 adopted the default ISM grain distribution implemented in CLOUDY. However, they always used the intrinsic fluxes provided by the CLOUDY code for all the analysed emission lines, i.e. those that not require any correction for the dust extinction. Finally, since the emission lines they are interested in require very high gas kinetic temperature (i.e. T > 20, 000 K) to be produced, they interrupted the calculation at the point in

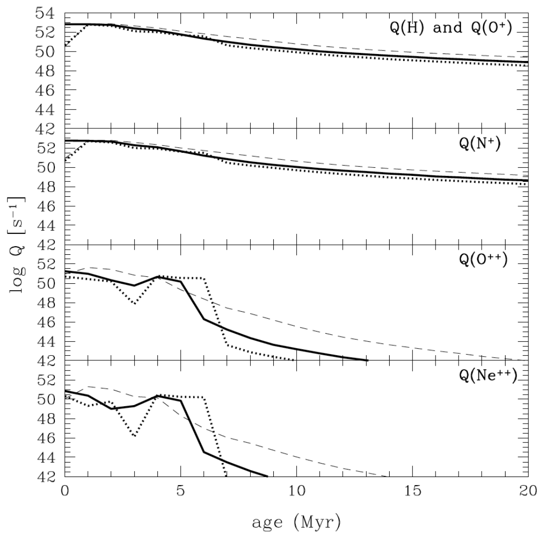

FIGURE 2.2: Time evolution of the number of photons able to ionize H and O^+, N^+, O^{++} and Ne^{++}, from top to bottom. Note that H and O^+ have the same ionization potential (i.e. 13.6 eV) and thus are illustrated within the same panel. Curves are relative to a Starburst99 SSP with $\log(M/M_\odot) = 10^6$ and three different metallicities (Z = 0.004, dashed; Z = 0.02, solid; Z = 0.04, dotted). From Citro et al. (2017)
.

which the kinetic temperature of the gas has fallen down to T $\sim$ 4.000 K, since at this temperature not even the hydrogen can be ionized.

The reliability of C17 models was verified by a comparison with data and literature. About test of comparison with other predictions available in the literature see Citro et al. (2017). Here, we focus on the test for the capabilities of their models in reproducing properties of true galaxies. C17 performed the comparison with data using the Baldwin, Phillips & Terlevich diagram (BPT Baldwin, Phillips, and Terlevich, 1981), which is generally adopted to distinguish star-forming from AGN ionization sources (Kauffmann et al., 2003; Stasińska et al., 2006). To verify the consistency of their models with real data, C17 used a sample of $\sim$ 174.000 star-forming galaxies extracted from the Sloan Digital Sky Survey Data Release 8 (see chapter 3, for details), classified as star-forming on the basis of the BPT diagram itself, using the definition by Kauffmann et al. (2003). As illustrated in Figure 2.3, models are able to reproduce the bulk of the data distribution in the BPT star-forming branch, with galaxies spanning the entire range of ionisation parameters and metallicities considered in the study.

2.5 Quenching diagnostic

The behaviour of individual emission lines is reflected in the two emission line ratios considered in our study, as illustrated in Figure 2.4. In particular, both [O III]/Hα and [Ne III]/[O II] decrease with increasing age and metallicity, at each $\log(U)_0$. For both emission line ratios, the decline is more pronounced at higher metallicities,

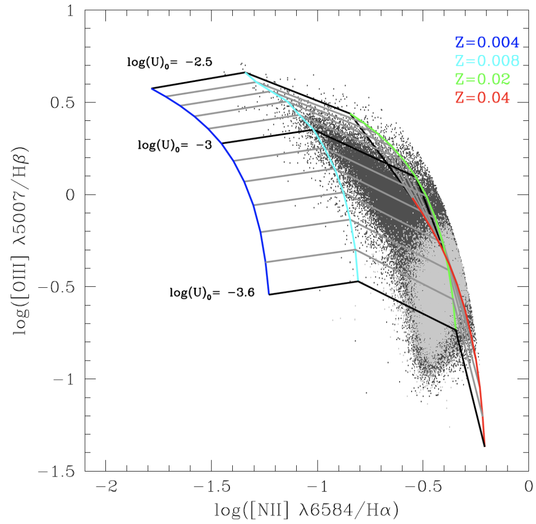

FIGURE 2.3: Comparison between C17 models and observations. Dark grey points are galaxies extracted from the SDSS DR8 with S/N(Hα) > 5, S/N(Hβ) > 3 and S/N([N II]), S/N([O III]) > 2, while light grey points are galaxies with S/N([O III]) < 2. The superimposed grid is our set of fixed-age models with different metallicities (Z = 0.004 blue; Z = 0.008 cyan; Z = 0.02 green; Z = 0.04 red) and different log(U)$_0$ (going from -3.6 to -2.5 with steps of 0.1 dex from bottom to top). Black curves mark the levels log(U)$_0$ $= -3.6$,-3,-2.5, from bottom to top, as indicated. From Citro et al. (2017)

.

since for a given age, more metallic massive stars have softer UV spectra. Indeed, at log(U)$_0$ $= -3$ and at the lowest Z, [O III]/Hα and [Ne III]/[O II] decrease by ~ 0.1 dex and ~ 0.2 dex within ~ 2 Myr from the SF quenching respectively, while at the highest Z they drop by ~ 1.3 dex and ~ 1 dex, within the same time interval. However, regardless of metallicity, the two emission line ratios are characterized by a decline by a factor about 10 within ~ 10 Myr from the epoch of the SF quenching. Although fixed-age models assume a fixed shape for the SED of the ionizing source, the ones which are characterized by the lowest log(U)$_0$ can in some sense describe star-forming regions that are quenching their SF, since low ionisation parameters are related to low numbers of ionizing photons and then to low levels of star formation. For this reason, it can be interesting to investigate the behaviour of the emission line ratios under analysis as a function of both log(U)$_0$ and log(U)$_t$. Figure 2.5 illustrates the case of [O III]/Hα. For Z=0.02, a decline by a factor about 10 of this ratio corresponds to a decrease in log(U)$_t$ by 0.1 dex (starting from an initial log(U)$_0$ = -3), within a time interval of $\sim$2 Myr, while a decrease by $\sim$1 dex in log(U)$_0$ can produce the same effect. Therefore, the decline of [O III]/Hα is more rapid for evolving-age models than for fixed-age ones. This is due to the fact that the former include the additional effect of the UV softening as a function of time.

The instantaneous star formation quenching modelled so far can be considered an extreme case, which allows to better show the strength of C17 approach to probe star formation quenching on very short time-scales. Now we show how the behaviour of [O III]/Hα and [Ne III]/[O II] changes if different SFHs and if a more realistic and smoother SFHs are assumed. In particular, using Starburst99 models, C17 analysed

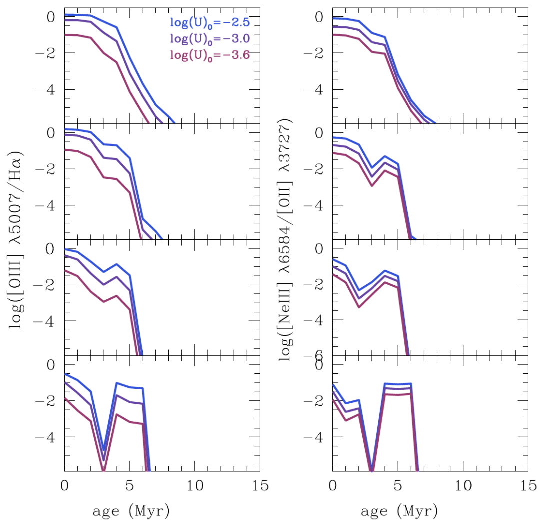

FIGURE 2.4: [O III]/Hα and [Ne III]/[[O II]] (right) evolution as a function of time, metallicity and log(U)$_0$. Metallicity (Z = 0.004, 0.008, 0.02, 0.04) increases from the top to the bottom panel. In each panel, we show the results for log(U)$_0$ -2.5, -3, -3.6, with log(U)$_0$ decreasing from blue to red, as indicated. From Citro et al. (2017)

.

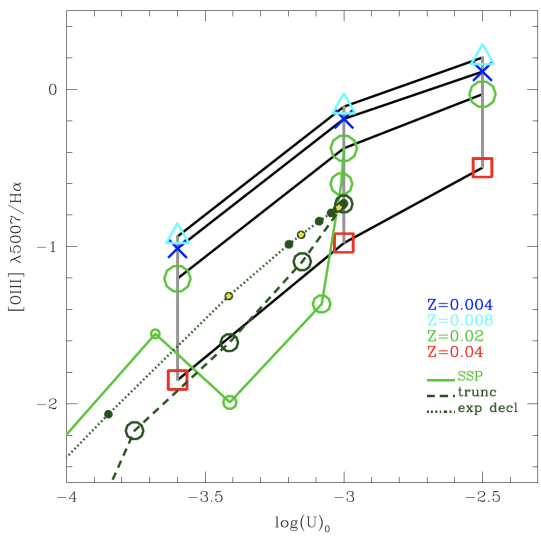

FIGURE 2.5: [O III]/Hα as a function of log(U)$_0$ and log(U)$_t$. Grey curves connect models with the same log(U)0, for the three log(U)$_0$ = -3.6,-3,-2.5 and different metallicity (Z = 0.004 blue; Z = 0.008 cyan; Z = 0.02 green; Z = 0.04 red), while black curves connect models with the same metallicity. For Z = 0.02, evolving-age models for SSP (light green empty circles), truncated (dark green empty circles) and the exponentially declining (dark green filled circles) SFHs are shown, for an initial log(U)$_0$ = -3. The emission line ratio evolution is illustrated with a time step of 1 Myr within the first 10 Myr after quenching, about 20 Myr from 10 to 100 Myr after quenching, and 100 Myr even further. For the exponentially declining SFH, gold small stars mark the values of the emission line ratios corresponding to 10, 80, and 200 Myr after the SF quenching, from the highest to the lowest value of [O III]/Hα. From Citro et al. (2017)

.

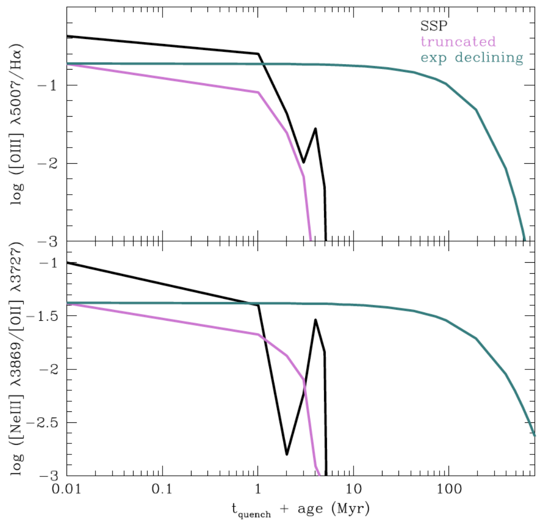

FIGURE 2.6: [O III]/Hα and [Ne III]/[O II] emission line ratios as a function of time for different SFHs and Z = 0.02. The SSP (black curve), truncated (violet curve) and the exponentially declining (green curve) SFHs are shown up to $\sim$ 800 Myr from the time of quenching (indicated as t_{quench}). From Citro et al. (2017)

.

the case of a truncated SFH, with SFR = 1 $M_{\odot}$ yr^{-1} up to 200 Myr and zero at older ages, and the case of a smoother decline described by an exponentially declining SFR (i.e. SFR / e-t/τ), with $\tau = 200$ Myr, since this is the SFH shape generally assumed to describe local star-forming galaxies (e.g. Bell and de Jong, 2001). For the truncated SFH, a SFR = 1 $M_{\odot}$ yr^{-1} is chosen to match the typical SFRs of SDSS star-forming galaxies (Brinchmann et al., 2004; Whitaker et al., 2014) at stellar masses comparable with the ones of the C17 sample. For the exponentially declining SFH, models are normalized to 10^6 $M_{\odot}$. Moreover, C17 do not consider very high values of $\tau > 200$ Myr, since in this case the SFH would extend at much larger times, incompatible with the assumption that galaxies are quenching their star formation. Furthermore, larger τ's have been demonstrated to produce galaxies which never leave the blue cloud (e.g. Schawinski et al., 2014). Figure 2.6 shows the time evolution of [O III]/Hα and [Ne III]/[O II] for the three assumed SFHs, starting from the time of quenching. For the truncated SFH stopping at 200 Myr, the two emission line ratios drop by a factor $\sim$ 10 within about 2 Myr from the beginning of the quenching and by more than a factor $\sim$ 1000 within about 10 Myr from the quenching of the SF, similarly to the SSP case. In the case of an exponentially declining SFR, instead, they decrease following the decline of the SFR. In particular, C17 find that the star-forming region takes about 80 Myr to become quiescent, reaching a specific star-formation rate (sSFR) $\sim 10 - 11$ yr^{-1} (which is typical of quiescent galaxies) and, within this time interval, both [O III]/Hα and [Ne III]/[O II] decrease by a factor $\sim$ 2. This decline corresponds to a decrease in $\log(U)_t$ by only ~ 0.2 dex, as illustrated in Figure 2.5, implying that, when smoother SFHs are considered, $\log(U)_t$ has a smoother decline. Moreover, $\sim$ 500 Myr are necessary for the two emission line ratios to decline by a factor about 10. It is interesting to note that the value of the two emission line ratios at the age at which the star formation stops (200 Myr for the truncated and $\sim$ 10 Myr for the exponentially declining SFH) is lower by a factor $\sim$ 2 for more complex SFHs

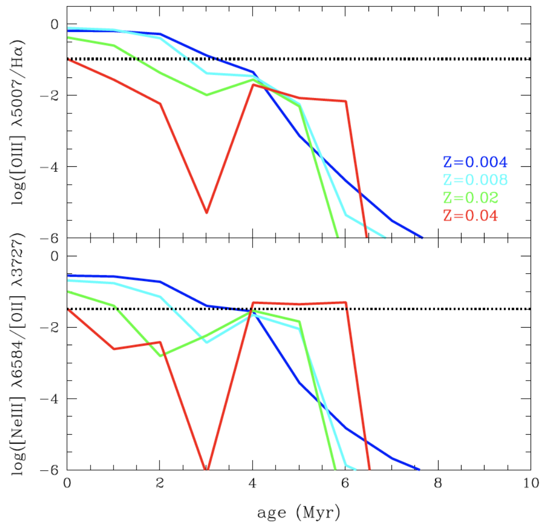

FIGURE 2.7: [O III]/Hα (top) and [Ne III]/[O II] (bottom) as a function of time, for $\log(U)_0 = -3$, and different metallicities (Z = 0.004, blue; Z = 0.008, cyan; Z = 0.02, green; Z = 0.04, red). In each panel, the black dotted line marks the initial value of the emission line ratios for Z = 0.04. From Citro et al. (2017)

.

than for a 0.01 Myr SSP with the same $\log(U)_0 = -3$. Therefore, if an ionizing stellar population forms stars continuously on a longer time interval, its SED at the time of quenching is softer than the SED of a stellar population which forms all its stars into a single burst. This can be due to the accumulation of long lived stars contributing mostly to the flux at longer wavelengths. All these trends confirm that the decline of [O III]/Hα and [Ne III]/[O II] takes place regardless of the shape of the assumed SFH and that very low values of these emission line ratios are expected whether galaxies have abruptly quenched their SF or they have gradually reached low levels of SF.

2.6 The degeneracy between ionisation and metallicity

High metallicity in the photosphere of massive stars heavily affects the UV ionising radiation, due to an increasing opacity. The resulting effect is that, without additional criteria, the ionising SEDs of a high metallicity population or low-ionisation level is indistinguishable from a SED with a lower metallicity and a lower ionization level (ionisation-metallicity degeneracy). Figure 2.7 shows the impact of the ionisation-metallicity degeneracy on [O III]/Hα and [Ne III]/[O II] ratios. For $\log(U)_0 = -3$, the same value of the two ratios can be reproduced by different combination of metallicity and young star-forming regions with high metallicity can produce the same outcome as old star-forming regions with low metallicity. The degeneracy between ionisation and metallicity makes this approach less trivial, and additional criteria must be used to identify the most reliable sample of quenching galaxies. In chapter 3 we expose our method to mitigate the ionisation-metallicity degeneracy and the extraction and characterisation of the most reliable quenching galaxy candidates from a SDSS sample.

3. Catching galaxies in the act of quenching star formation

In this chapter, we present the definition of the parent sample, the methods applied to mitigate the ionisation- metallicity degeneracy, the extraction of the most reliable quenching galaxy (QG hereafter) candidates, and the general properties of the selected sample.

3.1 The sample selection

3.1.1 The parent sample

Our sample is selected from the Sloan Digital Sky Survey Data Release 8[1] (SDSS-DR8, Aihara et al., 2011), adopting the following criteria:

(i) keyword 'class' = 'GALAXY';

(ii) redshift range $0.04 \leq z < 0.21$;

(iii) keyword 'LEGACY_TARGET1' = 64

The first criterion is clearly used to avoid stars and quasars. The second one is adopted to minimise the biases due to the fixed aperture of SDSS spectroscopy. We identify systems where star formation is being quenched globally across the entire size of the galaxy. In order to ensure that the properties of the galaxy fraction measured inside the fibre aperture are reasonably representative of the global values, Kewley, Jansen, and Geller, 2005 found that the fibre should cover at least the 20 per cent of the observed B_{26} isophote light of the galaxy. For SDSS, this fraction corresponds roughly to a redshift cut $z > 0.04$. Furthermore, we set an upper limit of $z < 0.21$, beyond which the number of objects rapidly decreases and do not significantly contributes to the sample statistic.

The third criterion ensures a homogeneous selection focusing on the Main Galaxy Sample (see Strauss et al., 2002, for details), therefore avoiding mixing galaxies with different selection criteria.

With the application of these three criteria, our total sample is constituted by 513596 galaxies. This sample is called *parent sample* hereafter, and includes all galaxy types

[1]The data were downloaded from the CAS database, which contains catalogs of SDSS objects (`https://skyserver.sdss.org/CasJobs/`)

(from passive systems to star-forming objects) as well as Type 2 AGNs. In order to avoid the spectral contamination due to sky lines residuals, we exclude ~ 62400 objects for which the centroids of the main emission lines (i.e. [O II] $\lambda3727$ - hereafter [O II], Hβ,[O III], Hα and [N II] $\lambda6584$ - hereafter [N II]) are overlapped with the strongest sky lines.

The spectral line measurements and physical parameters of the selected galaxies are obtained from the database of the Max Planck Institute for Astrophysics and the John Hopkins University (MPA-JHU measurements[2]). In particular, we retrieve the following quantities:

- *Emission lines flux*. The fluxes are measured with the technique described in Tremonti et al. (2004), which is based on the subtraction of the (Bruzual and Charlot, 2003, BC03) best-fitting population model of the stellar continuum, followed by a simultaneous fit of the nebular emission lines with a Gaussian profile.

- *Uncertainty in emission lines fluxes*. We use the updated uncertainties provided by Juneau et al., 2014, which are obtained comparing statistically the emission line measurements of the duplicate observations of the same galaxies.

- *Stellar mass*. The stellar masses are estimated through SED fitting to the SDSS *ugriz* galaxy photometry, using a Bayesian approach to a BC03 model grid. The magnitudes are corrected for the contribution of the nebular emission lines assuming that these contributions to the broad-band magnitudes *u*,*g*,*r*,*i*,*z* are the same inside and outside the 3″ fibre of the SDSS spectrograph. The obtained estimates are referred to the region sampled by the fibre. To obtain the total stellar mass, the MPA-JHU group corrected the stellar masses with a factor obtained by the difference between fibre magnitudes and total magnitudes. For this work, we assume the *total stellar masses* corresponding to the median of their Bayesian probability distribution function.

- *Rest-frame absolute magnitude*. The rest-frame absolute magnitudes are derived from the *ugriz* broad-band photometry, and corrected for the AB magnitude system.

- *Nebular Oxygen abundance*. Nebular oxygen abundance are estimated using a Bayesian approach, adopting the Charlot and Longhetti, 2001 models as discussed in Tremonti et al. (2004) and Brinchmann et al., 2004. The estimates of oxygen abundances are expressed in 12 + log(O/H) values, and were derived only when the signal-to-noise ratio S/N in Hα, Hβ, [O III] and [N II] is > 3. In this work, we consider the 12 + log(O/H) value corresponding to the median of the Bayesian probability distribution function.

- *EW(Hα)*. We adopt the rest-frame equivalent widths estimated by the SDSS pipeline with a continuum corrected for emission lines.

- *D_n4000*. We use the D_n4000 (Balogh et al., 1999) corrected for emission lines contamination.

[2] see http://wwwmpa.mpa-garching.mpg.de/SDSS/.

- *Galaxy size and light concentration*. The size is represented by the radius enclosing the 50 percent of the r-band Petrosian flux (R50). The light concentration is defined as C=R90/R50, where R90 is the radius containing the 90 percent of the r-band Petrosian flux.

In addition to these quantities, we also collect information about the galaxy *environment* by cross-matching our sample with the catalog provided by Tempel et al., 2014, that contains environmental information relative to SDSS-DR10[3] and we found a match for about the 87% of galaxies in our sample. In particular, we use the environmental density they provide for each galaxy ($\rho_{\rm env}$, hereafter), which represents an estimate of the overdensity with respect to the mean galaxy density within a scale of 1 h^{-1} Mpc centered on each galaxy. Furthermore, we use their *Richness* and *Brightness Rank*, that are defined, respectively, as the number of members of the group/cluster the galaxy belongs to, and the luminosity rank of the galaxy within the group/cluster.

Finally, we analyze the SDSS morphological probability distribution of the galaxies provided by Huertas-Company et al., 2011[4], which is built by associating a probability to each galaxy of belonging to one of four morphological classes (Scd, Sab, S0, E).

3.1.2 The Hα emission subsample

As anticipated in the Section 2, our aim is to identify galaxies in the critical phase when the star formation is being suppressed. In the case of an instantaneous quenching (see Figure 2.1), this translates in searching for star-forming galaxies where high-ionisation lines (e.g. [O III]) are suppressed due to the disappearance of the most massive O stars, whereas Balmer emission lines are still present because their luminosity decrease more slowly due to photo-ionisation from lower mass (longer lived) OB stars.

For these reasons, we select a subsample of galaxies with Hα emission considering the following criteria:

(i) EW(Hα) and EW(Hβ) ≤ 0, in order to select galaxies with Balmer emission lines.

(ii) S/N(Hα) ≥ 5. For the SDSS this corresponds to objects with Hα fluxes above $\simeq 1.1 \times 10^{-16}$ erg s^{-1} cm^{-2}.

(iii) S/N(Hβ) ≥ 3, to be able to properly correct for dust extinction using the Hα/Hβ ratio. With this criterion, we exclude $\sim$ 6% of galaxies, and the corresponding limiting flux is $\simeq 3.2 \times 10^{-17}$ erg s^{-1} cm^{-2}.

By construction, the Hα sample includes galaxies with S/N(Hα) ≥ 5; however, the other emission lines can have a lower S/N. When a line flux has S/N < 2, we assign

[3]The catalogue is available at `http://cosmodb.to.ee`

[4]We downloaded the SDSS morphological probability distribution of the galaxies together with the Tempel et al., 2014 catalogue.

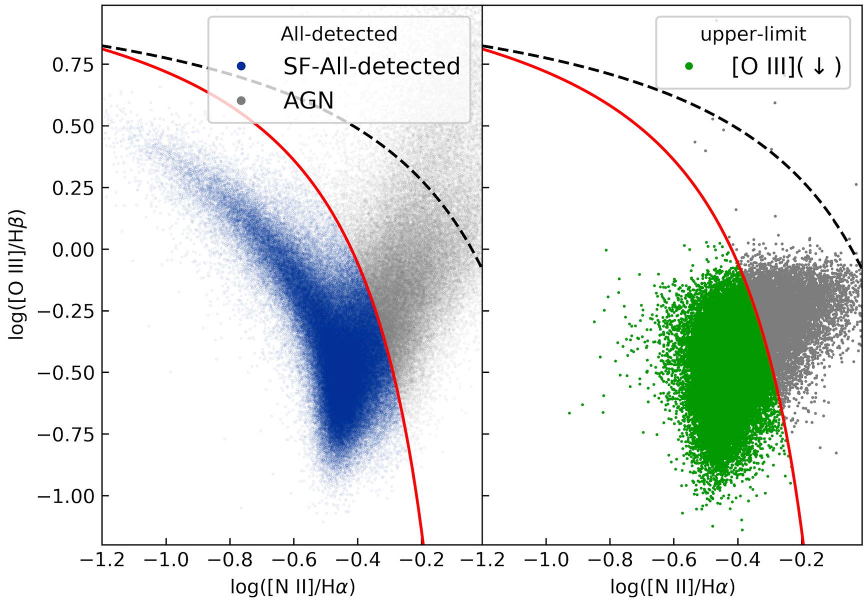

FIGURE 3.1: The BPT diagram of the Hα subsample. In the left panel we show the diagram for the galaxies whose all the BPT emission lines are detected (i.e. S/N > 5 for Hα, S/N > 3 for Hβ and S/N > 2 for [O III] and [N II]). The red solid line is taken from Kauffmann et al., 2003, while the black dashed line was determined theoretically by Kewley et al., 2001. The blue dots represent the SF-Alldet galaxies, while the gray ones the AGNs. In the right panel we show the BPT diagram for galaxies with upper limit in [O III] line (i.e. galaxies with S/N([O III]) < 2). The green dots represent those galaxies that, despite their upper limit, satisfy the Kauffmann et al., 2003 criterion for star-forming galaxies, while the gray ones represent objects for which we cannot be sure about their actual condition.

an upper limit to the flux defined as:

$$\mathrm{F} \leq 2 \times \sigma_{\mathrm{F}}; . \tag{3.1}$$

In the case of [O III], which is the most important signature of quenching in our study, this upper limit corresponds to $\mathrm{F} \lesssim 2.2 \times 10^{-17}$ erg s^{-1} cm^{-2}.

The full Hα emission sample contains 244362 objects. Clearly, this sample includes a heterogeneous ensemble of galaxies where emission lines are powered by different ionisation processes (star-forming, type 2 AGNs, LINERs, etc.).

3.1.3 The subsample of star-forming galaxies

Since we are interested in purely star-forming systems, we cleaned the Hα sample from contaminating galaxies. In order to separate the star-forming population from objects hosting AGN activity, we use the diagnostic diagram of Baldwin, Phillips, and Terlevich (1981, hereafter BPT).

Figure 3.1 shows the BPT diagram of our sample. We remind that the emission lines involved in this diagram are close enough in wavelength that the correction for dust

TABLE 3.1: Numbers and median redshift of galaxies in the different subsamples.

Sample	Subsample	Number	median z
SF-Hα		174056	0.08
	SF-Alldet	148145	0.08
	SF-[O III]undet	25911	0.12
no-Hα		201527	0.12
Total		375583	0.10

extinction is negligible. We adopt the Kauffmann et al., 2003 criterion[5] to reject type 2 AGNs, LINERs and composite objects from the Hα sample. For galaxies, where all lines are detected, the star-forming population can be easily isolated, while for galaxies where [O III] is undetected (i.e. S/N[O III] < 2), we select only those galaxies whose upper limits of [O III] flux lie below the Kauffmann et al., 2003 relation. With this approach, we exclude 62125 AGNs and LINERs, and obtain the final subsample of 174056 star-forming galaxies.

Then, we divide this sample into two subsamples:

SF-Alldet (148145 galaxies). These are star-forming (SF) galaxies where all the main emission lines (Hβ, [O III], Hα and [N II]) are significantly detected. We, therefore, reject all the objects with S/N([N II]) < 2 (i.e. 241 objects).

SF-[O III] undetected (25911 galaxies). These galaxies differ from the previous ones for their [O III], that in this case is undetected (i.e. S/N < 2).

In order to compare the SF galaxies with the other galaxy types, we also select a complementary subsample of galaxies without Hα emission from the parent sample (subsection 3.1.1). Hereafter, the extracted sample is called **no-Hα** subsample, and includes 201527 galaxies with S/N(Hα) $<$ 5. Table 3.1 summarizes the number of galaxies in the different subsamples, while Figure 3.2 shows some of the main parameter distributions of the subsamples (i.e. redshift, masses and color excess).

3.1.4 The correction for dust extinction

Since all the SF-Alldet and SF-[O III]undet galaxies have Hβ with S/N>3, we correct their emission line fluxes for dust attenuation based on the Hα/Hβ ratio, adopting the Calzetti et al., 2000 attenuation law. The colour excess E(B-V) is derived assuming the Case B recombination and a Balmer decrement Hα/Hβ $= 2.86$ (typical of H II regions with electron temperature $T_e = 10^4$ K and electron density $n_e \sim 10^2 - 10^4\,\mathrm{cm}^{-3}$, Osterbrock, 1989) For galaxies with Hα/Hβ <2.86 (2072 galaxies, $\sim$ 1%), i.e. with a negative colour excess, between $\sim -0.2 \leq$ E(B-V) < 0, we decide to set E(B-V) = 0. The E(B-V) distribution is shown in Figure 3.2.

[5] Their criterion is defined as $\log([\mathrm{O\,III}]/\mathrm{H}\beta) < 0.61/\{\log([\mathrm{N\,II}]/\mathrm{H}\alpha) - 0.05\} + 1.3$.

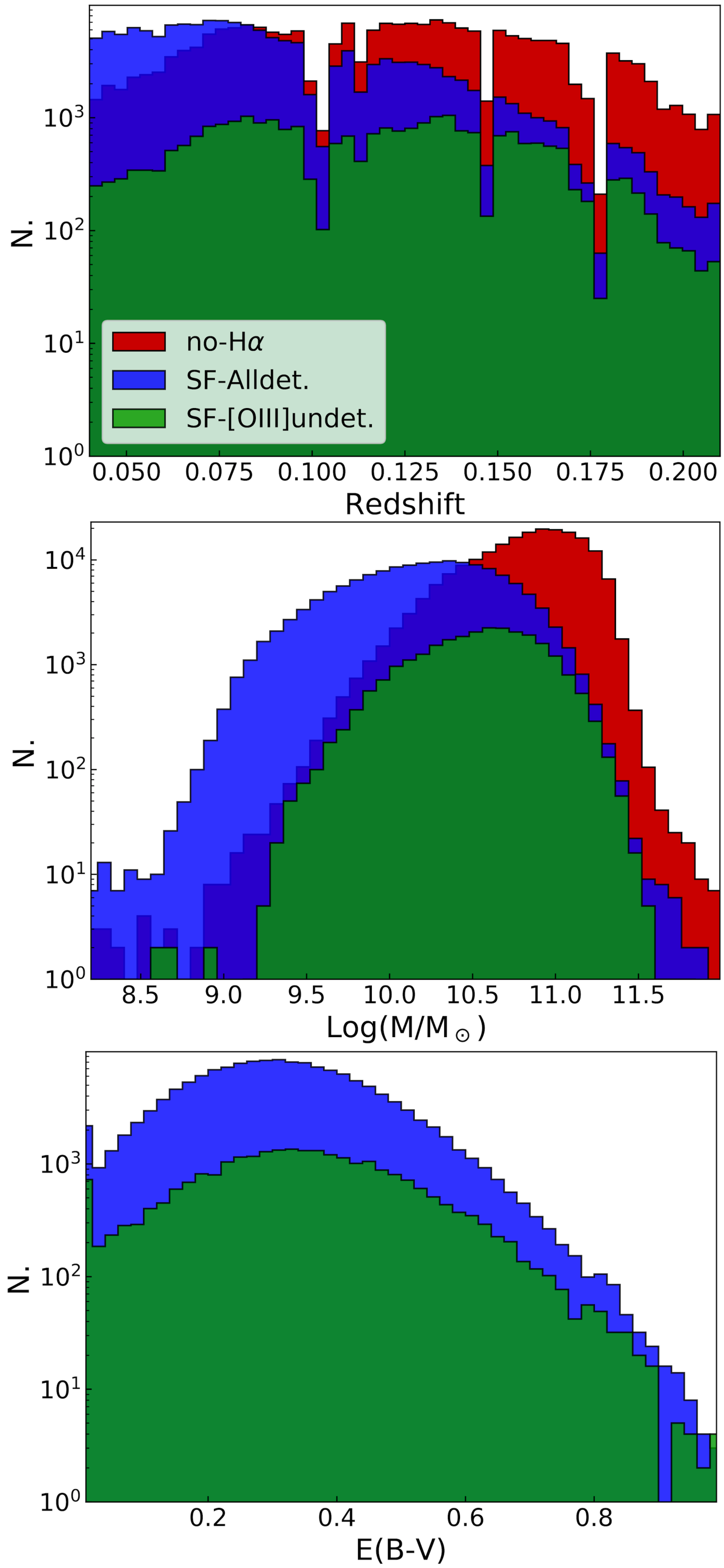

FIGURE 3.2: Main distributions of the three main subsamples: SF-Alldet in blue, SF-[O III]undet in green and no-Hα in red: redshift (left panel), masses (central) and color excess E(B-V) (right).

3.1.5 The estimate of star formation rate

After correcting the emission lines for dust extinction, we derive the star formation rates (SFRs) for the star-forming galaxies. The SFR is derived using the Hα luminosity and adopting the Kennicutt (1998a) conversion factor for Kroupa, 2001 initial mass function (IMF):

$$\mathrm{SFR} = \mathrm{L(H}\alpha)/10^{41.28}\ [\mathrm{M}_{\odot}\mathrm{yr}^{-1}] \tag{3.2}$$

In order to obtain the total SFRs, we correct the fibre SFRs for aperture effects. Following Gilbank et al., 2010 and Hopkins et al., 2003 we apply an aperture correction A based on the ratio of the u-band Petrosian flux (which is a good approximation to the total flux) to the u-band flux measured within the fibre:

$$A = \frac{\mathrm{f_{tot}}(u)}{\mathrm{f_{fib}}(u)} = 10^{-0.4(u_{\mathrm{fib}}-u_{\mathrm{tot}})} \tag{3.3}$$

This method provides results which are in good agreement with the measurements of Brinchmann et al., 2004 obtained with a more complex approach (Salim et al., 2007).

3.2 Finding the quenching galaxies

3.2.1 The general approach

In this analysis, we decide to follow the approach discussed in C17 to select galaxies in the phase when the quenching of their star formation takes place. In particular, C17 showed how the ratio of high-ionisation (e.g. [O III] and [Ne III] λ3869 - hereafter [Ne III]) to low-ionisation (e.g. Balmer lines) lines can be used to identify galaxies as close as possible to the time when the star formation starts to cease. Here, we explore in particular the dust corrected [O III]/Hα ratio (see subsection 3.1.4) to select quenching galaxies. This ratio is highly sensitive to the ionisation parameter U and hence to the star formation evolutionary phase. In particular, higher values of U correspond to higher ionisation and star-formation levels (for a more extensive discussion, seeC17). However, [O III]/Hα is also dependent on the metallicity Z of the ionising stellar population, in the sense that low [O III]/Hα values can be reproduced with both low U or high Z (i.e. ionisation-metallicity degeneracy, Z-U hereafter). In order to find QG candidates, it is therefore necessary to mitigate this degeneracy. To address this issue, we devise two independent methods that are described in the following sections.

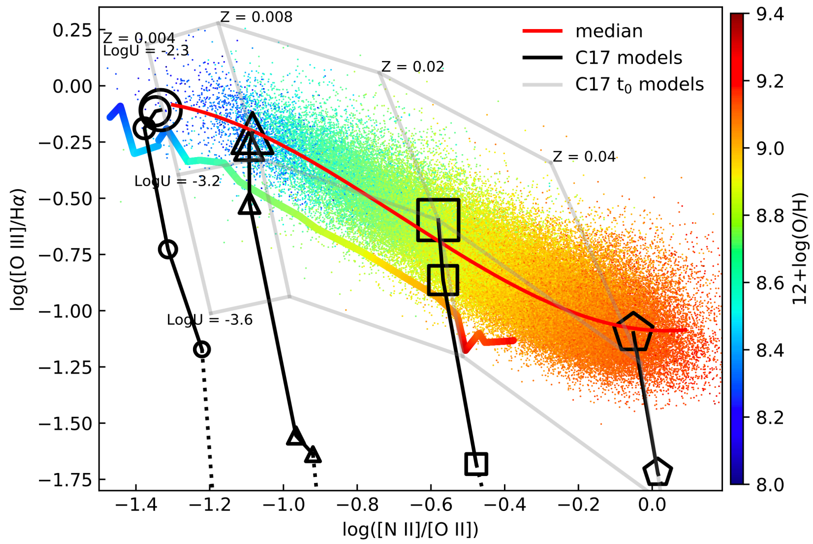

FIGURE 3.3: [O III]/Hα vs. [N II]/[O II] diagram. The colour of the dots shows the metallicity estimate 12+log(O/H) by Brinchmann et al., 2004 and the colorful line represents the dispersion at 3σ of the [N II]/[O II] for a given value of 12+log(O/H). The red curve represents the median of the relation. Superimposed in gray is reported a grid of zero-ages C17 models with different metallicities and ionisation parameters, while in black are shown the evolutive tracks by C17 (circles for Z = 0.004, triangle for Z = 0.008, square for Z = $Z_\odot$ = 0.02, pentagon for Z = 0.04), where the size of the symbol is reported in time-step of 1 Myr with decreasing sizes.

3.2.2 Method A

To mitigate the Z-U degeneracy, we firstly need to find an estimator for the metallicity independent of [O III]. Following C17, we exploit the [N II]/[O II] ratio as metallicity indicator, as suggested e.g. by Nagao, Maiolino, and Marconi, 2006. Figure 3.3 shows the dust corrected [O III]/Hα vs. [N II]/[O II] diagram as a function of the metallicity 12+log(O/H). In this analysis we discard 7712 objects with [O II] undetected (i.e. S/N [O II] < 2).

Figure 3.3 clearly shows a very good correlation between [N II]/[O II] and metallicity, with the advantage of having an almost orthogonal dependence between metallicity and log U with respect to the BPT diagram, as confirmed also by the C17 models shown in the figure. This allows to reduce the Z-U degeneracy, since, at fixed [N II]/[O II], the spread of the distribution in [O III]/Hα mainly reflects a difference in the ionisation status. For comparison, we also show the dispersion at 3σ of the [N II]/[O II] at a given 12+log(O/H). In this diagram, therefore, at each [N II]/[O II] (i.e. at fixed metallicity) galaxies with [O III]/Hα lower than the 3σ dispersion due to metallicity can be considered as galaxies approaching the quenching, having an intrinsic lower ionisation parameter.

The QG population should represent a population that separates from the SF sequence and starts transiting to the quenched phase. To isolate this extreme population, we analyse the SF-Alldet distribution of [O III]/Hα in slices of [N II]/[O II], searching for an excess of objects (using a Gaussian distribution as reference) with extremely low [O III]/Hα values (i.e. lowest ionisation levels, see Figure 3.4). A similar approach was used to select starburst galaxies above the main sequence (Rodighiero et al., 2011). We focus in particular on the half part of the Gaussian distribution below the median, not considering the part above since it is dominated by ongoing SF, and could be biased by starburst systems and by a residual contamination of AGNs.

In detail, we proceed as follows:

- We divide the distribution in bins of width Δ[N II]/[O II]$\approx$ 0.12 dex.
- In each bin of [N II]/[O II], we estimate the median and the 16th percentile, and describe the distribution of SF-Alldet galaxies with an half-Gaussian whose mean and standard deviation (σ) are fixed to the median and the 16th percentile of the distribution. The typical value of σ is ~ 0.14 dex.
- We compare the 3σ value of the Gaussian distribution with the 0.15th percentile, which corresponds to the 3σ value in the case of a Gaussian distribution.
- When the median-3σ value is higher than the 0.15th percentile, i.e. there is a positive detection of a deviation with respect to a Gaussian distribution, we identify our quenching galaxies as the excess beyond 3σ with respect to the half-Gaussian (as shown in the upper panel of Figure 3.4).

Following this approach, we find an excess of galaxies in the tail of the distribution in all bins with [N II]/[O II] < -0.33 (corresponding to 12+log(O/H)$\lesssim 9$). Above this threshold, instead, the limiting flux of our sample approaches [O III]/H$\alpha \approx -1.5$, not allowing to detect candidates beyond the 3σ value, as also shown in the bottom panel of Figure 3.4.

To provide a less discrete description of the data, we generalise our method deriving the running median, the 16th percentile (representing also the σ of the half-Gaussian), the 0.15th percentile and the median-3σ for our SF-Alldet sample in the [O III]/Hα vs. [N II]/[O II] plane. We fit these relations with a third-order polynomial[6], and, to be more conservative, we define our QGs as the SF-[O III]undet galaxies lying below the median-3σ polynomial of SF-Alldet population. This threshold is always below the dispersion in [N II]/[O II] at 3σ due to the metallicity (see Figure 3.5) and this suggests that the low [O III]/Hα values are not related with the metallicity.

To further clean our sample, we discard also the 10 candidates that have [Ne III] detected, since it is a high-ionisation line and its presence is incompatible with the star-formation quenching (seeC17).

With this approach, we find 192 QG candidates (hereafter QG-A). Figure 3.5 shows the [O III]/Hα vs. [N II]/[O II] diagram, together with the selected QGs.

[6]Defined $x =$ [N II]/[O II]) and $y =$ [O III]/Hα, the polynomials are: $y(\text{median}) = -1.09 - 0.11x + 1.39x^2 + 0.67x^3$, $y(\text{16 perc.}) = -1.22 - 0.09x + 1.48x^2 + 0.76x^3$ and $y(\text{0.15 perc}) = -1.47 - 0.21x + 1.04x^2 + 0.53x^3$.

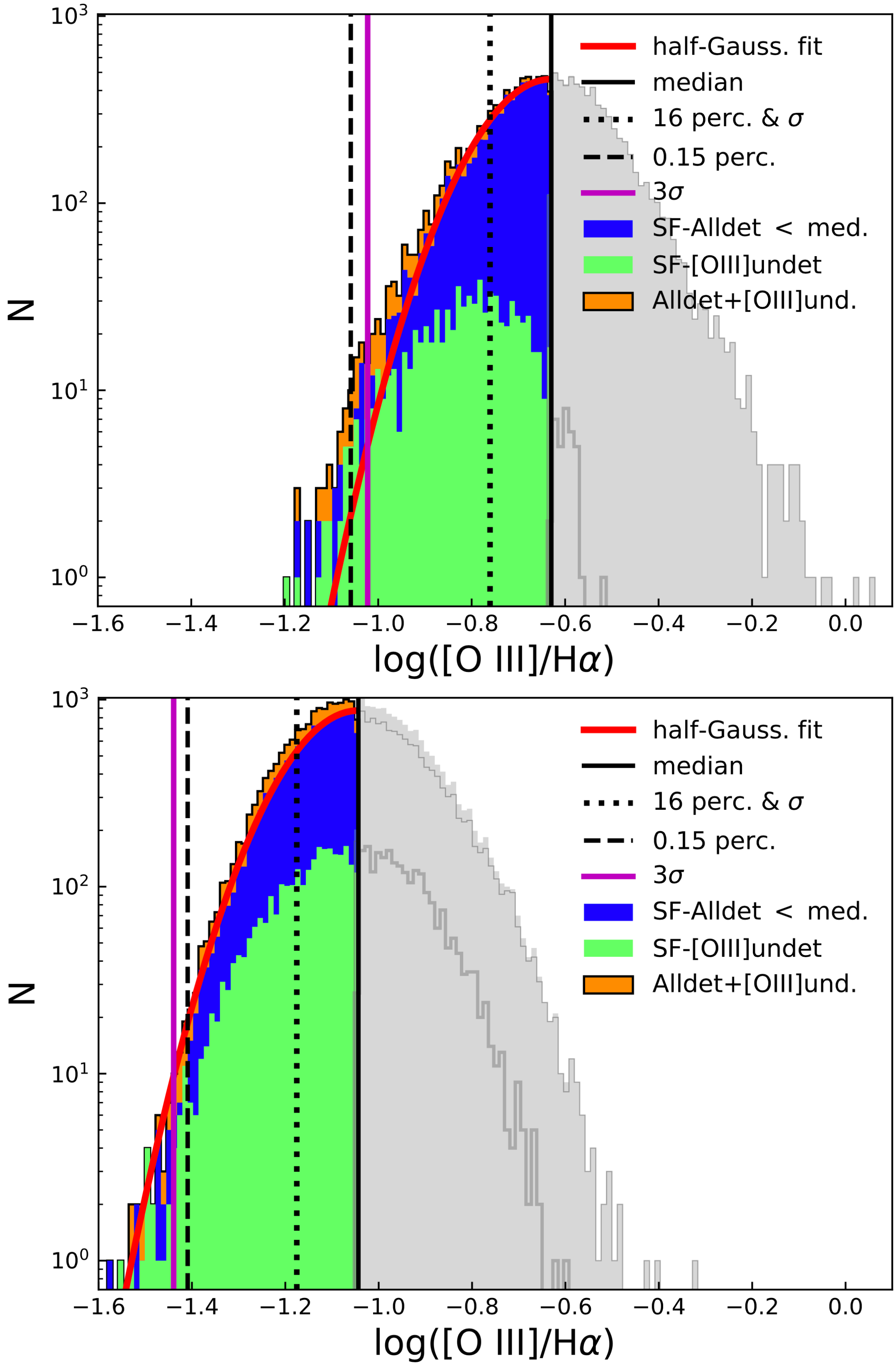

FIGURE 3.4: Distribution of [O III]/Hα in bins of [N II]/[O II]. For illustrative purposes, we show only two bins, namely $-0.7 \leq$ [N II]/[O II] < -0.58 and $-0.2 \leq$ [N II]/[O II] < -0.08. The blue and gray histograms represent the distributions of the SF-Alldet galaxies respectively below and above the median, and the vertical lines are the median (solid line), the 16th percentile (dotted line) and 0.15th percentile (dashed line) of the distribution. The red solid line shows the Gaussian distribution obtained setting as mean and σ the median and the 16th percentile of the distribution, respectively, and the purple vertical line represents the corre-

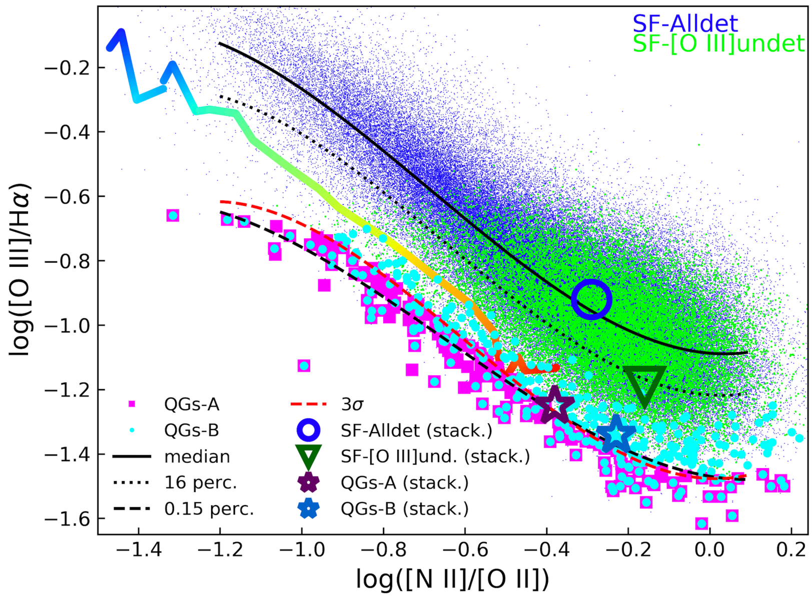

FIGURE 3.5: [O III]/Hα vs. [N II]/[O II] diagram. In blue are shown the SF-Alldet galaxies. The continue black curve represents the median of the relation, while the dotted and the dashed ones represent the 16th and the 0.15th percentiles, respectively. The dashed red curve represents the dispersion at 3σ of the relation. The superimposed colorful line represents the dispersion at 3σ of the [N II]/[O II] for a given value of 12+log(O/H) (as in Figure 3.3). In green, instead, are shown the SF-[O III]undet galaxies (i.e. upper limit in [O III]). Bigger dots represent the QG-A (magenta) and the QG-B (cyan). The empty symbols represent the values estimated on the stacked spectra of SF-Alldet (blue circle), SF-[O III]undet (green triangle), QGs-A (purple star) and QGs-B (blue star) samples.

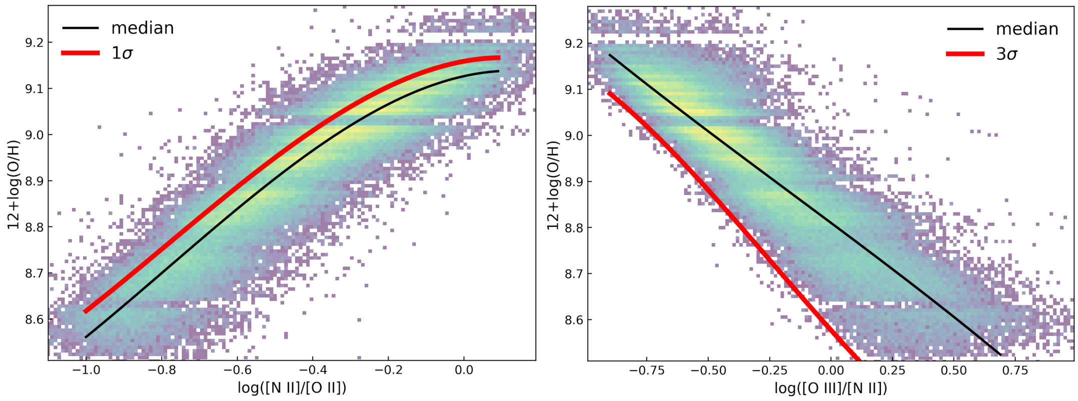

FIGURE 3.6: Left panel: 12+log(O/H) vs [N II]/[O II] relation. The black curve represents the median of the relation, while the red curve represents the median +1σ, where σ is the dispersion of the distribution. Right panel: 12+log(O/H) vs. [O III]/[N II] relation. The black curve represents the median of the relation, while the red curve represents the median-3σ.

A possible issue with this method is that it is based on emission lines that are quite separated in wavelength, and therefore could be affected by inappropriate correction for dust extinction. To test the impact of the extinction law on [O III]/Hα and [N II]/[O II], we consider also the Seaton, 1979 extinction law instead of the Calzetti et al., 2000 one, finding a difference in the ratios at most of 0.1%, and therefore not affecting strongly our selection.

We also explore an alternative diagnostic diagram, considering the [O III]/Hβ vs. [N II]/[S II][7], discarding the redshift ranges in which the measurement of [S II] doublet could be biased by strong sky lines. The [N II]/[S II] ratio has metallicity sensitivity similar to the one of [N II]/[O II], and [O III]/Hβ is very similar to [O III]/Hα, with the drawback of Hβ being weaker than Hα. This diagram has the advantage that the pairs of lines involved are close enough that it is possible to neglect the effect of dust extinction. Following the same procedure described above, we select 144 quenching candidates. However, since [S II] is intrinsically weaker than [O II], the S/N([S II]) distribution of these candidates peaks at S/N $\sim$ 2 and, consequently, their identification is more uncertain. We, therefore, decide not to consider them in the following.

3.2.3 Method B

An alternative method to mitigate the Z-U degeneracy is to select galaxies for which [O III] is weaker than the minimum flux expected for the maximum metallicity. In this way, we can safely assume that the observed value of [O III]/Hα is unlikely to be due to high-metallicity. To investigate this possibility we proceed as follow:

[7][S II] (i.e. [S II]λ6720) represents the sum of [S II]λ6717 and [S II]λ6731 fluxes.

- We derive a metallicity estimate (Z) for each galaxy in our sample. We exploit the 12+log(O/H) vs. [N II]/[O II] relation suggested by Nagao, Maiolino, and Marconi, 2006 (see Figure 3.6), estimating the running median and the corresponding dispersion σ_Z for the SF-Alldet sample. We therefore associate to each galaxy the median 12+log(O/H) corresponding to the observed [N II]/[O II][8] as metallicity value.

- We estimate the maximum metallicity (Z_{max}) of each galaxy, as:

$$Z_{max} = Z + \sigma_Z, \tag{3.4}$$

  where Z and σ_Z are the median and the dispersion associated to this relation (with $\sigma_Z \approx 0.13$ dex); since the dispersion would be higher than the typical metallicity errors, hence, Z_{max} represents a statistical significant estimate for the maximum metallicity.

- In addition, we estimate the minimum expected [O III] flux for any given Z_{max}. To do that, we consider another relation between metallicity and emission lines that includes [O III]. In particular, we adopt [O III]/[N II] as a function of Z (Nagao, Maiolino, and Marconi, 2006) (see Figure 3.6). This relation allows to estimate the minimum expected [O III]/[N II] for any given Z_{max}:

$$[\mathrm{O\,III}]/[\mathrm{N\,II}]_{\mathrm{min.}} = [\mathrm{O\,III}]/[\mathrm{N\,II}] - 3\sigma_{[\mathrm{O\,III}]/[\mathrm{N\,II}]}, \tag{3.5}$$

  where $\sigma_{[\mathrm{O\,III}]/[\mathrm{N\,II}]}$ is the dispersion of the [O III]/[N II] vs. 12+log(O/H) relation (the typical dispersion is $\sigma_{[\mathrm{O\,III}]/[\mathrm{N\,II}]} \approx 0.18$ dex).

- We identify as quenching candidates those galaxies with a [O III]/[N II] lower than $[\mathrm{O\,III}]/[\mathrm{N\,II}]_{\mathrm{min}}$. For these galaxies, the low observed values of [O III]/[N II] are unlikely due to their metallicity. Finally, as in method A, we discard 11 galaxies with detected [Ne III], since it can be a sign of ongoing star formation.

In this way, we select 308 'method B' quenching candidates (hereafter QG-B), that are shown in Figure 3.7.

3.2.4 Comparing the two methods

In this section, we explore the differences and the complementarities between the two methods.

We first notice that there are 120 QGs in common between the two methods. In the [O III]/Hα vs. [N II]/[O II] diagram (i.e. the plane described in subsection 3.2.2, see Figure 3.5) there is a good agreement between Methods B and A: the bulk of QGs-B are located below ($\sim$ 40%) or close to the 3σ curve that is the threshold criterion to select QGs-A. We also show the location of QGs-A candidates in the diagram used

[8]Note that we evaluate the expected metallicity also for galaxies with [O III] undetected, while Tremonti et al. (2004) derived metallicity only for galaxies with all emission lines detected (i.e. with the original S/N > 3).

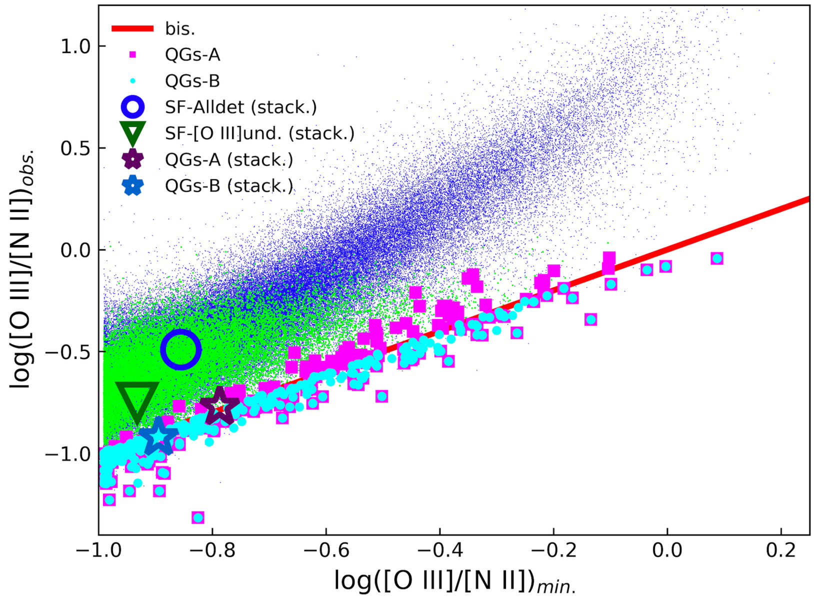

FIGURE 3.7: [O III]/[N II]$_{obs.}$ vs. [O III]/[N II]$_{min.}$ diagram. In blue are shown the SF-Alldet galaxies, while in green the SF-[O III]undet galaxies. Bigger dots represent the QG-A (magenta) and the QG-B (cyan). The empty symbols represent the values estimated on the stacked spectra of SF-Alldet (blue circle), SF-[O III]undet (green triangle), QGs-A (purple star) and QGs-B (blue star) samples.

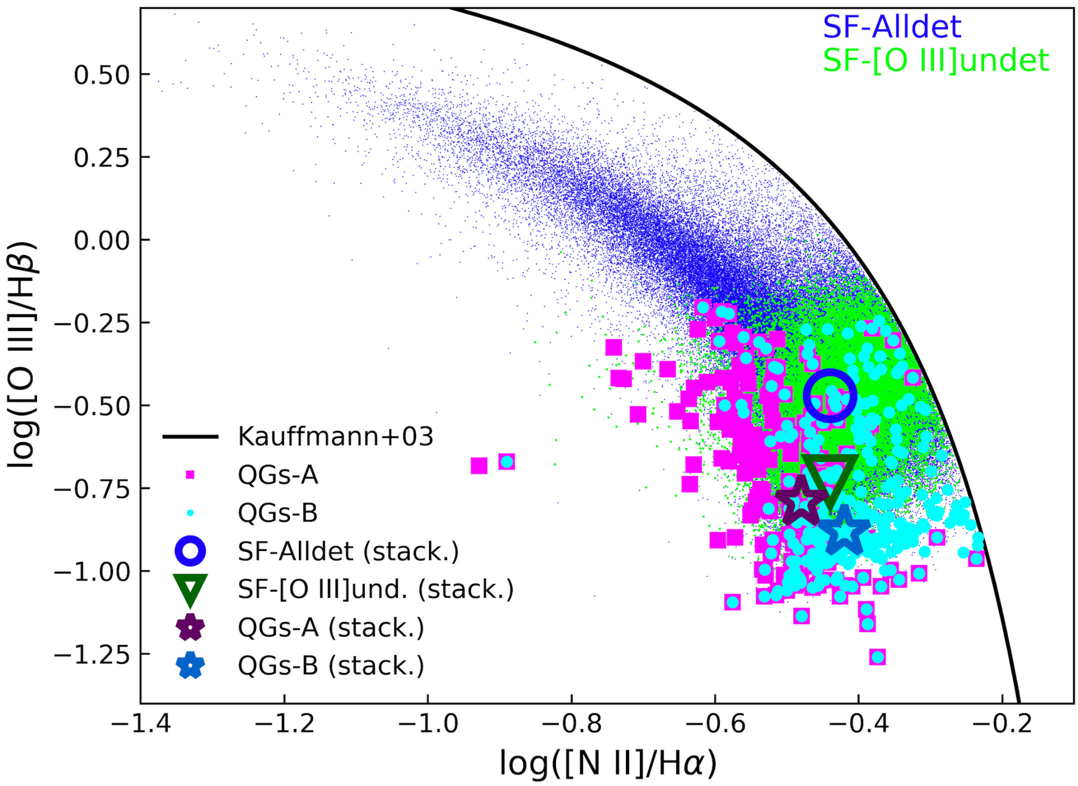

FIGURE 3.8: The BPT diagram of our sample galaxies. The colour code is the same of Figure 3.7.

to select QGs-B (Figure 3.7). Also in this case there is a good agreement between the two samples, with QGs-A located below ($\sim 60\%$) or just above the threshold criterion, having slightly higher upper limits for the observed [O III]/[N II]. We could obtain a better agreement just slightly relaxing the thresholds adopted in the two methods. For example, if we adopt 2.5σ as thresholds instead of 3 for both methods, we obtain that about 60% and 70% of QGs-B are identified also as QGs-A and vice versa. More conservative choices guarantee, however, to obtain more solid results and higher purity at the cost of a lower overlap. Moreover, the residual discrepancy is due to an intrinsic difference between the two methods, that leads to select quenching candidates with different but complementary characteristics. In Figure 3.8 we show the BPT diagram with the candidates selected from the two methods. The bulk of QGs-A are distributed in the lower envelope of the BPT diagram at $\log([\mathrm{O\,III}]/\mathrm{H}\beta) < 0$ and $\log([\mathrm{N\,II}]/\mathrm{H}\alpha) < -0.3$, while QGs-B are complementary located in a region at higher [N II]/Hα values ($\log([\mathrm{N\,II}]/\mathrm{H}\alpha) > -0.5$).

3.3 The properties of quenching galaxies

In this section we analyse the properties of the QGs in order to identify or to constrain plausible quenching mechanism.

In Table 3.3 we report the median, the 16th and 84th percentiles of the distribution of the main properties of our QGs, compared with those of the three control samples defined in Section 3.1.3: SF-Alldet, SF-[O III]undet and no-Hα. We first notice that the median and the range in redshift of QGs candidates are similar to that of star forming galaxies (SF-Alldet). On the contrary, SF-[O III]undet and no-Hα sample cover different redshifts ranges.

3.3.1 Spectral properties

We first inspect the spectra of our QG candidates. In order to increase their S/N, in particular around [O III] and [Ne III] to confirm their low ionisation status, we stack their spectra. Figure 3.9 shows the median stacked spectrum of QGs-A and QGs-B. As a comparison, we show also the spectra of two control samples, stacking all galaxies from SF-Alldet and SF-[O III]undet samples, respectively, in the same mass and redshift range of QGs. The [O II], Hα and Hβ lines (i.e. low-ionisation lines) are the strongest emission lines, while [O III] and [Ne III], which are high-ionisation emission lines, are very weak in both QGs stacked spectra despite the increased S/N (see the zoom of the stacked spectra in the wavelength range around the [O III] and the Hβ lines).

Furthermore, in order to measure high-to-low ionisation emission line ratio and confirm the low ionisation level of our QGs, we derive the dust-corrected stacked spectrum, correcting the individual spectra for the dust extinction[9] before stacking them

[9] We derive it from the Hα/Hβ flux ratio using the Calzetti et al., 2000 extinction law, the same that we have adopted for the dust correction of the emission lines.

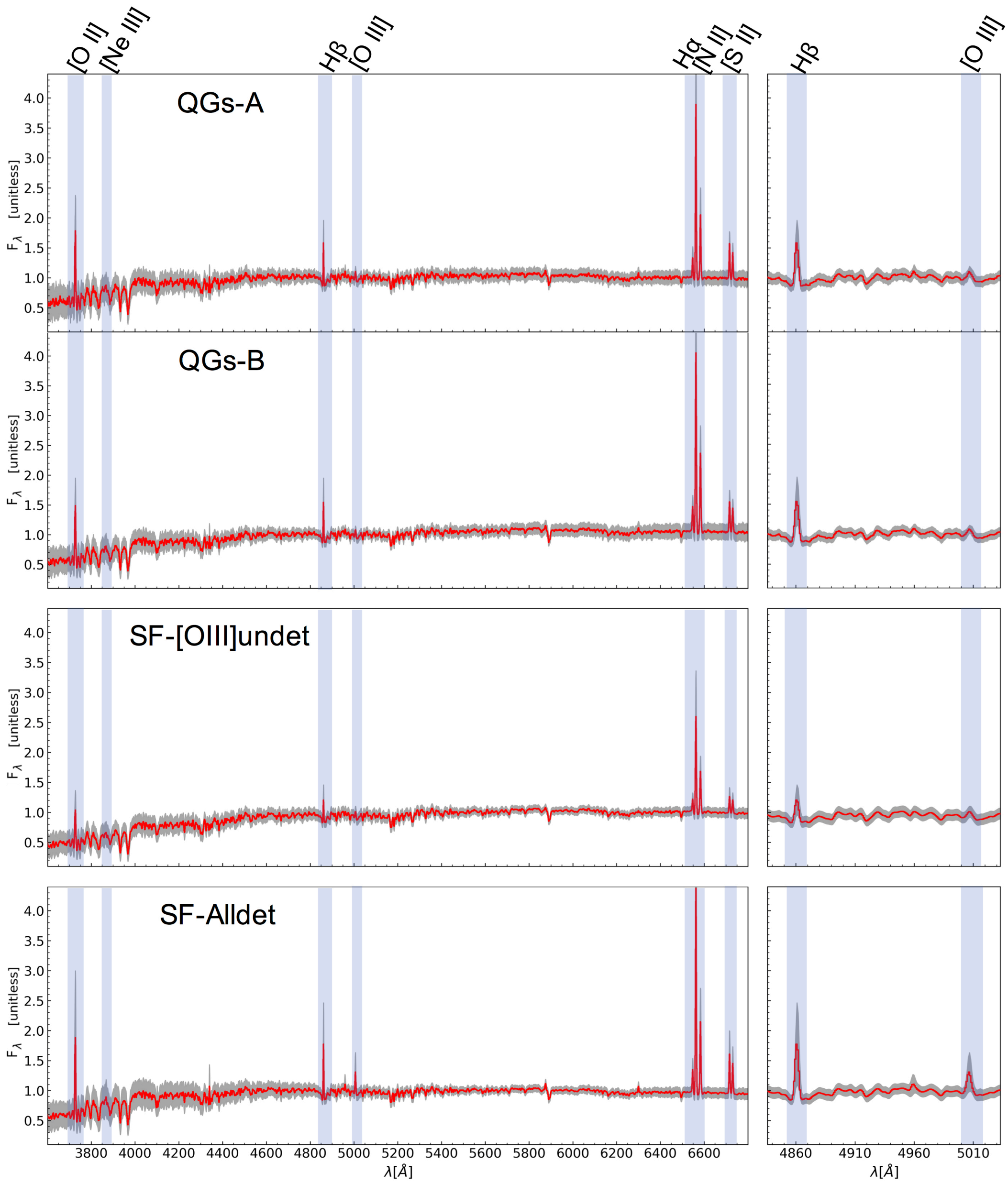

FIGURE 3.9: The median stacked spectra (in red) of QGs-A, QGs-B, SF-[O III]undet and SF-Alldet galaxies. The gray shaded area represents the dispersion of the stacked spectra. The percentiles of the redshift distributions of galaxies in each stacked spectrum are listed in Table 3.3.

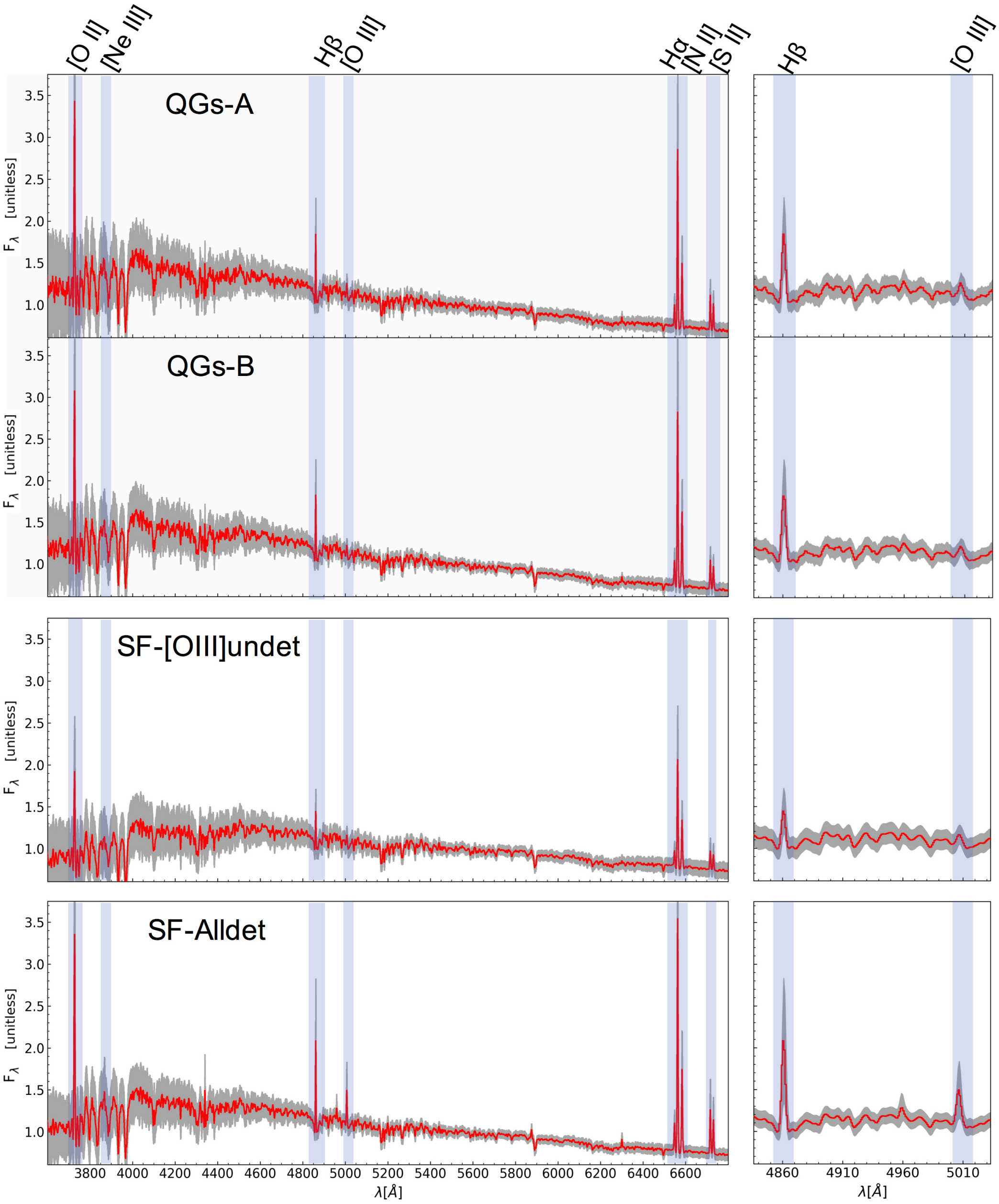

FIGURE 3.10: The median stacked spectra corrected for the dust extinction (in red) of QGs-A, QGs-B, SF-[O III]undet and SF-Alldet galaxies. The gray shaded area represents the dispersion of the stacked spectra. The percentiles of the redshift distributions of galaxies in each stacked spectrum are listed in Table 3.3.

TABLE 3.2: Main emission lines ratios measured on stacked spectra of QGs-A, QGs-B, SF-[O III]undet and SF-Alldet samples.

Property	QGs-A	QGs-B	[O III]und.	SF-Alldet
[O III]/Hα	-1.25 ± 0.04	-1.34 ± 0.04	-1.19 ± 0.02	-0.92 ± 0.04
[N II]/[O II]	-0.23 ± 0.02	-0.29 ± 0.02	-0.16 ± 0.02	-0.29 ± 0.02
log([O III]/Hβ)	-0.79 ± 0.04	-0.88 ± 0.04	-0.73 ± 0.03	-0.47 ± 0.02
log([N II]/Hα)	-0.48 ± 0.02	-0.42 ± 0.02	-0.44 ± 0.02	-0.44 ± 0.04
log([O III]/[N II])	-0.77 ± 0.03	-0.92 ± 0.03	-0.75 ± 0.02	-0.49 ± 0.02
D_n4000	1.23 ± 0.01	1.25 ± 0.01	1.34 ± 0.01	1.23 ± 0.01
EW_{rf}(Hα) [Å]	-18.62 ± 0.09	-18.19 ± 0.07	-12.30 ± 0.01	-21.38 ± 0.01

together (see Figure 3.10). Also in this case we confirm the weakness of [O III] (and of other high-ionisation emission lines, such as [Ne III]) in both QGs stacked spectra. We, further, note that in QGs spectra the stellar continuum is blue, suggesting a still young mean stellar population, consistent with a recent quenching of the star formation (see C17 for discussion on the expected colors of QGs).

We run the *Gandalf* code (Sarzi et al., 2006; Cappellari and Emsellem, 2004) on the dust-corrected stacked spectra. We fit the continuum with the stellar population synthesis models of Bruzual and Charlot (2003), used also by Tremonti et al. (2004), and measure the main emission lines and spectral properties on the stacked spectra. We list them in Table 3.2 and show them in Figures 3.5, 3.7, 3.8 and 3.11.

From this analysis, we find evident Hα emission in QGs stacked spectra, although slightly weaker than in the star-forming, and given that the samples have similar median redshift, we find that $\frac{L(H\alpha)_{QGs\text{-}A}}{L(H\alpha)_{SF\text{-}Alldet}} = 0.82 \pm 0.07$, while $\frac{L(H\alpha)_{QGs\text{-}B}}{L(H\alpha)_{SF\text{-}Alldet}} = 0.91 \pm 0.08$. Further, we measure, in particular, the [O III]/Hα and [N II]/[O II] ratios of the median stacked spectra (see Table 3.2), obtaining values consistent with the low ionisation level of our QG candidates and far below the control sample of star-forming galaxies. We note, instead, that the [O III]/Hα value measured on the SF-[O III]undet stacked spectrum is intermediate between SF and QG candidates, suggesting that also SF-[O III]undet galaxies have a lower ionisation state with respect to the star-forming population, but not as extreme as QG candidates. In Figures 3.5, 3.7 and 3.8 we show the ratios measured on stacked spectra. In particular, from Figures 3.5 and 3.7 we confirm that the ratios measured on stacked spectra of QGs are consistent with both our selection criteria and a low-ionisation state, while the ratios for star-forming galaxies lie consistently on their median relations, compatible with ongoing star formation (see Figure 3.3 and C17). Finally, we note that the ratios for SF-[O III]undet lie only slightly above our selection criteria, suggesting a lower ionisation level with respect to SF galaxies. This also indicates that also amongst these galaxies there are good QG candidates. In this case, the limiting flux of the survey does not allow to pre-select individual QG candidates from single spectra, and to separate them from a residual contamination of SF galaxies. From this analysis, we also confirm that QGs-A have slightly higher [O III]/Hα and [O III]/[N II] values, and slightly lower [N II]/[O II] and [N II]/Hα values compared to QGs-B, suggesting a lower value for their metallicity, consistently with, on average, lower masses (see subsection 3.3.2). We further note that the [N II]/[O II] ratios of our QGs are in

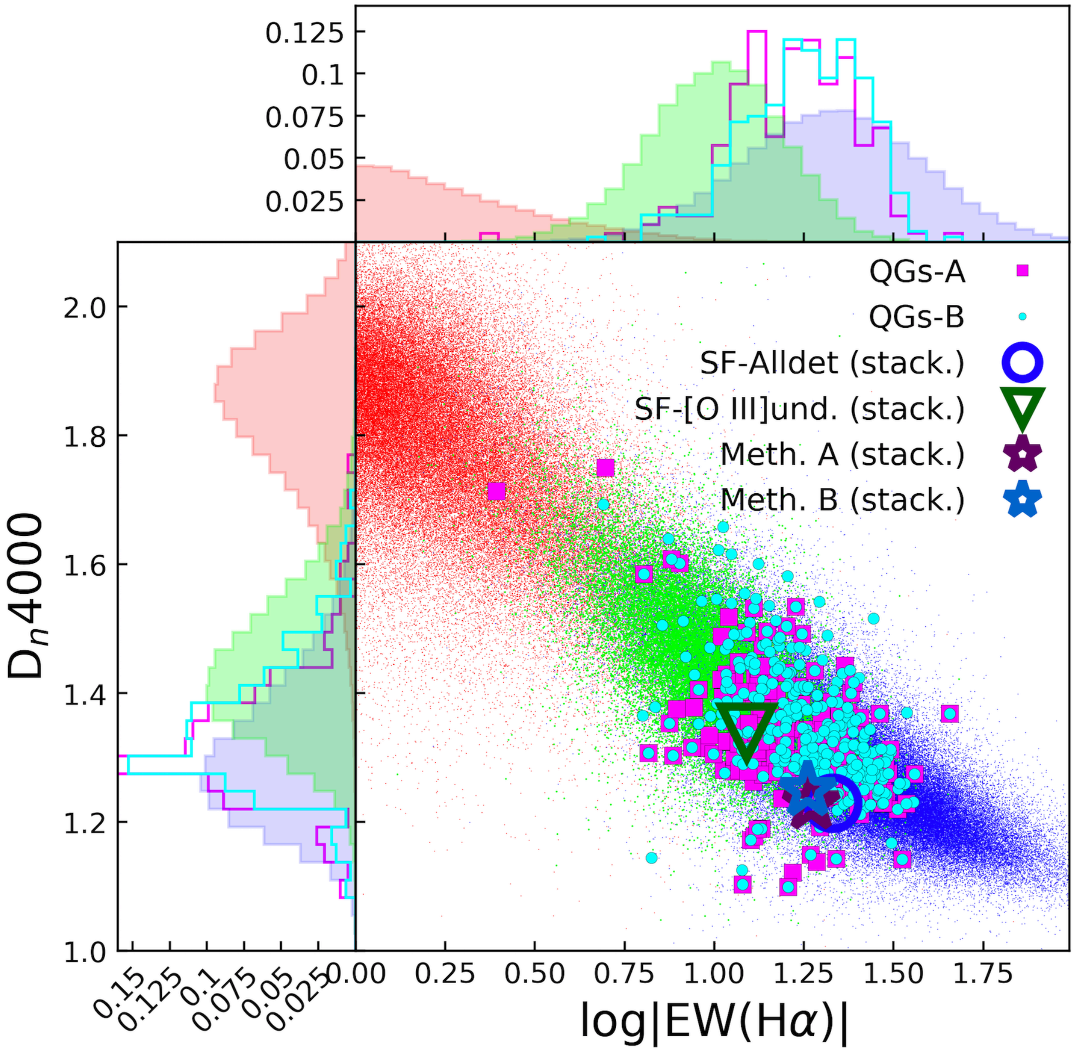

FIGURE 3.11: The D_n4000 as a function of the EW(Hα). The layout is the same of Figure 3.7.

both cases similar to those of the SF-Alldet sample, suggesting that our QGs have metallicities similar to the ones of the SF galaxies parent sample.

D_n4000 vs EW(Hα)

In this subsection we analyse two spectral features of QGs. The rest-frame equivalent width EW(Hα), that represents an excellent indicator of the presence of young stellar populations (e.g. Levesque and Leitherer, 2013) and of the specific SFR (sSFR), and the break at 4000 Å rest-frame, that provides an estimate of the age and metallicity of underlying stellar populations (e.g. Moresco et al., 2012). Using them jointly allows to qualitatively evaluate the connection between the newborn stars and the mean stellar population of the galaxy.

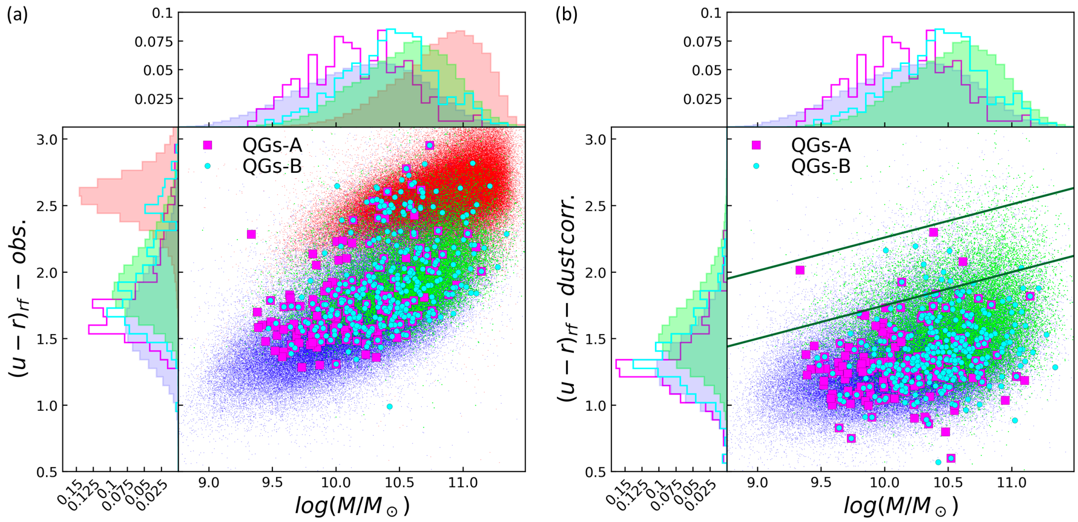

FIGURE 3.12: (a) The rest-frame (u-r) colour - mass diagram. The colours are not corrected for the dust extinction. (b) The same diagram with colours corrected for the dust extinction. We represent the SF-alldet subsample with small blue dots, the SF-[O III]undet subsample with small green dots and the control sample of galaxies with no-Hα emission with small red dots. We use magenta squares for QGs-A and cyan circles for QGs-B. The two dark green straight lines represent the edge of the green valley defined by Schawinski et al., 2014.

In Figure 3.11 we show the relation between the D_n4000 and log(|EW(Hα)|). Some interesting trends emerge from it. As expected, there is a strong anti-correlation between these quantities and a clear separation of the no-Hα galaxies from the SF ones. Furthermore, we note that the SF-[O III]undet sample is shifted toward higher D_n4000 and lower log|EW(Hα)| with respect to the distributions of the SF-Alldet sample. This suggests that the SF-[O III]undet galaxies are characterized, on average, by older stellar populations than the SF-Alldet ones. Finally, we find that both QGs-A and -B lie in a region between the bulk of SF-Alldet and the SF-[O III]undet. Interestingly, a few QGs show an intermediate EW(Hα) but very low D_n4000, that could be a fingerprint of recent star-formation quenching. We confirm these differences by the measurements from the stacked spectra, i.e. the values of D_n4000 and log(|EW(Hα)|) of QGs-A and -B are intermediate between SF-Alldet and no-Hα sample (see values reported in Table 3.3 and Figure 3.11). The different distribution of these populations in both D_n4000 and EW(Hα) is also confirmed by Kolmogorov-Smirnov tests (hereafter KS) at high significance level.

This analysis suggests that our QG candidates have stellar populations which are intermediate between SF and already quenched galaxies, confirming that they are interrupting their SF.

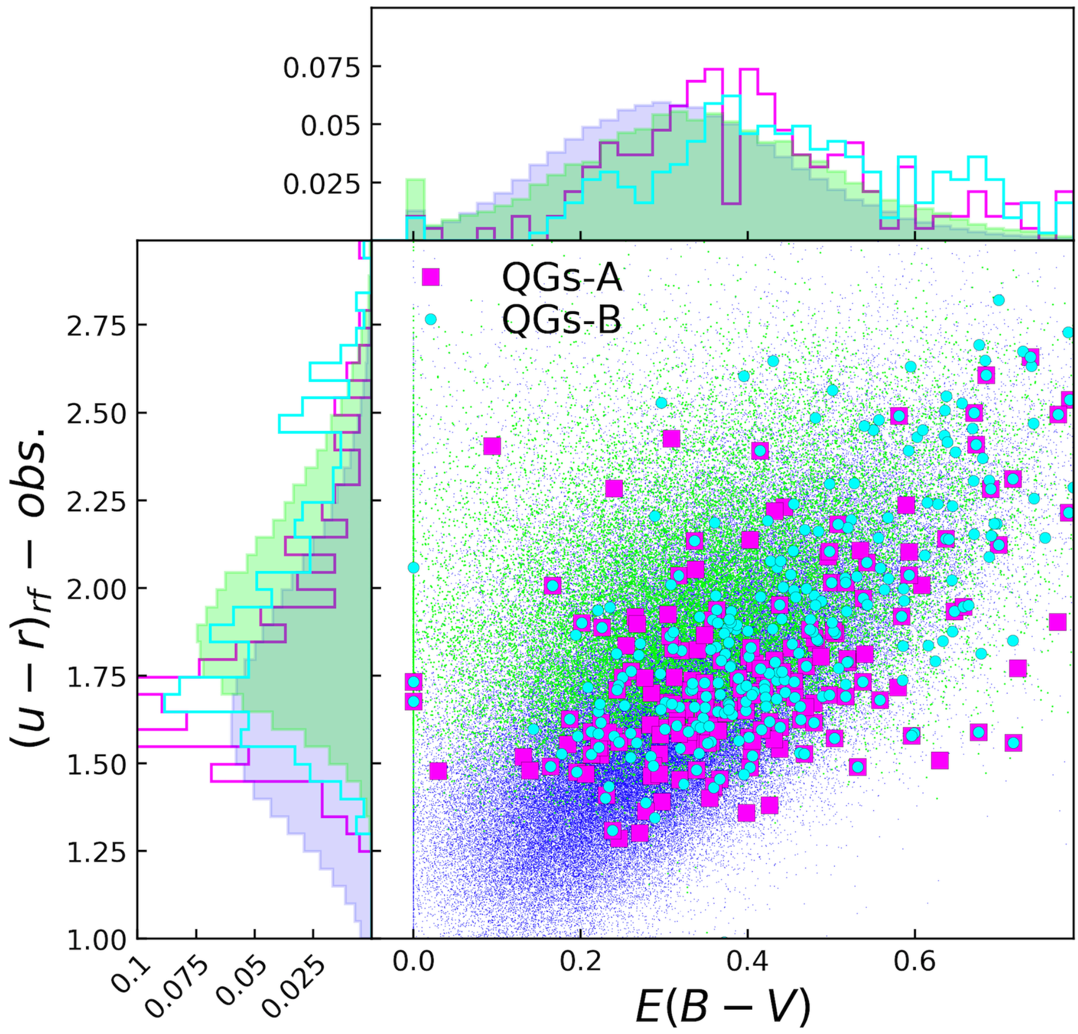

FIGURE 3.13: The (u-r) colours as a function of the E(B-V). The layout is the same of Figure 3.12.

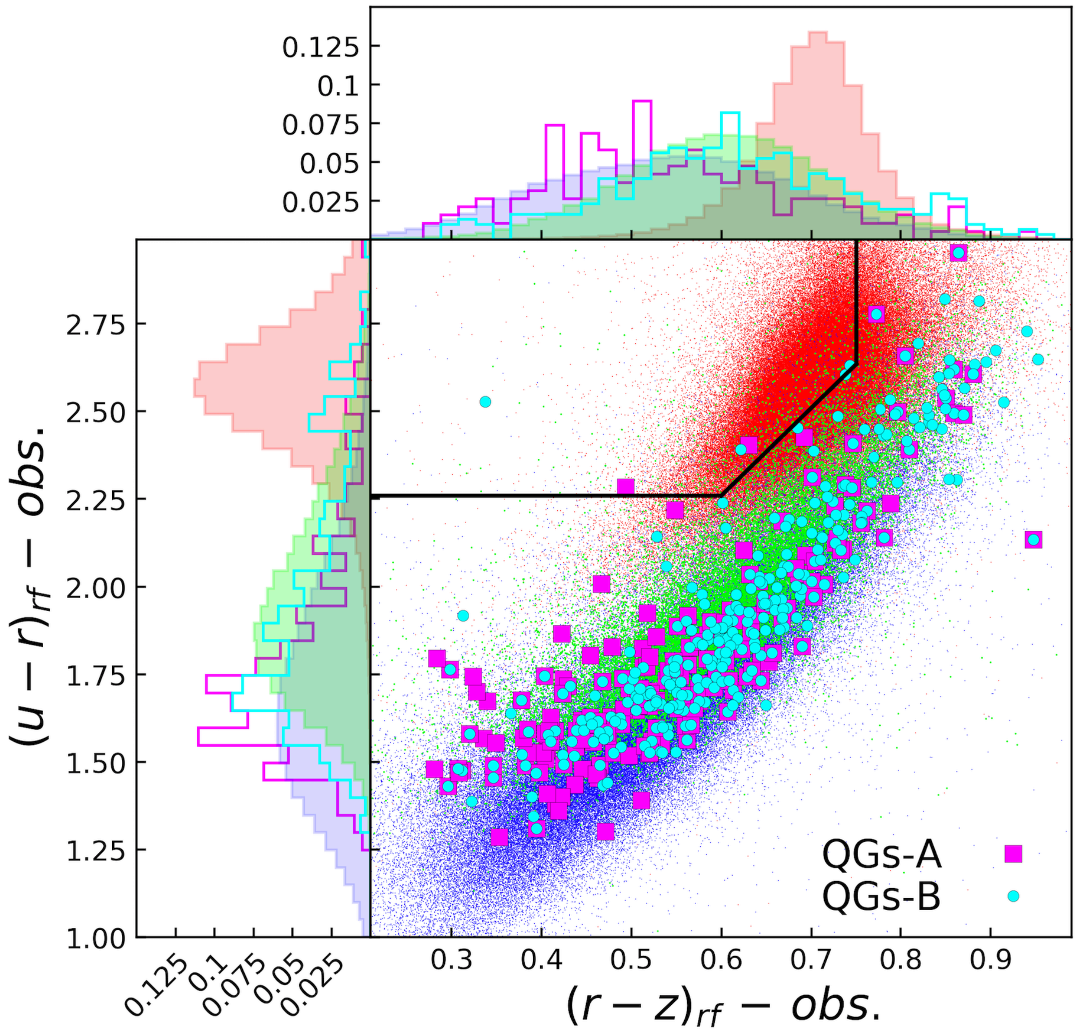

FIGURE 3.14: The rest-frame dust-uncorrected colours (u-r) - (r-z) diagram. The layout is the same of Figure 3.12. The boundary in black is from Holden et al., 2012.

3.3.2 QGs in the colour-mass diagram

Figure 3.12 (a) shows the rest-frame, dust-uncorrected colour (u-r) as a function of stellar mass. Our SF-alldet sample forms the well-known blue cloud, while the complementary sample of no-Hα emission sample shapes the red sequence. The SF-[O III]undet sample overlaps with the blue cloud in the intermediate region between the two sequences. The QGs-A are mainly located in the blue cloud region at colours $1.5 \lesssim$ (u-r) $\lesssim 2.1$, while only a few of them have redder colours, near or in the lower part of the red sequence. We verify that the red colours of these QGs are due to a strong dust extinction (see following discussion and Figure 3.13). The colours of QGs-B have instead a larger spread ($1.6 \lesssim$ (u-r) $\lesssim 2.4$), with a median value redder than the SF-Alldet sample and QGs-A, but still blue. Their colour distribution presents also a significant tail reaching the red sequence (15.9% of the sample has colours (u-r) > 2.4). As for QGs-A, we verify that these red candidates are reddened by dust extinction (see Figure 3.13).

In Figure 3.13 we show the observed (u-r) colour as a function of the E(B-V) derived from the Hα/Hβ ratio, in order to analyse the contribution of the dust extinction to the colour distribution. Obviously, the no-Hα control sample is not included, since its galaxies have S/N(Hα) and S/N(Hβ) lower than 3. There is a clear correlation between colour and E(B-V), also in QGs samples, with the reddest galaxies having the highest values of E(B-V). About 16% of QGs-A show E(B-V) higher than 0.6, while the same percentage of QGs-B have even higher dust extinction, showing E(B-V)> 0.7. As anticipated, the QGs with the reddest colours are those with the highest E(B-V) values, which confirm that their intrinsic colours are still blue, as expected from their recent quenching phase (see also the discussion inC17).

In order to better distinguish the dust-reddened quenching candidates from the intrinsic red ones, we exploit the Holden et al., 2012 rest-frame dust-uncorrected colour-colour plane (u-r) vs (r-z), showing the results in Figure 3.14. Only a few candidates are located in the region of pure passive red galaxies, whose boundaries are defined by Holden et al., 2012. On the contrary, the other red candidates are actually reddened by the dust extinction.

Finally, Figure 3.12 (b) shows the colour-mass diagram with the (u-r) corrected for the dust extinction. In particular, we adopt the attenuation law of Calzetti et al., 2000, with the stellar continuum colour excess E_S(B-V) = 0.44 E(B-V). As already shown, we confirm that none of our QG candidates has intrinsic red colours and only a few of them lie in the green valley region defined by Schawinski et al., 2014. However, although they are mainly in the blue cloud, their colour distributions are different from that of SF-Alldet, showing a peak at (u-r) $\sim$ 1.3 and on average redder colors (see Figure 3.12 (b)). This is also confirmed by the KS test at a significance level α = 0.05.

We stress here that most of our QG candidates would not be selected using dust-corrected green colours, i.e. they do not lie within the so called "Green Valley", which separate star-forming galaxies from quiescent passive ones.

From our analysis we find that the mass distribution of QGs-A is spread (i.e. 16th-84th percentiles) over the range $9.8 \lesssim \log(M/M_{\odot}) \lesssim 10.6$, being comparable with that of SF-Alldet galaxies ($9.7 \lesssim \log(M/M_{\odot}) \lesssim 10.7$), however, QGs-A are slightly less massive than the global SF-[O III]undet sample ($10.1 \lesssim \log(M/M_{\odot}) \lesssim 10.9$). The masses of QGs-B are in the range $\sim 10 < \log(M/M_{\odot}) <\sim 10.8$, i.e. they are more massive than those derived by method A. This evidences are also confirmed by the KS test at a significance level α = 0.05, verifying that the masses of QGs-A and SF-Alldet are drawn from the same distribution (i.e. p-value = 0.052) , differently from that of QGs-B. Moreover, both the QGs masses have distributions which are different from that of [O III]undet. Furthermore, we note that no QG candidates have masses lower than $\log(M/M_{\odot}) <\sim 9.5$ for both methods (A and B). This suggest that, as expected in a downsizing scenario, quenching has not started yet for the low-mass galaxies. This is supported also by the lack of a population of low-mass red galaxies among our no-Hα sample in the red sequence.

3.3.3 Star formation rates

Figure 3.15 shows the SFR-mass plane of our samples. As described in subsection 3.1.1, the SFR is estimated from the dust-corrected Hα luminosity. For the no-Hα sample, instead, the SFR are derived from a multi-band photometric fitting. We stress, however, that for the QG candidates these SFRs estimates should be considered as upper limits to their current SFR, due to their past SFR preceding the quenching. Indeed, even when the O stars die, the longer-lived B stars have sufficient photons harder than 912 Å to ionise hydrogen, explaining their Hα emission. In this case their Hα emission can be considered as an upper limit to their current SFR. As expected, our SF-Alldet sample forms the well known SF main sequence[10] (MS), while the SF-[O III]undet sample lies just below it, but it is well separated and above the no-Hα sample of low-SFR/passive galaxies. We find that both QGs-A and -B show high SFRs, with only few of them having very low SFRs, compatible with them being already passive. The QGs-A sample has SFR in the range $0.6 <$ SFR $[M_{\odot}\ yr^{-1}] < 11.5$, with a distribution similar to that of the SF-Alldet galaxies[11](see Table 3.3), but above the SF-[O III]undet galaxies. These evidences are confirmed by KS tests with a significance level $\alpha = 0.05$. Instead, the KS tests show that the SFR distribution of QGs-B and SF-Alldet are different. This result arises also from the 16th-84th percentiles of the distribution (see Table 3.3), where the SFR of QGs-B are slightly shifted towards higher SFR than those of the SF-Alldet population. This effect is mainly due to the higher average mass for QGs-B sample.

From this analysis we also stress that most of our QG candidates would not be selected as intermediate between SF and passive quiescent ones from the SFR-mass plane.

[10]The straight-line representing the SF-Alldet MS is log(SFR) = $0.79 \times \log(M/M_{\odot}) - 7.74$.

[11]The straight-lines representing the QGs MS are log(SFR) = $1.10 \times \log(M/M_{\odot}) - 10.93$ and log(SFR) = $1.04 \times \log(M/M_{\odot}) - 10.36$, respectively for QGs-A and -B.

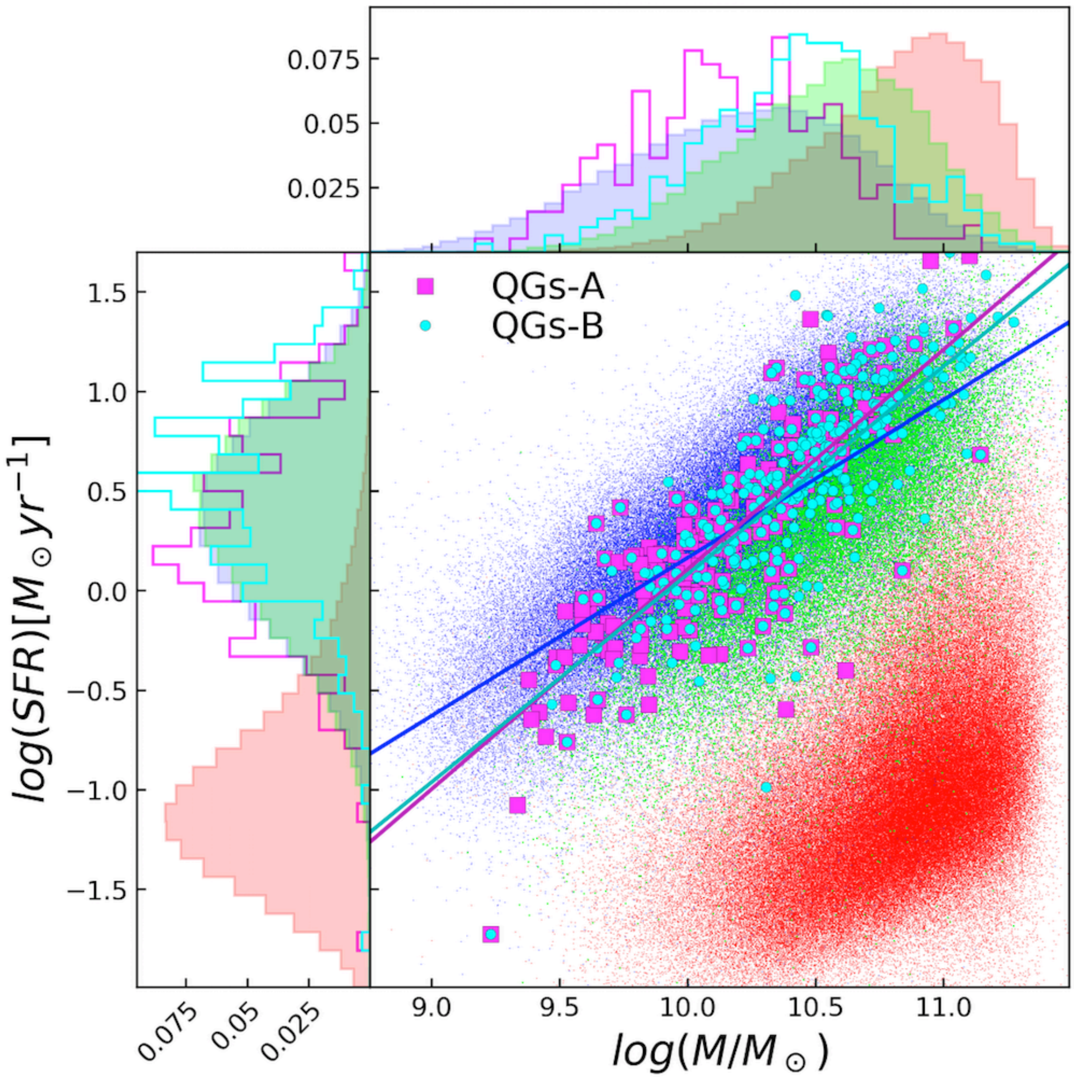

FIGURE 3.15: The log(SFR_{tot}) as a function of the stellar mass. The layout is the same of Figure 3.12.The blue straight line represents the main-sequence (MS) of the SF-Alldet sample, while the magenta and the cyan ones are the MS of QGs-A and QGs-B, respectively.

TABLE 3.3: Fundamental properties of the QGs, compared against three control samples: SF-Alldet, SF- [O III]undet (the subsample in which the candidates are selected) and no-Hα. For each parameter we report the 50th (16th, 84th) percentiles of its distribution.

Property	QGs-A	QGs-B	SF-[O III]undet	SF-Alldet	no-Hα
N.	192	308	25911	148145	201527
redshift	0.08 (0.05, 0.11)	0.08 (0.06, 0.13)	0.12 (0.07, 0.16)	0.08 (0.05, 0.13)	0.12 (0.08, 0.16)
$\log(M/M_\odot)$	10.1 (9.7, 10.6)	10.4 (10.1, 10.8)	10.6 (10.1, 10.9)	10.2 (9.7, 10.7)	10.9 (10.4, 11.2)
$(u\text{-}r)_{\rm rf}$ obs.	1.73 (1.53, 2.10)	1.88 (1.61, 2.40)	1.93 (1.69, 2.27)	1.68 (1.38, 2.05)	2.57 (2.37, 2.75)
E(B-V)	0.40 (0.26, 0.59)	0.45 (0.30, 0.68)	0.34 (0.19, 0.51)	0.31 (0.17, 0.46)	/
SFR [$M_\odot$ yr^{-1}]	0.33 (0.08, 1.63)	0.78 (0.22, 2.88)	0.38 (0.09, 1.31)	0.47 (0.12, 1.75)	0.03 (0.01, 0.08)
log(sSFR) [yr^{-1}]	-10.6 (-11.0, -10.3)	-10.5 (-10.8, -10.2)	-11.0 (-11.4, -10.6)	-10.5 (-10.9, -10.1)	-12.4 (-12.7, -11.9)
C(R90/R50)	2.20 (2.01, 2.53)	2.28 (2.05, 2.62)	2.19 (1.97, 2.55)	2.27 (2.04, 2.60)	2.86 (2.52, 3.13)
D_n4000	1.31 (1.25, 1.41)	1.34 (1.27, 1.45)	1.43 (1.33, 1.55)	1.30 (1.20, 1.42)	1.84 (1.70, 1.95)
$EW_{\rm rf}(H\alpha)$ [Å]	-16.9 (-24.4, -11.6)	-18.1 (-26.1, -12.0)	-10.1 (-15.3, -6.5)	-21.2 (-37.8, -11.8)	-0.8 (-2.1, -0.2)

TABLE 3.4: The 50th (16th, 84th) percentiles of the morphological probability distribution of QGs-A and QGs-B, compared against three control samples: SF-Alldet, SF-[O III]undet (the subsample in which the QGs are selected) and no-Hα.

	P(Scd)	P(Sab)	P(S0)	P(E)
QGs-A	0.35 (0.13,0.70)	0.30 (0.17,0.60)	0.04 (0.01,0.14)	0.01 (0.00,0.03)
QGs-B.	0.25 (0.12,0.65)	0.35 (0.18,0.65)	0.05 (0.02,0.22)	0.01 (0.01,0.04)
SF-Alldet	0.33 (0.14,0.65)	0.35 (0.19,0.61)	0.06 (0.03,0.20)	0.01 (0.01,0.04)
SF-[O III]undet	0.27 (0.07,0.66)	0.34 (0.15,0.67)	0.04 (0.01,0.14)	0.01 (0.00,0.03)
no-Hα	0.06 (0.03,0.23)	0.13 (0.04,0.58)	0.19 (0.09,0.61)	0.05 (0.01,0.72)

3.3.4 Morphology

In this section we analyse the morphologies of our quenching candidates. The favorite scenario for the transformation of star forming galaxies into passive ones suggests both the migration from the blue cloud to the red sequence and the morphological transformation from disks to spheroids (e.g. Faber et al., 2007; Tacchella et al., 2015). It is still unclear if this transformation occurs during the migration or via dry merging, when a galaxy has already reached the red sequence. Our QGs samples, catching the galaxies in an early phase after SF quenching, are therefore crucial to address this open question.

In Table 3.4 we report the 16th-50th-84th percentiles of the morphological probability distribution of the four morphological classes (Scd, Sab, S0, E) for our subsamples. In Figure 3.16 we further show the distribution built assigning to each galaxy the morphological class with the highest probability. SF-Alldet and SF-[O III]undet galaxies have the same distribution: roughly 50% of SF objects are late Scd galaxies, while 40% of them are Sab and less than 10% are S0. On the contrary, the no-Hα sample shows a different distribution, in which the early type classes are more common then the late type ones. For comparison, the bulk of QGs-A are Scd ($\sim$ 60%), while 35% are Sab. Also QGs-B are disk galaxies with a similar probability of being disk dominated Scd galaxies or bulge dominated Sab disk galaxies. Only $\sim 7\%$ of QGs-A and $\sim 10\%$ of QGs-B are instead S0 or E galaxies. Therefore, we conclude that our candidates have the same morphology classes as the SF galaxies. Therefore, our analysis suggests that no morphological transformation has yet occurred in the early phase after the quenching of the SF.

We further analyse the concentration-redshift relation, shown in Figure 3.17. The concentration is defined as C=R90/R50, where R90 and R50 are the radii containing 90 and 50 per cent of the Petrosian flux in *r*-band. This parameter is strongly linked to the morphology of the galaxies, and there is general consensus that C=2.6 is the threshold concentration dividing early type galaxies from the other types (e.g. Strateva et al., 2001). This value is, indeed, confirmed by the crossing point between the C distributions of our SF and no-Hα samples. The bulk of QGs have C < 2.6, but some of them ($\sim 12\%$ of QGs-A and $\sim 17\%$ of QGs-B) have higher concentrations. This suggests that they could be quenching galaxies which have experienced morphological transformation during the transition from blue cloud to red sequence.

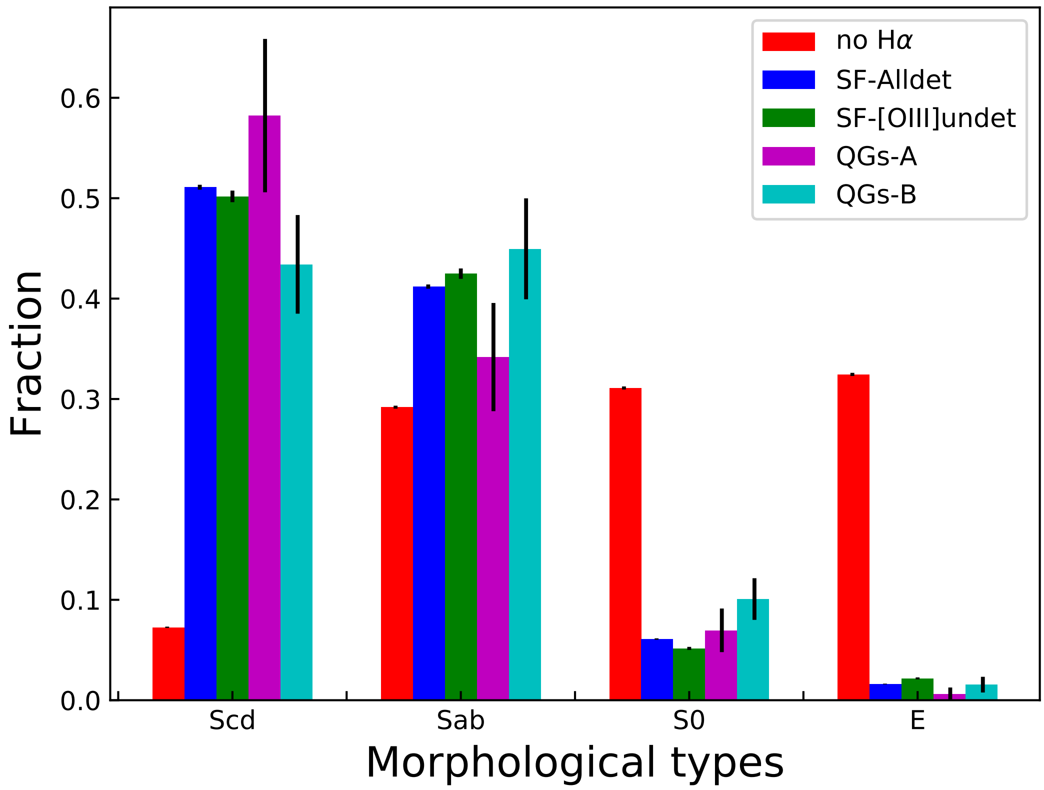

FIGURE 3.16: Distribution of no-Hα (red), SF-Alldet (blue), SF-[O III]undet (green), QGs-A (magenta) and QGs-B (cyan) in 4 morphological types (Scd, Sab, S0 and E).

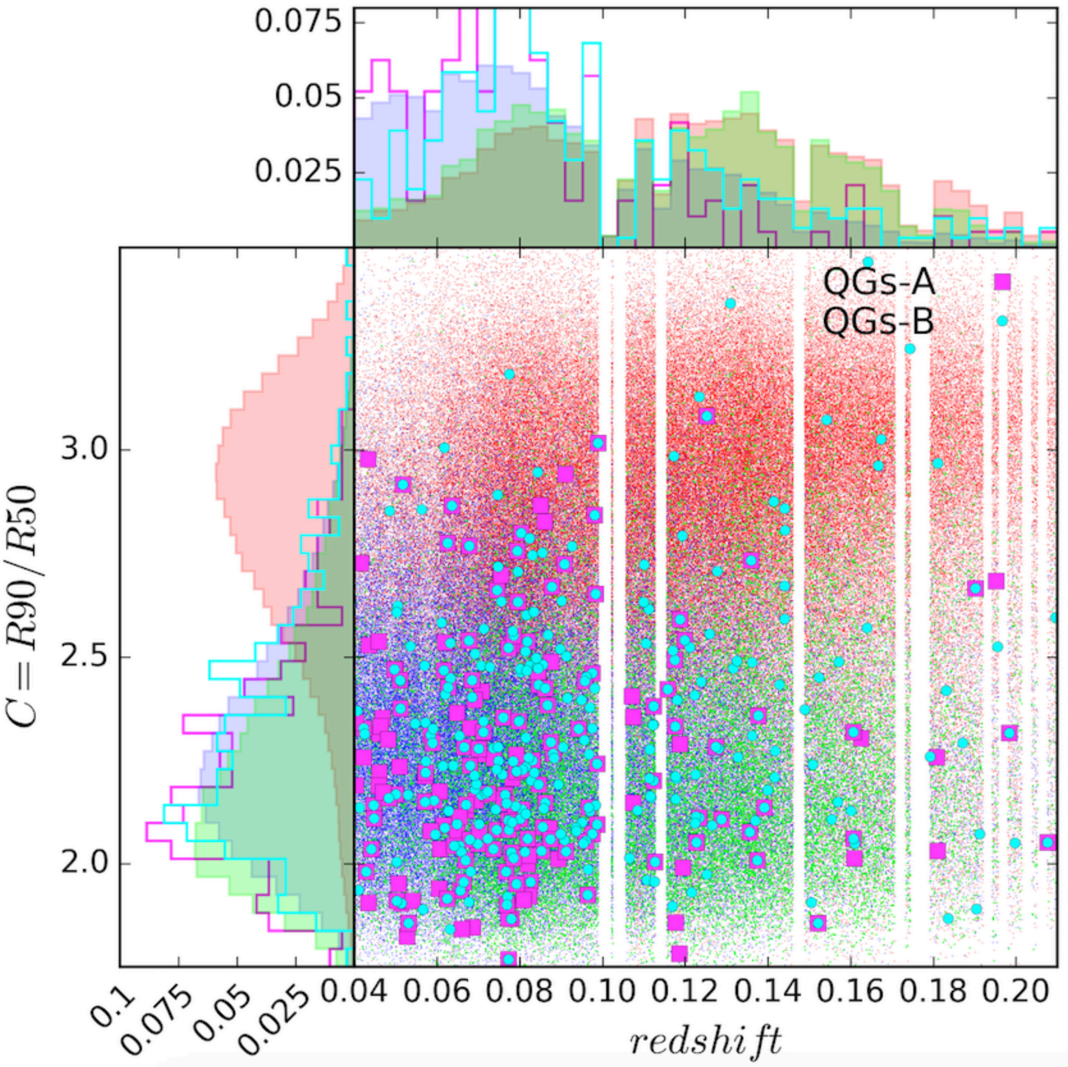

FIGURE 3.17: The light concentration - redshift relation for our sample and QGs. The layout is the same of Figure 3.12

TABLE 3.5: The environment of the quenching candidates with methods A and B compared against three control samples: SF-Alldet, SF-[O III]undet (the subsample in which the candidates are selected) and no-Hα. The column Global lists the ratio between the number of objects in common with the Tempel et al., 2014 sample over the total number in each sub-sample.

	Global	low-D ($\rho_{env.} < 22.45$)	interm-D ($22.45 \leq \rho_{env.} < 62.87$)	high-D ($\rho_{env.} \geq 62.87$)
QGs-A	158/192	$27.2 \pm 4.7\%$	$31.7 \pm 5.1\%$	$41.1 \pm 6.1\%$
QGs-B	258/308	$22.5 \pm 3.3\%$	$34.1 \pm 4.2\%$	$43.4 \pm 4.9\%$
SF-Alldet	130651/148145	$33.3 \pm 0.2\%$	$33.3 \pm 0.2\%$	$33.3 \pm 0.2\%$
SF-[O III]undet	22667/25911	$13.3 \pm 0.3\%$	$29.1 \pm 0.4\%$	$57.6 \pm 0.6\%$
no-Hα	174741/201527	$8.6 \pm 0.1\%$	$22.4 \pm 0.1\%$	$69.0 \pm 0.3\%$

3.3.5 Environment

In this section, we examine the environment of our sample of QGs. Studying the local environment of a galaxy is crucial to disentangle between several known mechanisms able to remove the cool gas needed for star formation.

Figure 3.18 shows the 'environmental density' of galaxies ρ_{env} normalised at a smoothing radius of 1 h^{-1} Mpc (see subsection 3.1.1), as a function of stellar mass. It is possible to note a general trend, but with a wide spread, in which the highest stellar mass of the galaxies increases for increasing density and this behavior is true also for our QGs. We note, in particular, that at the highest densities there are QGs with a large mass spread, while low density environments are populated only by galaxies and QGs with stellar mass lower than $\sim 10^{10.5}$M$_\odot$. Viceversa, galaxies and QGs with the highest masses reside only in high density environments.

We divide the sample into three environmental classes, separated at $\rho_{env} = 22.45$ and $\rho_{env} = 62.87$, respectively, which are defined basing on the tertiles of the ρ_{env} distribution of the parent SF-Alldet population. We define 'low-D' those galaxies belonging to the first tertile; 'interm-D' those in the second tertile and 'high-D' those galaxies belonging to the third tertile. We compare the environment of the QG candidates against that of the parent SF population, finding a hint of a lack of QGs in low-D environment and an excess in high-D environment, at high significance level ($\sim 3\sigma$) only for QGs-B (see Figure 3.19). Indeed, a KS test confirms this behavior at a significance level α=0.05 only for QGs-B, while QG-A and SF-Alldet populations appear to have a compatible ρ_{env}.

In Table 3.5 we compare also the fraction in the three different environments of the QG candidates against other two reference samples of no-Hα and SF-[O III]undet galaxies. As it is possible to note, SF-OIIIundet galaxies are even more extreme than QGs-B, given that the 57.6 $\pm$0.6% of them in the high-D tertile, and reside at each mass in environments which are intermediate between SF and no-Hα galaxies.

We also analyse the Richness (R) and the 'Brightness Rank' (hereafter BR) to evaluate whether the candidates are either the dominant/brightest galaxies or satellites within their group/cluster. BR ranges from the values of the group/cluster richness R to 1. In particular, BR=richness and BR=1 indicate that the considered galaxy is

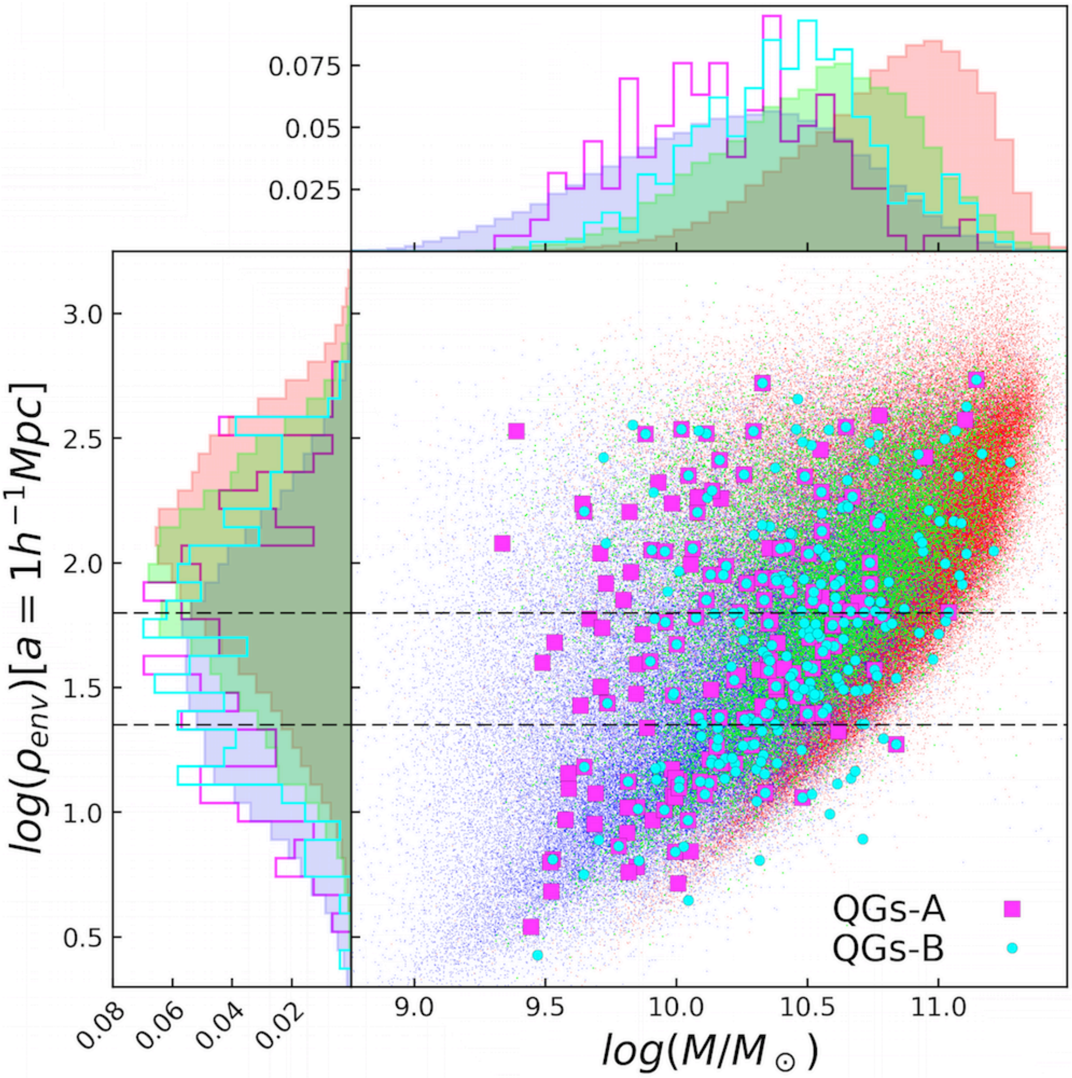

FIGURE 3.18: Normalised environmental density of galaxies $\rho_{\rm env}$ (smoothing scales of 1 h^{-1} Mpc) vs. stellar mass. The two dashed lines (at $\rho_{\rm env} = 22.45$ and $\rho_{\rm env} = 62.87$, respectively) divide the SF-Alldet $\rho_{\rm env}$ distribution into three tertiles.

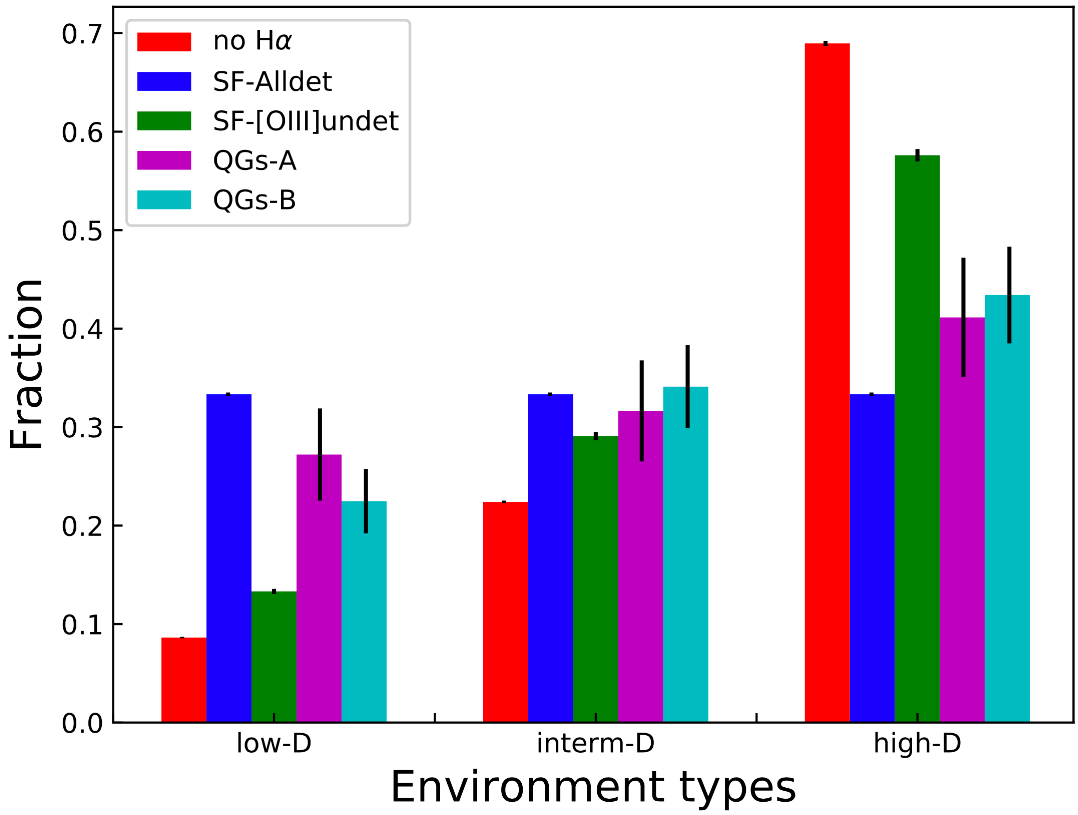

FIGURE 3.19: Distribution of no-Hα (red), SF-Alldet (blue), SF-[O III]undet (green), QGs-A (magenta) and QGs-B (cyan) in 3 environment types (i.e. low-D, interm-D, high-D).

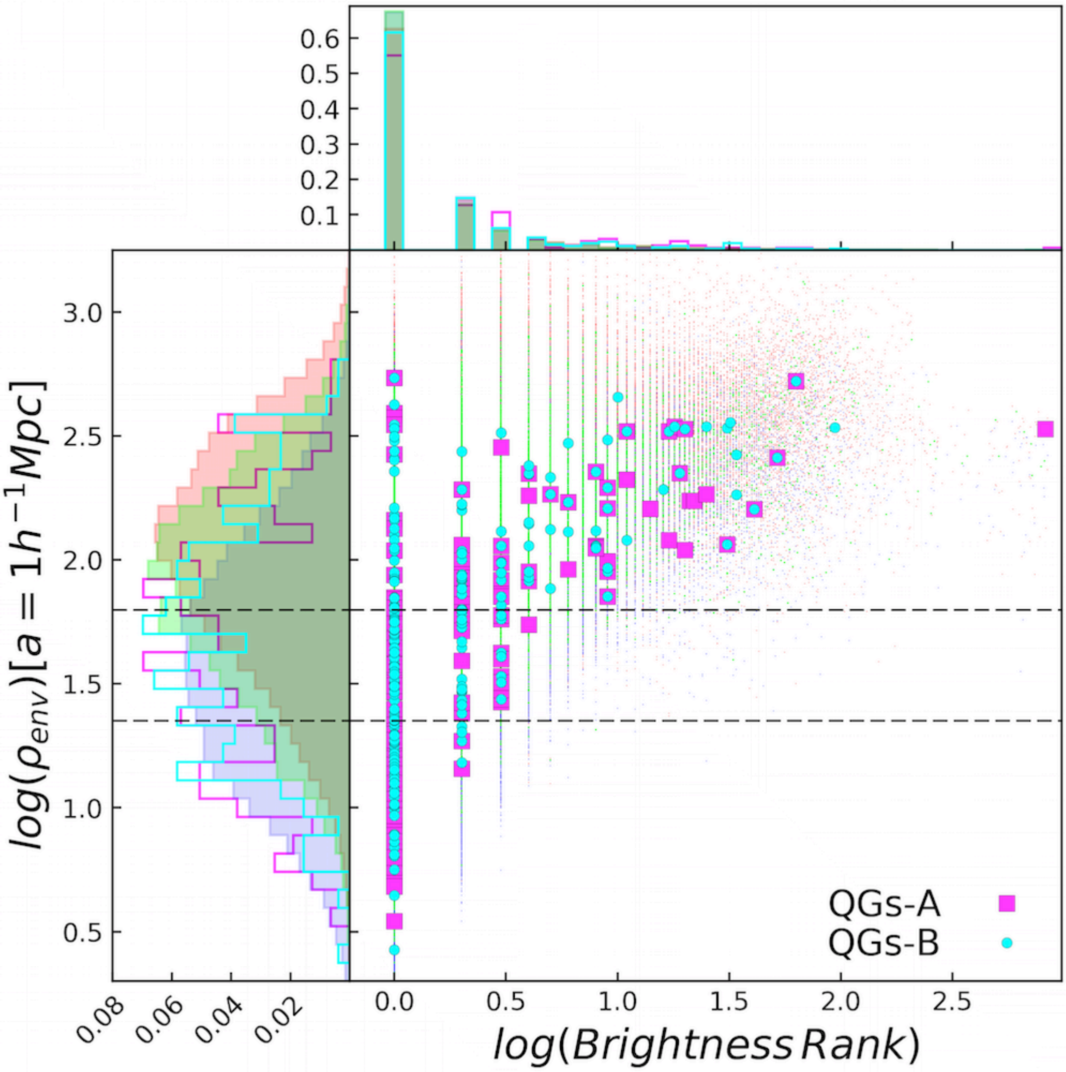

FIGURE 3.20: Normalised environmental density of galaxies ρ_{env} (smoothing scales of 1 h^{-1} Mpc) vs. the brightness rank. The two dashed lines (at $\rho_{\text{env}} = 22.45$ and $\rho_{\text{env}} = 62.87$, respectively) divide the SF-Alldet ρ_{env} distribution into three tertiles.

the faintest or the brightest (and thus the most massive) in its group/cluster, respectively. We define as 'central' a galaxy whose brightness rank is equal to 1.

Figure 3.20 shows ρ_{env} as a function of BR of the galaxies in their own environment. We find (see Figure 3.20) that the bulk of QGs in high-D enviroments are satellites (76.9% and 63.4%, respectively for QGs-A and -B), with percentages higher than those of the parent SF-Alldet population (57.3%) and of the SF-OIIIundet population (46.1%). Finally, almost all ($> 90\%$) galaxies belonging to groups/clusters including more than 30 members (R > 30) are in high-D environment and all the QGs in these extreme dense environments (i.e. $5.70 \pm 1.95\%$ of QGs-A and $4.65 \pm 1.37\%$ of QGs-B) are satellites.

Therefore, we conclude that our QGs are preferentially satellite galaxies within groups of medium and high density, showing an excess in high density environments compared to SF galaxies.

3.4 Discussion

3.4.1 Quenching timescale

In this section, we use the fraction of our selected QGs to estimate the timescale of the star-formation quenching, as suggested by C17. We define t_Q as the time elapsed from when the candidate was a typical star forming galaxy to the moment in which it is observed. For QGs-A, this happens when our tracer of the ionisation parameter (i.e. [O III]/Hα) becomes 3σ lower (i.e. about 0.4 dex) than the median of the [O III]/Hα distribution of SF galaxies. For QGs-B this occurs instead when [O III]/[N II] becomes 3σ lower than the [O III]/[N II] expected from its estimated metallicities.

Firstly, we derive the fraction of the QGs-A and QGs-B as the number of QGs over the number (i.e. 174000) of star-forming galaxies (SF-Alldet plus SF-[O III]undet). We obtain a fraction of 0.11% and 0.18%, for the QGs-A and QG-B, respectively. To obtain the observed quenching timescale of our QGs, following C17, we multiply this fraction (F_{QGs}) by the typical lifetime of a star-forming galaxy, that could be represented by the doubling mass time t_{doubling} (i.e. the time needed to a galaxy for doubling its stellar mass (~ 1/sSFR; e.g.) Guzmán et al., 1997; Madau and Dickinson, 2014):

$$t_Q = F_{QGs} \times t_{\mathrm{doubling}} = F_{QGs} \times \frac{1}{\mathrm{sSFR}} \tag{3.6}$$

Following the empirical relations by Karim et al., 2011, we derive the quantity 1/sSFR, which amounts to $\sim$ 8.8 and $\sim$ 10 Gyr for QGs-A and -B, respectively (assuming a median mass $\log(M/M_\odot) \simeq 10.1$ and 10.4 for -A and -B, respectively). Then we obtain $t_Q \sim 9.7 - 18$ Myr. This t_Q is a lower limit because of the several conservative assumptions taken into account for the selection of the candidates and because the flux limit of the survey allows to select only the most extreme candidates.

We derive also an upper limit to t_Q by assuming that about 50% of SF-[O III]undet population (i.e. ~ 13000 galaxies) is in a low ionisation state. This is supported by the fact that the [O III]/Hα ratio in their median stacked spectrum (see Figure 3.5) is 1σ below the median value of SF galaxies (therefore at least 50% of SF-[O III]undet are above 1σ value of SF galaxies, i.e. are consistent to be star-forming galaxies). In this case, the observed fraction of SF-[O III]undet is $\sim 7.5\%$ and, with a median $\log(M/M_\odot) \sim 10.6$ (i.e. 1/sSFR ~ 10.1 Gyr, following Karim et al., 2011), the t_Q is ~ 0.76 Gyr, compatible with galaxies which are experiencing a smoother and slower quenching.

Finally, we perform a survival analysis (ASURV, i.e. Kaplan-Meier estimator) of the distribution of [O III]/Hα in slices of [N II]/[O II]. We find that 938 (i.e. a fraction of 0.58%) among [O III]undet galaxies are re-distributed below 3σ (i.e. the thresholds for QGs-A), representing therefore the global fraction of QGs-A and leading to a quenching timescale of $\hat{t}_Q \sim 50$ Myr. This time $\hat{t}_Q$ should represents a good statistical measurement of the true quenching timescale for the adopted threshold. With the same ASURV analysis we confirm the consistency of the assumption that about 50% of [O III]undet galaxies are re-distributed below 1σ, accordingly to the value obtained from the median stacked spectra.

We, therefore, convert these values of t_Qs in an *e*-folding time τ_Q for the star formation quenching history. Adopting the C17 models, we derive the relation between the time needed by the [O III/Hα] ratio to decrease by 0.42 dex and τ_Q. We find that our lower limit timescales are compatible with an exponential $\tau_Q \simeq 18 - 34$ Myr for -A and -B respectively. Instead, from a linear extrapolation at $t_Q \sim 0.76$ Gyr we obtain a $\tau_Q \sim 1.5$ Gyr for the upper limit timescale. Finally, from $\hat{t}_Q$ we obtain an estimate of $\hat{\tau}_Q \sim 90$ Myr.

In summary, from the fraction of our QGs candidates, we derive a broad range of quenching timescales of 10 Myr $< t_Q < 0.76$ Gyr, and a statistically estimate of $\hat{t}_Q \sim 50$ Myr for QGs-A. These values correspond to a range for the *e*-folding time scale of the star formation quenching history of 18 Myr $< \tau_Q < 1.5$ Gyr and an estimate of $\hat{\tau}_Q \sim 90$ Myr.

3.4.2 Quenching mechanisms

Our sample of QG candidates is fundamental to get insights on the physical mechanisms driving the quenching of their SF. From our sample, we find a relatively rapid timescale for quenching (from few Myr to at most 1.5 Gyr) acting in galaxies with $\log(M/M_\odot) > 9.5$, being preferentially satellites in intermediate to high-density environments, and having their morphology almost unaffected. A smaller fraction ($\sim 25\%$) of our QGs is, however, also in low-density environments, and likely isolated. Only a small fraction ($12 - 17\%$) of them have already a compact morphology consistent with a morphological transformation. Therefore, different mechanisms should have driven their quenching, in particular in isolated and in high-D environments, and in different evolutionary epochs.

In general, the SFR in the inner star-forming regions of main-sequence galaxies is thought to be fueled through a continuous replenishment of low-metallicity and relatively low-angular momentum gas from the surrounding hot corona (Pezzulli and Fraternali, 2016), regulated via stellar feedback (e.g. galactic fountain accretion Shapiro and Field, 1976; Fraternali and Binney, 2006) until a quenching mechanism shall act to break the process. Recently, Armillotta, Fraternali, and Marinacci, 2016 found that the efficiency of fountain-driven condensation is strictly dependent on the coronae temperature. In coronae with temperatures higher than 4×10^6 K the process is highly inefficient. Hence, isolated QG candidates which are more massive than the Milky Way could have lost the ability to cool coronae gas and, after the consumption of their gas reservoir, they could start to quench the star-formation. Instead, in isolated QGs less massive than the Milky Way, strong stellar feedback (i.e. SN and strong stellar wind) may have inhibited the accretion of cold gas from the corona (Veilleux, Cecil, and Bland-Hawthorn, 2005; Sokołowska et al., 2016) .

In denser environments there are several quenching mechanisms which can affect our satellite QGs. However, the most likely process should leave the morphology almost unaffected. In dense environment, in which the velocity of galaxies may be sufficiently high, the ram pressure could remove cold gas from the reservoir of the satellite galaxies (e.g. Gunn and Gott, 1972; Quilis, Moore, and Bower, 2000; Poggianti et al., 2004). This 'ram pressure stripping' results in a quenching of the star-formation, with a relatively short timescale (~ 200 Myr - ≥ 1 Gyr, e.g. Steinhauser, Schindler, and Springel, 2016). However, there is general consensus that 'strangulation' (or 'starvation') is the dominant quenching mechanism in satellite galaxies (e.g. Treu et al., 2003; van den Bosch et al., 2008; Peng, Maiolino, and Cochrane, 2015). When the corona of a galaxy interacts hydro-dynamically with the hot and dense intra-cluster medium of a larger halo, its hot and diffuse gas could be stripped (e.g. Larson, Tinsley, and Caldwell, 1980; Balogh, Navarro, and Morris, 2000). This effect leads to a suppression of the accretion onto the disk, thus resulting in a gradual decline of the SFR until the exhaustion of the gas reservoir of the galaxy. Peng, Maiolino, and Cochrane, 2015 claimed that the primary quenching mechanism for galaxies is the strangulation. They derive the quenching timescale due to this mechanism as the gas depletion time needed to explain the differences in metallicity between the star-forming population and the quiescent one, finding that models of 4 Gyr are the most suitable for this task (see also Maier et al., 2016). We compare this timescale with the estimate of the time (t_P) needed by a galaxy to decrease its sSFR from typical main sequence values (i.e. ~ -10 in log-scale for $\log(M/M_\odot) \sim 10.4$, e.g. Karim et al., 2011) to the typical sSFR of the passive population. (i.e. ~ -11 in log scale, e.g. Pozzetti et al., 2010; Ilbert et al., 2013). For the *e*-folding time τ_Q we derive a lower limit timescale t_P of $\sim 40 - 80$ Myr and an upper limit of ~ 3.5 Gyr.

Recently, it is gaining consensus a scenario (i.e. 'Delayed then rapid' quenching Wetzel et al., 2013; Fossati et al., 2017) in which the quenching of satellites in dense environments has been proposed to be divided into two phases: a relatively long period ("the delay time") in which the star-formation does not differ strongly from the main-sequence values (2-4 Gyr after first infall), followed by a phase in which the SFR drops rapidly ("the fading time") with an exponential fading with an e-*folding* time of $0.2 - 0.8$ Gyr (lower for more massive galaxies) that is independent on host halo mass.

About 70% and 80% of QGs-A and -B reside in high- and intermediate- density environments and the vast majority of them are satellites. Hence, the derived τ_Q for our QGs allow to perform a direct comparison with the quenching timescales in Wetzel et al., 2013. Although the range derived for τ_Q is quite broad, we can at least confirm that our timescales are compatible with theirs.

We can also make a further comparison with the Wetzel et al., 2013 predictions by using the median L(Hα) of the stacked spectra (see subsection 3.3.1) as a proxy of the median SFR, and comparing them to the value of the SF galaxy sample (0.8 for QGs-A and 0.9 for QGs-B). Assuming that, after the start of the quenching, the SFR of a star-forming galaxy decreases to the value of $\mathrm{SFR_{QGs}(t_Q)}$, we can estimate the exponential *e*-folding time, deriving $\tau_Q \sim 50 - 190$ Myr for the median QGs-A and -B spectra, that are closer to those found by Wetzel et al., 2013.

It is also interesting to limit the discussion to the central quenching galaxies. There is consensus that the quenching is slower for central galaxies (e.g. Hahn, Tinker, and Wetzel, 2017). Focusing on central galaxies in high density environment we found a lower limit t_Q of $8.8 - 20$ Myr respectively for central QGs-A and -B and an upper limit $t_Q \sim 1.4$ Gyr. These timescales are compatible with lower limit exponential e-folding τ_Q of $16 - 38$ Myr and an upper limit $\tau_Q \sim 2.8$ Gyr. Following an approach similar to that of Wetzel et al., 2013, Hahn, Tinker, and Wetzel, 2017 found that central galaxies quench the star formation with an *e*-folding time between 0.5 and 1.5 Gyr (lower for massive galaxies) and also in this case we are compatible with their result.

There is general consensus that environmental mechanisms take longer time ($2 - 3$ Gyr, (e.g. Balogh, Navarro, and Morris, 2000; Wang et al., 2007) to start to affect the SFR of satellites. Hence, this should be the most probably scenario also for our satellites before the starting of the quenching. Moreover, we found that our quenching timescales are compatible with an exponential decrement like that of Wetzel et al., 2013, although without an overwhelming. We can conclude that the properties of our QG candidates can be preferentially explained by a 'Delayed then rapid' quenching of satellites galaxies, due to the final phase of an environmental quenching mechanism(s).

Strangulation, ram-pressure stripping and harassment (e.g. Farouki and Shapiro, 1981) are the most important mechanisms that act on satellites leading to the quenching of their star formation. Since we can safely exclude from a visual inspection that any of our candidates are experimenting harassment, the natural conclusion for our QGs that reside in high- and intermediate- density environment is that strangulation and ram-pressure stripping should play a primary role in the halt of the star-formation. However, different mechanisms can also work together to quench the star-formation in galaxies. Moreover, even if our methods are not sensitive to AGN feedback (e.g. De Lucia et al., 2006; Fabian, 2012; Cimatti et al., 2013; Cicone et al., 2014) as quenching mechanism, due to our a priori exclusion of AGNs, we cannot exclude that an early AGN phase could be responsable and could have quenched our QGs. In this case, the AGN phase should have finished before the quenching of the star formation. On the other end, it is important to remind that other authors predict the formation of ETGs without invoking the AGN feedback (e.g. Naab, Khochfar, and Burkert, 2006; Johansson, Naab, and Ostriker, 2012).

Finally, we stress that our QGs still have a ionised-gas phase, as witnessed by their Hα emission, even if weaker than in the parent sample of star forming galaxies, suggesting that gas depletion is indeed on going. In the future, after the disappearance of late-B stars and the consequently disappearance of hard-UV photons, this gas could be cooled down being available for a new phase of star formation. However, if we are witnessing a minimum in the SFH of our quenching candidates, we should observe QGs at all masses, also lower than $10^{9.5}M_{\odot}$ (i.e. the less massive QG in our sample). To confirm the final passive fate of our QGs, connected to the presence or absence of residual gas and, at the same times explaining the observed Hα emission, more observations are needed and in particular we need to study the cold gas phase distribution from ALMA observations (see, for instance, Decarli et al., 2016; Lin et al., 2017).

3.5 Summary

In this work, we analyse a sample of $\sim$ 174000 SDSS-DR8 star-forming galaxies at $0.04 \leq z < 0.21$ to provide for the first time a sample of quenching galaxy (QGs) candidates selected just after the interruption of their star formation.

We follow the approach introduced by C17 to select QG candidates on the basis of emission line flux ratios of higher-to-lower ionisation lines (i.e. [O III]/Hα) which are sensitive to the ionisation level. The main issue of this approach is that the [O III]/Hα ratio is affected by a ionisation-metallicity degeneracy.

In order to mitigate this degeneracy we set up two different methods:

- *Method A*: following C17, we exploit the plane [O III]/Hα vs. [N II]/[O II] to select galaxies with the lowest [O III]/Hα values for a given metallicity (i.e. using [N II]/[O II] as metallicity indicator). By analysing the statistical distribution of our samples, we identify an excess of galaxies consistent with being a population separated from the star-forming sample, having intrinsically lower [O III]/Hα values, and hence lower ionisation levels. This method is demonstrated to be stable against the choice of the dust attenuation law. We also tested an alternative diagram involving [O III]/Hβ vs. [N II]/[S II], which has the advantage of being less affected by dust extinction, although it involves weaker lines.

- *Method B*: an alternative method to mitigate the metallicity degeneracy is to select galaxies for which the [O III] flux is weaker than the minimum value expected from their metallicity, exploiting the two relations [N II]/[O II] vs. 12+log(O/H) and 12+log(O/H) vs. [O III]/[N II].

Applying these methods we select two samples of QG candidates and analyze their main properties. Our results can be summarized as follows:

1. We select 192 candidates (QGs-A) and 308 candidates (QGs-B), using Method A and B, respectively. There is an intersection of 120 QGs between them, and the QGs out of the intersection are close to the threshold criterion of both methods. QGs-B show, on average, higher values of [N II]/Hα and of [N II]/[O II]

compared to QGs-A, suggesting they have a statistically higher metallicity than QGs-A.

2. The median stacked spectra, corrected for dust extinction, of QGs-A and QGs-B have a blue stellar continuum, suggesting a young mean stellar population. The analysis confirms a weak [O III] emission and that also other high ionisation emission lines (such as [Ne III]) are weak in both QGs stacked spectra, and the [O III]/Hα ratios are consistent with a low ionisation level. On the contrary, [O II], Hα and Hβ (i.e. low ionisation lines) are still strong and with an Hα flux slightly weaker ($\sim 80\%$) than the one of star-forming galaxies.

3. We find that QGs have D_n4000 and EW(Hα) values intermediate between SF and already quenched galaxies, confirming that they have just stopped their star formation and have a young/intermediate mean stellar population.

4. In the colour-mass diagram, the bulk of the QGs-A and QGs-B resides in the blue cloud region, and only few of them ($\sim$ 3%) lie in the green valley region. The QGs have masses log(M/M$_\odot$) > 9.5, comparable with those of the SF population, being the QGs-B, on average, more massive. This suggests that, as expected in a downsizing scenario, star formation quenching has not started yet for low-mass galaxies, consistently with a lack of low-mass red galaxies. Their Hα emission, is compatible with a just quenched SFR of the order of 0.6 - 10 M$_\odot$ yr^{-1}, similar to that of the SF main sequence population, suggesting the presence of residual ionised gas in our QGs. The emission from the median stacked spectra is, however, weaker than in the SF population, suggesting that the depletion of the gas has started.

5. The morphology and concentration index (C=R90/R50) of QGs are similar to those of the star-forming population, suggesting that no morphological transformation has occurred yet, in the early phase after the quenching of the star formation. However, some of them have a concentration index higher than the threshold that divides the early-type from the other galaxy types (i.e. C > 2.6) and they could have experienced morphological transformation during the interruption of the star formation.

6. Compared to the parent SF population, we find an excess of QGs in high density environments ($\sim$ 42%), in particular for QGs-B. QGs in high density environments are preferentially satellites (from $\sim$ 60 to 80%). Approximatively 5% of QGs are in groups/clusters which have more than 30 members, but no one of them is the brightest galaxy in its environments.

7. From the fraction of QG candidates ($\sim 0.11 - 0.18\%$ of the SF population) we estimate the quenching timescales for these populations to be between 10 and 18 Myr. These values are compatible with the sharp quenching models by C17. If we assume that at most 50% the entire SF-[O III]undet population ($\sim$ 7.5%) is in a low ionisation state, as witnessed by the low but not extreme [O III]/Hα ratio in their stacked spectrum, we obtain an upper limit to the quenching timescale of $\simeq$ 0.76 Gyr. In this case, the quenching timescale is compatible with galaxies which are experiencing a more smoothed and slower quenching (C17). We convert this range into a e-folding timescale for the SFR quenching history, finding 18 Myr $< \tau_Q < 1.5$ Gyr.

8. From a survival analysis we find that 938 ($\sim 0.58\%$) among SF-[O III]undet galaxies are consistent to be QGs candidates. We, therefore, derive a statistical measurement of the quenching timescale $\hat{t}_Q$ of ~ 50 Myr and $\hat{\tau}_Q \sim 90$ Myr.

This analysis, based on a new spectroscopic approach, leads to the identification of a population of galaxy candidates selected right after the quenching. Most of our QGs would not have been selected as an intermediate population using colour criteria, or in the SFR-mass plane.

We conclude that these galaxies, that are quenching their star formation on a short timescale (from few Myr to less than 1 Gyr), preferentially reside in intermediate-to high-density environments, are satellites and have not morphologically transformed into spheroidal red passive galaxies yet. All these properties could be explained by a 'Delayed then rapid' (see Wetzel et al., 2013) quenching scenario in satellites galaxies, due to the final phase of strangulation or ram pressure stripping.

However, to confirm the proposed scenario and the presence or absence of a reservoir of gas more observations are needed. For example, cold gas phase distribution could be derived from ALMA observations (e.g. Decarli et al., 2016; Lin et al., 2017), while the spatial distribution of quenching can be analyzed using integral field unit (IFU) spectroscopic data to get insights about the inside-out scenario (e.g. the MANGA public survey, Bundy et al., 2015; the SAMI galaxy survey, Green et al., 2018; the MUSE-VLT data Bacon et al., 2010 and, in the future, WEAVE-IFU data, Dalton et al., 2014).

APPENDIX

3.A Fibre aperture effects

As mentioned in subsection 3.1.1, we select galaxies at z > 0.04, following the prescription of Kewley, Jansen, and Geller, 2005, in order to avoid strong fibre aperture effects on SFRs, extinction and metallicity. Indeed, we stress that our analysis is limited to the area of galaxies covered by the fibre. With the adopted cosmology, at z $= 0.04$ and z $= 0.21$, the SDSS fibre radius (1.5 arcsec) corresponds to ~ 1.2 kpc and ~ 5.2 kpc, respectively. In Figure 3.A.1 we show the size-redshift relation for our sample. The size is represented by the R50 radius. Roughly all the candidates have R50 larger than the fibre radius. Therefore, we can analyse the quenching only in the inner part of our QG candidates. In order to test whether we could extend our results to the whole galaxy, we explore the impact of the aperture on the ionisation indicator [O III]/Hα. Figure 3.A.2 shows the [O III]/Hα as a function of the fraction of flux inside the fibre (u-band) with respect to the total u-band flux, (u-band Petrosian flux, Strauss et al., 2002). There is no evident trend, with QGs candidates distributed over the whole range, even at the lowest ionisation levels (log([O III]/Hα) < -1.3). This test suggests that, in this redshift range, the fibre aperture does not affect significantly our analysis, even if our results are clearly relative only to the region included in the fibre.

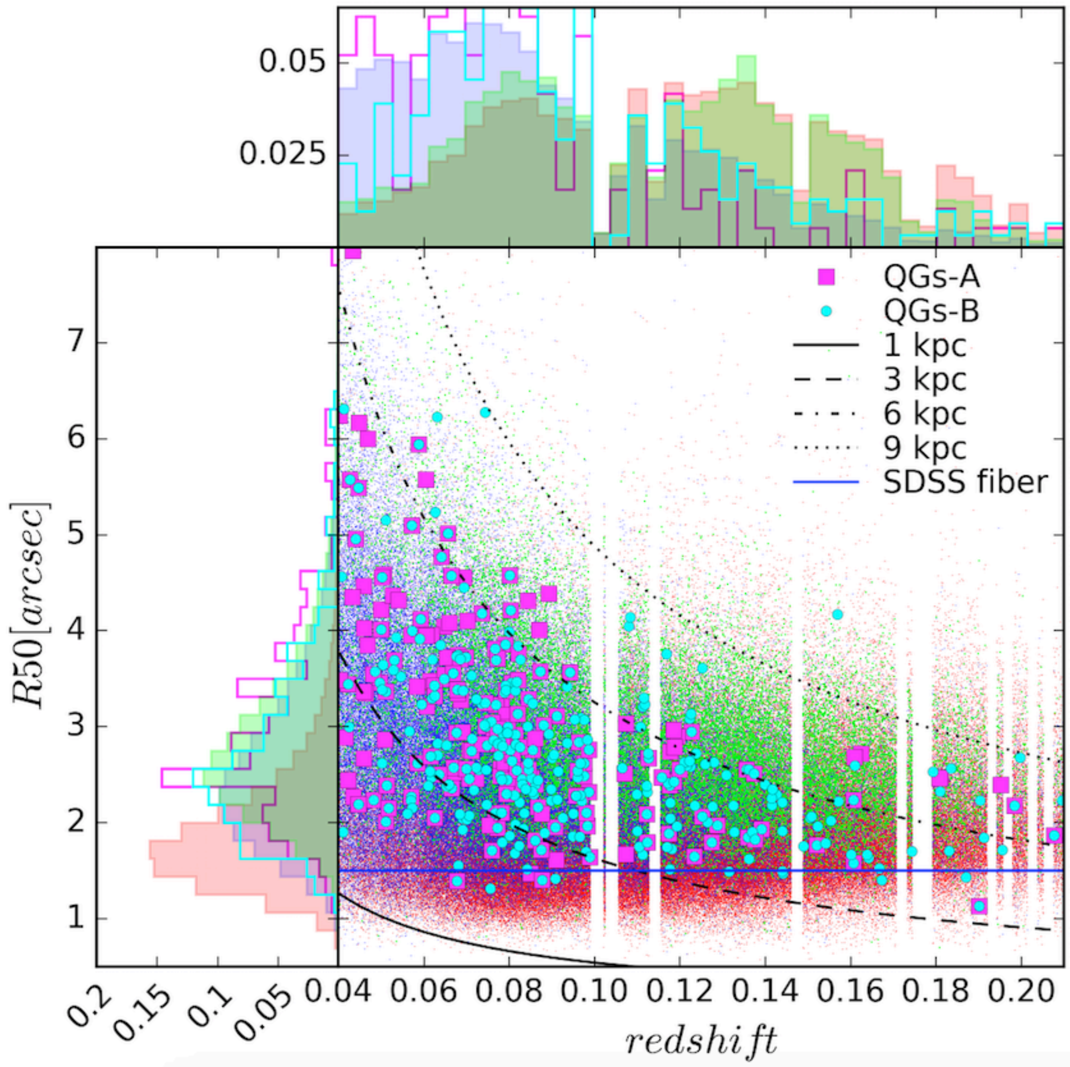

FIGURE 3.A.1: The size-redshift relation for our sample and quenching candidates. The horizontal blue line represents the radius of the SDSS fibre aperture, while the black curves represent the kpc/arcsec relations obtained from the adopted cosmology.

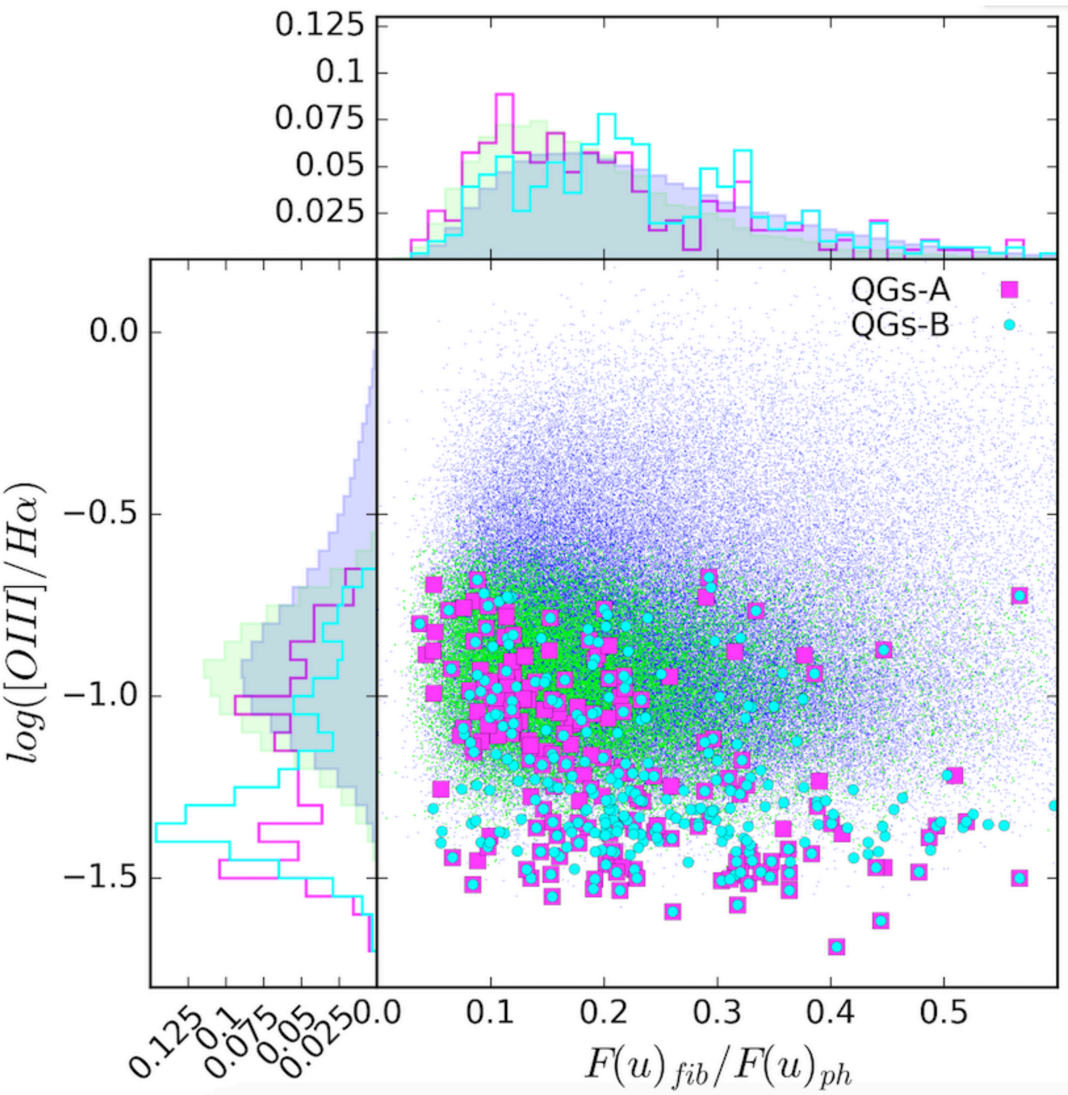

FIGURE 3.A.2: [O III]/Hα as a function of the ratio between the u-band flux inside the fibre and total. The colour code is the same of Figure 3.7.

4. Spatially resolved signature of the quenching

Since the advent of integral field unit (IFU) spectroscopy era, galaxies can be studied with enough spatial resolution to allow analysis of physical properties even at galactocentric distances larger than 2 effective radii. In this Chapter, we extend the method devised in Q18 to select quenching galaxies in the SDSS main sample to IFU data from the SDSS-IV MaNGA survey (Bundy et al., 2015; Blanton et al., 2017). Our aim is to search for regions where quenching had started and, therefore, to derive spatial information on the quenching process within galaxies.

We structure this Chaprer as follows: in section 4.1 we briefly recall the method introduced in Quai et al. (2018) and we describe our MaNGA sample. We use section 4.2 to focus on two cases illustrating the detailed procedure and analysis done and then, in section 4.3 we present the general properties of the entire sample. Finally, in section 4.4 we discuss our results and we provide our concluding remarks.

4.1 The method and the sample

As shown by Citro et al. (2017, , see also Chapter 2), the [O III]/Hα emission lines ratio rapidly reacts to the star formation quenching. However, this ratio is affected by a significant degeneracy between ionisation and metallicity, because the [O III] λ5007 emission line can be depressed both by a reduction of ionising photons and by high metallicity. From the analysis of a sample of ~174.000 star-forming galaxies at $0.04 < z < 0.21$ extracted from the SDSS-DR8 catalogue (Quai et al., 2018), we devised a method aimed both at avoiding the degeneracy and selecting reliable quenching galaxies candidates. It was found, indeed, that pairs of emission line ratios nearly orthogonally dependent on ionisation (i.e. [O III]/Hα) and metallicity (i.e. [N II]/[O II]) can strongly mitigate the degeneracy (see Q18 for further details). Hence, in the [O III]/Hα vs [N II]/[O II] plane they identified about 300 quenching galaxy candidates satisfying the following criteria:

1. [O III] weak enough to be undetected inside the SDSS fibre (i.e. S/N([O III]) < 2),

2. [O III]/Hα ratios, at fixed [N II]/[O II] (i.e. fixed gas-phase metallicity), lower than the $3 \times 1\sigma$ value of the SDSS star-forming distribution (see Figure 4.1). They represent a population of galaxies well segregated from the global sample of galaxies with ongoing star-formation.

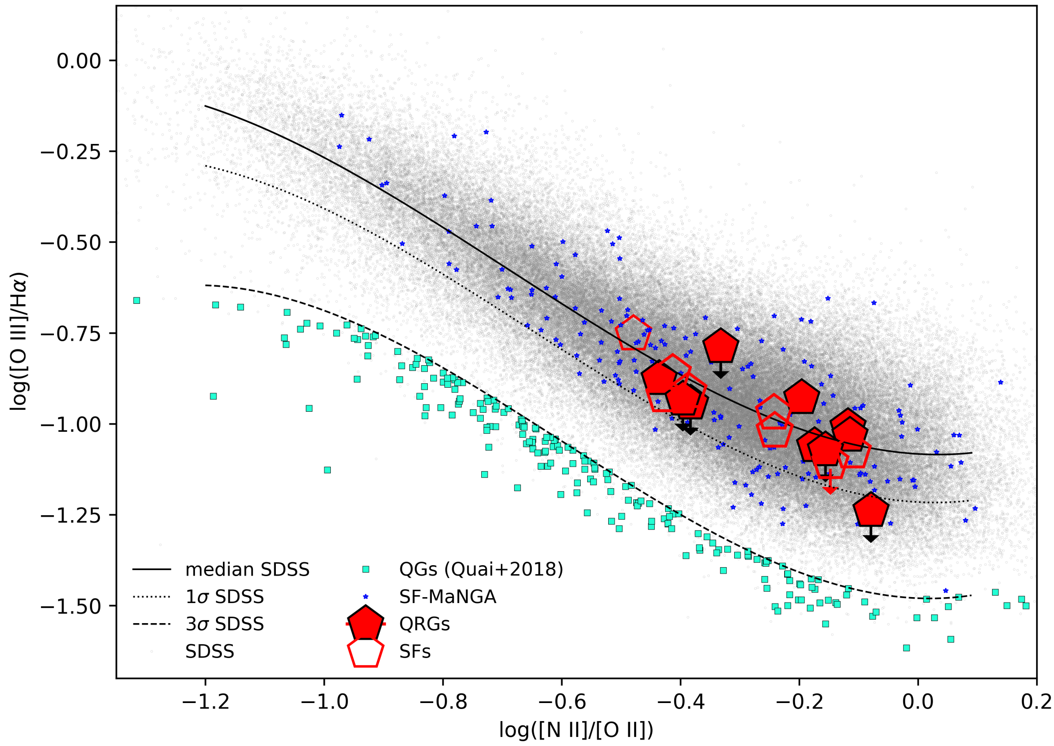

FIGURE 4.1: The diagnostic [O III]/Hα vs [N II]/[O II] diagram. The black curves represent median, 1σ and $3 \times 1\sigma$ limits of the SDSS star-forming galaxies sample (see Quai et al., 2018), which are represented by grey dots. The cyan squared dots below the $3 \times 1\sigma$ limits represent the SDSS quenching candidates selected in Quai et al. (2018). The blue dots represent the SDSS galaxies that have a match in MaNGA-DR14. The red pentagons represent the SDSS position of the MaNGA galaxies analysed in this Chapter: full symbols for the galaxies with quenching regions (QRG) and empty symbols for the star forming (SF) galaxies, as defined in subsection 4.1.5. The arrows indicate the upper limits in [O III]/Hα.

In order to derive spatial information on the quenching process within the galaxies, we extend these criteria to MaNGA IFU observations by exploiting the [O III]/Hα vs [N II]/[O II] diagnostic of spatially resolved galaxies. To this aim, we cross-match the $\sim$ 174.000 galaxies selected in the main SDSS survey (Q18) with the MaNGA data-release 14 (Abolfathi et al., 2018), and we find 208 matches. However, none of $\sim$ 300 SDSS quenching primary candidates selected in Quai et al. (2018) has been observed with MaNGA. Nevertheless, we find matches with MaNGA data for 10 galaxies with [O III] undetected (S/N([O III]) < 2) within the SDSS fibre, which should represent promising candidates of galaxies which could be in the very first phase of the quenching. In fact, in Q18 we argued that about 50% of these objects (that they called [O III]undet galaxies) can be quenching galaxies, while the other ones should actually be normal star-forming galaxies with fainter emission lines. We discard MaNGA 1-245686 because it appears almost edge-on (i.e. a ratio b/a $= 0.2$) and we do not further analyse also MaNGA 1-38802 because it is at a redshift considerably higher (i.e. z $= 0.11$) than the other [O III]undet galaxies in the sample. The remaining 8 [O III]undet galaxies are located at redshift between 0.04 and 0.06 and have masses between $10^{9.6}$ and $10^{10.8}$ $M_{\odot}$. We decide to include as a control sample 12 SDSS star-forming galaxies with similar mass and [N II]/[O II] range, which emission line ratios lie, in the [O III]/Hα vs [N II]/[O II] diagram, along the median SDSS sequence of star-forming galaxies. The diagnostic diagram for the original Q18 sample and for the MaNGA galaxies considered in this analysis is presented in Figure 4.1. Our aim is to search for galaxies with regions that are quenching, using the same diagnostic used in SDSS (see Quai et al., 2018), but applied to each resolved galaxy regions.

4.1.1 From MaNGA to pure-emission cube

Starting from the MaNGA datacubes processed by the data reduction pipeline (DRP, Law et al., 2016), the final emission lines maps are obtained applying the following spectral-fitting procedure, similar to that proposed by Belfiore et al., 2016:

1. *Increasing the signal-to-noise of the continuum.* To create a pure-emission datacube, it is necessary to accurately subtract the stellar continuum from the original datacube. At first, the noise is corrected for the effect of the spatially correlated noise between adjacent spaxels, as discussed in García-Benito et al., 2015. Then, in order to increase the signal-to-noise ratio (S/N) of the continuum and at the same time preserve the spatial resolution, spaxels which S/N lower than 10 in the restframe $4740 - 4840$ Å range are binned together with a Voronoi tessellation approach[1] (Cappellari and Copin, 2003). Spaxels with undetected continuum (i.e. S / N < 2) are not included in the binning, and they are not further considered in our analysis. The size of the bins is not forced to be larger than the typical MaNGA point spread function (PSF, i.e. ~ 2.5 arcsec at FWHM, see Table 4.1), therefore, it is possible that adjacent bins are statistically correlated.

2. *Fitting the continuum.* In the spatially binned spectra the emission-lines and the strong sky-lines (i.e. O Iλ5577, NaDλ5890,O Iλ6300,O Iλ6364) are masked within a window of 1400 km s^{-1}. Then, the spectral continuum has been fitted choosing among various simple stellar population models from MILES (Vazdekis et al., 2012) using penalised pixel fitting[2] (pPXF, Cappellari and Emsellem, 2004) without taking into account dust extinction and using a set of additive polynomials up to the 4th order to correct the continuum shape.

3. *The pure-emission datacube.* The best-fit continuum of each spatial bin is subtracted from the single original spaxels composing the bins, and the resulting data cube is composed by spaxels of pure-emission spectra.

[1] The Voronoi tessellation routine can be found at http://www-astro.physics.ox.ac.uk/~mxc/software.

[2] pPXF code can be downloaded from http://www-astro.physics.ox.ac.uk/~mxc/software.

4.1.2 Emission-lines maps

In this sub-section, we describe the routine that we apply to pure-emission datacube to obtain maps of individual emission-lines (i.e. Hα, Hβ, [O III] λ5007, [O II] λ3726-29, [N II] λ6584).

1. *Increasing the signal-to-noise of nebular lines.* Hα fluxes are measured in each spaxel from the pure-emission datacube. In order to reach an S/N(Hα)> 5 we perform a further Voronoi binning tessellation, not considering spaxels with S/N(Hα)< 1, which are not further considered in our analysis. This procedure allows studying nebular emission properties also in the outskirts of galaxies, at the cost of slightly worsening the spatial resolution. We find that no spaxels needs to be binned inside the effective radius of the analysed galaxies since their S/N(Hα) is always higher than 5. Therefore, the original central spatial resolution is preserved and dominated by the point spread function (PSF) of MaNGA datacubes, which has a typical value of $2.5''$ at FWHM (i.e. an area covered by almost 20 spaxels).

2. *Fluxes and errors.* In each spaxel, fluxes are measured by integrating the Gaussian best fit to the lines Hα, Hβ, [O III], [O II] (we consider [O II] = [O II] λ3726 + [O II] λ3729), [N II] λ6584 (hereafter [N II]), and [S II] $\lambda\lambda$6717-6731. Errors on the fluxes are obtained by the propagation of errors on a Gaussian amplitude and standard deviation.

   In our analysis, we need reliable measures of [N II] and [O II]; hence the spaxels with S/N < 2 in these lines are not considered either. Instead, since the fingerprint of the method is the weakness or lack of the [O III] emission, spaxels with S/N([O III]) < 2 are kept as upper-limit values with [O III] = $2 \times \sigma$[O III], where σ[O III] is the error on the [O III] flux.

4.1.3 The derived quantities from MaNGA data

The maps of Hα, Hβ, [O III], [O II] and [N II], which form the starting point of our classification criteria (see subsection 4.1.4), are corrected for dust attenuation based on the Hα/Hβ ratio. In order to perform a proper correction for dust extinction, spaxels with S/N(Hβ) < 3 and S/N(Hα) < 5 are not further considered in the analysis. For the other spaxels, the colour excess E(B-V) is derived adopting the Calzetti et al., 2000 attenuation law and assuming the Case B recombination and a Balmer decrement Hα/H$\beta = 2.86$ (typical of H II regions with electron temperature $T_e = 10^4$ K and electron density $n_e \sim 10^2 - 10^4\,\mathrm{cm}^{-3}$, Osterbrock, 1989; Dopita and Sutherland, 2003) . Negative values of E(B-V) between about -0.05 and < 0 (i.e. inverted Balmer decrement, with $\sim 2.7 \leq$ Hα/H$\beta < 2.86$) are found in almost all galaxies in our sample, with percentages between 2% and 14% of the spaxels (but the galaxy 1-352114 shows E(B-V)< 0 in $\sim 52\%$ of its spaxels). However, these values are still compatible with case B, though at electron temperature between 10^4 and 2×10^4 K (i.e. $2.74 \leq$ Hα/H$\beta < 2.86$, Hummer and Storey, 1987). In these spaxels we set E(B-V) $= 0$. Figure 4.2 shows the E(B-V) maps of MaNGA 1-43012 and 1-178443 which represent case studies that we will extensively present in section 4.2.

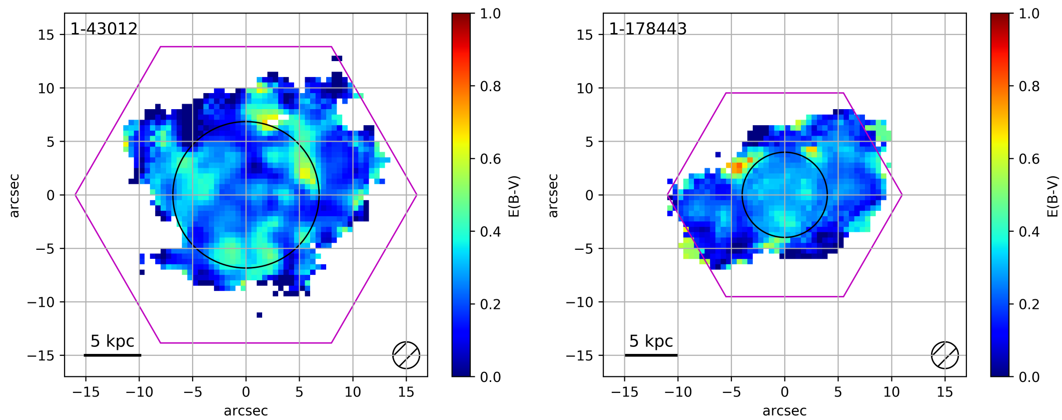

FIGURE 4.2: The E(B-V) maps of MaNGA 1-43012 (*left*) and MaNGA 1-178443 (*right*). Overlapped in magenta are the hexagonal shapes of the MaNGA IFU bundles, while the black circles represent the R50. The $2.5''$ circle in the bottom-right corner of the maps represent the typical PSF (FWHM) of MaNGA data.

The dust corrected fluxes are converted to luminosity surface density (erg s^{-1} kpc^{-2}). Then, the SFR surface density (ΣSFR) is derived using the dust corrected Hα luminosity surface density and adopting the Kennicutt (1998a) conversion factor for Kroupa, 2001 initial mass function (IMF):

$$\Sigma\mathrm{SFR} = \Sigma(\mathrm{L(H}\alpha)/10^{41.28})\ [\mathrm{M}_{\odot}\mathrm{yr}^{-1}\mathrm{kpc}^{-2}]. \tag{4.1}$$

In order to obtain estimates of the ionisation parameter log U and gas-phase metallicity Z from the observables, in the [O III]/Hα vs [N II]/[O II] plane, we compared the observed values with a grid of theoretical values obtained with photo-ionisation models by C17. To do this, we interpolate the original models with a denser grid in which the theoretical Z spans from 0.004 to 0.04 with steps of 0.001 and log U from -3.6 to -2.5 with steps of 0.01. When a spaxel lies in a region of the diagram that is not covered by the models we assign the values of the closest knot on the grid. This assumption has an impact in galactic regions with [N II]/[O II] higher than 0, for which the metallicity estimation of $Z = 0.04$ shall be regarded as a lower limit.

Redshifts and effective radii (R50, i.e. elliptical Petrosian 50% light radius in SDSS r-band) are obtained from the NASA Sloan Atlas v1_0_1 (Blanton et al., 2011). Stellar masses, total star-formation rates (SFR) are taken from the database of the Max Planck Institute for Astrophysics and the John Hopkins University (MPA-JHU measurements[3]) as in Quai et al. (2018). We use also the SDSS morphological probability distribution of the galaxies provided by Huertas-Company et al. (2011), which is built by associating a probability to each galaxy of belonging to one of four morphological classes (Scd, Sab, S0, E).

[3]see http://wwwmpa.mpa-garching.mpg.de/SDSS/.

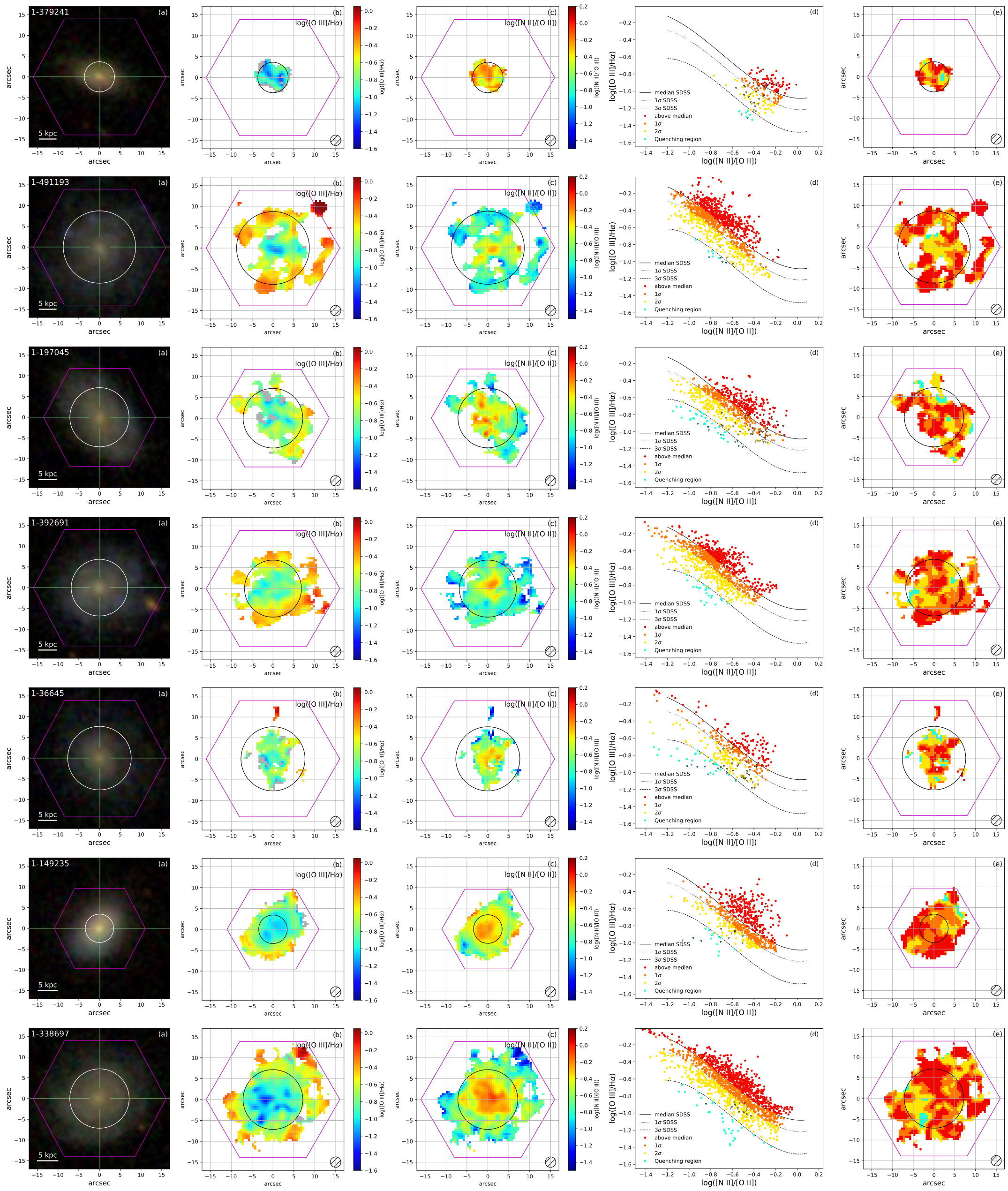

FIGURE 4.3: A summary of the 10 QRG galaxies in our sample. (a) The g-r-i images composite from SDSS. Each image covers a region of 17×17 arcsec^2 and in the bottom-left corner of each image is reported the scale of 5 kpc. (b) The dust-corrected [O III]/Hα maps. The grey areas show regions with S/N([O III]) < 2. (c) The dust-corrected [N II]/[O II] maps. (d) The [O III]/Hα vs [N II]/[O II] diagnostic diagram for the quenching. The spaxels are colour-coded according to their position on the plane: red dots for those lying above the median curve, orange dots for them between the median and 1σ , yellow dots for spaxels which lie between 1σ and $3 \times 1\sigma$ and, finally, cyan dots for spaxels below the $3 \times 1\sigma$ curve that, according with our classification criteria described in the text, represent likely quenching regions. The triangles represent spaxels with an upper limit in [O III]/Hα (i.e. spaxels with S/N([O III]) < 2). (e) The map of the galaxies colour-coded according to the position of spaxels as in (d). In (a), (b), (c) and (e) the overlapped-magenta hexagonal shapes the MaNGA IFU bundles, while the white circle represents the R50. Finally, the $2.5''$ circle in the bottom-right corner of the maps in (b), (c) and (e) represent the typical PSF (FWHM) of MaNGA data.

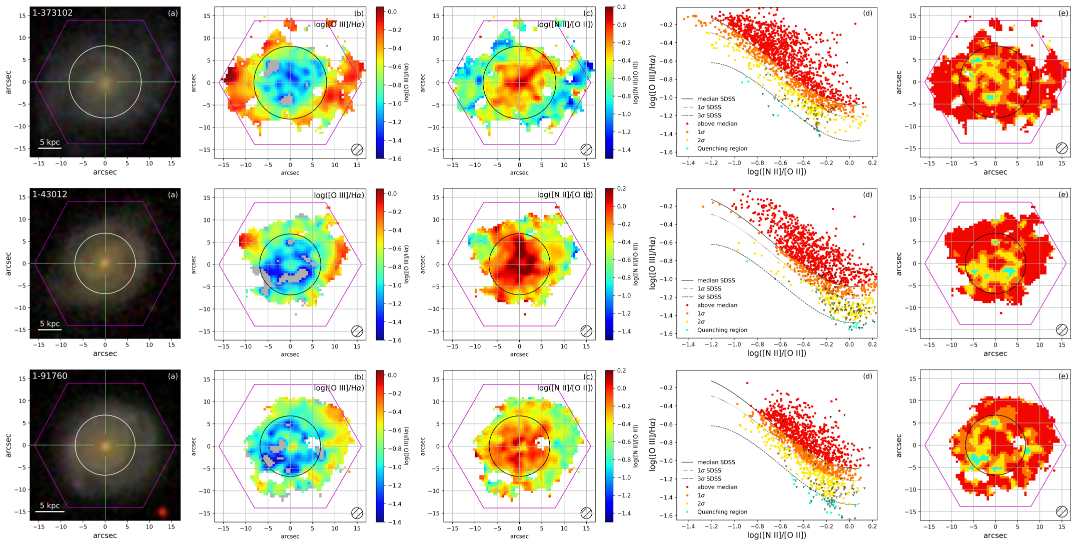

FIGURE 4.4: Continued.

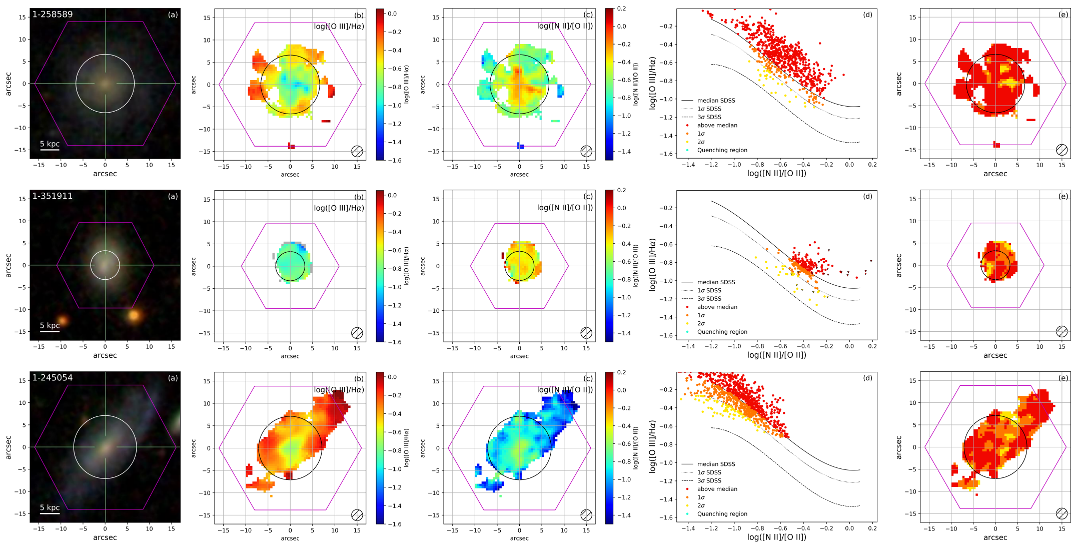

FIGURE 4.5: A summary of the 8 SF galaxies in our sample. (a) The g-r-i images composite from SDSS. Each image covers a region of 17×17 arcsec^2 and in the bottom-left corner of each image is reported the scale of 5 kpc. (b) The dust-corrected [O III]/Hα maps. The grey areas show regions with S/N([O III]) < 2. (c) The dust-corrected [N II]/[O II] maps. (d) The [O III]/Hα vs [N II]/[O II] diagnostic diagram for the quenching. The spaxels are colour-coded according to their position on the plane: red dots for those lying above the median curve, orange dots for them between the median and 1σ , yellow dots for spaxels which lie between 1σ and $3 \times 1\sigma$ and, finally, cyan dots for spaxels below the $3 \times 1\sigma$ curve. The triangles represent spaxels with an upper limit in [O III]/Hα (i.e. spaxels with S/N([O III]) < 2). (e) The map of the galaxies colour-coded according to the position of spaxels as in (d). In (a), (b), (c) and (e) the overlapped-magenta hexagonal shapes the MaNGA IFU bundles, while the white circle represents the R50. Finally, the 2.5″ circle in the bottom-right corner of the maps in (b), (c) and (e) represent the typical PSF (FWHM) of MaNGA data.

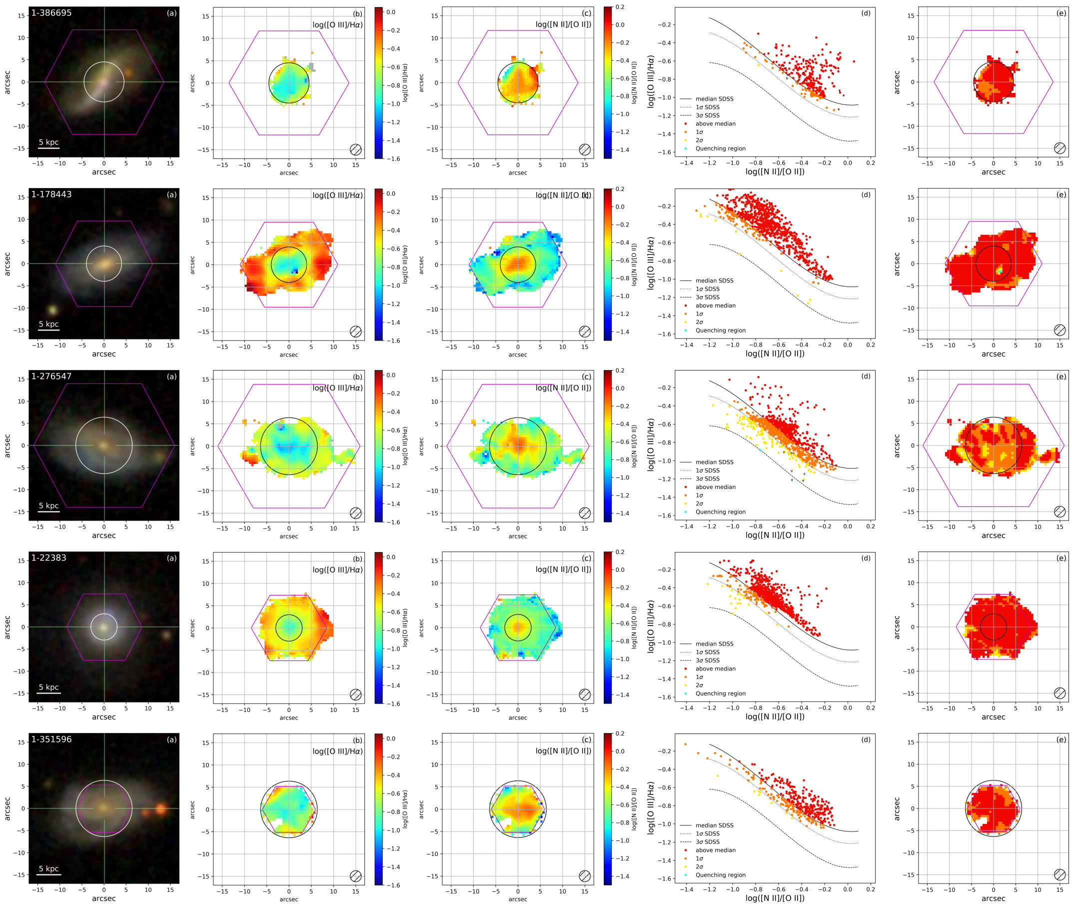

FIGURE 4.6: Continued.

4.1.4 The classification scheme

In this subsection, we present the classification scheme applied to the 20 MaNGA galaxies in our sample. We stress that none of the Quai et al. (2018) best candidates from SDSS are in the MaNGA catalogue. Thus, we do not expect to find galaxies in an advanced phase of quenching, but more likely galaxies which could have just started it.

In Figure 4.3 and Figure 4.5 we show the main pieces of information needed to characterise the sample, along with the g-r-i images from SDSS. Starting from the maps of [O III]/Hα (i.e. our observable for the ionisation status) and [N II]/[O II] (i.e. the observable for the metallicity) of each galaxy, we build the spatially resolved [O III]/Hα vs [N II]/[O II] diagnostic diagram for the quenching. We classify the spaxels into 4 groups according to their position on the plane in relation to the SDSS distribution: (i) spaxels lying above the median curve of the SDSS, which represent galaxy regions whose ionisation status is compatible with ongoing star formation; (ii) spaxels between the median and the 1σ limit of the SDSS distribution, regions characterised by slightly lower ionisation, though still compatible with radiation due to star formation; (iii) spaxels between 1σ and $3 \times 1\sigma$ SDSS limits, which are galactic regions in a grey area between star formation and quenching; (iv) spaxels lying below the $3 \times 1\sigma$ limit of the SDSS distribution are galaxy regions which are likely experiencing the star formation quenching.

4.1.5 The sample of Galaxies with Quenching Regions and the sample of Star-Forming galaxies

Once having classified all spaxels within each galaxy, we define as **QRGs**, i.e. Galaxies with Quenching Regions, those galaxies in our sample which have at least 1.5% of their spaxels below the $3 \times 1\sigma$ curve, representing a conservative excess of spaxels with respect to those expected below the $3 \times 1\sigma$ (i.e. $\sim 0.13\%$) for a star-forming galaxy. The QRGs will be further analysed as galaxies with regions potentially undergoing the quenching. In particular, the already mentioned Figure 4.3 refers to the 10 QRGs galaxies which show such plausible quenching regions.

On the contrary, the other 10 galaxies, do not show any sign of quenching, with the most of their spaxels lying above and along the median of the SDSS star-forming galaxies relation, as shown in Figure 4.5). Hence, their behaviour in the [O III]/Hα vs [N II]/[O II] diagram is perfectly coincident with that of a typical star-forming galaxy. We will show in Figure 4.5 and in the on-line material that also their resolved BPT diagram confirms their star-forming nature. Hence, we can simply call them star-forming galaxies (**SFs**) and in the follow we compare their properties (i.e. parameter of ionisation log U, gas-phase metallicity Z, star formation rate densities ΣSFR, etc.) with those of the QRGs ones.

TABLE 4.1: Main properties of our MaNGA QRGs and SFs samples. The blue lines indicate two galaxies analysed in detail in the text.

sample	MaNGA-ID	z	RA	DEC	$\log(M/M_\odot)$	Mg [mag]	sSFR [yr^{-1}]	R50 [arcsec]	n (Sers.)	b/a	$PSF_{FWHM}(G)$ [arcsec]	Morph.
QRGs	1-379241	0.0405	119.3	52.7	9.7	-19.6	-10.5	3.1	1.3	0.5	2.45	Sab
	1-491193	0.0405	171.5	22.1	9.6	-19.3	-10.4	8.6	1.3	0.9	2.61	Scd
	1-197045	0.0430	212.1	52.9	10.0	-19.5	-10.7	6.0	0.8	0.6	2.57	Sab
	1-392691	0.0435	156.2	36.0	9.8	-19.8	-9.9	6.4	1.3	0.8	2.46	Scd
	1-36645	0.0440	40.5	-1.0	9.7	-19.0	-9.7	6.6	1.5	0.8	2.85	/
	1-149235	0.0464	169.3	51.0	10.2	-20.1	-10.1	3.1	1.3	0.7	2.41	Sab/Scd
	1-338697	0.0499	115.0	43.0	10.2	-20.2	-10.0	6.7	1.0	0.9	3.09	Scd
	1-373102	0.0511	23.7	30.6	10.2	-20.1	-9.9	7.8	1.4	0.8	2.36	Scd
	1-43012	0.0527	112.9	38.3	10.5	-20.5	-10.5	6.2	1.1	0.8	2.46	Scd
	1-91760	0.0660	240.0	54.8	10.8	-20.9	-10.2	6.4	0.8	0.9	2.45	Scd
<QRGs>		0.0478			10.0	-19.9	-10.2	6.1	1.2	0.8	2.57	
SFs	1-258589	0.0405	186.7	44.9	9.7	-19.4	-10.0	6.7	1.6	0.9	2.67	/
	1-351911	0.0420	122.0	51.8	9.7	-19.2	-9.8	2.8	1.1	0.7	2.55	Scd
	1-245054	0.0428	212.5	53.6	9.9	-19.7	-9.9	5.5	2.2	0.4	2.48	Sab
	1-386695	0.0474	138.0	27.9	10.1	-20.1	-10.1	3.7	1.4	0.3	2.32	Sab
	1-178443	0.0477	260.8	27.6	10.4	-20.5	-9.9	3.2	2.3	0.5	2.46	Sab
	1-276547	0.0487	163.5	44.4	10.2	-20.6	-9.9	5.2	0.8	0.5	2.40	Scd
	1-22383	0.0542	253.3	64.5	10.2	-20.7	-9.6	3.0	1.5	0.9	2.52	/
	1-351596	0.0554	118.6	49.8	10.4	-21.0	-10.1	5.3	0.9	0.5	2.52	Sab/Scd
<SFs>		0.0473			10.08	-20.2	-9.9	4.4	1.5	0.6	2.49	

The main global properties of the QRGs and SFs are listed in Table 4.1. By construction, the two samples have a similar stellar mass and redshift range, with an average (and also median) mass of 10^{10} $M_{\odot}$ and a mean redshift of z $\sim$ 0.048. However, we find that two SF galaxies (i.e. 1352114 and 1-197704) have a central [N II]/[O II] ~ -0.6, that means ≈ 2 dex lower than the lowest QRGs. Therefore, their gas-phase metallicity is considerably lower than the metallicity range of the QRGs sample. We exclude these two objects and in the following, we will further analyse the remaining 8 SFs galaxies. In Figure 4.1 we report the position in the [O III]/Hα vs [N II]/[O II] diagram of the SDSS measures of the galaxies in the two samples.

Both samples show, on average, a typical Sersic profile of disc galaxies (i.e. $<n_{\mathrm{Sersic}}>$ $1.2 - 1.4$), and they show <b/a> (i.e. the ratio between the semi-axis of the galactic plane) higher than $0.5 - 0.6$. Instead, we find differences in the specific-SFR (sSFR) and R50: the QRGs have, on average, lower sSFR and larger R50 than the SFs ones.

As mentioned earlier, we expect about 50% of the [O III]undet SDSS galaxies to be in quenching, and we find that 5 out to the 8 analysed [O III]undet galaxies belong to the QRG sample, while the other ones are actually star-forming galaxies. The discrepancy can be ascribed to an increased deepness of MaNGA data with respect to the SDSS ones, resulting in [O III] still weak, but measurable with a higher S/N. Instead, it is interesting that 5 out of the 12 galaxies originally selected as star-forming are instead classified as QRG galaxies. Later, we will investigate the distribution of the quenching regions within QRGs, however, we anticipate here that they are mainly placed off-centre, explaining why the regions inside the SDSS fibre have been classified as star-forming.

To summarise, according to the distribution of the spaxels on the [O III]/Hα vs [N II]/[O II] diagnostic diagram for the quenching, we obtain two MaNGA samples:

- **QRGs:** 10 galaxies that show regions (at least 1.5% of the total galaxy) satisfying our quenching criteria (i.e. lie below the $3 \times 1\sigma$ of the SDSS star-forming distribution).
- **SFs:** 8 star-forming galaxies which have same redshifts, stellar masses and gas-phase metallicity range of the QRGs.

In section 4.3, we will extensively analyse the global behaviours of the two samples and we will compare their properties. In the next section, we will focus on the study of two galaxies, one for each sample, with the purpose of providing the details of the analysis that we have done on the galaxies in our sample.

4.2 RESULTS

We will discuss the general results of the two populations in section 4.3, and we will present individual details of the objects in our samples in the online materials. With the purpose of showing our research method, we present In the following the detailed analysis of two objects: QRG 1-43012 representing an example of a QRG, and SF 1-178443 among the galaxies in the SF sample. We choose SF 1-178443 because it has similar mass and redshift of QRG 1-43012, allowing a direct comparison of the two systems, in terms, in particular, of ionisation parameter.

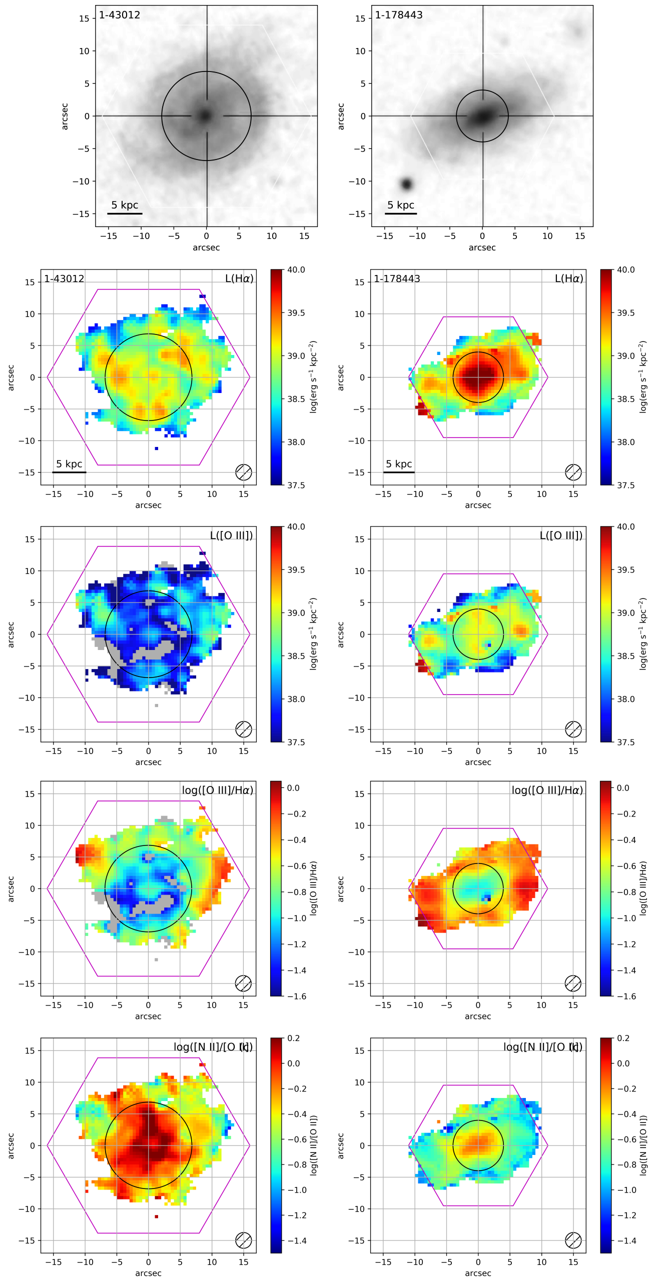

FIGURE 4.1: Each row shows, from top to bottom (1) r-band images (2) luminosity surface density maps of dust-corrected Hα, (3) luminosity surface density maps of dust-corrected [O III], (4) dust corrected [O III]/Hα maps and (5) dust corrected [N II]/[O II] maps. Each column shows, from left to right (a) maps of QRG 1-43012 and (b) maps of SF 1-178443. Spaxels coloured in grey represent regions with S/N([O III])$<$ 2). Overlapped in magenta are the hexagonal shapes of the MaNGA IFU bundles, while the black circles represent the R50. The $2.5''$ circle in the bottom-right corner of the maps represent the PSF (FWHM) of MaNGA datacubes. The galaxies go over the edge of the IFU shape because of the effect of the dithering, resulting in a coverage of a larger area of the sky.

4.2.1 Emission lines maps

Figure 4.1 shows the r-band image, the logarithmic luminosity surface density maps of Hα and [O III] and the maps of [O III]/Hα and [N II]/[O II] for the two galaxies. We find some differences, both structural and physical, between the two targets. They differ in size, being the SF smaller by a factor of ~ 0.5 than the QRG one (i.e. R50 ~ 3.7 kpc and ~ 7.0 kpc, respectively) despite they have similar masses (i.e. log($M/M_{\odot}$) = 10.48 and 10.35, respectively). The analysis of Figure 4.1 shows that:

- QRG 1-43012 has some spiral arms in r-band and, according with the morphological probability distribution of the SDSS galaxies provided by Huertas-Company et al. (2011), it can be classified as a Scd galaxy. Instead, it remains difficult to see any significant spiral arm in the r-band image of SF 1-178443, while it shows a prominent bulge (or pseudo-bulge) and it has been classified as a Sab galaxy.

- The Hα emission is distributed not homogeneously in the QRG galaxy. It shows clumps which reach a maximum intensity of Σlog L(Hα) ~ 39.3 erg s^{-1} kpc^{-2}, while in the SF the Hα is mostly concentrated and homogeneously distributed in the region inside the effective radius, where the emission reaches at values higher than Σlog L(Hα) 40 erg s^{-1} kpc^{-2} and then degrades at lower values toward the outskirts.

- The QRG galaxy has a globally weak emission in [O III], that rarely exceeds Σlog L([O III]) ~ 38.5 erg s^{-1} kpc^{-2} and, as a result, the 12.6% of its spaxels have an upper limit in [O III] (i.e. S/N([O III])< 2). Instead, the [O III] emission of the SF galaxy follows the pattern of the Hα though slightly weaker, as we expected since arises from stellar ionising sources. In this case, only a few spaxels (i.e. 0.4%) have S/N([O III]) < 2.

- The distribution of [O III]/Hα ratio (i.e. our ionisation level indicator) in the QRG galaxy (see Figure 4.1) does not show a uniform gradient from the centre towards outer regions, but it reaches a minimum in an irregular annular region between ~ 2 and ~ 5.5 kpc (i.e. between ~ 0.3 and ~ 0.9 R/R50) around the centre of the galaxy and then increases towards more considerable distances. Instead, in the case of the SF galaxy, the [O III]/Hα shows a typical gradient with the [O III]/Hα that grows up from the centre towards the outskirts of the galaxy.

- The distribution of [N II]/[O II] ratio (i.e. our metallicity indicator) shows in both QRG and SF galaxies an opposite behaviour with respect to [O III]/Hα, with values increasing towards the inner parts of the galaxies. This relation between distributions of [O III]/Hα and [N II]/[O II] in galaxies is in part due to the well-known U-Z degeneracy between the ionisation parameter and gas metallicity (see Citro et al., 2017; Quai et al., 2018).

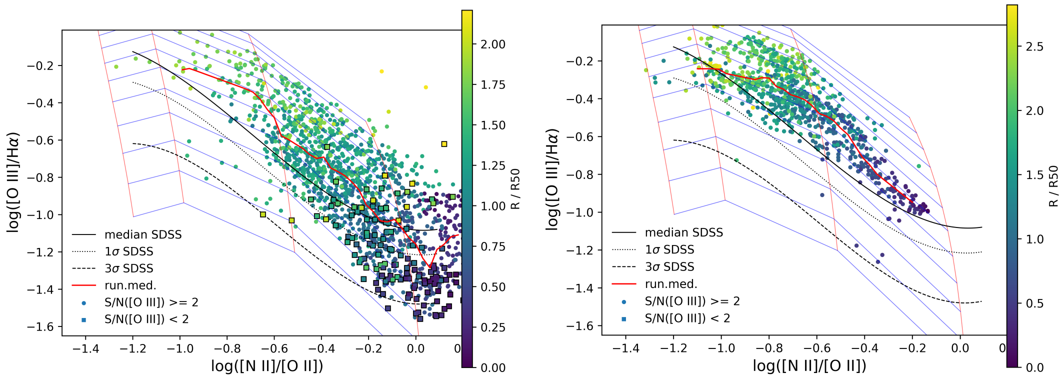

FIGURE 4.2: The resolved [O III]/Hα vs [N II]/[O II] diagram of QRG 1-43012 (*left*) and SF 1-178443 (*right*). Each round dot represents a spaxel in which the S/N([O III]) ≥ 2, while the square dots represent spaxels in which the S/N([O III]) < 2 and their [O III]/Hα values are upper-limits. The colours of the dots change according to the distance R/R50 of the spaxels from the centre of the galaxy. The red curve represents the running median (continue) of the relation. Instead, the black curves (polynomial of degree 4) represent the median (continue),1σ (dotted) and $3 \times 1\sigma$ (dashed) of the distribution of SDSS star-forming galaxies (see Quai et al., 2018). Superimposed is reported the grid of photo-ionisation models by Citro et al. (2017), with the red straight lines representing different metallicities (i.e. Z = $\{0.004, 0.008, 0.02, 0.04\}$ from left to right) and the blue straight lines representing different levels of the ionisation parameter U (i.e. from log U -2.3 in the top to -3.6 in the bottom).

4.2.2 The quenching diagnostic diagram

The [O III]/Hα vs [N II]/[O II] diagram

In Figure 4.2 we show the [O III]/Hα vs [N II]/[O II] diagram of the two galaxies with the spaxels coloured according to their galactocentric distance and a grid of ionisation models by Citro et al. (2017). The U-Z degeneracy is strongly mitigated, with the gas-phase metallicity Z increasing with [N II]/[O II] while the ionisation parameter log U varying with [O III]/Hα at fixed metallicity. Results from Figure 4.2 suggests that a negative gradient of metallicity with radial distances is present in both galaxies. However, in SF 1-178443 at fixed metallicity, the ionisation parameter does not vary significantly while in QRG 1-43012 it shows a large spread revealing differences in the ionising stellar populations in different regions of the galaxy. We stress that in this plane, at fixed values of [N II]/[O II] (i.e. fixed metallicity), those spaxels lying below the $3 \times 1\sigma$ limit curve of the relation obtained from the star-forming population of SDSS represent regions compatible with the quenching. This region corresponds roughly to a log U < -3.4. While in next sections we show in more details the U and Z profiles for our targets, from Figure 4.2 is already evident that the QRG galaxy, on average, is more metallic than the SF one. About 72% of its spaxels have a super-solar metallicity (i.e. Z> 0.02), against 15.6% of the SF one. Moreover, the spaxels of the QRG galaxy are spread across the entire plane covering the entire scale of ionisation levels, from log U -2.4 to -3.6. About 1.6% of its spaxels are in the quenching region below the $3 \times 1\sigma$ curve of the SDSS distribution, and

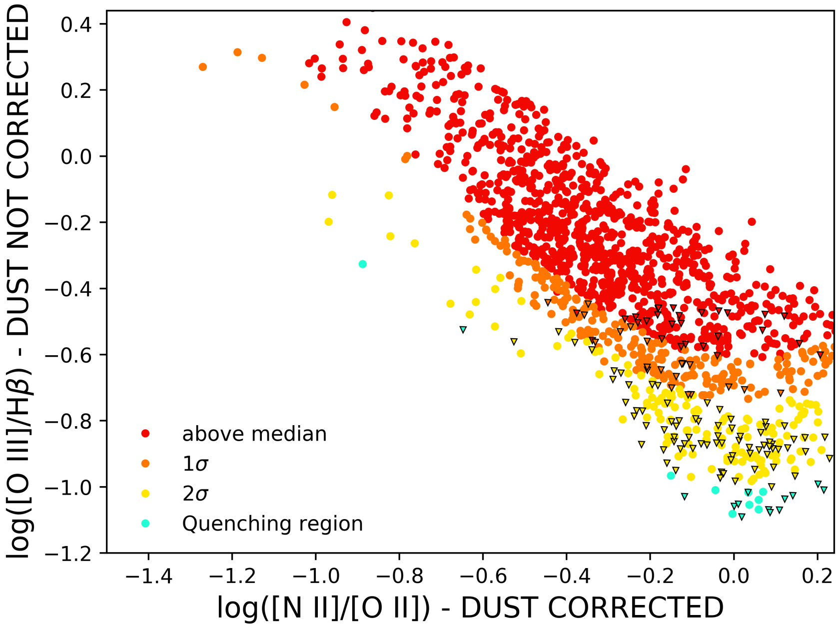

FIGURE 4.3: The resolved [O III]/Hβ (not corrected for dust extinction) vs [N II]/[O II] (corrected for dust extinction) diagram of QRG 1-43012. The dots colour code is based on the position of each spaxel on the [O III]/Hα vs [N II]/[O II] diagram, and it is the same as in Figure 4.1. The cyan is representing quenching regions, followed by the yellow for the galactic regions that lie between $3 \times 1\sigma$ and 1σ of the diagram, orange for those between 1σ and the median and red for regions of pure star-formation that are above the median of the diagram.

14% of the spaxels lie between 1σ and $3 \times 1\sigma$. Instead, the 98% of the spaxels of the SF galaxy are in the pure star-forming region, above the 1σ curve of the SDSS distribution and with log U higher than -3.2.

The impact of dust extinction on ionisation and metallicity indicators

As shown in Quai et al. (2018), we can mitigate the U-Z degeneracy using the resolved [O III]/Hα vs [N II]/[O II] diagram. The wavelength separation between the lines in the two ratios requires caution because of the not negligible effect of the dust extinction. The classical approach of the Balmer decrement could be not perfectly exact in recovering the intrinsic emission lines of an object deviating from the average star-forming galaxies. We could use other line ratios less sensitive to this effect. For example, the [O III]/Hβ ratio would have the same sensitivity to the ionisation parameter of [O III]/Hα with the advantages to be less affected by dust extinction. To guarantee a high level of precision in the ratio measurement, we should impose an S/N(Hβ) ≥ 5. However, this threshold would introduce a strong bias toward high SFR, to the disadvantage of the quenching galaxies we want to select.

Therefore, to evaluate the impact of dust extinction, we tested an alternative diagnostic diagram, with [O III]/Hβ not corrected for dust extinction (in place of dust-corrected [O III]/Hα) vs dust-corrected [N II]/[O II]. In Figure 4.3 is shown the

[O III]/Hβ vs [N II]/[O II] of QRG 1-43012. We find that the spaxels classified as quenching regions according to their position in the [O III]/Hα vs [N II]/[O II] diagram (i.e. the spaxels lying below the $3 \times 1\sigma$ of the SDSS relation, see Figure 4.3) remain those showing the lowest [O III]/Hβ values at fixed [N II]/[O II]. We find the same result also in the other QRGs (see the online materials), hence we can state that our classification and results do not depend on the dust correction.

We note that also that the [O III]/[O II] ratio is sensitive to the ionisation status. However, it is known to be also rather sensitive to the gas-phase metallicity (e.g. Nagao, Maiolino, and Marconi, 2006), and it would be less effective to mitigate the U-Z degeneracy. The line ratio between [Ne III] $\lambda3869$ and [O II] ([Ne III]/[O II]) is less affected by dust-extinction than [O III]/Hα and it is sensitive to the ionisation level of a star-forming galaxy. However, the [Ne III] line is usually faint to be detected at high S/N. We achieve to measure this line only in the central region of some galaxies in our SF sample. At larger wavelength, the line ratio [S III]/[S II] between the lines [S III] $\lambda\lambda9060-9532$ and the doublet [S II] $\lambda\lambda6726-6731$ is another ionisation tracer. The [Ne III] lines are measurable in MaNGA data up to redshift z~ 0.08, however, at the redshifts of our targets these lines end up in a spectral region dominated by a series of OH skylines. To perform the continuum fit with pPXF, we cut the original spectra at $\lambda7200$Å. We try, therefore, to measure the [S III] lines by fitting the stellar continuum with a straight line but we found not reliable, faint and irregular residuals challenging to be interpreted as actual emission lines.

Similar remarks can be done about the metallicity indicator. We could, in principle, use different couples of emission lines closer in wavelength than [N II] and [O II], whose ratio is sensitive to the gas-phase metallicity. For example, [N II]/[S II] ratio shows a similar sensitivity to the metallicity as [N II]/[O II]. However, the doublet [S II] $\lambda\lambda6717-6731$ is considerably fainter than the [O II] $\lambda\lambda3726-3729$ one and the cut in S/N with [N II]/[S II] would end up in excluding wider galactic area than with [N II]/[O II]. However, the test of the equivalence between [O III]/Hβ not corrected for dust extinction and [O III]/Hα allows to safely use [N II]/[O II] as metallicity indicator.

Summarising, we can conclude that the [O III]/Hα vs [N II]/[O II] diagram is robust against the Balmer decrement approach for correcting dust extinction and that these line ratios are the most suitable for mitigating the U-Z degeneracy.

The maps of the quenching regions

In Figure 4.4 we show the resolved maps of the [O III]/Hα vs [N II]/[O II] diagram for the two galaxies. For QRG 1-43012 the quenching regions are mainly located in an annulus around the centre of the galaxy, and they cover an effective quenching area of $\sim$ 7.1 kpc^2, that becomes an extended quenching area of $\sim$ 67 kpc^2 if we consider the spaxels that lie between 1σ and $3\times1\sigma$ as regions in which the quenching could be started. They are distributed around the proper quenching regions, and it is likely that the quenching is propagating in their direction.

Figure 4.5 shows the resolved diagnostic diagram of Baldwin, Phillips, and Terlevich (1981, herafter BPT) for QRG 1-43012 in which appears that the quenching regions

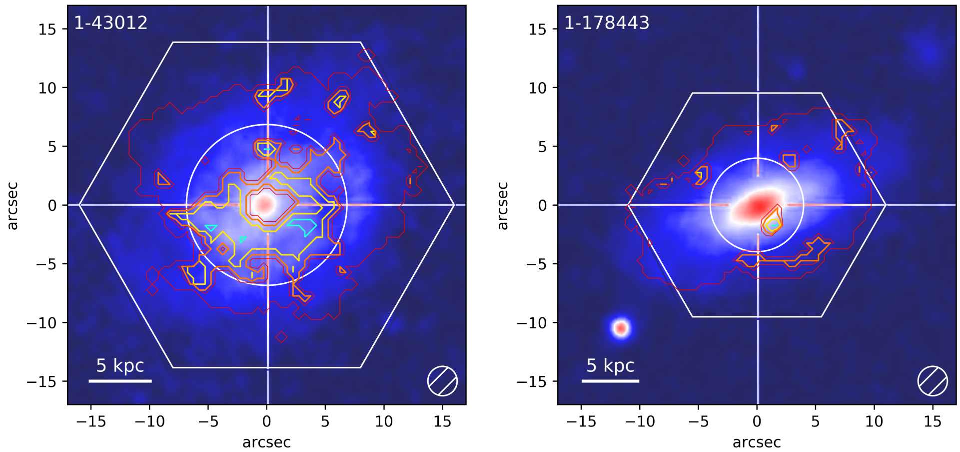

FIGURE 4.4: The contours of the resolved [O III]/Hα vs [N II]/[O II] diagram are superimposed to the G images (in false colours) of QRG 1-43012 (*left*) and SF 1-178443 (*right*). The contours colour code is based on the position of each spaxel on the diagram, and it is the same as in Figure 4.1. The cyan is representing quenching regions, followed by the yellow for the galactic regions that lie between $3 \times 1\sigma$ and 1σ of the diagram, orange for those between 1σ and the median and red for regions of pure star-formation that are above the median of the diagram. In the bottom-left corner is reported the scale of 5 kpc. Overlapped are the hexagonal shapes of the MaNGA IFU bundles, while the circles represent the R50. The $2.5''$ circle in the bottom-right corner of the maps represent the PSF (FWHM) of MaNGA datacubes.

are compatible with emission due to stellar ionisation, therefore, we can safely exclude the presence of an AGN. It should be noted that some spaxels, mostly located at the edge of the galaxy, lie above (but close) the BPT curve of Kauffmann that separates the region where the ionisation is due to star formation and that dominated by AGNs and LINERs systems. These spaxels are observed in almost all the galaxies analysed (see the on-line material) and their behaviour is due to the uncertainties in [O III]/Hα. The emission lines, indeed, become weaker towards the outskirts of galaxies, increasing the uncertainties of the emission line ratio measures. For example, the typical S/N([O III]/Hα) within R50 of QRG 1-43012 is between 4 and 25, while it drops below 1.5 above ~ 1.6 R50.

4.2.3 Radial profiles

In this section, we extend the analysis of the two galaxies by investigating the radial profiles of the main quantities used in this work. We compute no projection of the galactic plane, and we normalise the distance to the elliptical R50, that we consider as a circular radius. Figure 4.6 shows the radial profiles of the colour excess E(B-V) and the observables [O III]/Hα and [N II]/[O II], the radial profiles of the parameters log U and gas-phase Z and that of the star formation rate density. Our findings can be briefly summarised as following:

- The E(B-V) radial profile of QRG 1-43012 is quite scattered between $0 \leq$ E(B-V) < 0.4 at any radius. The spaxels marked as quenching regions show intermediate values of colour excess. The profile of SF 1-178443 is less scattered and it

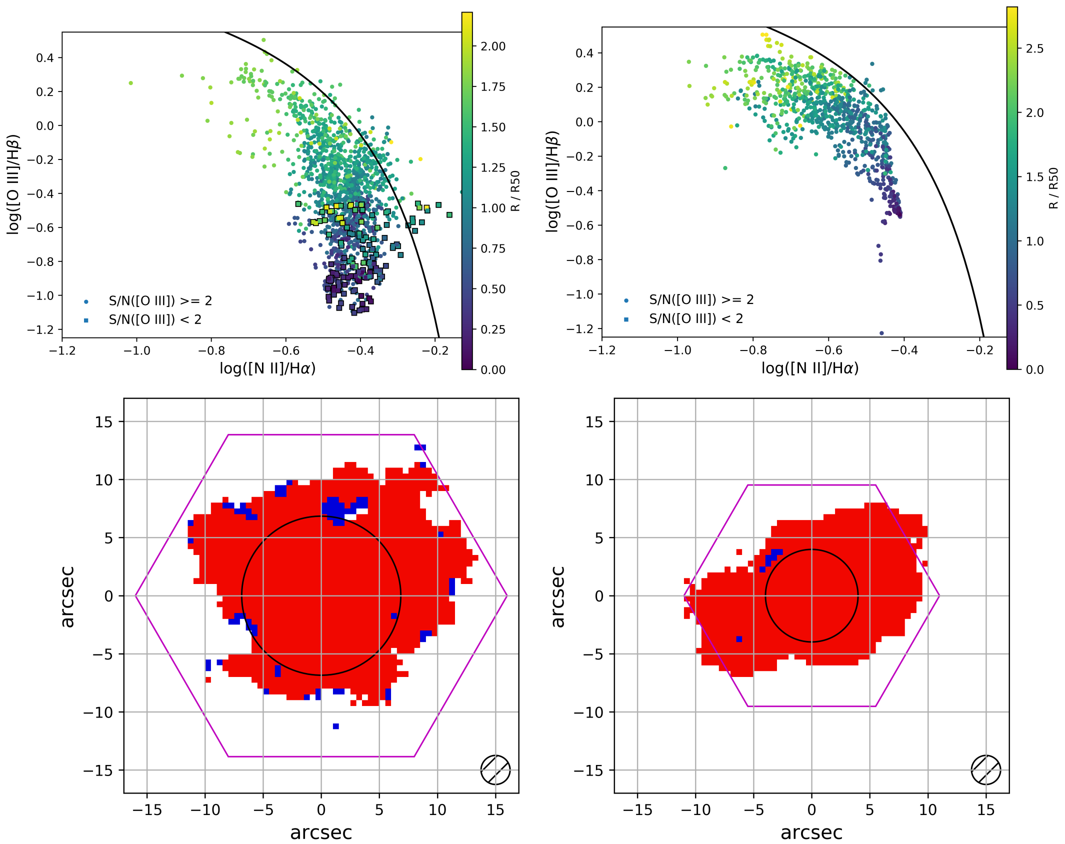

FIGURE 4.5: *Top:* the resolved BPT diagram of QRG 1-43012 (*left*) and of SF 1-178443 (*right*). Each round dot represents a spaxel in which the S/N([O III]) ≥ 2, while the square dots represent spaxels in which the S/N([O III]) < 2 and their [O III]/Hα values are upper-limits. The colours of the dots change according to the distance R/R50 of the spaxels from the centre of the galaxy. The black curve is from Kauffmann et al., 2003. *Bottom:* map of the resolved BPT of the two galaxies. Spaxels with ionisation dominated by star-formation (below the Kauffmann et al., 2003 curve) are represented in red, while those whose the ionisation is dominated by AGN radiation are represented in blue. Overlapped is the hexagonal shape of the MaNGA IFU bundle, while the circle represents the R50. The 2.5″ circle in the bottom-right corner of the maps represent the PSF (FWHM) of MaNGA datacubes.

shows an almost flat median.

- As mentioned in the previous sections, the profile of [O III]/Hα (i.e. ionisation level profile) for QRG 1-43012 shows a central peak, then it decreases until it reaches a minimum log([O III]/Hα) $\sim -1.2 \pm 0.2$ between $\sim 0.3 <$ R/R50 $<\sim 0.75$ that is followed by a steep increment towards larger radii. This minimum corresponds to the region in which are concentrated almost all the spaxels compatible with quenching (see also Figure 4.4). Instead, SF 1-178443 shows a more homogeneous behaviour with a positive gradient in the [O III]/Hα profile, which is steeper at small radii, while it grows slowly at larger radii. Moreover, the [O III]/Hα values are higher than those of QRG 1-43012 at any radius.

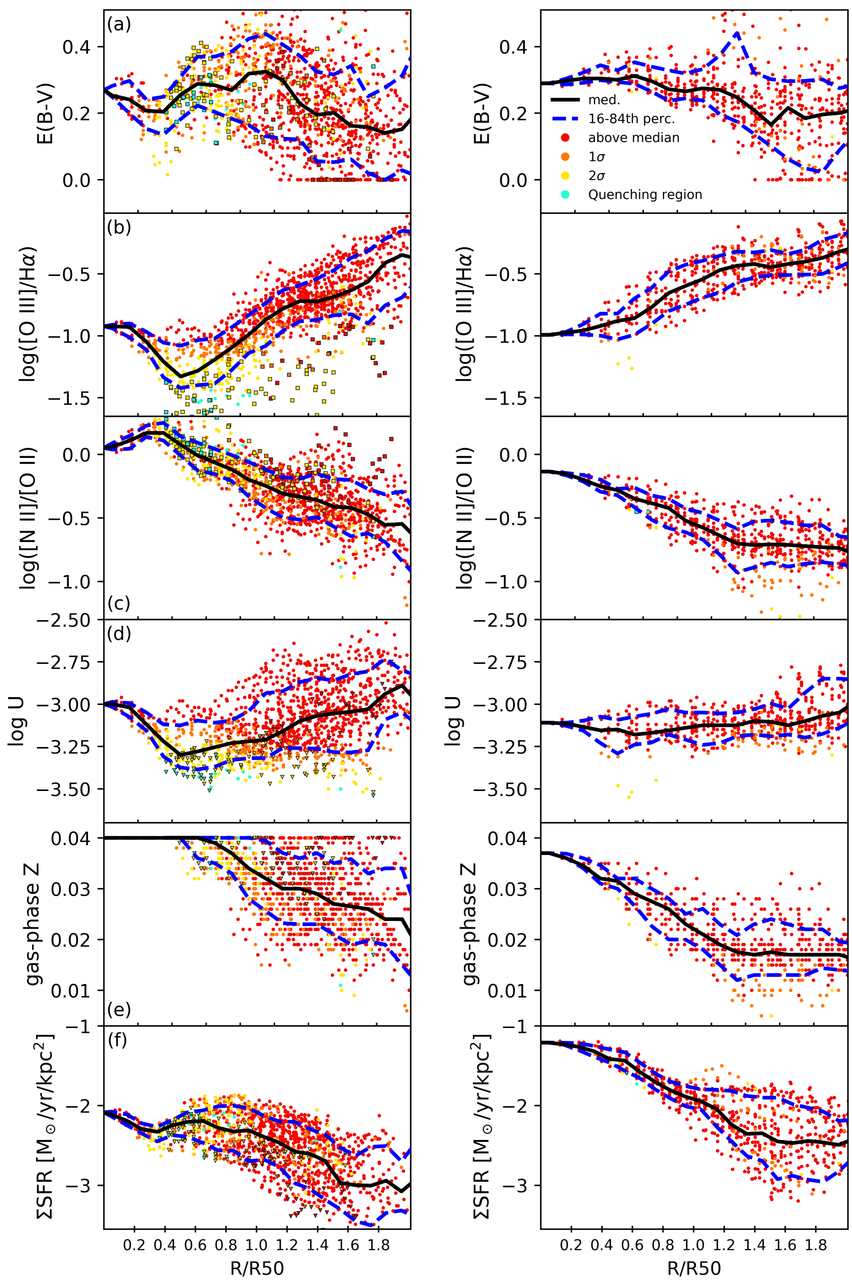

FIGURE 4.6: Radial profiles of QRG 1-43012 (*left*) and of SF 1-178443 (*right*): (a) E(B-V), (b) [O III]/Hα, (c) [N II]/[O II], (d) log U, (e) gas-phase Z, (f) ΣSFR. The black curves represent the median of the relations in bins of width 0.1R/R50 , while the blue ones represent the 16-84$^{\text{th}}$ percentile of the relations. Each round dot represents a spaxel in which the S/N([O III]) ≥ 2, while the square dots represent spaxels in which the S/N([O III]) < 2 and their [O III]/Hα values are upper-limits. The dots colour code is the same as in Figure 4.4, and it is based on the position of each spaxel on the [O III]/Hα vs [N II]/[O II] diagram (Figure 4.1 and Figure 4.2). The cyan is representing quenching regions, followed by the yellow for the galactic regions that lie between $3 \times 1\sigma$ and 1σ of the diagram, orange for those between 1σ and the median and red for regions of pure star-formation that are above the median of the diagram.

- The profile of [N II]/[O II] follows a complementary pattern, with the peak decentred set near 0.25 effective radius. The relation is tight in the centre's proximity, with a 1σ scatter of about 0.1 dex, but becomes higher than 0.2 at radii larger than R50. This galaxy shows lower [N II]/[O II] values, that suggests lower metallicity than QRG 1-43012 at any radius, with a maximum value in the centre that decreases rapidly approximately at R50, then it becomes almost flat.

- The log U profile of QRG 1-43012 confirms the trend of the observable [O III]/Hα, though with a larger spread. It shows a peak in the centre of the galaxy that is followed by a decrement, which reaches the minimum log U $= -3.2 \pm 0.1$ between 0.5 and 0.75 R50 in correspondence of the [O III]/Hα minimum. At larger radii the profile increases again, though the spaxels are scattered through all the available ionisation levels between log U -2.5 and -3.5. This find suggests that the minimum in the observable [O III]/Hα radial profile is due to a minimum in the ionisation level and not to the effect of the metallicity. Instead, the SF 1-178443 trend of log U with radius is almost flat up to 1.75 R50, with log U ~ -3.1 , suggesting that this star-forming galaxy is homogeneous in ionisation level, with spaxels less scattered than those of the QRG galaxy and only a handful of them have log U lower than -3.2.

- The gas-phase metallicity radial profile of QRG 1-43012 can be adequately studied only at radii larger than 0.5 R50. In fact, at closer distances, the metallicity estimate is fixed at the maximum value of Z $=$ 0.04 (i.e. the highest metallicity in Citro et al. (2017) models), and it represents a lower limit of the actual metallicity in the inner part of the galaxy. At such high metallicity, a secondary nucleosynthesis origin of the nitrogen could explain this behaviour. In these circumstances, indeed, the [N II]/[O II] ratio (i.e. a tracer of the N/O ratio) overestimates the oxygen abundances (i.e. O/H ratio), leading to higher values of gas-phase metallicity. However, the galaxy QRG 1-91760 (see the online materials) shows characteristics similar to those of QRG 1-43012, though having, on average, a lower [N II]/[O II] (i.e. lower gas-phase metallicity). Its Z radial profile increases from the center of the galaxy and it reaches a maximum value around 0.3 R50 (see the online materials). This trend suggests a similar behaviour for the true Z radial profile for QRG 1-43012. At radii larger than 0.5R50 the Z profile decreases following the classical negative gradient, though showing a large spread (e.g. at R50 the metallicity is Z $= 0.029 \pm 0.007$). The Z radial profile of SF 1-178443 shows a negative gradient up to 1.25 R50; then it becomes almost flat. In this galaxy, the gas-phase metallicity is lower than that of the QRG one at any radius, and it shows a smaller spread.

- The log ΣSFR radial profiles of the two galaxies are different, with QRG 1-43012 having ΣSFR values lower than those of SF 1-178443 at any radius. Its radial profile shows a weak negative gradient between log ΣSFR ~ -2 in the center to 3 ± 0.4 at 2 R50. It can also be seen a relative minimum around 0.3 R50 but less evident than that of the [O III]/Hα profile. Instead, the ΣSFR radial profile of SF 1-178443 shows a negative gradient with a steeper slope until ~ 1.25 R50 with values between ~ -1.2 and -2.3 ± 0.4, then the profile becomes almost flat.

To summarise, the two galaxies show different characteristics, both concerning ionised phase and gas-phase metallicity and also regarding different distributions of the star-formation rate surface density across the galactic plane.

4.3 A comparison between QRGs and SFs

In the previous section we gave details about the method we applied to each galaxy in our QRG and SF samples. In this section, we present the general results concerning the analyses of the behaviour of the two samples. We stress that the two samples are in the same redshift range and they have same stellar masses and central gas-phase metallicity, therefore, we can directly compare their properties. We focus on the [O III]/Hα vs [N II]/[O II] diagram, and on the average radial profiles of the quantities we showed in the previous section (i.e. E(B-V), [O III]/Hα, [N II]/[O II], log U, gas-phase Z, ΣSFR).

4.3.1 The average [O III]/Hα vs [N II]/[O II]

Figure 4.1 shows the average curves of QRG and SF galaxies in the resolved [O III]/Hα vs [N II]/[O II] diagram. The QRG curve is compatible with the trend of the median distribution of the Quai et al. (2018) SDSS sample, though at log([N II]/[O II]) values lower than about -0.6 it deviates showing lower [O III]/Hα values at fixed [N II]/[O II]. The two sample share a very similar slope, though they differ in normalisation being the average curve of SF sample above the QRG one of about 0.15 dex at any [N II]/[O II] value. The lower panel of Figure 4.1 shows the difference in [O III]/Hα, as a function of [N II]/[O II], between QRGs and SF galaxies. We average the differences and we define the significance to be the distance of this mean in units of σ, where σ is the error in the average. We find a $< \Delta\log(\text{[O III]}/\text{H}\alpha) >_{\text{[N II]/[O II]}} = -0.12 \pm 0.01$ dex with a significance over 10σ level (see Table 4.1). The result does not change if we analyse the median of the difference in place of the weighted average.

4.3.2 The average E(B-V) radial profile

Figure 4.2 shows the average radial profiles of the colour excess E(B-V) of the two samples. The SFs have higher extinction at any radius, with increasing values toward the centre. Figure 4.2 shows also the difference in E(B-V) as a function of R/R50, between QRG and SF galaxies. We average the differences and we estimate the significance as the distance of the mean in units of σ, where σ is the error in the average. We find that the difference between QRGs and SFs is confirmed at a significance of about 5σ level (see Table 4.1). This result does not change by using the median in place of the weighted average.

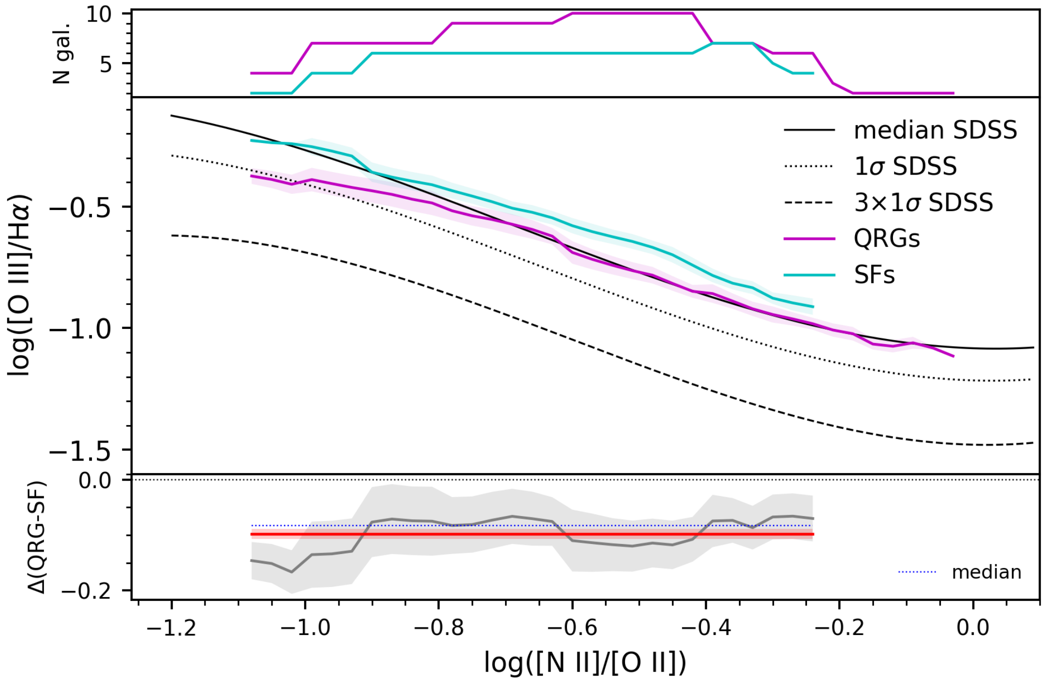

FIGURE 4.1: The average [O III]/Hα vs [N II]/[O II] diagram for the QRG and SF samples. *Top*: the number N of galaxies that contribute to the average. *Centre*: The magenta curve represents the mean curve of the QRG galaxies, that we obtain by averaging their means; the magenta shaded area shows the error of the average (i.e. $\sigma_{\rm mean}/\sqrt{N}$). The cyan curve shows the mean curve of the SF sample. The black curves represent median, 1σ and $3 \times 1\sigma$ limit of the SDSS star-forming galaxies sample (see Quai et al., 2018). *Bottom*: the grey curve represents the differences in [O III]/Hα, as a function of [N II]/[O II], between QRGs and SF galaxies and the grey shaded area shows the propagated errors. The red shaded area represents the weighted mean of these differences averaged over the [N II]/[O II] range (see Table 4.1).

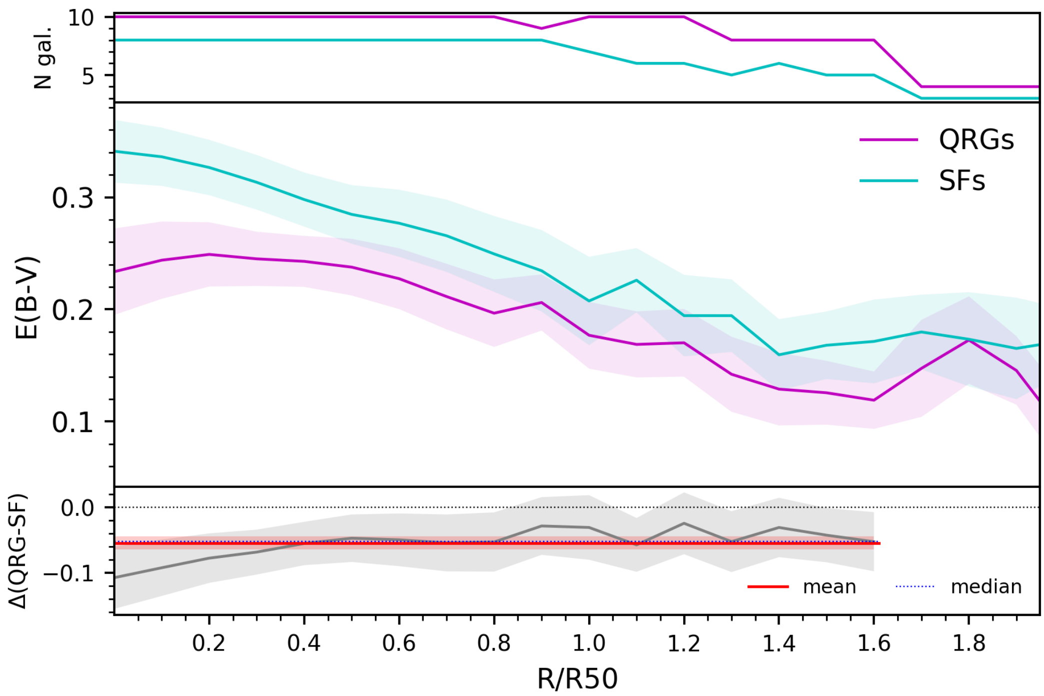

FIGURE 4.2: The average radial profiles of E(B-V) for QRG and SF samples. The colour code is the same as in Figure 4.1. The upper panels of the two plots show the number N of galaxies that contribute to the average. The grey curve in the lower panel of the two plots represents the differences in log U and Z, respectively, as a function of R/R50, between QRGs and SF galaxies. The red shaded area represents the mean of these differences averaged over R/R50 (see Table 4.1). We exclude from the significance analysis the trends at galactocentric distances larger than 1.6 R50 due to the exiguous number of objects in our samples that extend at this radii.

4.3.3 The average radial profiles of [O III]/Hα and [N II]/[O II] ratios

In Figure 4.3 we show the average radial profiles of [O III]/Hα and [N II]/[O II] ratios. At any radius, the SF sample shows, on average, higher [O III]/Hα and a slightly lower [N II]/[O II] values than the QRG population, though this one has more significant errors. In the same way as in [O III]/Hα as a function of [N II]/[O II], we study the significance of the differences in [O III]/Hα and [N II]/[O II] as a function of R/R50, between QRGs and SFs. We find a significance difference in [O III]/Hα at a level of about 5σ and a weak significance difference in [N II]/[O II] at a level slightly lower than $< 3\sigma$ (see Table 4.1). This result does not change if we use the median in place of the weighted average.

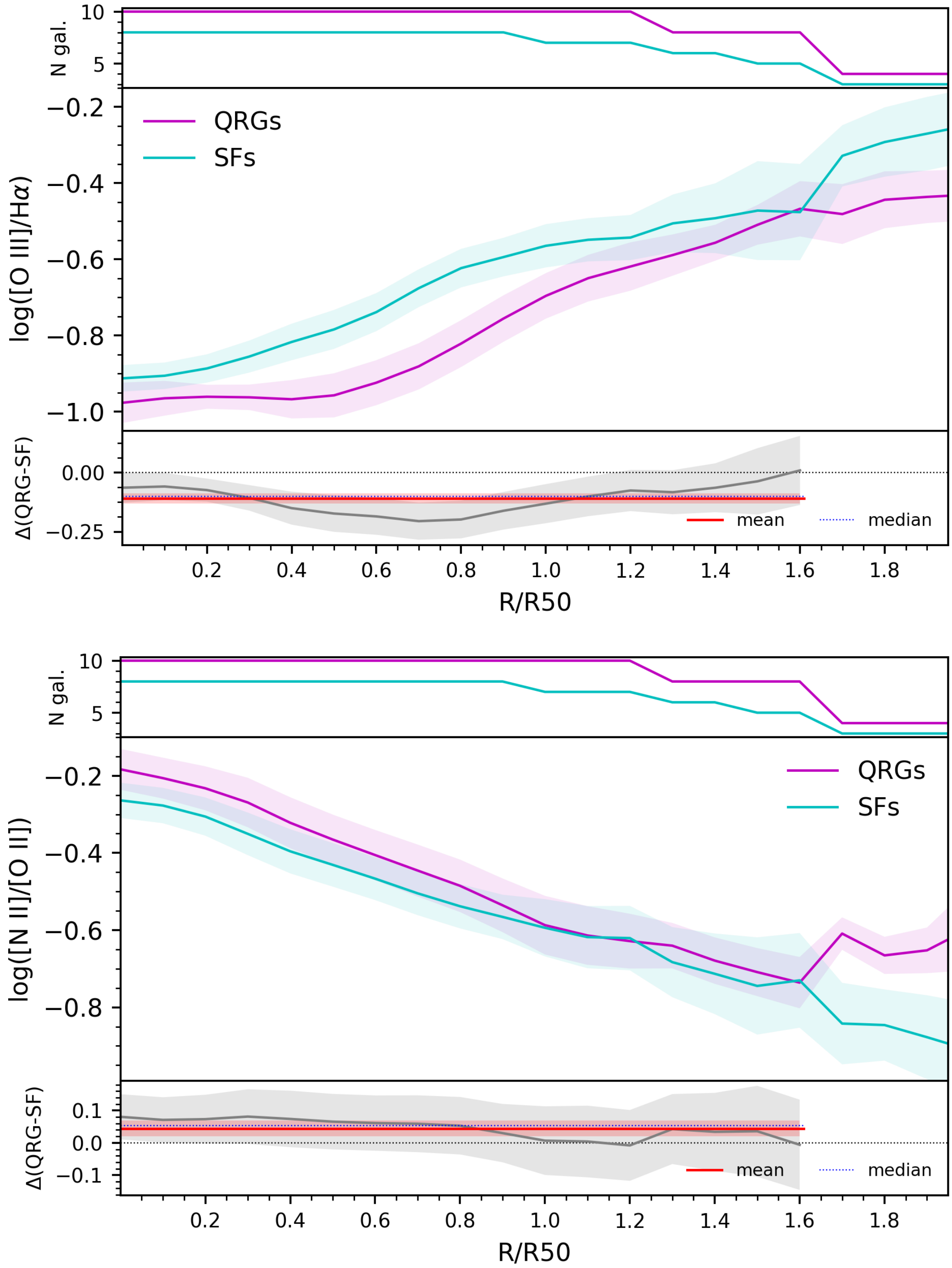

FIGURE 4.3: The average radial profiles of [O III]/Hα (*top*) and [N II]/[O II] (*bottom*) for QRG and SF samples. The layout of the figure is the same as in Figure 4.1.

4.3.4 The average log U radial profile

Figure 4.4 shows the radial profiles of the ionisation parameter log U for the two samples. The average log U radial profile of SF galaxies increases very slowly from log U ~ -3.2 in the centre, toward ~ -3.1 in the outskirts. The trend of QRG galaxies, instead, has a maximum of log U ~ -3.2 in the centre, then it decreases to a minimum log U ~ -3.3 around 0.5 R50 before rising again to log U ~ -3.1 towards the outskirts. Figure 4.4 show the difference in log U as a function of R/R50, between QRGs and SF galaxies. In the inner part there is no evidence of difference between the two samples, while it is strong between 0.3 and 1.2 R/R50, and hence the average difference is confirmed at a high significance of about 5.5σ level (see Table 4.1).

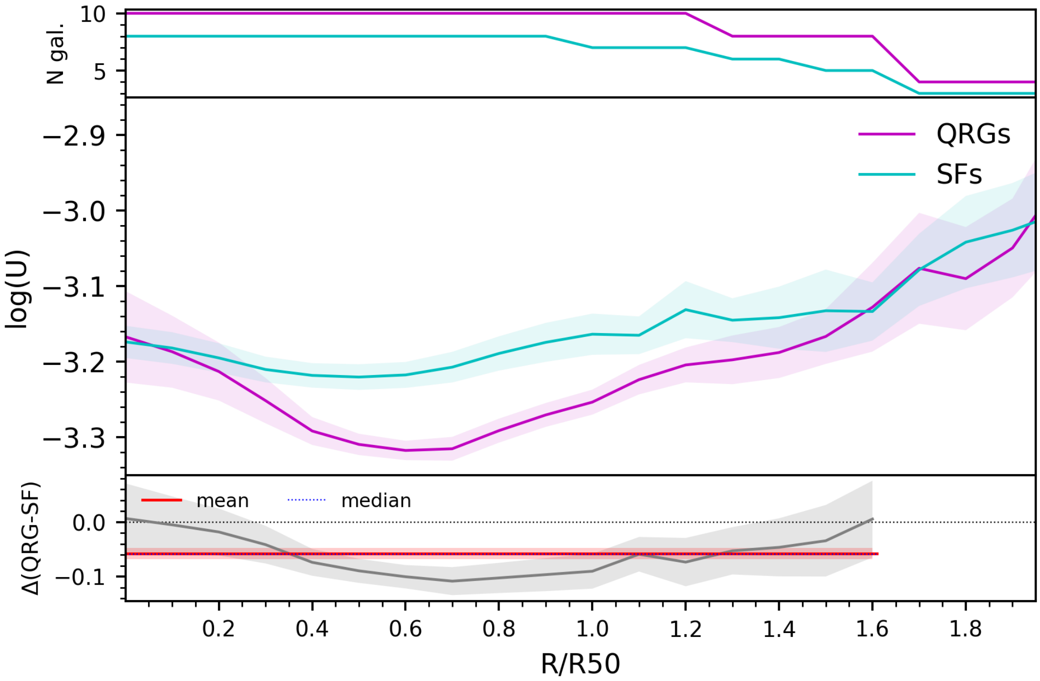

FIGURE 4.4: The average radial profiles of log U for QRG and SF samples. The layout of the figure is the same as in Figure 4.1.

4.3.5 The average gas-phase metallicity radial profile

The gas-phase metallicity radial profiles (see Figure 4.5) of the two samples have a similar slope and normalisation. We fit with a straight line the average radial profile at galactocentric distances larger than 0.5 R50 (as suggested in Belfiore et al., 2017a, to avoid smearing effects due to the MaNGA PSF in the inner part of galaxies) and smaller than 1.6 R50. We obtain a slope of ~ -0.009/R50 for QRGs, though the average profile of the QRG galaxies shows a larger error than that of SF ones[4]. In this case, the difference between the sample is rejected (significance level $< 3\sigma$). This result confirm that the two samples have a similar gas phase metallicity.

[4]If we convert the gas-phase metallicity in terms of 12+log(OH) (i.e. 12+log(OH) = log($Z/Z_\odot$) + 8.69, with $Z_\odot = 0.02$), we will obtain a slope of ~ -0.15dex/R50 for QRGs.

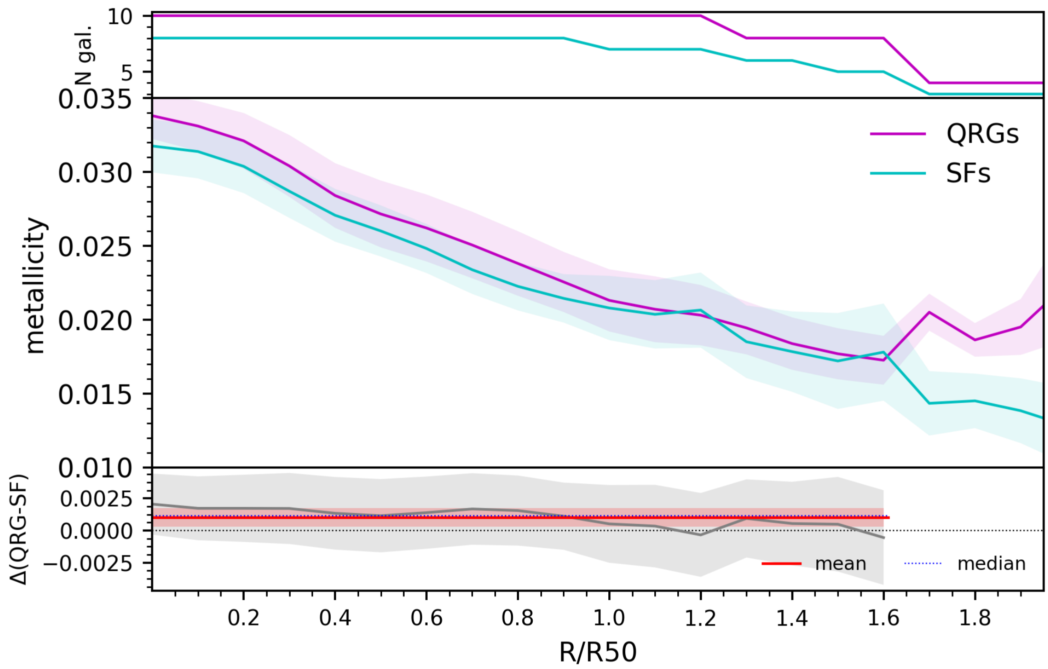

FIGURE 4.5: The average radial profiles of the gas-phase metallicity Z for QRG and SF samples. The layout of the figure is the same as in Figure 4.1. The two dotted lines represent the linear fit of the radial profiles between 0.5 and 1.6 R50.

4.3.6 The average ΣSFR radial profile

From the analysis of the average radial profiles of the SFR surface density (log ΣSFR) of the two samples (see Figure 4.6) arises that, on average, in the central regions of the galaxies the SF galaxies show higher SFR density than the QRG ones, with a difference of about 0.4 dex, in log-scale, though showing an error of about 0.2 dex. The average profile of QRG galaxies has a central value of log ΣSFR of about -2 and a slow decline towards large radii up to log ΣSFR ~ -2.5 at 1.5R50. The lower panel of Figure 4.6 shows the difference in log ΣSFR as a function of R/R50, between QRGs and SF galaxies. As expected, the difference is larger at small galactocentric distances and it become negligible in the outskirts. In the same way, as for the other parameters, we average the differences, and we define the significance as the distance of this mean in units of σ, where σ is the error in the average. We find strong differences in ΣSFR between the two samples, with a significance at about 8σ level (see Table 4.1).

TABLE 4.1: Median, mean, mean error and significance (expressed in units of σ) of the differences in the listed quantities between QRGs and SF galaxies.

	median	mean	error	$\#\sigma$
$<$E(B-V)$>_{R/R50}$	-0.05	-0.05	0.01	5.2
$<\Delta$log([O III]/Hα)$>_{[N II]/[O II]}$	-0.08	-0.1	0.01	10.7
$<\Delta$log([O III]/Hα)$>_{R/R50}$	-0.1	-0.1	0.02	5.2
$<\Delta$log([N II]/[O II])$>_{R/R50}$	0.05	0.04	0.02	1.8
$<\Delta$log(U)$>_{R/R50}$	-0.06	-0.06	0.01	5.5
$<\Delta$ Z$>_{R/R50}$	0.001	0.001	0.0007	1.4
$<\Delta$log(ΣSFR)$>_{R/R50}$	-0.4	-0.4	0.05	7.9

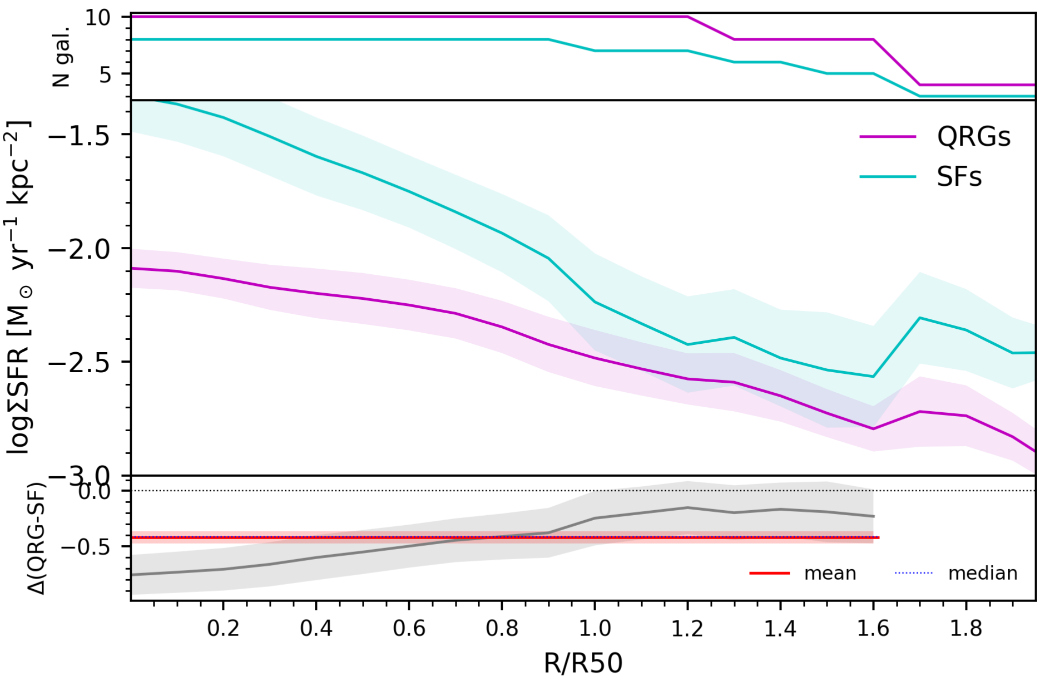

FIGURE 4.6: The SFR surface density (log ΣSFR) radial profile for QRG and SF samples. The layout of the figure is the same as in Figure 4.1.

Stochasticity on the initial mass function

Lee et al., 2009 showed that assuming a Salpeter IMF, a conservative level of SFR of 1.4×10^{-3} M$_\odot$ yr^{-1} (i.e. log SFR = -2.8) is required to sustain the ability of robustly populate the entire IMF. Otherwise, the massive end of the IMF could result in a certain amount depleted, with the number of the most massive stars regulated by stochasticity. Therefore, for values of log SFR ≤ -3 and fixed metallicity emerges a degeneracy between low [O III] flux due to incomplete sampling of the massive end of the IMF and the quenching of the star-formation. It is important to note that these kinds of studies regard the total SFR through the galaxy, especially dwarf ones. In our sample, the lowest total log SFR from SDSS data is -0.79 M$_\odot$ yr^{-1} (i.e. MaNGA 1-352114), however, with MaNGA we measure SFR on small scales (i.e. about a squared kpc per spaxel) and we can study the impact of stochasticity on the spaxels of our galaxies. In QRG 1-43012 (i.e. the galaxy analysed in previews sections) the vast majority of the spaxels show log ΣSFR < -2 (see Figure 4.6) but only a small amount of 8% have log ΣSFR < -3 $M_\odot$ yr^{-1} kpc^{-2}. We observe a similar situation in the other QRG galaxies (see Figure 4.6 and online materials).

Paalvast and Brinchmann, 2017 widely studied the impact of the stochastic sampling of the mass function on the production of lines requiring high energetic photons (i.e. [O III]) relative to that of the Balmer ones. All of their stochastic models predict a significant increase of the scatter of [O III]/Hβ ratios with decreasing of the SFR with respect to the typical BPT values, while at higher SFR the models well reproduce the BPT locus of the SDSS star-forming galaxies. For log SFR < -3, the lack of massive stars extends the scatter of [O III]/Hβ for solar metallicity from the BPT locus to values of log([O III]/Hβ) lower than -4 (i.e. ~ -4.5 using the [O III]/Hα ratio, alternatively), but also for log SFR -2 the scatter is considerably larger than that expected for a fully populated IMF. Moreover, the effect becomes more relevant with increasing metallicity.

In order to evaluate the impact of the stochasticity on our sample, we study galactic regions within our galaxies showing the lowest SFR values and super-solar gas phase metallicity. This combination of parameters maximises the effect in Paalvast and Brinchmann (2017) models. To this aim, we gathered in a bin all the spaxels with $-3 \leq$ log ΣSFR < -2.5 and super-solar metallicity (i.e. $0 \leq$[N II]/[O II] < 0.2) and we analyse the distribution of their [O III]/Hα. By definition, for effect of the stochasticity, we should obtain a wide distribution that covers the scatter due to the imperfect IMF sampling. We analyse an extreme conservative case in which all the spaxels showing an upper limit in [O III] (i.e. spaxels with S/N([O III])< 2, about 22% of the spaxels in the bin) are considered with [O III]/H$\alpha = -4.$, as if all of them are the lowest outcome of the stochasticity models of Paalvast and Brinchmann, 2017. In Figure 4.7 we show the [O III]/Hα distribution together with its cumulative curve. Even in this conservative situation, the distribution is mostly ($> 77\%$) comprised at log([O III]/Hα)values higher than about -1.5 with a small scatter. Therefore, we can exclude the stochasticity on the IMF as the prime process that leads to the low ionisation values observed in our galaxies. Moreover, in a galaxy with recent quenching is likely that low [O III]/Hα values are due both to stochasticity on the IMF sampling and to the death of the massive stars and the degeneracy between the two effects is less relevant.

4.3.7 The spatial distribution of the quenching

In this section, we focus on the QRG galaxies with the aim to analyse the spatial distribution and extension of their plausible quenching regions. None of the QRGs shows extended regions compatible with our quenching criteria, instead they have groups of small regions ($2 - 5$ members each), with extension between 2 and 4 kpc^2, that are smaller than the PSF of MaNGA (i.e. $2.5''$ of FWHM, or about 5 kpc^2 at these redshifts that corresponds to a percentage of the entire galaxies between $\sim 1\%$ and $\sim 8\%$). However, these groups of plausible quenching regions are always interconnected in more extended areas that are characterized by slightly higher ionisation

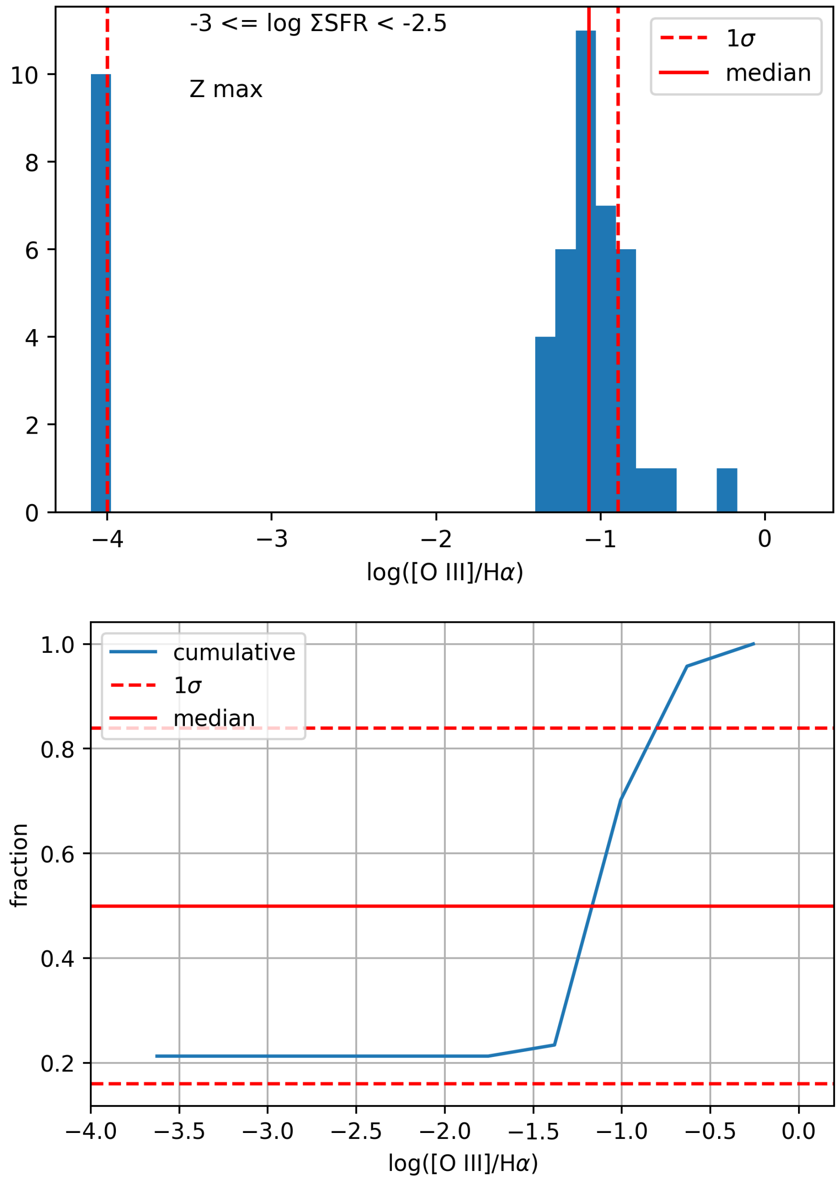

FIGURE 4.7: (*Top:*) the [O III]/Hα distribution for the spaxels with $-3 \leq \log\,\Sigma$SFR < -2.5 and $0 \leq$[N II]/[O II] < 0.2. The peak at [O III]/H$\alpha = -4$ represents the limit point that we choose for spaxels showing S/N([O III])< 2. (*Bottom:*) the cumulative curve of the distribution.

level and in the [O III]/Hα vs [N II]/[O II] diagram lie in the region between 1σ and $3 \times 1\sigma$ of the SDSS data (see Figure 4.1, and, for example the yellow area in Figure 4.4). Therefore, for effect of the PSF, it is likely that the actual size of the quenching regions is broader than that observed and it is mixed with the adjacent areas. In Figure 4.8 is shown the total size of the likely quenching regions (i.e. the sum of the size of these regions) as a function of their average distance (R/R50) from the galactic centre of the QRG galaxies. Only 2 out to 14 galaxies have significant quenching areas. They are QRG 1-38802, with an area of about 47 kpc^2 and QRG 1-91760, with an area of about 20 kpc^2. The other 10 galaxies have smaller sizes, between ~ 1.5

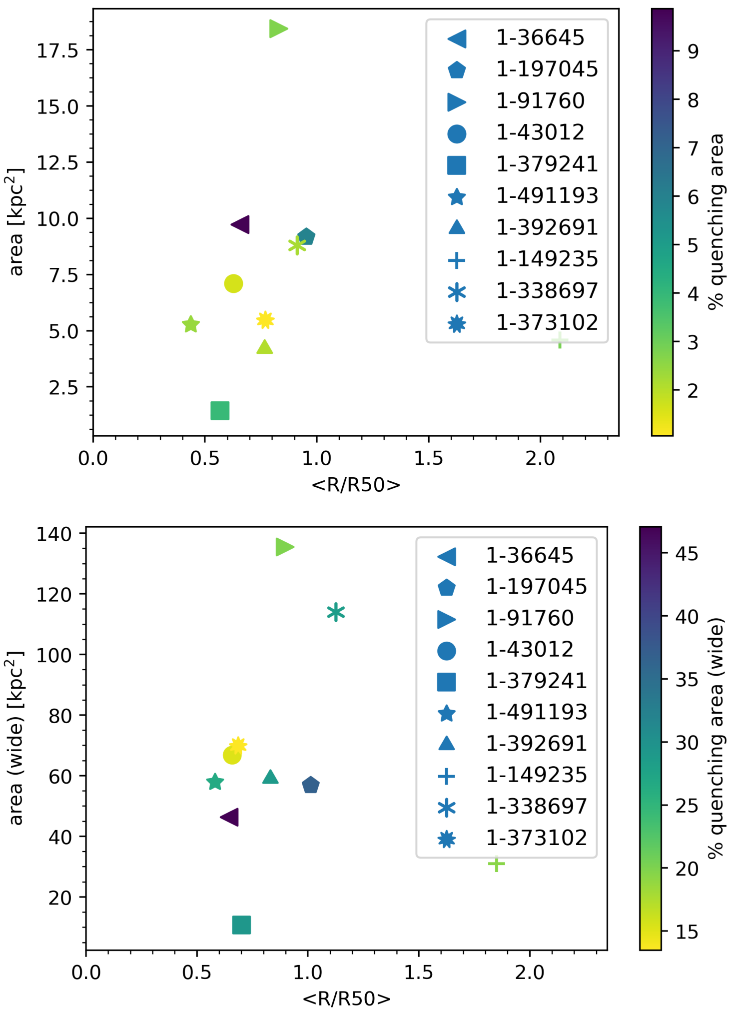

FIGURE 4.8: The total size of the likely quenching regions as a function of their average distance (R/R50) from the galactic centre of the QRG galaxies. In the *top* panel we consider only the regions that satisfied our quenching criteria, while in the *bottom* panel we consider the area comprising the plausible quenching regions and the less extreme adjacent areas. The symbols represent different galaxies, while the colour represents the percentage of spaxels in the area with respect to the whole spaxels of the galaxy.

and 10 kpc^2, or between $\sim 1.1\%$ and $\sim 10\%$ in percentage of the entire galaxies. The spaxels belonging to these regions represent a percentage between ~ 0.5 and ~ 10 of the total amount of spaxels in the galaxies. Moreover, all of them are located, on average, between 0.5 and 1 R50 and no one of the galaxies have quenching regions in their inner part (closer than 0.5 R50).

It is interesting to consider, as an upper limit of the total size of the quenching distribution in these galaxies, the broader areas obtained by summing the dimension of quenching regions together with that of their adjacent less extreme areas. The result is shown in Figure 4.8. In this case, 12 out to 14 galaxies have sizes larger than 30 kpc^2, with percentages between ~ 15 and 47% of all the spaxels. Even taking into account this broader area, the average distance from the centre of the galaxies remains between about 0.5 and 1.1 R50, confirming that no one of our galaxies have plausible quenching regions in the inner part.

4.4 Discussion

In previous sections, we discuss the general characteristics of the QRG and SF galaxies concerning metallicity, ionisation status, color excess E(B-V) and SFR. We recall that the two samples have the same stellar masses. central gas-phase metallicity (from the SDSS measures) and they are in the same redshift range.

We find that:

- despite the average gas-phase metallicity radial profile of QRG galaxies is slightly higher than that of SF ones at any radius, the difference between the two profiles is not significant. This result confirms that statistically, the two samples have a similar gas-phase metallicity.
- The average ionisation parameter log U radial profile of QRGs reaches a minimum between 0.5 and 0.8 effective radii, while that of the star-forming sample shows a slow increase of log U towards the outskirts of the galaxies. We confirm this difference at a high significance level.
- The average radial profile of the star formation rate surface density of QRGs is lower than that of the sample of SFs, at any radii, suggesting a sharp decline in their star-formation rate. The difference is larger approaching small radii. As expected, this trend is similar to that of the colour excess E(B-V). We confirm these differences between the QRGs and the SFs at a high significance level.

Additional details that can help to shed light on this behaviour may be obtained from the analysis of individual galaxies . In section 4.2, we find that the radial profiles of log U (i.e. ionisation level) and ΣSFR of QRG 1-43012 have a minimum in an annular region around the centre of the galaxy and a corresponding maximum in the radial profile of the gas-phase metallicity. Moreover, QRG 1-91760 shows a very similar pattern, with a vast annular region around the galactic centre with a low-ionisation level compatible with recent quenching. Other two QRGs (i.e. 1-491193 and 1-392691) show a similar pattern, though less clear than QRG 1-43012 and 1-91760. Besides, we also studied the distribution and size of the quenching regions in QRGs. They are located between 0.5 and 1.1 effective radii from the centre and occupy a total area between ~ 10 and ~ 140 kpc^2 (i.e. between $\sim 15\%$ and $\sim 45\%$ of the total galactic area[5]). It is interesting to note that none of these quenching regions is found in the inner part of our QRGs, despite the low level of the SFRs measured.

A strong star formation activity concentrated in an annular region of classical ring galaxies can explain the peak of the metallicity. An axial penetration of compact objects close to its centre (Lynds and Toomre, 1976; Higdon, 1995; Mapelli and Mayer,

[5]When we refer to the total galactic area, we mean the total area of all the spaxels covering a galaxy.

2012) may cause such rings of SFR around the centre of spiral galaxies. These kinds of encounters bring additional gravitational force that generates annular propagation of the ISM (e.g. Figures 5-6 in Lynds and Toomre, 1976) that is compressed triggering an intense star formation activity. A possible interpretation of the results regarding the QRGs, is that in these galaxies a quenching wave is presumably propagating from the inner region towards the outskirts because of the entire consumption of the available gas in intense episodes of star formation and we are witnessing the quenching phase on an annular region around the galactic centre. However, none of the galaxies in our sample that show a ring profile have evidence of recent interaction in their morphology (see Figure 4.3) and our results are more likely to be ascribed to the effect of a secular evolution of these galaxies (e.g. Kormendy and Kennicutt, 2004). Several simulations (e.g. Prendergast, 1983; Sellwood and Wilkinson, 1993; Regan and Teuben, 2003) show that in the inner regions of barred galaxies the gas flows toward the centre and the gas is often concentrated near the Lindblad resonance because of the dynamical interaction with the potential of the bar. There, the gas feeds intense episodes of star formation. However, we see neither bars nor rings of stars in the images of our galaxies. Nevertheless, even if the star formation is mostly in the ring, hardly ever it leads to form a ring of long-lived stars (e.g. Kormendy and Kennicutt, 2004). Moreover, near-infrared images show that bars are hidden in approximately two-thirds of spiral galaxies, despite their appearance in optical wavelengths (e.g. Block and Wainscoat, 1991; Eskridge et al., 2002; Block et al., 2001; Laurikainen and Salo, 2002; Kormendy and Kennicutt, 2004).

The star formation is supported by a continuous replenishment of fresh gas from the corona. Uninterrupted radial flows of gas towards the centre end up in the annular region for effect of the bar where the gas is converted into stars at high rates. The metallicity peak we observe in the annular regions around the galactic centre of QRGs is compatible with high SFR typically associated with rings. However, we find that there is a depletion of the Hα luminosity and a minimum of the parameter of ionisation.

If a mechanism could be able to interrupt the radial flow of gas toward the centre or the replenishment of gas from the hot halo, the star formation would continue by burning the remaining gas in the galaxy's reservoir. Tacconi et al. (2013) found that this reservoir can sustain the star formation for less than a Gyr before a typical star-forming galaxy runs out of gas. In these circumstances, at regimes of intense star formation, the region of the ring should be the first to consume the fuel and to interrupt the star formation. Therefore, it plausible that we are witnessing the very early phase of the quenching in our QRGs. Then, the quenching would propagate from the annular region, reaching soon the close inner part of the galaxies.

We stress that we do not expect to find galaxies in advanced quenching phase among the QRGs because they are not as extreme as the quenching candidates by Quai et al. (2018), which should provide decisive clues on the early phase of the quenching. Another crucial question that needs to be addressed is whether the regions that satisfied our quenching criterion are actual quenching regions in a permanent quenching phase which is propagating throughout the centre and the outskirts of the galaxy or if they are the marks of a minimum in the star formation history of the galaxy. In a future perspective, maps of the distribution of the cold gas would help to disentangle between the two possibilities.

4.5 Summary

In this Chapter, we present a spatially resolved study of 10 MaNGA galaxies (extracted from SDSS-IV MaNGA DR14, Bundy et al., 2015; Abolfathi et al., 2018) which show regions compatible with a recent quenching of the star formation (QRGs). These quenching regions are those satisfying the criteria devised in Quai et al. (2018), that we presented in the previous sections. The aim of this work is to derive spatial information about the quenching process within galaxies.

The detailed analysis of the QRGs reveals that in 4 of them the quenching regions are located in an ring around the centre, in correspondence of a minimum in the ionisation parameter log U radial profile. This behaviour can be ascribed to the effect of a secular evolution of these galaxies (e.g. Kormendy and Kennicutt, 2004), in which we observe the quenching in an annular region in which a past intense star formation activity was propagating radially from the inner part towards the outskirts of the galaxies.

We compare the properties of these 11 QRGs with those of a control sample of 10 MaNGA star-forming galaxies. The quenching regions in QRGs are located between 0.5 and 1.1 effective radii from the centre, suggesting that in these galaxies a quenching wave is presumably propagating from the central region towards the outskirts and we see the quenching phase on an annular region. This result is supported by their average radial profile of the ionisation parameter, that reaches a minimum at the same radii, while the average radial profile of the star-forming sample shows an almost flat trend. Moreover, the radial profile of the gas-phase metallicity of QRGs suggests that they have a higher metallicity than the star-forming ones at any radius, as expected from more evolved systems. Finally, the average radial profile of the star formation rate surface density of our QRGs is lower than that of the SFs, at any radii, suggesting a drop in their star-formation rate. All these difference between the QRGs and the SFs are confirmed at a high significance level.

APPENDIX

4.A Other QRG targets

In this section we collect the main plots (i.e. emission line maps, [O III]/Hα vs [N II]/[O II] diagram, BPT diagram and the radial profiles of the main characteristics) of each galaxy belonging to the QRG sub-sample.

4.B Other SF targets

In this section we collect the main plots (i.e. emission line maps, [O III]/Hα vs [N II]/[O II] diagram, BPT diagram and the radial profiles of the main characteristics) of each galaxy belonging to the SF sub-sample.

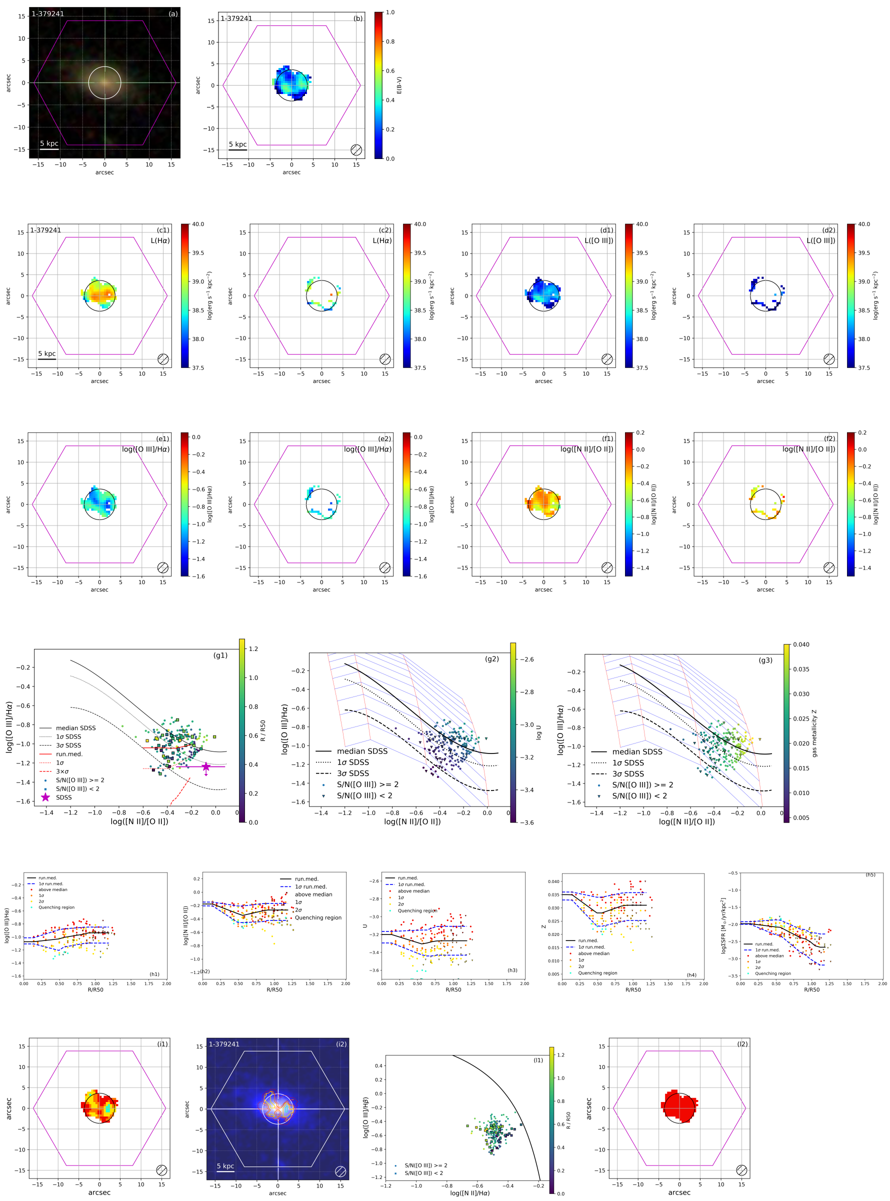

FIGURE 4.A.1: QRG 1-379241. (a) the g-r-i image composite from SDSS. (b) the E(B-V) maps. (c1) the luminosity surface density maps of dust-corrected Hα with S/N([O III]) $\geq$ 2 and (c2) with upper limit in [O III] (S/N([O III]) $<$ 2). (d1) the luminosity surface density maps of dust-corrected [O III] with S/N([O III]) $\geq$ 2 and (d2) with upper limit in [O III] (S/N([O III]) $<$ 2). (e1) the dust-corrected [O III]/Hα map of spaxels with S/N([O III]) $\geq$ 2 and (e2) with upper limit in [O III] (S/N([O III]) $<$ 2). (f1) the dust-corrected [N II]/[O II] map of spaxels with S/N([O III]) $\geq$ 2 and (f2) with upper limit in [O III] (S/N([O III]) $<$ 2). The panels (g1), (g2) and (g3) show the [O III]/Hα vs [N II]/[O II] diagram with spaxels coloured according to the distance R/R50, ionisation level log U and gas-phase metallicity Z, respectively. The panels (h1), (h2), (h3), (h4) and (h5) show radial profiles of [O III]/Hα, [N II]/[O II], log U, Z and star-formation rate surface density ΣSFR, respectively and the colour code is the same as in **??**. (i1) map of the resolved [O III]/Hα vs [N II]/[O II] diagram and (i2) contours of the resolved [O III]/Hα vs [N II]/[O II] diagram superimposed to the G image as in Figure 4.4 (l1) the resolved BPT diagram with spaxels coloured according to R/R50 and (l2) the resolved BPT map, as in Figure 4.5. The magenta hexagons overlapped in the maps represent the MaNGA IFU bundles, while the black circles represent the R50. The 2.5$''$ circle in the bottom-right corner of the maps represent the PSF (FWHM) of MaNGA datacubes.

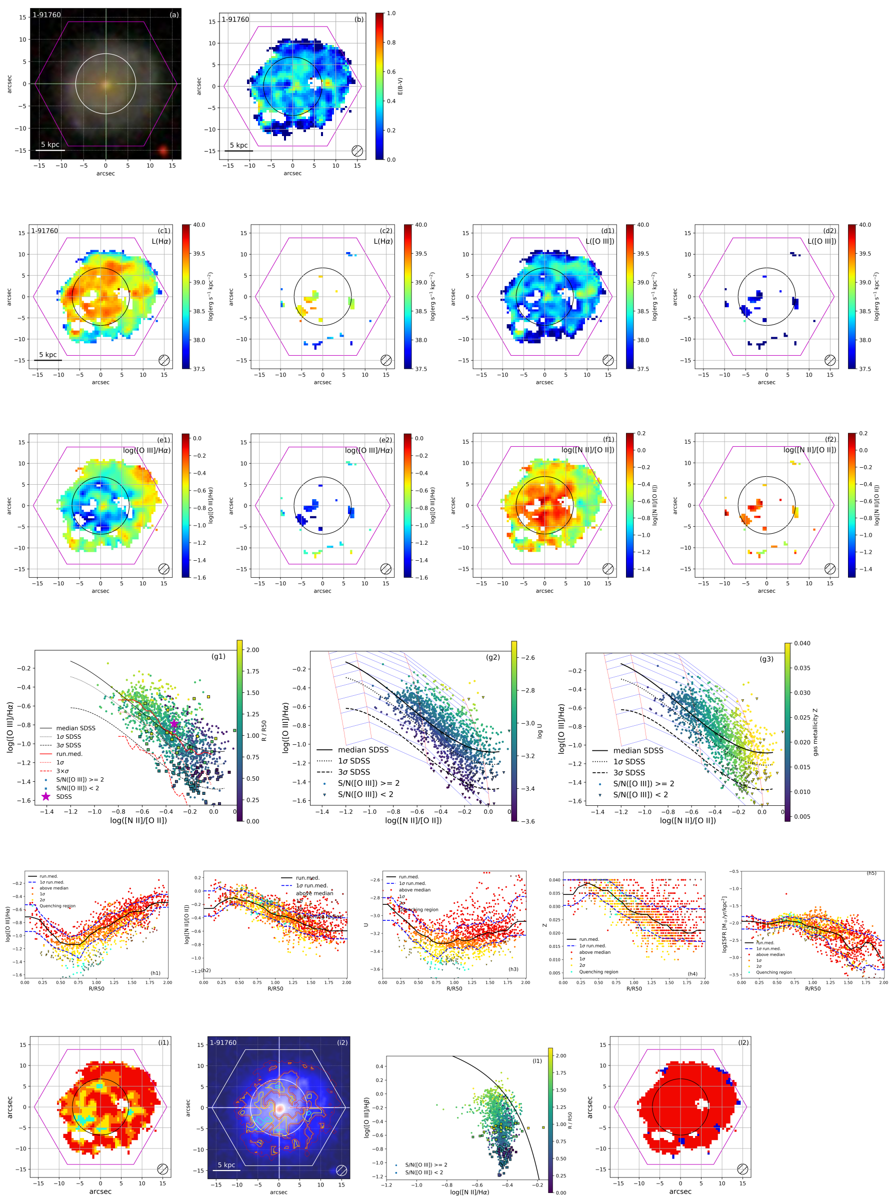

FIGURE 4.A.2: QRG 1-91760. See Figure 4.A.1 for panels description.

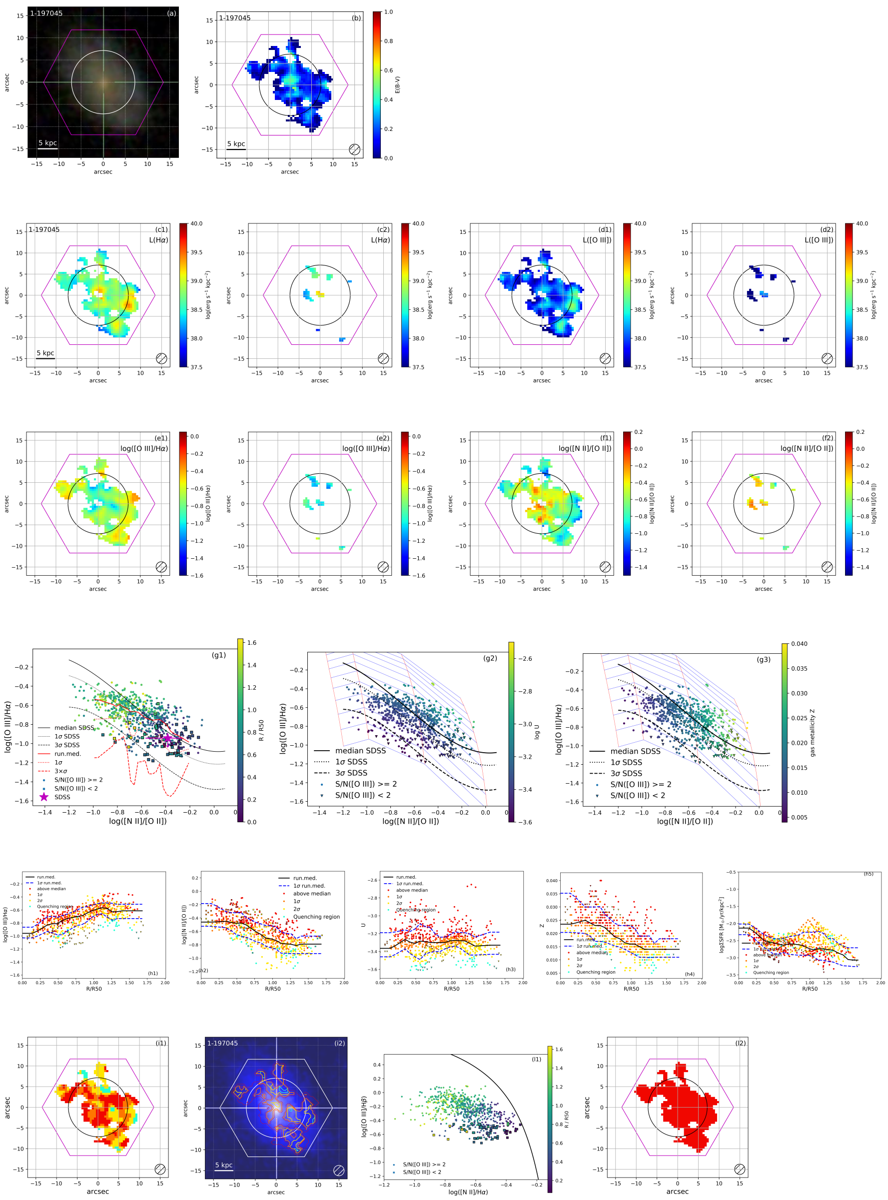

FIGURE 4.A.3: QRG 1-197045. See Figure 4.A.1 for panels description.

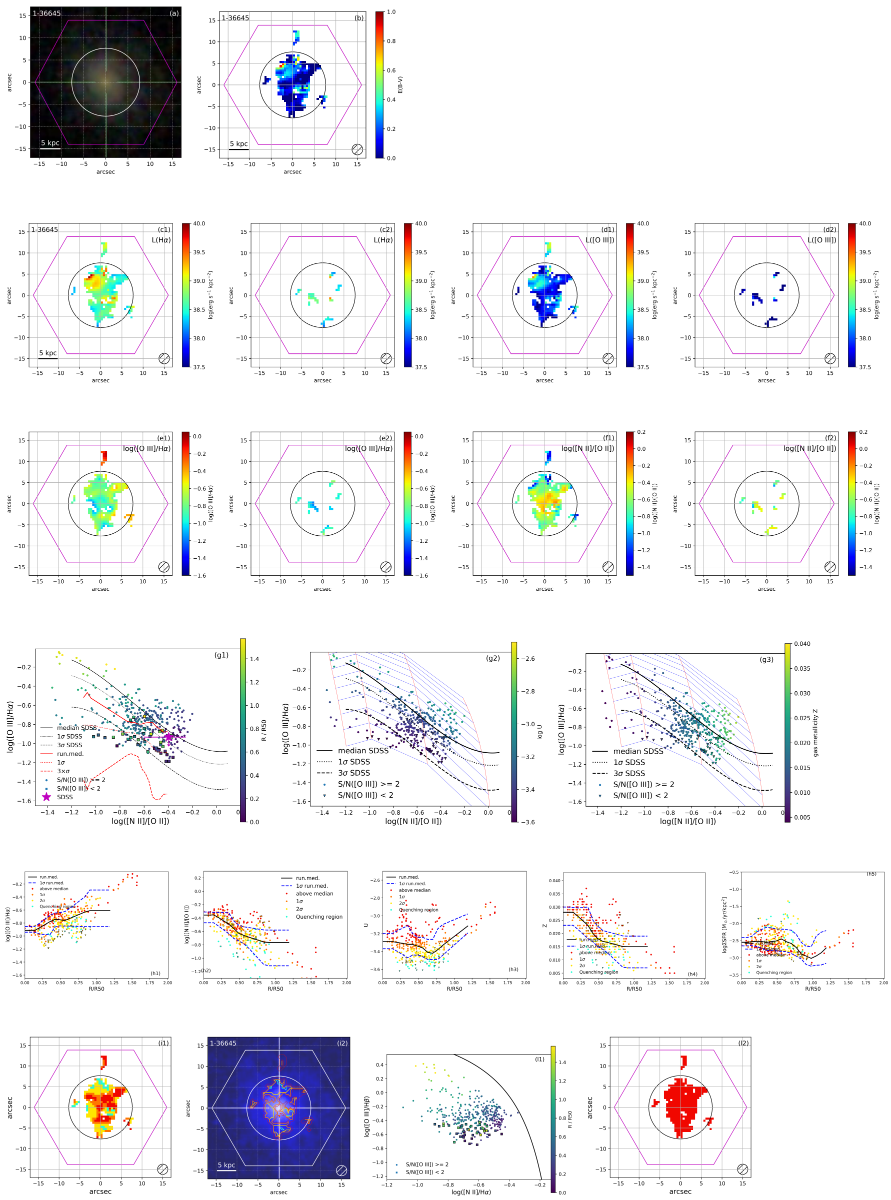

FIGURE 4.A.4: QRG 1-36645. See Figure 4.A.1 for panels description.

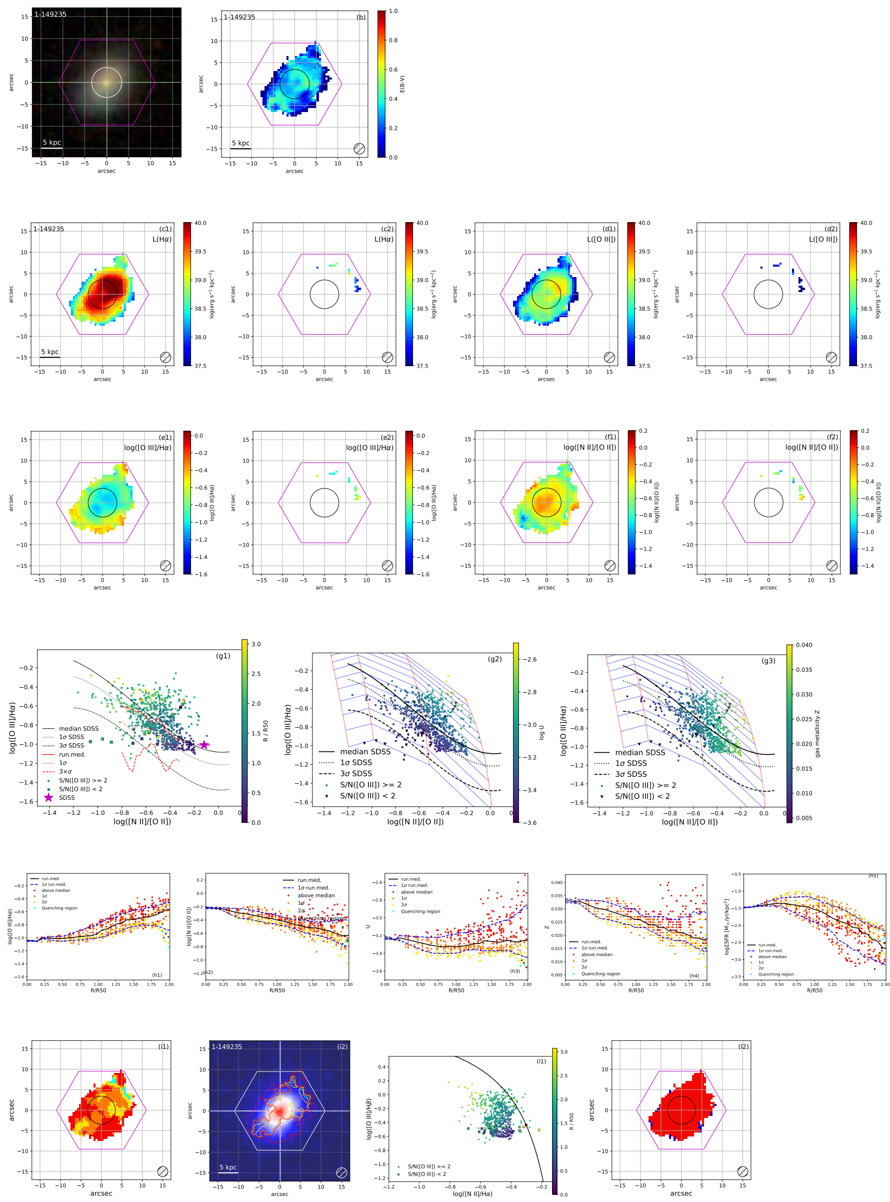

FIGURE 4.A.5: QRG 1-149235. See Figure 4.A.1 for panels description.

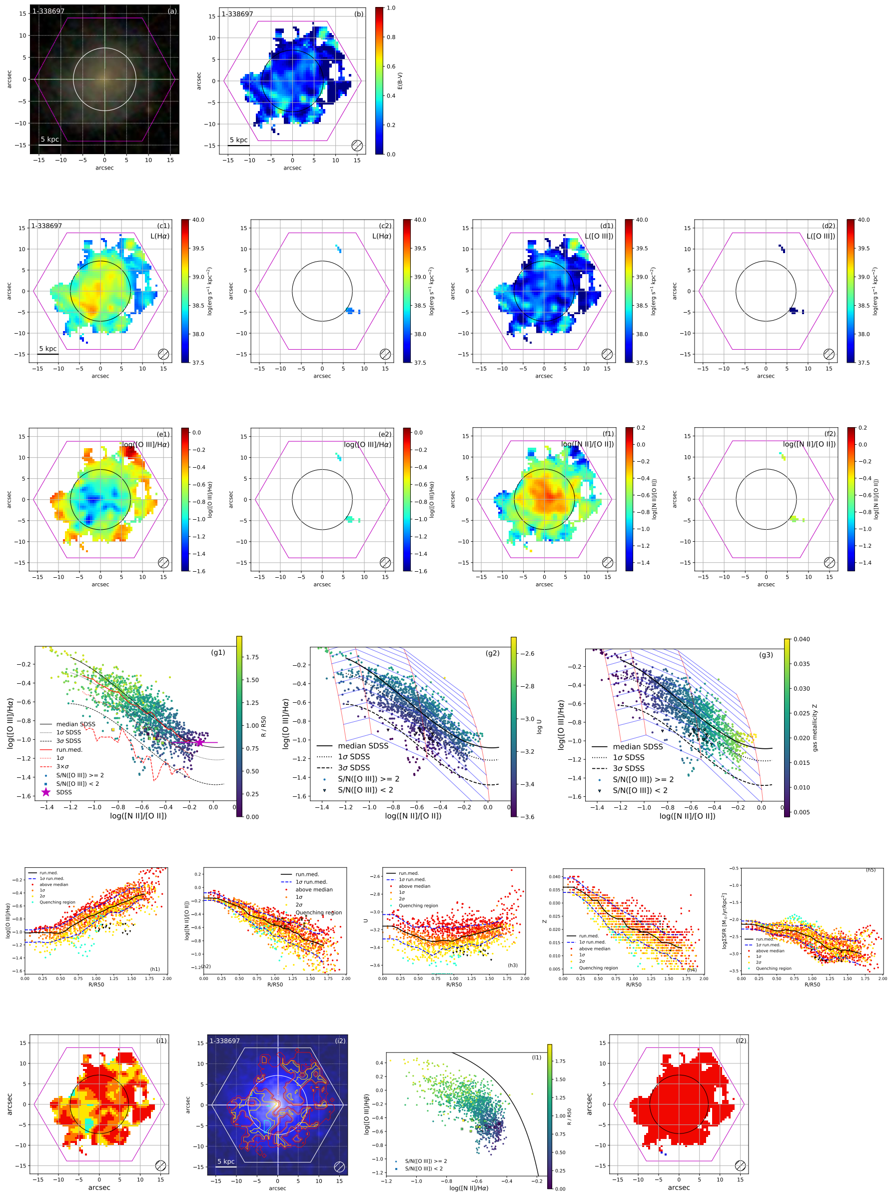

FIGURE 4.A.6: QRG 1-338697.

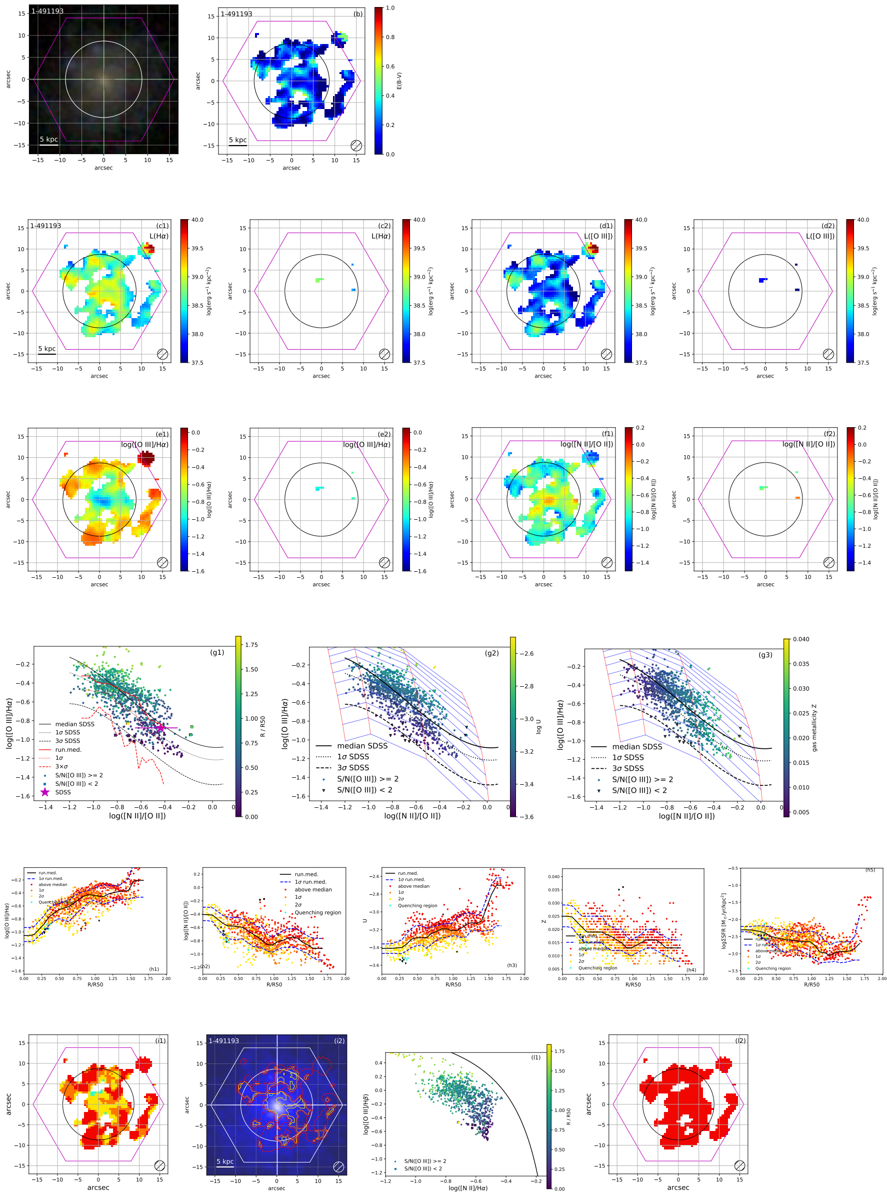

FIGURE 4.A.7: QRG 1-491193. See Figure 4.A.1 for panels description.

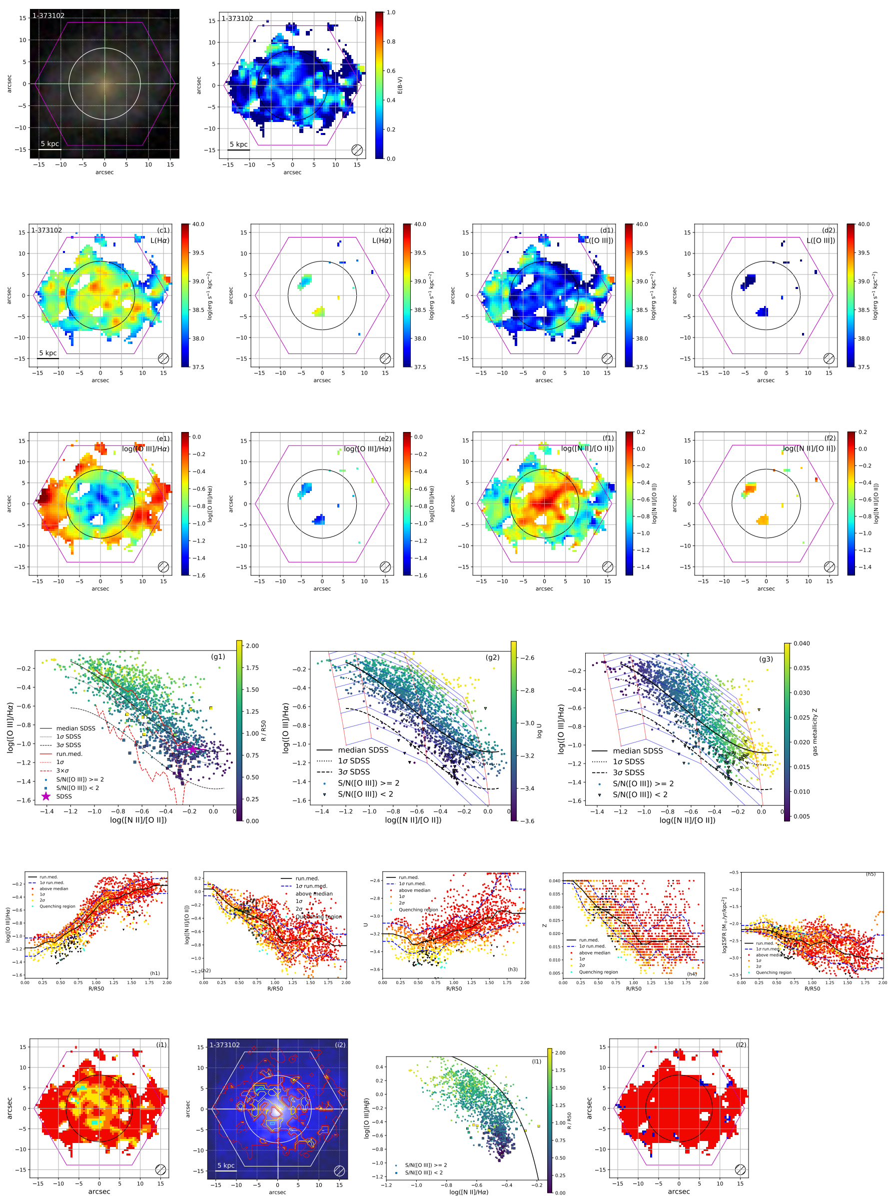

FIGURE 4.A.8: QRG 1-373102. See Figure 4.A.1 for panels description.

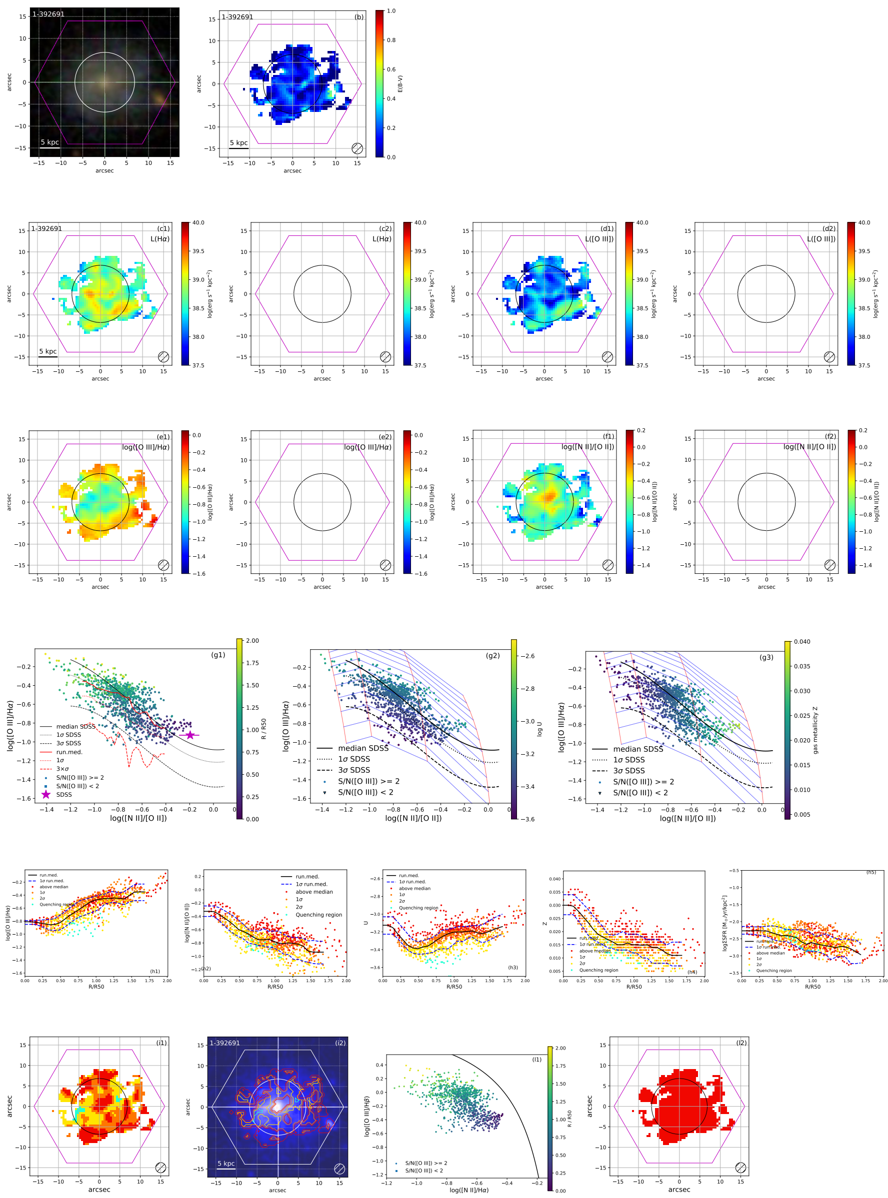

FIGURE 4.A.9: QRG 1-392691. See Figure 4.A.1 for panels description.

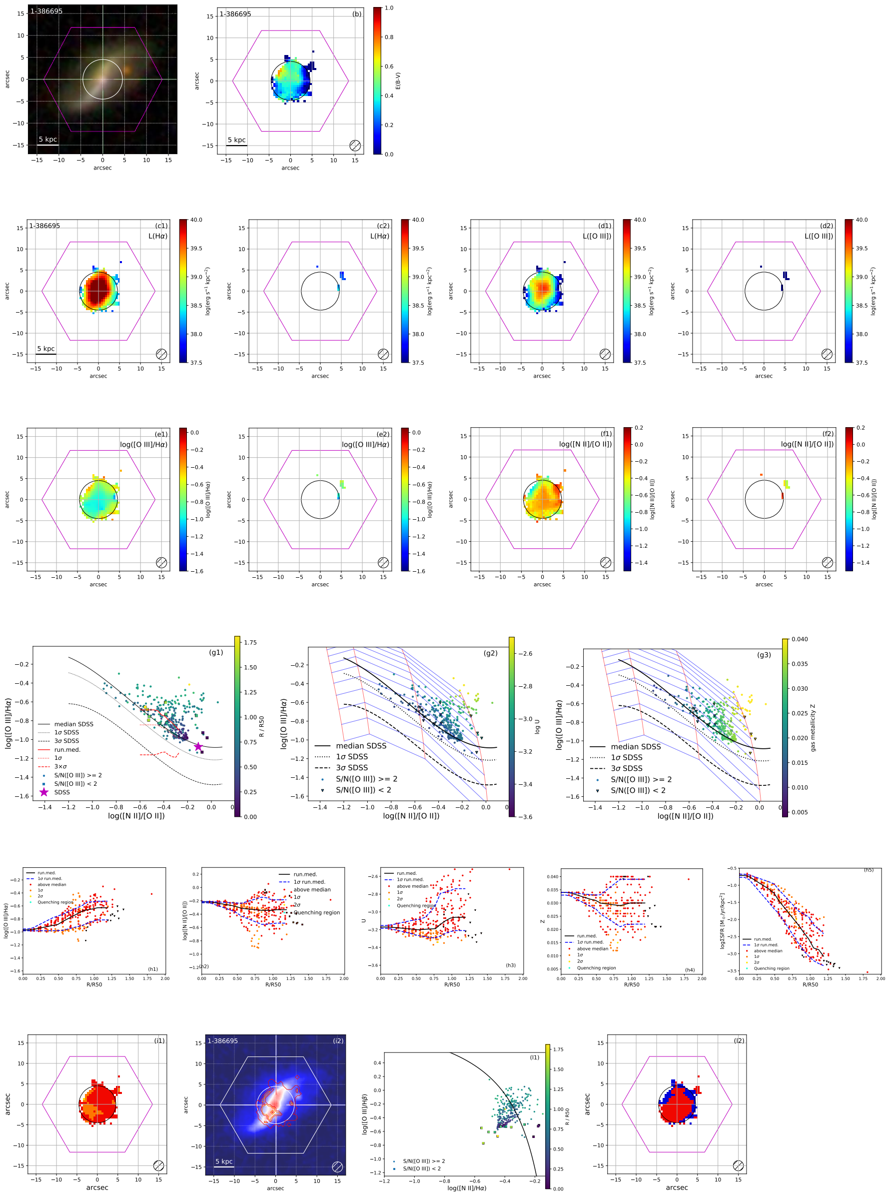

FIGURE 4.B.1: SF 1-386695. See Figure 4.A.1 for panels description.

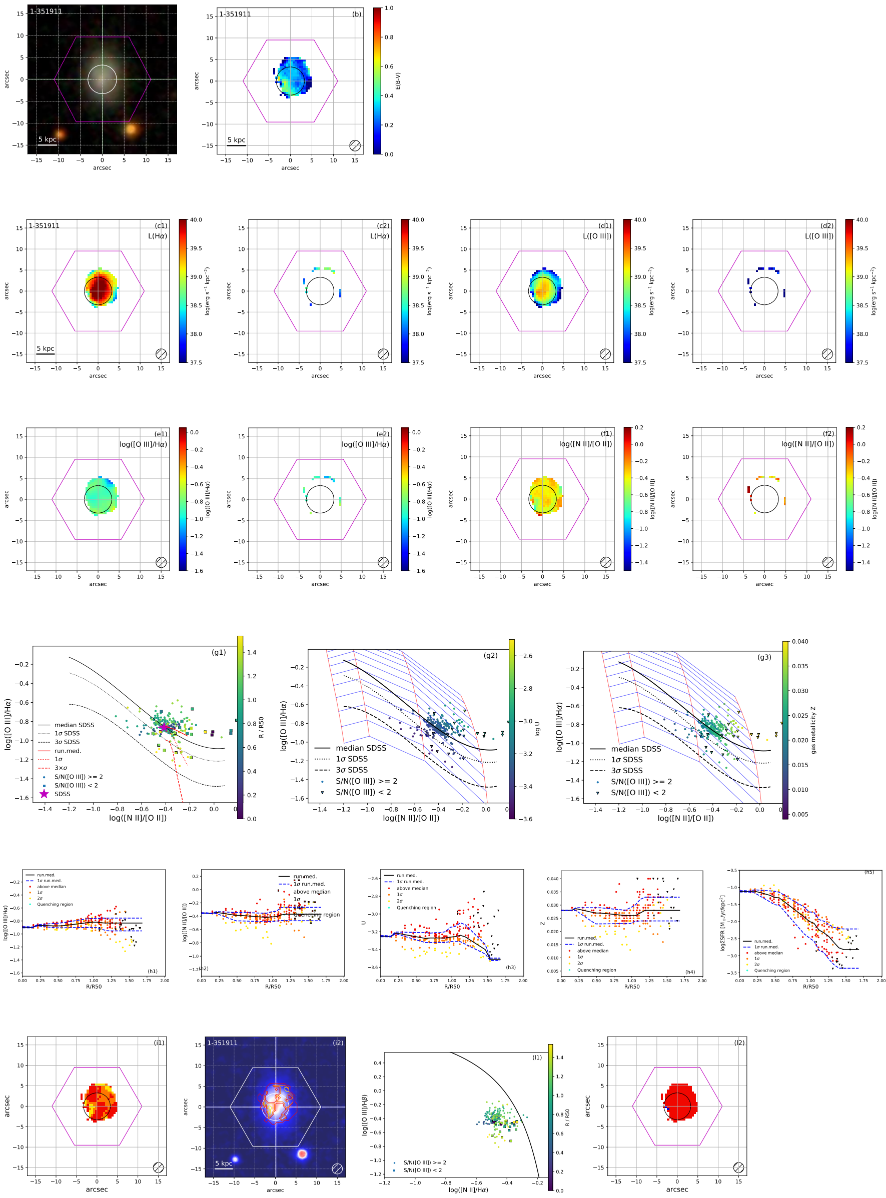

FIGURE 4.B.2: SF 1-351911. See Figure 4.A.1 for panels description.

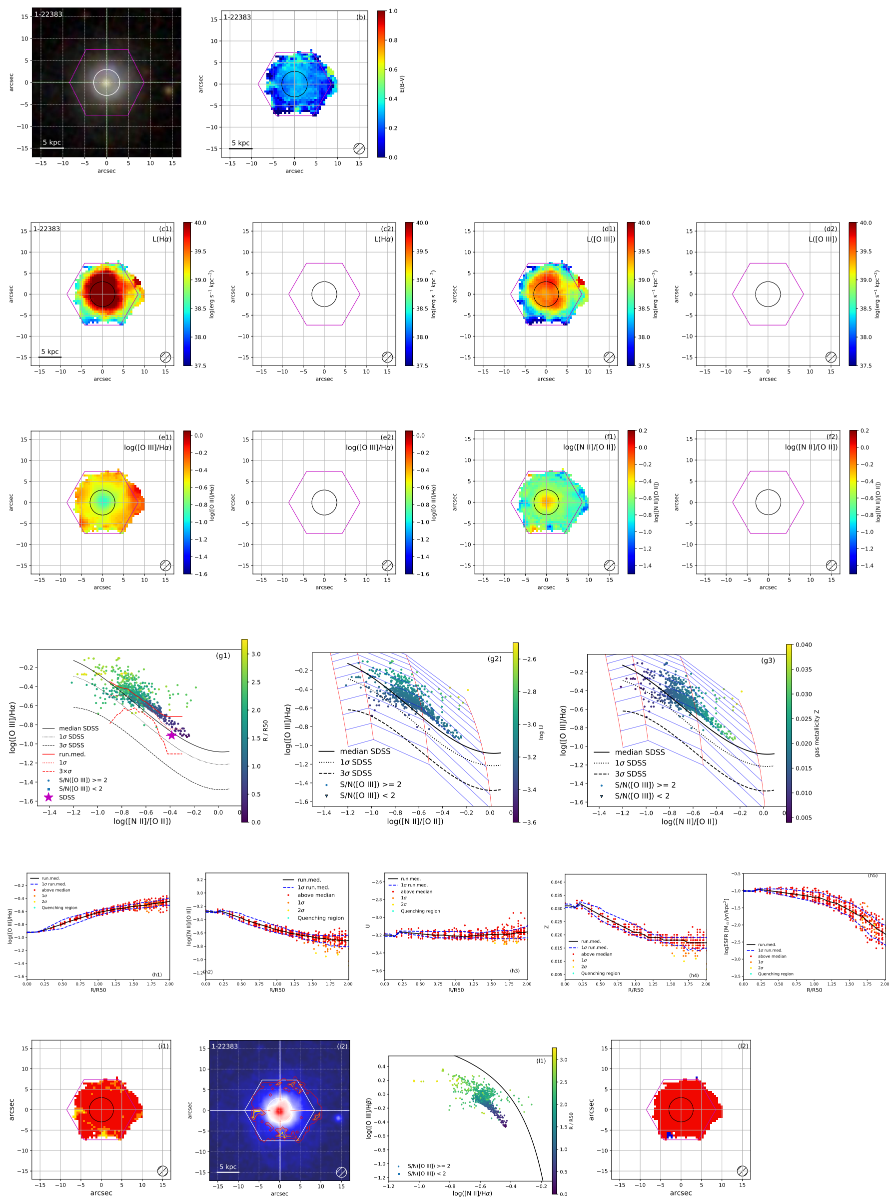

FIGURE 4.B.3: SF 1-22383. See Figure 4.A.1 for panels description.

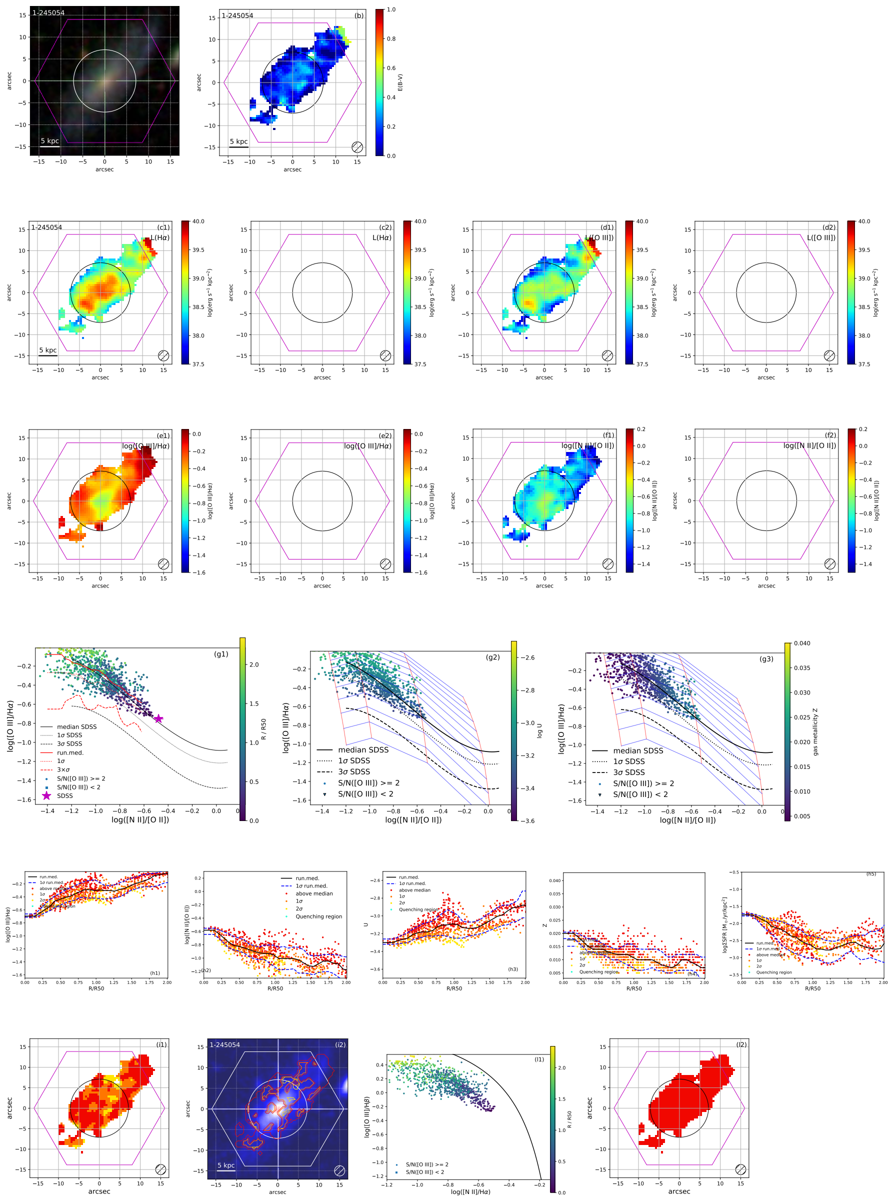

FIGURE 4.B.4: SF 1-245054. See Figure 4.A.1 for panels description.

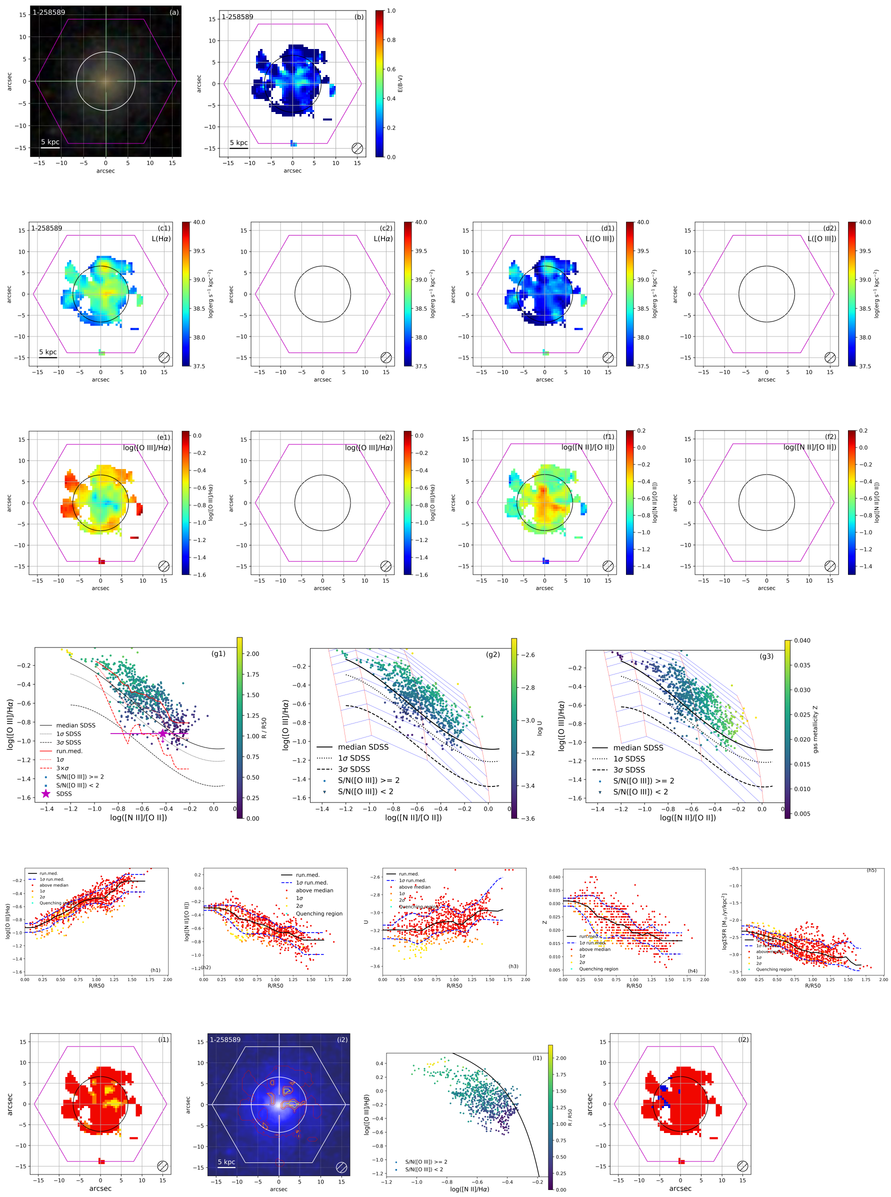

FIGURE 4.B.5: SF 1-258589. See Figure 4.A.1 for panels description.

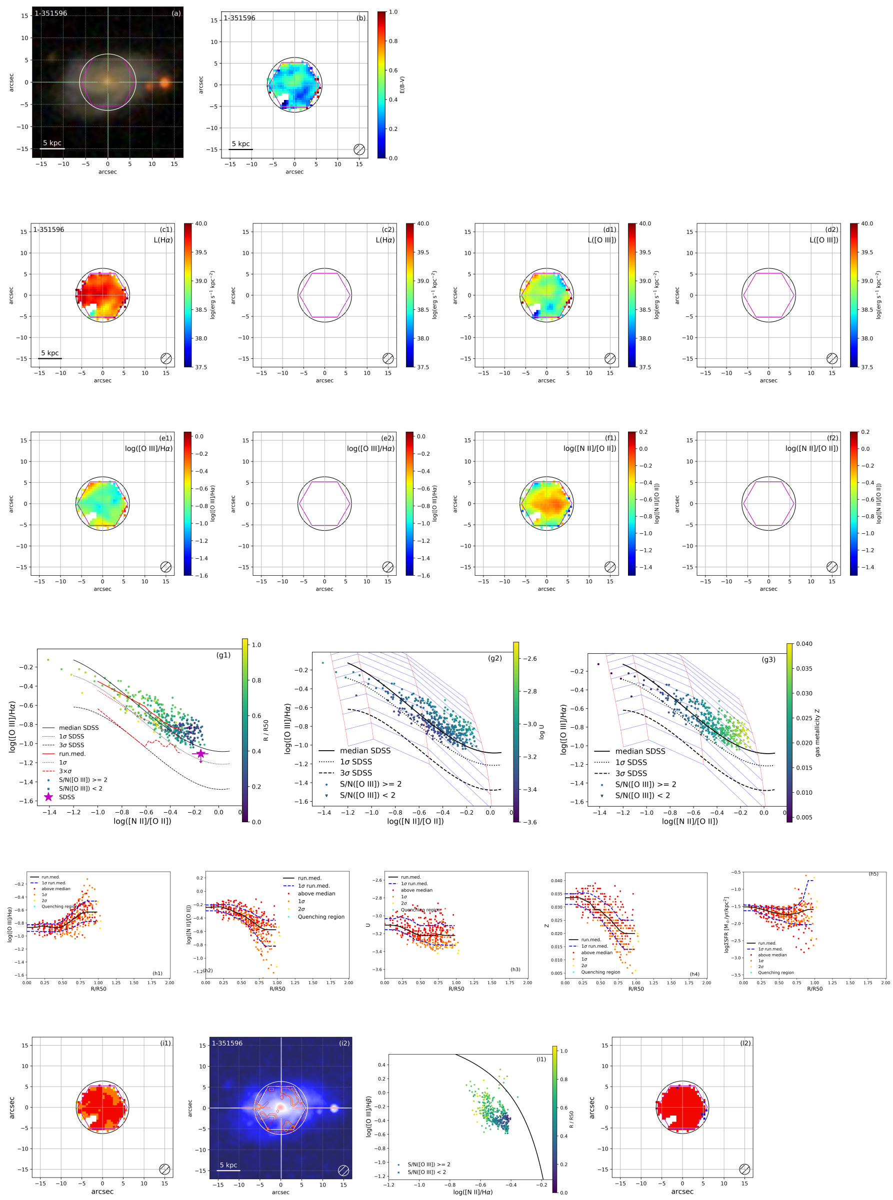

FIGURE 4.B.6: SF 1-351596. See Figure 4.A.1 for panels description.

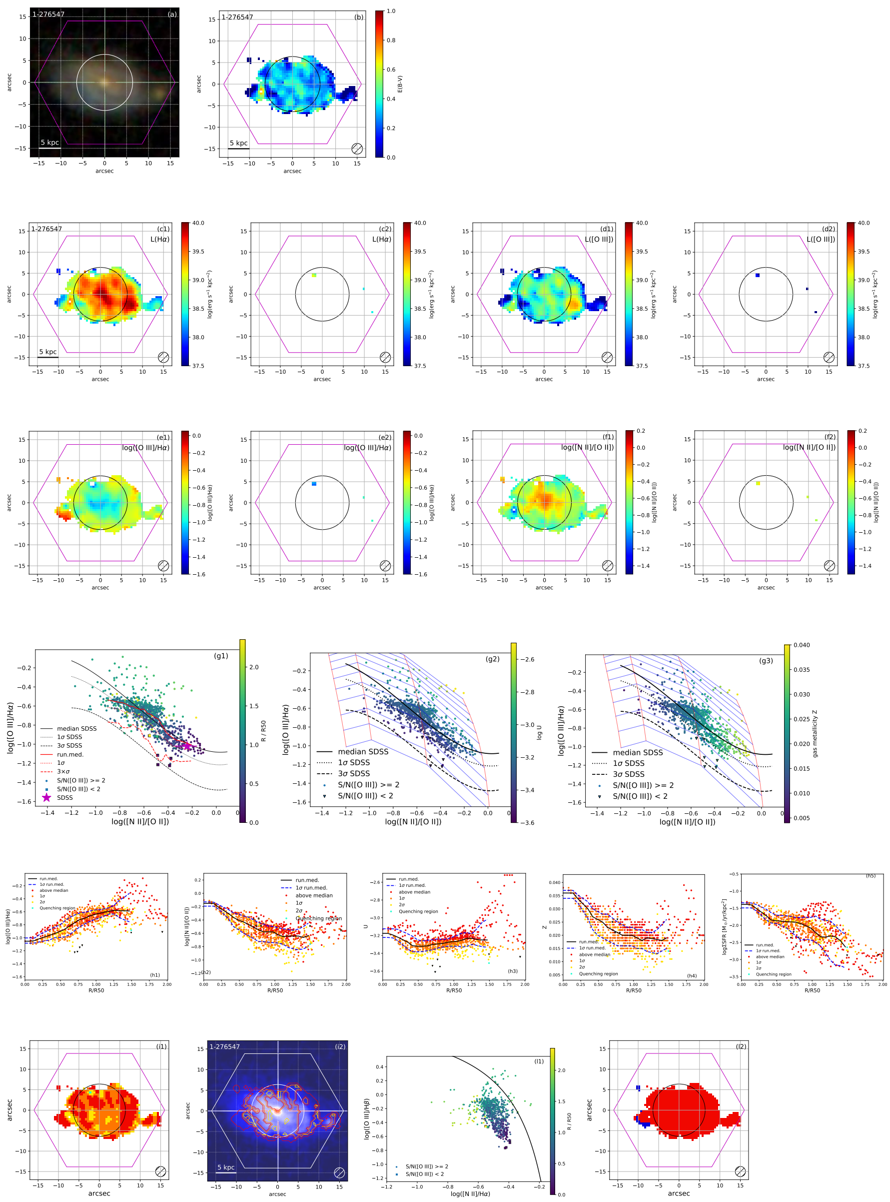

FIGURE 4.B.7: QRG 1-276547. See Figure 4.A.1 for panels description.

5. THE EVOLUTION OF LOW MASS Hδ-STRONG GALAXIES IN THE MUSE-HUDF

In this chapter, we present preliminary results regarding the analysis of a population of post-starburst galaxies, which are systems in an advanced phase of quenching due to a sharp interruption of the star formation occurred $\lesssim 1$ Gyr ago. This work attempts to link the evolution of these galaxies with the properties of local early-type galaxies. Post-starburst galaxies are identifiable by strong Balmer absorption lines in their optical spectra. The equivalent width (EW) of absorption in Hδ is usually chosen to estimate stellar ages because it is less contaminated by nebular emission lines than Hα and Hβ. The EW(Hδ) strongly increases during a few 10^8 yr after a sharp quenching, reaching a maximum value of about 10Å when A-type stars dominate the population (e.g. Couch and Sharples, 1987), and later, it gradually decreases continuously. This trend implies that such values of EW(Hδ) can be measured only in galaxies whose star formation ceased suddenly between 300 and $\lesssim 1$ Gyr ago.

Classical post-starburst systems are the so-called K+A galaxies. They have spectra compatible with passive evolution (no sign of emission lines), and they have disturbed morphology typically associated merging (e.g. Quintero et al., 2004; Poggianti et al., 2004; Balogh et al., 2011; Muzzin et al., 2012; Mok et al., 2013; Wu et al., 2014; Wild et al., 2016). However, there exists a population of galaxies that differs from K+A because of the presence of emission lines in their spectra (i.e. usually strong [O II]λ3726-29 emissions) and are called Hδ-strong galaxies (e.g. Le Borgne et al., 2006; Wild et al., 2009). The emission lines in Hδ-strong galaxies are often linked to narrow-line AGNs or LINERs emissions (Yan et al., 2006; Wild et al., 2007; Wild et al., 2009; Wu et al., 2014; Lemaux et al., 2017).

The majority of these works have focused on massive galaxies. The availability of the MUSE integral field unit spectrograph on the Very Large Telescope (VLT) has opened up the possibility to assemble significant samples of galaxies without a preceding selection based on broad-band photometry. This improvement has provided a few key gains relative to multi-slit or multi-fibre spectroscopic survey: the ability to obtain spectra of galaxies with a much higher spatial density, a nearly star formation rate limited sample of galaxies and hence also relatively low mass galaxies, and, for the brighter galaxies, resolved spectroscopy. In this chapter, we will exploit these advances by using very deep MUSE spectra (>10 hours of exposure time typically) to study low mass Hδ-strong galaxies at $\sim 0.3 <$z< 1.24.

5.1 Data

The Multi Unit Spectroscopic Explorer (MUSE Bacon et al., 2010), is an integral field unit (IFU) on the ESO Very Large Telescope (VLT) Yepun (UT4). In Wide Field Mode it has a large FoV ($1' \times 1'$), a wide wavelength coverage (4650–9300 Å) and a relatively high spectral resolution (R $\sim$ 3000). The MUSE instrument was initially designed for deep spectroscopic observations; however it can be used to observe a variety of objects, including H II regions, globular clusters, local galaxies and quasars. Thanks to an angular resolution of $0.3-0.4$ arcsec and a spatial sampling of 0.2×0.2 arcsec^2 , MUSE can observe dense fields without making any target pre-selection.

For this study, we analyse spectra of galaxies extracted from the MUSE Hubble Ultra Deep (HUDF) survey (Bacon et al., 2017), that consists of a mosaic of nine pointings ($\approx 3' \times 3'$) in the original Hubble Ultra Deep Field (HUDF) region with a long integration time of approximately ten hours.

One major success of MUSE is that it allows blind identifications of previously unknown sources by searching for emission lines directly in the data cube (Bacon et al., 2015). This provided about an order of magnitude improvement in spectroscopically confirmed redshifts in the HUDF, with 1338 high-quality redshifts obtained from MUSE data in this sky region (see Inami et al., 2017).

Spectra in this survey are extracted using a mask region that is built from the MUSE white light image. Then, a simple unweighted sum of the flux in the mask region is used as the spectrum of each galaxy. The spectral features of the galaxies are measured using the software platefit (Tremonti et al., 2004), while the stellar masses are obtained from spectral energy distribution (SED) fitting using the FAST (Fitting and Assessment of Synthetic Templates) algorithm (Kriek et al., 2009) with a Bruzual and Charlot (2003) library and the Chabrier (2003) IMF (see Paalvast et al., 2018, for details). The Lick index $H\delta_A$ is well suited to probe stellar populations dominated by A stars in the optical domain (Worthey and Ottaviani, 1997). We measure $H\delta_A$ on the stellar continuum obtained subtracting the strong nebular emission lines (i.e. [O II] $\lambda3727$, Hδ, Hβ, [O III] $\lambda5007$, Hα, [N II] $\lambda6584$) from the MUSE spectra. The uncertainties on $H\delta_A$ are computed following Cardiel et al. (1998).

In this paper, we start the analysis from the 403 galaxies with secure redshift (i.e. parameter zconf > 1) in the range $0.288 \leq z \leq 1.235$, that represents the maximum interval over which it is possible to measure $H\delta_A$ and both D_n4000 and [O II] emission in MUSE data. In the following, we exclude 91 objects (that leaves 312 galaxies): (i) 9 galaxies without measures of mass or with dlog$(M/M_\odot) \geq 1$ dex, where dlog$(M/M_\odot)$ is the uncertainty 16^{th}-84^{th} percentile of the galaxy mass; (ii) 18 galaxies at redshift $0.826 \leq z \leq 0.883$, and 64 galaxies at redshift $1.073 \leq z \leq 1.145$, whose $H\delta_A$ falls in the spectral region of two strong sky lines (i.e. $\lambda\lambda7605-7615$Å and $\lambda\lambda8625-8670$Å). Moreover, since the definition of the Lick index might be a source of systematic errors, we define a criterion of reliability of the measures of $H\delta_A$ based on the averaged signal-to-noise (S/N) of the stellar continuum in the spectral regions of the rest-frame blue and red band-passes of $H\delta_A$ (i.e. $4042.85-4081.00$Å and $4129.75-4165.25$Å, respectively). Therefore, we further restrict the analysis to the resulting 119 galaxies (i.e. $\sim 38\%$) which have S/N(Hδ_A) ≥ 3 in the stellar continuum, and that form our **hδ sample**. We want to highlight that in the selection criteria of the Hδ sample we do not include a limit that defines a Hδ-strong population. This choice gives us the possibility to study the properties of galaxies showing different values of Hδ. We divide the Hδ sample into three redshift bins, covering

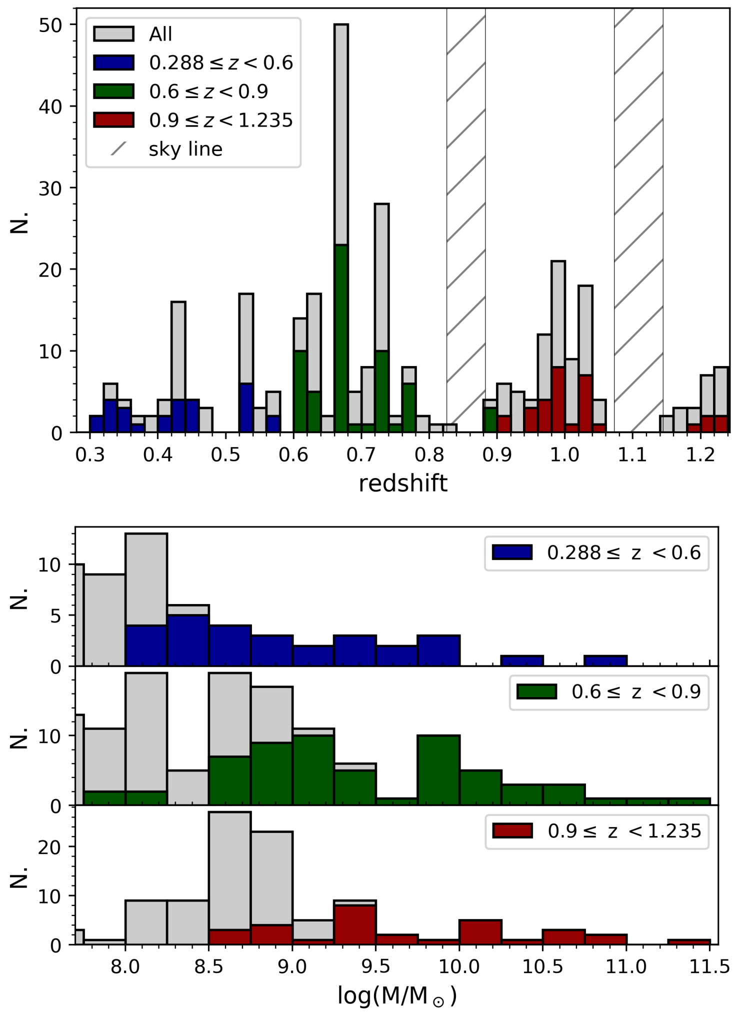

FIGURE 5.1: *Top*: the distribution of redshift of the 312 galaxies in the sample (in grey). Different colours represent the distribution of the 119 galaxies in the Hδ sample (i.e. S/N of the continuum in the spectral region of Hδ larger than 3) for the three redshift bins: blue for galaxies between $0.288 \leq$z< 0.6, green for galaxies between $0.6 \leq$z< 0.9 and red for them between $0.9 \leq$z< 1.235. The hatched stripes show the intervals of redshift in which the Hδ_A falls in the spectral regions of two strong sky lines. *Bottom*: distribution of stellar masses for the three redshift bins.

dz~ 0.3 each (i.e. $0.288 \leq z < 0.6$, $0.6 \leq z < 0.9$ and $0.9 \leq z < 1.235$). In Figure 5.1 we show the redshift and mass distributions of the sample, and we list them in Table 5.1. The redshift distribution is not homogeneous, and it shows spikes, such as the one at z~ 0.66 in the intermediate redshift bin, that contains 22 objects.

Figure 5.2 shows an example of a typical spectrum of galaxies in our Hδ sample.

TABLE 5.1: Redshift and mass distributions of the galaxies in our catalogue and the defined Hδ sample. The distributions are expressed in terms of percentiles (16th, median, 84th). The first row lists the global distributions.

Sample	z bin	N obj.	z 16-50-84	$\log(M/M_\odot)$ 16-50-84
All	$0.288 \leq z < 1.235$	312	0.531-0.701-1.016	7.7-8.6-9.4
Hδ sample	$0.288 \leq z < 1.235$	119	0.458-0.669-0.993	8.6-9.3-10.2
	$0.288 \leq z < 0.6$	28	0.337-0.429-0.524	8.3-8.8-9.7
	$0.6 \leq z < 0.9$	60	0.620-0.667-0.746	8.7-9.2-10.2
	$0.9 \leq z < 1.235$	31	0.959-0.998-1.070	9.0-9.5-10.6

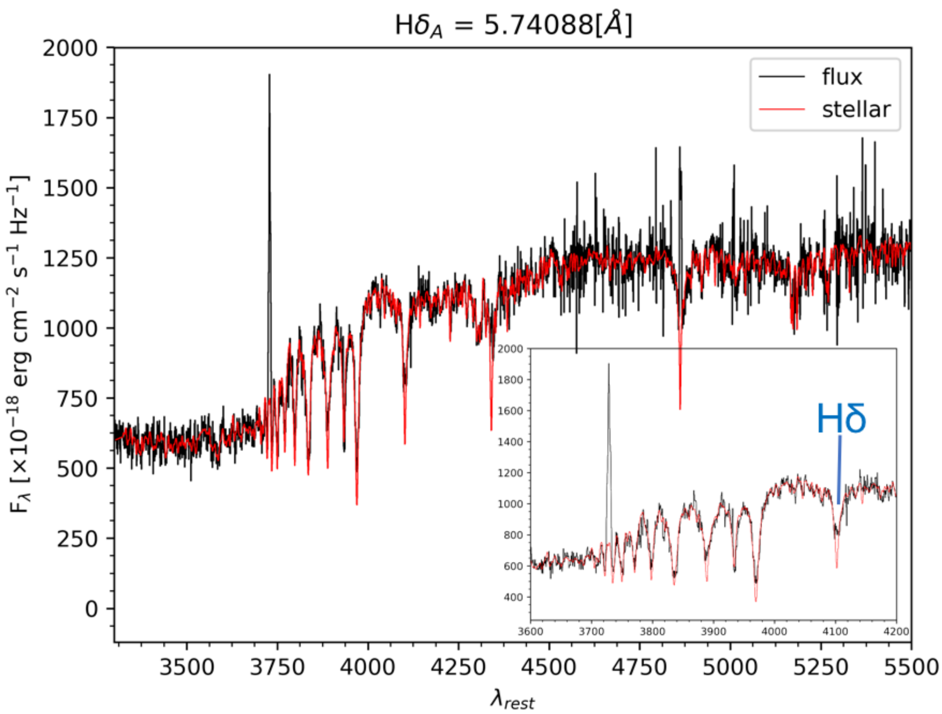

FIGURE 5.2: The rest-frame spectrum of MUSE-HUDF 871 and a zoom of the wavelength region between [O II] and Hδ.

5.2 The stellar mass function of Hδ-strong galaxies

For the stellar mass function (SMF) estimates, we use the V_{max} (Schmidt, 1968) technique. In this section, we describe the derivation of V_{max} for galaxies in our sample.

The SMF is defined as the number of Hδ-strong galaxies per unit volume per unit stellar mass, and has the following general form:

$$\Phi[\log(M/M_{\odot})] = \frac{1}{\Delta \log M} \cdot \frac{4\pi}{\Omega} \sum_{i} \frac{1}{V_{i,\max}}, \tag{5.1}$$

where, V_{max} represents the maximum volume out to which the i-th Hδ-strong would be visible to and still be part of the survey, $\Delta \log M$ is the stellar mass bin width and Ω represents the solid angle of the survey.

5.2.1 The V_{max} determination

The MUSE-HDUF survey is obtained from a blind search of star-forming galaxies. That makes it difficult to estimate a reasonable selection function. For each i-th Hδ-strong galaxy in our sample, we measure its $V_{i,max}$ as:

$$V_{i,\max} = \min[V_{i,\max,\,H\delta_A}, V_{i,z_{\lim}}], \tag{5.2}$$

where $V_{i,max}$ is the minimum between the maximum volumes that the i-th galaxy would have, given the S/N limit chosen for the stellar continuum in the $H\delta_A$ spectral region, and the volume of the survey in the considered range of redshift. Since we divide the sample into 3 redshift bins, the limits in which compute the $V_{i,z_{lim}}$ will be the bounds (z_1 and z_2) of the redshift bin the i-th galaxy belongs to. The $V_{i,max,\,H\delta_A}$, instead, is the volume at which we can measure a reliable $H\delta_A$. We adopt a criterion of reliability of $S/N_{H\delta_A} \geq 3$, where $S/N_{H\delta_A}$ represents the signal-to-noise of the stellar continuum in the region of $H\delta_A$. In the next section we illustrate the procedure to measure $S/N_{H\delta_A}$ as a function of the redshift and we will adopt it to estimate $V_{i,max,\,H\delta_A}$ in subsection 5.2.3.

5.2.2 The signal-to-noise of $H\delta_A$

Here, we present our procedure to define the S/N of $H\delta_A$ as a function of the redshift ($S/N_{H\delta_A}(z)$). If we image to radially shift a source from the observed position (z_{obs}) to a new one placed at any redshift $z=z_k$, the $S/N_{H\delta_A}$ will, therefore, vary for the combination of two effects:

1. the flux of the source will be attenuated or amplified, depending on whether the source is moved to a z_k further or closer than z_{obs}. The variation of the flux, as a function of rest-frame wavelengths λ and z_k will change as:

$$F(\lambda, z_k) = F(\lambda, z_{obs}) \cdot \frac{1+z_{obs}}{1+z_k} \cdot \left(\frac{d_L(z_{obs})}{d_L(z_k)}\right)^2. \tag{5.3}$$

The latter term is the ratio between the luminosity distance ($d_L(z)$) of the source at the two redshifts.

2. The spectrum of the source at z_k will fall in a different region of the noise spectrum with respect to that at z_{obs}. The noise spectrum $\sigma(\lambda)$ associated to observation is intrinsic, and it does not change if we shift the observed source radially along the line of the sight. However, for effect of the redshift, the source moved to z_k will end up in a different wavelength region of the noise spectrum. To take into account this effect, we can define:

$$\hat{\sigma}(\lambda, z_k) = \sigma(\lambda \cdot (1 + z_k)), \tag{5.4}$$

that is the noise at wavelength $\lambda \cdot (1 + z_k)$.

We define the S/N of the continuum in the $H\delta_A$ region ($S/N_{H\delta_A}(z_k)$) as the ratio, measured at the $H\delta_A$ centroid, between the linear stellar continuum and the noise. The linear stellar continuum is defined as the straight line between two bandpasses of $H\delta_A$:

$$S(\lambda, z_k) = S_b(z_k) \cdot \frac{\lambda_r - \lambda}{\lambda_r - \lambda_b} + S_r(z_k) \cdot \frac{\lambda - \lambda_b}{\lambda_r - \lambda_b}, \tag{5.5}$$

with:

$$S_b(z_k) = \frac{1}{n_b} \sum_{j=b_1}^{b_2} F(\lambda_j, z_k), \qquad S_r(z_k) = \frac{1}{n_r} \sum_{j=r_1}^{r_2} F(\lambda_j, z_k), \tag{5.6}$$

where n_b and n_r are the number of pixels covering the blue and red bandpasses of $H\delta_A$, respectively[1], while $\lambda_b = \frac{\lambda_{b_1} + \lambda_{b_2}}{2}$, and $\lambda_r = \frac{\lambda_{r_1} + \lambda_{r_2}}{2}$, where ($\lambda_{b_1}$, λ_{b_2}) and (λ_{r_1}, λ_{r_2}) are the limits of the blue and red bandpasse of $H\delta_A$, respectively.

Similarly, we can obtain a pseudo-noise:

$$N(\lambda, z_k) = \hat{N}_b(z_k) \cdot \frac{\lambda_r - \lambda}{\lambda_r - \lambda_b} + \hat{N}_r(z_k) \cdot \frac{\lambda - \lambda_b}{\lambda_r - \lambda_b} \tag{5.7}$$

where $\hat{N}_b$ and $\hat{N}_r$ represent the averaged noise in the two bandpasses:

$$\hat{N}_b(z_k) = \frac{1}{n_b} \sum_{j=b_1}^{b_2} \hat{\sigma}(\lambda_j, z_k), \qquad \hat{N}_r(z_k) = \frac{1}{n_r} \sum_{j=r_1}^{r_2} \hat{\sigma}(\lambda_j, z_k), \tag{5.8}$$

which are measured after 5 iterations of a sigma clipping procedure on the noise distribution, with a cut-off of noise values out of 2σ. Finally, we can write the $S/N_{H\delta_A}(z_k)$ as:

$$S/N_{H\delta_A}(z_k) = \frac{S(\lambda, z_k)|_{\lambda=4101.7\text{Å}}}{N(\lambda, z_k)|_{\lambda=4101.7\text{Å}}}. \tag{5.9}$$

[1] In general, fractions of pixels must be considered in the borders of the bandpasses

5.2.3 The $V_{i,\text{max},\,\text{H}\delta_\text{A}}$

We can estimate the function (5.9) for each $z_k \in [z_1, z_2]$, where z_1 and z_2 are the bounds of the redshift bin of the galaxy. In Figure 5.1, we show three examples of

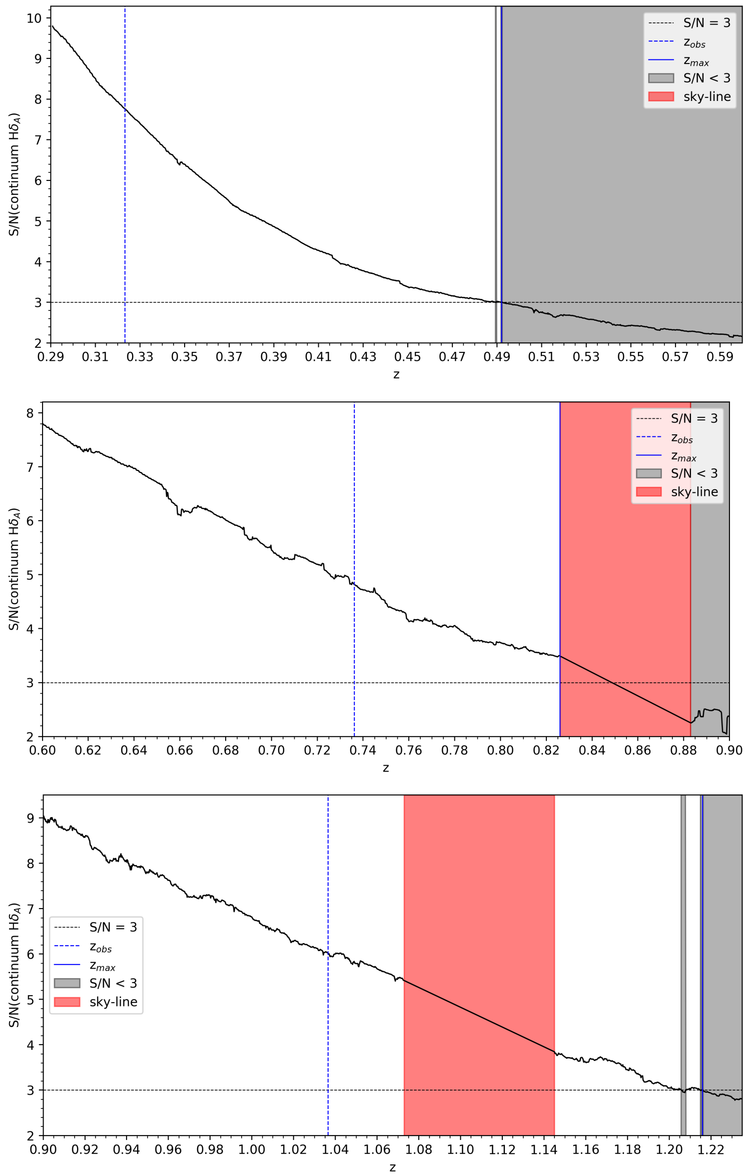

FIGURE 5.1: The $S/N_{\text{H}\delta_\text{A}}$ as a function of the redshift, for three galaxies in the redshift bins: $0.288 \leq z < 0.6$ (top), $0.6 \leq z < 0.9$ (centre), $0.9 \leq z < 1.235$ (bottom). The blue dashed line indicates the redshift at which the galaxy is observed; the solid blue line represents the maximum redshift at which the S/N of the continuum is higher than 3. The grey area represents the volume with $S/N_{\text{H}\delta_\text{A}} < 3$, while the red bands are volumes of the survey in which the $\text{H}\delta_\text{A}$ (the central and the two bandpasses) falls in the spectral regions of strong sky lines (see section 5.1), and they are not taken into account for the measure of the maximum volume.

$S/N_{H\delta_A}(z)$ of galaxies in each redshift bins. In the figure, we also report the redshift regions in which the $H\delta_A$ falls in the wavelength range of strong sky lines (see section 5.1). These regions must be subtracted from the maximum volume of the galaxies. Hence, the maximum volume that the i-th galaxy would have, given the S/N of its stellar continuum in the $H\delta_A$ spectral region is:

$$V_{i,\mathrm{max},\,H\delta_A} = \sum V_i(z|S/N_{H\delta_A}(z) \geq 3) - \sum_{\text{sky line}} V_i(z|S/N_{H\delta_A}(z) \geq 3). \tag{5.10}$$

5.3 Large-scale structure correction for V_{max}

The large-scale structure shows high density variability (see the redshift distribution of our sample in Figure 5.1). In a survey covering a small sky area, this effect is usually strong, and it must be corrected to obtain the SMF. Baldry et al. (2006) proposed a modification to the $1/V_{max}$ method that takes into account the density variation in the large-scale structure (see also Mahtessian, 2011; Baldry et al., 2012; Gunawardhana et al., 2015). We follow their approach defining, for each i-th galaxy, a maximum volume weighted by density:

$$V'_{i,max} = f_{V,i} \times V_{i,max}, \tag{5.11}$$

where $f_{V,i}$ represents the relative volume that the i-th galaxy in a particular environment could be observed over the redshift range given by V_{max} ($z_1 \leq z < z_{max}$). In other words, it represents the number density of galaxies with $z < z_{max}$ relative to the number density covering the entire redshift bin, and can be parametrised as:

$$f_{V,i} = \frac{\rho(z_1; z_{max,i})}{\rho(z_1; z_2)}. \tag{5.12}$$

We note that $\rho(z_1; z_2)$ should be the number density of a volume-limited sample between redshifts z_1 and z_2 (Baldry et al., 2006). As we mentioned earlier, we do not have a volume-limited sample, however the criterion of $S/N_{H\delta_A} \geq 3$ can be considered as a good approximation because the signal-to-noise of the stellar continuum strictly correlated with the magnitude of the galaxies (and mass). Figure 5.2 shows the relations between the corrected maximum volume (from equation (5.11)) and both the maximum redshift and the uncorrected maximum redshift (from equation (5.11)) for galaxies in the Hδ sample showing $H\delta_A \geq 4.5$ Å. As expected, the radial density correction becomes progressively more important towards galaxies with z_{max} lower than z_2 (i.e. the right bound of the redshift bin). In fact, by definition $f_V(z) \to 1$for $z_{max} \to z_2$.

5.4 The stellar mass function

In this section we present the resulting stellar mass functions obtained from equation (5.1). Figure 5.1 shows the number densities obtained for three different threshold adopted to define a Hδ-strong galaxy : $H\delta_A \geq 4$ Å, ≥ 4.5 Åand ≥ 5 Å, whit

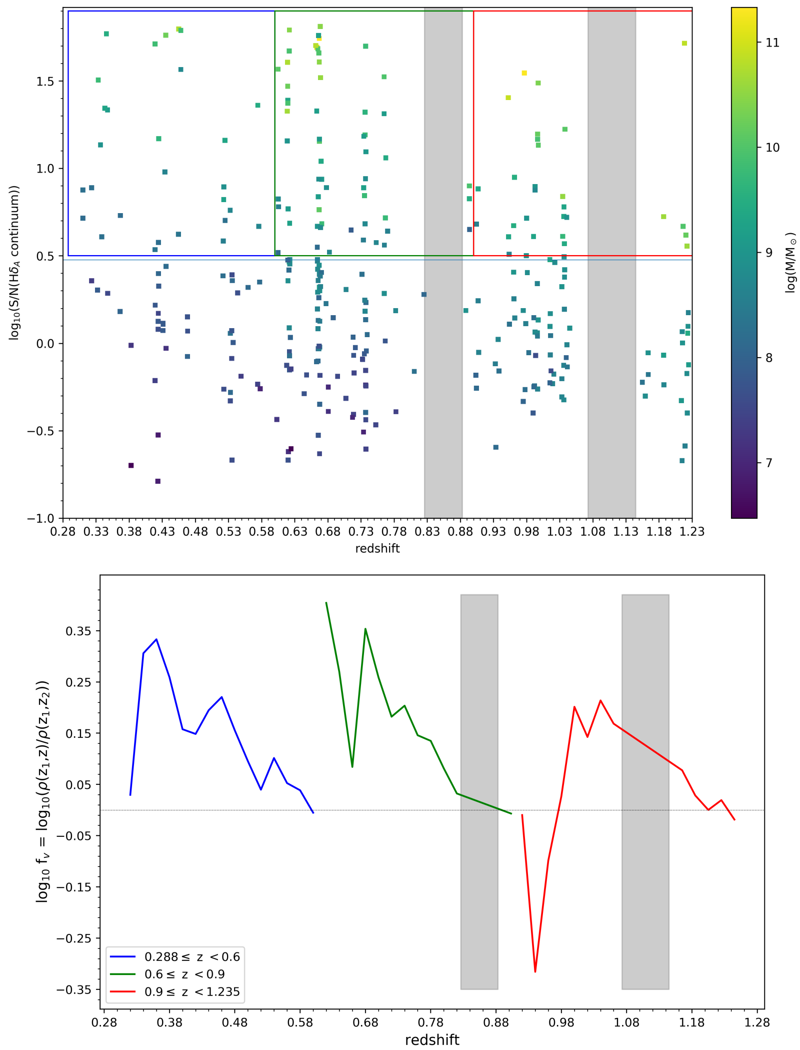

FIGURE 5.1: *T*op: The distribution of $S/N_{H\delta_A}$ in redshift for all the 312 galaxies between $0.288 \geq z < 1.235$ colour coded according with the stellar masses. The 119 galaxies in the Hδ sample are, by definition, those above $S/N_{H\delta_A} = 3$. The coloured boxes show the distributions of the three redshift bins. *B*ottom: For each redshift bin, we derive the relative volume $f_V(z)$ (see text).

uncertainties estimated as Poissonian errors of the maximum volume density corrected within each mass bin (see also Table 5.1 for details). We show the resulting mass functions with and without density corrections on the maximum volumes. The density correction f_V is stronger for low mass galaxies, because they typically show stellar continuum with S/N lower than that of more massive galaxies. Therefore, they have lower z_{max} and, consequently, larger f_V (see equation Figure 5.1). A more massive galaxy has, instead, more chances to have $z_{max} = z_2$ (i.e. the highest bound of the considered redshift bin) and, by definition f_V tends to the unit for $z_{max} \rightarrow z_2$ (see equation (5.12)). We find that the adopted threshold does not change the result significantly. Instead, we find a considerable difference between the number densities obtained in the highest redshift bin concerning the other two at lower redshift. In other words, the number density of Hδ-strong galaxies of given mass increases significantly from redshift ~ 1.1 to ~ 0.8.

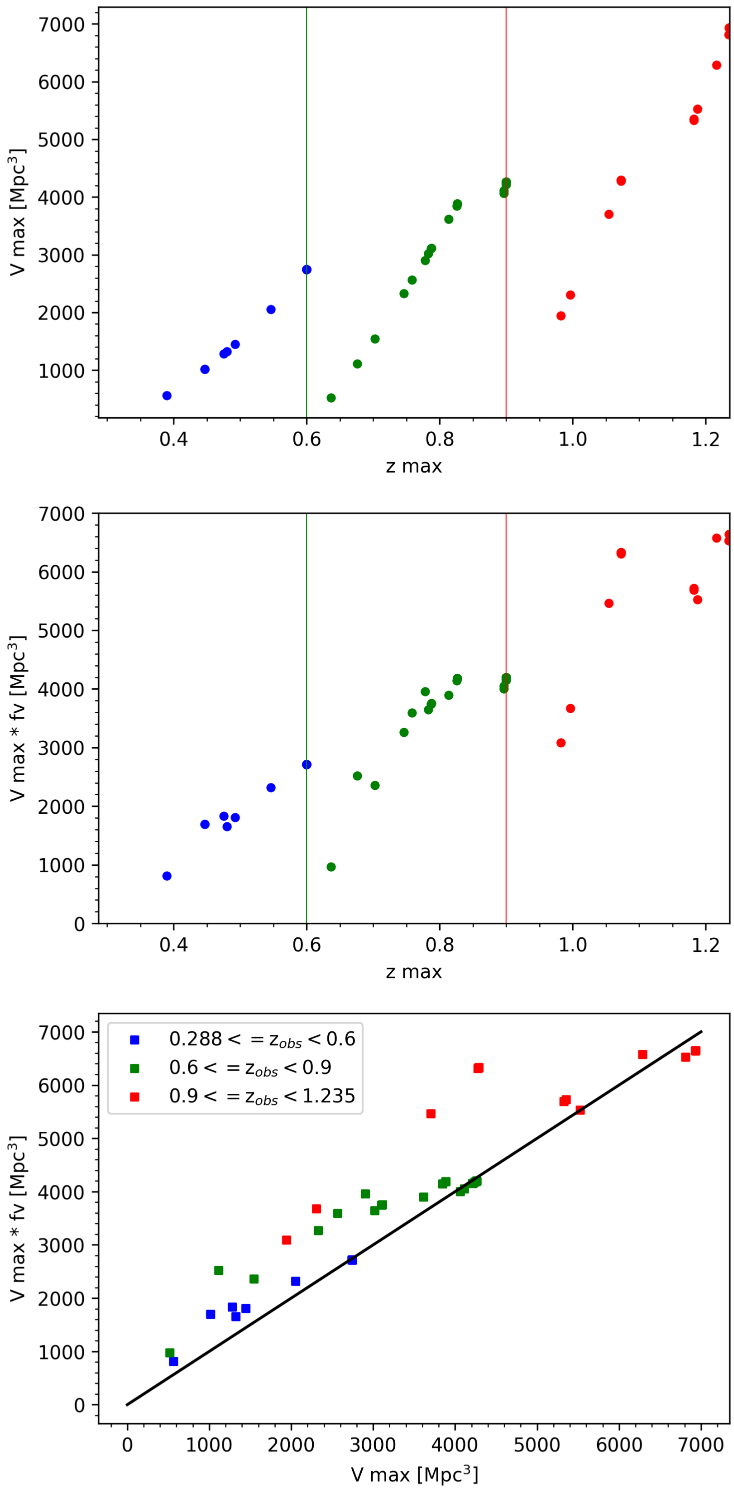

FIGURE 5.2: *Top*: the maximum volume (equation (5.2)) as a function of the maximum redshift for galaxies in the Hδ sample with H$\delta_A \geq 4.5$ Å. *Centre*: the corrected maximum volume (equation (5.11)) as a function of the maximum redshift. *Bottom*: the corrected maximum volume vs the maximum volume. Different colours represent different redshift bins (as reported in the legend).

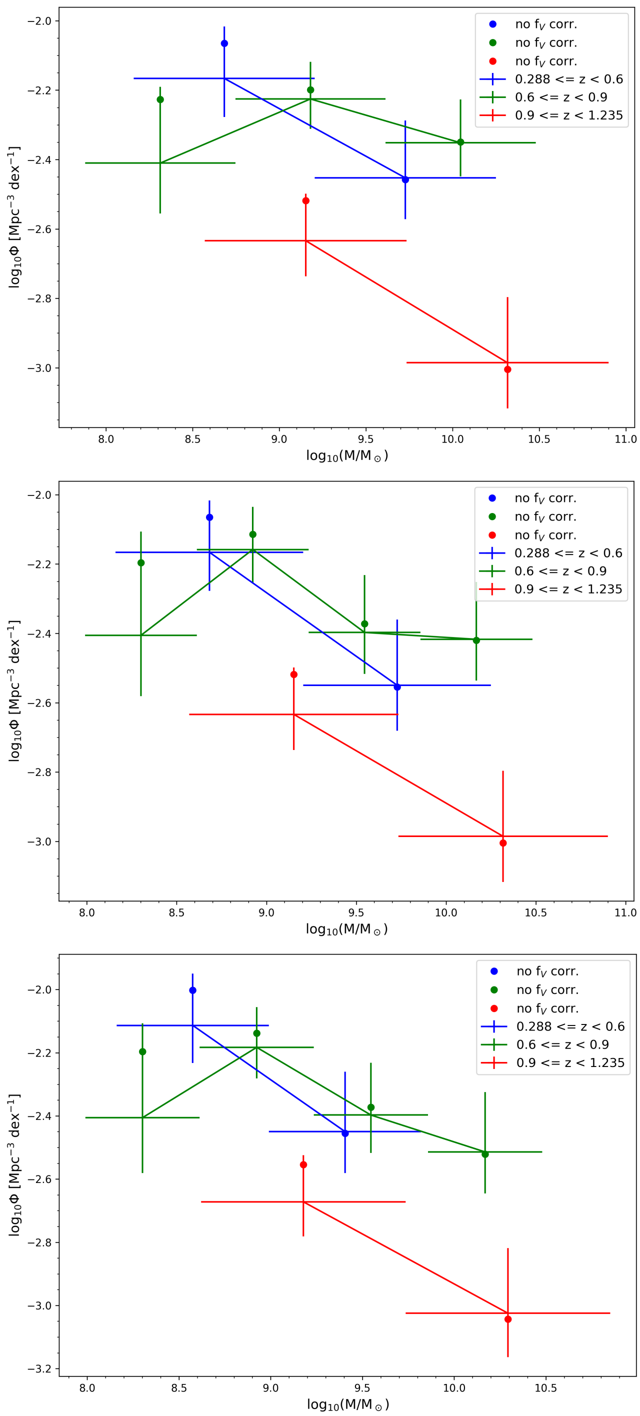

FIGURE 5.1: The stellar mass function of Hδ-strong galaxies in our sample, for three different thresholds for Hδ-strong definition: Hδ_A $\geq$ 4 Å(top), $\geq$ 4.5 Å(centre) and $\geq$ 5 Å(bottom). Dots represent the mass function with V_{max} not corrected for the density variation. The uncertainties in each mass bin are Poisson errors. The horizontal bars represent the width $\Delta\log M$ in each mass bin. The number densities of different mass bins at each redshift bin are linked with a solid line.

TABLE 5.1: The mass function values (both not-corrected and corrected for the radial density) for the three redshift bins. We list the results for three different thresholds for Hδ-strong definition: H$\delta_A = 4, 4.5$ and 5 Å. Column 4 lists the number of objects in the mass bins reported in column 3.

Hδ_A [Å]	[z1, z2]	mass $\pm\Delta$mass [log(M/M$_\odot$)]	N. obj.	Φ [Mpc^3 dex^{-1}]	dΦ [Mpc^3 dex^{-1}]	Φ (V$'_{max}$) [Mpc^3 dex^{-1}]	dΦ(V$'_{max}$) [Mpc^3 dex^{-1}]
4.0	[0.288-0.6]	8.7 $\pm$ 0.5	14	0.0086	0.0027	0.0068	0.0020
		9.7 $\pm$ 0.5	10	0.0035	0.0011	0.0035	0.0011
	[0.6-0.9]	8.3$\pm$ 0.4	9	0.0059	0.0027	0.0039	0.0015
		9.2 $\pm$ 0.4	21	0.0063	0.0014	0.0060	0.0013
		10.0 $\pm$ 0.4	16	0.0045	0.0011	0.0045	0.0011
	[0.9-1.235]	9.2$\pm$ 0.6	15	0.0030	0.0009	0.0023	0.0006
		10.3 $\pm$0.6	8	0.0010	0.0004	0.0010	0.0004
4.5	[0.288-0.6]	8.7 $\pm$ 0.5	14	0.0086	0.0027	0.0068	0.0020
		9.2 $\pm$ 0.5	8	0.0028	0.0010	0.0028	0.0010
	[0.6-0.9]	8.3 $\pm$ 0.3	6	0.0064	0.0035	0.0039	0.0020
		8.9 $\pm$ 0.3	17	0.0077	0.0020	0.0070	0.0017
		9.5 $\pm$ 0.3	10	0.0042	0.0014	0.0040	0.0013
		10.2 $\pm$ 0.3	10	0.0038	0.0012	0.0038	0.0012
	[0.9-1.235]	9.2 $\pm$ 0.6	15	0.0030	0.0009	0.0023	0.0006
		10.3 $\pm$ 0.6	8	0.0010	0.0004	0.0010	0.0004
5.0	[0.288-0.6]	8.6 $\pm$ 0.4	12	0.0099	0.0033	0.0077	0.0024
		9.4 $\pm$ 0.4	8	0.0035	0.0012	0.0036	0.0013
	[0.6-0.9]	8.3 $\pm$ 0.3	6	0.0064	0.0035	0.0039	0.0020
		8.9 $\pm$ 0.3	16	0.0073	0.0019	0.0066	0.0017
		9.5 $\pm$ 0.3	10	0.0042	0.0014	0.0040	0.0013
		10.2 $\pm$ 0.3	8	0.0030	0.0011	0.0031	0.0011
	[0.9-1.235]	9.2 $\pm$ 0.6	13	0.0028	0.0009	0.0021	0.0006
		10.3 $\pm$ 0.6	7	0.0009	0.0003	0.0009	0.0004

This result are in agreement with those regarding more massive galaxies obtained in previous works. For instance, in Figure 5.2 we report a plot from the work of

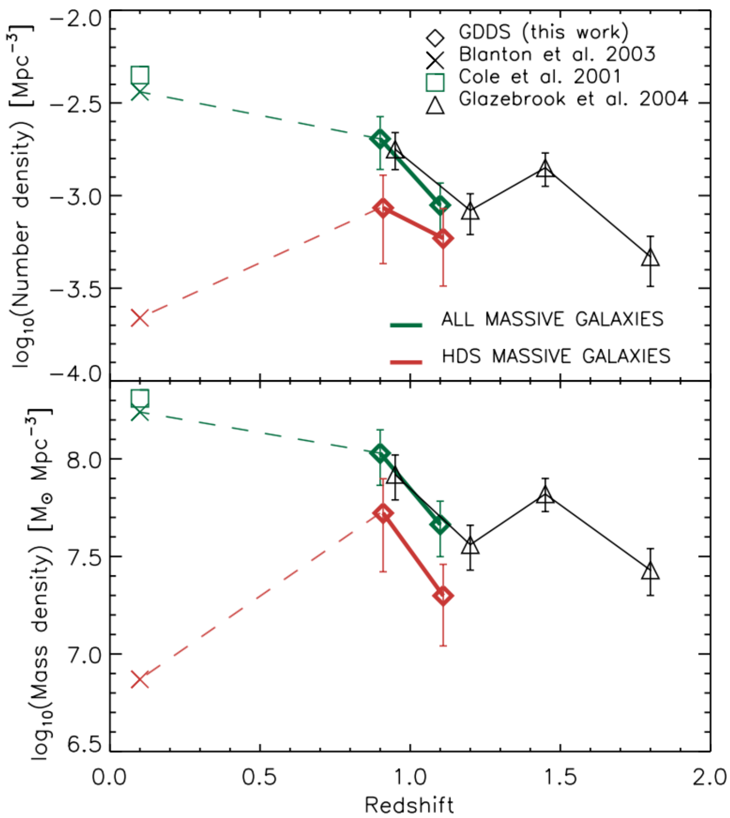

FIGURE 5.2: Evolution of the number and mass densities of massive galaxies and massive Hδ-strong ($H\delta_A > 4.0$ Å) galaxies. All these measurements concern only galaxies more massive than $\log(M/M_\odot) = 10.2$. Densities at low redshift were taken from Blanton et al. (2003; from SDSS data, crosses) and Cole et al. (2001; from 2dF data, squares) and corrected for the same IMF and cosmology. Mass densities from Glazebrook et al. (2004) are shown in the bottom panel for reference with a solid black line; the corresponding number densities are shown in the top panel. The high-redshift (GDDS) and low-redshift (SDSS) samples used in this study are linked with dashed lines. From Le Borgne et al. (2006).

Le Borgne et al. (2006), in which it is shown the evolution of the number density of Hδ-strong galaxies more massive than $10^{10.2}$ $M_\odot$. In their work the number density of massive Hδ-strong galaxies show a trend similar to that obtained in our study in a similar redshift range. If we compare our number density of Hδ-strong (with threshold $H\delta_A > 4$Å) more massive than $\log(M/M_\odot) \sim 10$ against that obtained by Le Borgne et al. (2006), we find a good agreement: $\log(\Phi)\sim -3$ vs $\log(\Phi)\sim -3.2$ [Mpc^{-3} dex^{-1}]. A perfect match is not expected: we have a smaller number of massive objects in our sample than that of Le Borgne et al. (2006). For example, the considered mass bin contains 8 Hδ-strong galaxies with $\log(M/M_\odot)$ in the range 10.3 ± 0.6, against the 25 massive Hδ-strong in their sample. Moreover, also the redshift range is similar but not equal. Finally, it is interesting to note that Le Borgne et al. (2006) also studied the evolution of the fraction of massive Hδ-strong with respect to the global population of massive galaxies, founding that it decreases from redshift ~ 1.1 towards the local Universe. One of our next steps will be to study the fraction of low mass Hδ-strong galaxies in our sample at different redshifts, to understand if their evolution follows that of the more massive ones.

5.5 Summury and future perspectives

In this chapter, we present the analyse of galaxies in an advanced quenching phase (between 300 Myr and $\lesssim 1$ Gyr after the quenching). To this aim, we search for Hδ-strong galaxies, which are systems with the optical spectra dominated by strong Balmer absorption lines (e.g. Hδ with equivalent width $> 4 - 5$ Å). These lines are strongest for stellar populations dominated by A-type stars, revealing that the formation of O- and early B-type stars have ceased suddenly (fast quenching of the star formation) about $300 - 700$ Myr ago. In this work, we exploit very deep MUSE spectra(>10 hours of exposure time) to study low mass Hδ-strong galaxies (i.e. $\log(M/M_{\odot}) \lesssim 10.2$) at $0.3 < z < 1.24$. We select about 115 Hδ-strong galaxies from a parent sample of about 400 galaxies in the MUSE Hubble Ultra Deep Field (MHUDF Bacon et al., 2017) and we estimated their mass function in three redshift bins by using the $1/V_{max}$ technique, also taking into account a correction due to the effects of the density variation in the large-scale structure. The results are in agreement with the redshift evolution of more massive Hδ-strong galaxies. At fixed mass, the number density of Hδ-strong with $\log(M/M_{\odot}) \lesssim 10$ increases from redshift z~ 1.1 to z~ 0.8 and then, it decreases weakly around $z \sim 0.45$.

The next steps will regard a study of the evolution of the fraction of low mass galaxies with respect to the global population of galaxies less massive than 10^{10} $M_{\odot}$. Moreover, we currently measure the number density of the low mass Hδ-strong in the SDSS DR7 sample, in order to follow the evolution of these systems from redshift ~ 1.2 to the local Universe.

We are also taking advantages from the recent Eagle cosmological simulation. We measure the Lick index Hδ_A on simulated spectra, which are obtained from the SFHs of the Eagle galaxies (see Trayford et al., 2017). The preliminary results are in disagreement with our findings. It seems, indeed, that Eagle predicts a decrement of the number density of low mass Hδ-strong from high redshift towards the local Universe.

The final steps of this work are ongoing and consist of the general interpretation of the results to understand how these low-mass galaxies evolve (e.g. passive evolution, bursty SFH, etc.).

6. CONCLUSIONS AND FUTURE PROSPECTS

The main goal of this Thesis work is twofold. On the one hand, we aim at defining new methods to select galaxies that are in the critical phase of quenching, or that have recently (e.g. within 0.5 Gyr) terminated their star formation. On the other hand, the final goal is to study the physical properties of the selected galaxies in order to investigate the origin of the quenching, place constraints on how and where (within the galaxies) star formation terminates and understand the possible evolutionary links with the population of E/S0 galaxies. Our main results can be summarised as follows:

1. As we show in chapter 2, C17 proved that [O III]/Hα ratio is a very sensitive tracer of the ongoing quenching as it drops by a factor ~ 10 within ~ 10 Myr from the quenching, assuming a sharp interruption of the star formation, and even for a smoother and slower star formation decline (i.e. an exponential declining star formation history with e-folding time $\tau = 200$ Myr) the [O III]/Hα decreases by a factor ~ 2 within ~ 80 Myr from the quenching.

2. In chapter 3 we devised a spectroscopic method aimed at finding galaxies just after the interruption of the star formation. Our approach represents a novel criterion complementary to the methods used so far to select quenched galaxies usually based on colours and specific star-formation rate. Our approach aims at finding galaxies where the lack of hard UV photons indicates the interruption of the star formation. When star formation ceases, O stars are the first to disappear, and emission lines requiring energetic photons (e.g. [O III] λ5007, [Ne III] λ3869) rapidly fade away due to the softening of the UV radiation. Instead, the luminosity of lines requiring less energetic photons (e.g. Hα, Hβ) decreases more slowly due to the presence of B stars that still keep providing softer UV photons (Osterbrock 1989). This method is affected by a significant degeneracy between ionisation and metallicity (e.g. [O III] λ5007 emission can also be depressed by high metallicity). However, we found that this problem can be mitigated using pairs of emission line ratios orthogonally dependent on ionisation (i.e.[O III]/Hα) and metallicity (i.e. [N II]/[O II]). Our method was applied to a sub-sample ~26.000 galaxies with undetected [O III], selected from a sample of ~174.000 star-forming galaxies at $0.04 < z < 0.21$ extracted from the SDSS-DR8. After a careful analysis, we identified a population of 300 quenching galaxies candidates (QGs), segregated from the main population of star forming galaxies in the plane OIII/Halpha vs. OII/NII, i.e. showing [O III]/Hα ratios, at fixed [N II]/[O II], which are too low to be explained by metallicity effects.

These selected galaxies are segregated from the global sample of galaxies with ongoing star-formation, and have stellar masses between $10^{9.7}$ $M_\odot$ and $10^{10.8}$ $M_\odot$, consistently with the mass range where the passive galaxy population grows at these redshifts. Moreover, their star- formation rates, colours and metallicities are comparable to those of the star-forming population, coherently with the hypothesis of recent quenching. Most candidates have morphologies similar to those of star-forming galaxies with the same stellar mass, suggesting that no morphological transformation has occurred yet. However, our galaxies are located preferentially in high-density environments, suggesting that the quenching may be linked with the density field. We attempted to estimate the quenching time-scale and obtained quite a wide range from $\sim$90 Myr to $\sim$1.5 Gyr depending on the assumed shape of the star formation history. Our results are compatible with a 'rapid' quenching scenario of satellites galaxies due to the final phase of strangulation or ram-pressure stripping. This approach represents a robust alternative to methods used so far to select quenched galaxies (e.g. colours, specific star-formation rate, or post-starburst spectra).

3. In chapter 4, we extended our method to IFU data from the SDSS-IV MaNGA survey, data release 14 (Bundy et al., 2015; Blanton et al., 2017; Abolfathi et al., 2018) in order to derive spatial information about the quenching process within the selected galaxies. To this aim, we analyse 12 SDSS-IV MaNGA galaxies that show regions with low [O III]/Ha compatible with a recent quenching of the star formation. We compare the properties of these 12 galaxies with those of a control sample of 10 MaNGA galaxies with ongoing star formation at same stellar mass, redshift and gas-phase metallicity range. The quenching regions are located between 0.5 and 1.1 effective radii from the centre. This result is supported by their average radial profile of the ionisation parameter, that reaches a minimum at the same radii, while that of the star-forming sample shows an almost flat trend. Moreover, the average radial profile of the star formation rate surface density of our sample is lower than that of the control sample, at any radii, suggesting a sharp decline in their star-formation rate. Finally, the radial profile of gas-phase metallicity of the two samples have a similar slope and normalisation, therefore, our results cannot be ascribed to a difference in the intrinsic properties of the analysed galaxies. All these difference between the QRGs and the SFs are confirmed at a high significance level. These results are being presented in a paper (Quai et al.) submitted to MNRAS.

4. As a final step of this Thesis work, in chapter 5 we analysed galaxies in an advanced quenching phase, whose star formation was quenched less than 1 Gyr ago. To this purpose, we searched for galaxies with strong Balmer absorption lines (Hδ with equivalent width $> 4-5$ Å, in particular) because these lines are strongest for stellar populations dominated by A-type stars with ages between 300 Myr and 1 Gyr after the interruption of the star-formation. In the literature, these systems have been called Hδ-strong galaxies, and they differ from the classical post-starburst galaxies for the presence of emission lines in their optical spectra. It has been found that their number density decreases with redshift (e.g. Le Borgne et al., 2006; Wild et al., 2009). In this work we

will exploit very deep MUSE spectra (>10 hours of exposure time) to study the recent star formation activity, and cessation thereof, in low mass galaxies (i.e. $\log(M/M_{\odot}) \lesssim 10.2$) at $0.3 < z < 1.24$. We selected about 115 Hδ-strong galaxies from a parent sample of about 400 galaxies in the MUSE Hubble Ultra Deep Field (MHUDF Bacon et al., 2017) and we estimated their mass function in three redshift bins by using the 1/Vmax technique, also taking into account a correction due to the effects of the radial variation in the large-scale structure. The results are in agreement with the redshift evolution of more massive Hδ-strong galaxies. At fixed mass, the number density of Hδ-strong with $\log(M/M_{\odot}) \lesssim 10$ increases from redshift z$\sim$ 1.1 to z$\sim$ 0.8 and then, it decreases weakly around $z \sim 0.45$. This behaviour is in contrast with the trend of Hδ-strong in the recent Eagle cosmological simulation, that predicts a decrement in the number density of low mass Hδ-strong from high redshift towards the local Universe. The final steps of this work are ongoing and consist of the general interpretation of the results to understand how these low-mass galaxies evolve (e.g. passive evolution, bursty SFH, etc.). The results will be presented in a paper (Quai et al. in preparation).

6.1 Future prospects

We are aimed at understanding the origin of the quenching through the analysis of galaxies that currently undergo this phase. To achieve this goal we need to tackle the following fundamental questions:

- where does the quenching start and how is it distributed inside the galaxies?
- Is it the gas sufficient to further sustain a new star-forming phase?
- Which physical mechanisms trigger and drive the quenching?

This Thesis work represents the start point to resolve the problem. The investigation can be further developed as follows.

1. On one hand, optical spectra offer efficient diagnostics of the quenching, on the other, a reservoir of cold-gas could ignite a further star-forming phase. *As a first step*, we will focus on obtaining a clean sample of quenching galaxies. In particular, we aim to disentangle between actual QGs in which the star formation is ended and those that are experiencing a temporary minimum in the star-formation history. At the same time, we derive spatial information on the quenching process, confirming the nature of quenching galaxies.

   To this aim, we will build a multi-wavelength sample of galaxies which both satisfy our optical criteria of the quenching and show no hint of a reservoir of cold gas. Catinella et al. (2018) showed that reservoirs of gas in star-forming galaxies is dominated by atomic hydrogen. Therefore, we propose the analysis of VLA data of atomic-gas in galaxies satisfying our optical criteria of the quenching, as a primary indication of a gas-depletion. Moreover, since molecular-to-atomic hydrogen mass ratios weakly increase with stellar mass

(Catinella et al. 2018) we propose also the analysis of high-resolution integral field spectroscopic unit (IFU) data of molecular gas (e.g. the rotational transition line J=1-0 of ^{12} CO at 2.6 mm, as a proxy for H_2). We will use data from the Atacama Large Millimeter/submm Array (ALMA) and the NOrthern Extended Millimeter Array (NOEMA). In the optical domain, we will extend our method to optical integral field unit (IFU) data (e.g. VLT-MUSE, CALIFA, MaNGA, SAMI), which offer the chance to study the spatial distribution of the quenching and its propagation across the galaxy. IFU data are fundamental for two reasons: (i) the spatial sampling and spatial resolution (e.g. MUSE samples 0.2×0.2 arcsec^2 with an angular resolution of $\sim$0.35 arcsec at FWHM), (ii) the sensitivity, which allows to measure faintest [O III] emission line with a high S/N. In this way, we can confirm the lack of [O III] emission due to the quenching.

In order to increase the opportunities to find useful data, another chance will be to enlarge the sample of QGs by extending our method to other public optical surveys at low redshift (e.g. GAMA, 2dFGRS, Millennium Galaxy Catalogue). Moreover, we can also apply to obtain observing time for some among the most reliable QGs via proposals at the same facilities (e.g. ALMA, VLT-MUSE, etc.).

2. It is well known that the cosmic star formation rate density peaks approximately at $z \approx 1.9$ (i.e. ~ 3.5 Gyr after the Big Bang) and drops at lower redshifts (Madau & Dickinson 2014). Therefore, the relative fraction of quenching galaxies at redshifts around the peak should be larger than in the local universe. An exciting development of the project would be to extend our method to select quenching galaxies from higher redshift surveys in order to achieve a more comprehensive view of the quenching population. We propose to analyse data from high-redshift public surveys such as zCOSMOS-Bright, the 3D-HST and MUSE Hubble Ultra Deep Field. To this aims, will be essential to adapt our method to reliable optical-UV emission lines that can be observed at these redshifts (see Citro et al. 2018). These samples will also be used as benchmarks for future data with ESO-MOONS and JWST-NIRspec. We will also plan to analyse ESO-KMOS spatially resolved spectra of some of these high-redshift QGs, in order to compare the physical properties of local and higher redshift quenching galaxies. This analysis will allow understanding if different mechanisms are responsible for the interruption of the star-formation in different epochs. Finally, KMOS data will allow to study the stellar population in high-redshift quenching galaxies and to infer their evolutionary status from the stellar continuum and absorption lines (e.g. D4000 break, Lick-indices, etc.), in order to understand if they can be considered as the progenitors of local evolute early-type galaxies.

3. Our sample of QGs is fundamental to shed light on the physical mechanisms driving the quenching. In Chapter 2 of this Thesis and Quai et al. (2018), we showed that most candidates have morphologies similar to those of star-forming galaxies with the same stellar mass, suggesting that no morphological transformation has occurred yet. However, our galaxies are located preferentially in high-density environments, suggesting that the quenching may

be linked with the density field. We will combine these results with those achieved from spatial analysis of the cold- and ionised- phase of the QGs to constraint the mechanisms driving the quenching.

Another way of exploring galaxies is through cosmological simulations. Currently, they still suffer from an insufficient spatial resolution on the scale of single HII regions around massive stars. However, the pioneering work of Kewley et al. (2013) has opened to the possibilities of post-process the cosmological simulations with physical models of nebular emission obtained from photoionisation codes (i.e. CLOUDY - Ferland et al. 1998,2013 or MAPPINGS-III - Groves et al. 2008). Therefore, we propose to apply our method to simulated spectra of galaxies (e.g. Hirschmann et al. 2017 and Trayford et al. 2017) to frame the quenching of the star-formation in the current cosmological scenario.

REFERENCES

Abolfathi, B. et al. (2018). "The Fourteenth Data Release of the Sloan Digital Sky Survey: First Spectroscopic Data from the Extended Baryon Oscillation Spectroscopic Survey and from the Second Phase of the Apache Point Observatory Galactic Evolution Experiment". In: *ApJS* 235, 42, p. 42. DOI: 10.3847/1538-4365/aa9e8a. arXiv: 1707.09322.

Agertz, O., R. Teyssier, and B. Moore (2009). "Disc formation and the origin of clumpy galaxies at high redshift". In: *MNRAS* 397, pp. L64–L68. DOI: 10.1111/j.1745-3933.2009.00685.x. arXiv: 0901.2536.

Aihara, H. et al. (2011). "The Eighth Data Release of the Sloan Digital Sky Survey: First Data from SDSS-III". In: *ApJS* 193, 29, p. 29. DOI: 10.1088/0067-0049/193/2/29. arXiv: 1101.1559 [astro-ph.IM].

Andrews, B. H. and P. Martini (2013). "The Mass-Metallicity Relation with the Direct Method on Stacked Spectra of SDSS Galaxies". In: *ApJ* 765, 140, p. 140. DOI: 10.1088/0004-637X/765/2/140. arXiv: 1211.3418.

Armillotta, L., F. Fraternali, and F. Marinacci (2016). "Efficiency of gas cooling and accretion at the disc-corona interface". In: *MNRAS* 462, pp. 4157–4170. DOI: 10.1093/mnras/stw1930. arXiv: 1608.06290.

Asplund, M., N. Grevesse, and A. J. Sauval (2005). "The Solar Chemical Composition". In: *Cosmic Abundances as Records of Stellar Evolution and Nucleosynthesis*. Ed. by T. G. Barnes III and F. N. Bash. Vol. 336. Astronomical Society of the Pacific Conference Series, p. 25.

Bacon, R. et al. (2010). "The MUSE second-generation VLT instrument". In: *Ground-based and Airborne Instrumentation for Astronomy III*. Vol. 7735. Proc. SPIE, p. 773508. DOI: 10.1117/12.856027.

Bacon, R. et al. (2015). "The MUSE 3D view of the Hubble Deep Field South". In: *A&A* 575, A75, A75. DOI: 10.1051/0004-6361/201425419. arXiv: 1411.7667.

Bacon, R. et al. (2017). "The MUSE Hubble Ultra Deep Field Survey. I. Survey description, data reduction, and source detection". In: *A&A* 608, A1, A1. DOI: 10.1051/0004-6361/201730833. arXiv: 1710.03002.

Baker, J. G. and D. H. Menzel (1938). "Physical Processes in Gaseous Nebulae. III. The Balmer Decrement." In: *ApJ* 88, p. 52. DOI: 10.1086/143959.

Baldry, I. K. et al. (2004). "Quantifying the Bimodal Color-Magnitude Distribution of Galaxies". In: *ApJ* 600, pp. 681–694. DOI: 10.1086/380092. eprint: astro-ph/0309710.

Baldry, I. K. et al. (2006). "Galaxy bimodality versus stellar mass and environment". In: *MNRAS* 373, pp. 469–483. DOI: 10.1111/j.1365-2966.2006.11081.x. eprint: astro-ph/0607648.

Baldry, I. K. et al. (2012). "Galaxy And Mass Assembly (GAMA): the galaxy stellar mass function at $z < 0.06$". In: *MNRAS* 421, pp. 621–634. DOI: 10.1111/j.1365-2966.2012.20340.x. arXiv: 1111.5707.

Baldwin, J. A., M. M. Phillips, and R. Terlevich (1981). "Classification parameters for the emission-line spectra of extragalactic objects". In: *PASP* 93, pp. 5–19. DOI: 10.1086/130766.

Balogh, M. L., J. F. Navarro, and S. L. Morris (2000). "The Origin of Star Formation Gradients in Rich Galaxy Clusters". In: *ApJ* 540, pp. 113–121. DOI: 10.1086/309323. eprint: astro-ph/0004078.

Balogh, M. L. et al. (1999). "Differential Galaxy Evolution in Cluster and Field Galaxies at $z{\sim}0.3$". In: *ApJ* 527, pp. 54–79. DOI: 10.1086/308056. eprint: astro-ph/9906470.

Balogh, M. L. et al. (2004). "The Bimodal Galaxy Color Distribution: Dependence on Luminosity and Environment". In: *ApJ* 615, pp. L101–L104. DOI: 10.1086/426079. eprint: astro-ph/0406266.

Balogh, M. L. et al. (2011). "Direct observational evidence for a large transient galaxy population in groups at $0.85 < z < 1$". In: *MNRAS* 412, pp. 2303–2317. DOI: 10.1111/j.1365-2966.2010.18052.x. arXiv: 1011.5509.

Baron, D. et al. (2017). "Evidence of ongoing AGN-driven feedback in a quiescent post starburst E+A galaxy". In: *ArXiv e-prints*. arXiv: 1705.03891.

Baugh, C. M., S. Cole, and C. S. Frenk (1996). "Evolution of the Hubble sequence in hierarchical models for galaxy formation". In: *MNRAS* 283, pp. 1361–1378. DOI: 10.1093/mnras/283.4.1361. eprint: astro-ph/9602085.

Behroozi, P. S., R. H. Wechsler, and C. Conroy (2013). "The Average Star Formation Histories of Galaxies in Dark Matter Halos from z = 0-8". In: *ApJ* 770, 57, p. 57. DOI: 10.1088/0004-637X/770/1/57. arXiv: 1207.6105 [astro-ph.CO].

Bekki, K. (2009). "Ram-pressure stripping of halo gas in disc galaxies: implications for galactic star formation in different environments". In: *MNRAS* 399, pp. 2221–2230. DOI: 10.1111/j.1365-2966.2009.15431.x. arXiv: 0907.4409.

Belfiore, F. et al. (2016). "SDSS IV MaNGA - spatially resolved diagnostic diagrams: a proof that many galaxies are LIERs". In: *MNRAS* 461, pp. 3111–3134. DOI: 10.1093/mnras/stw1234. arXiv: 1605.07189.

Belfiore, F. et al. (2017a). "SDSS IV MaNGA - metallicity and nitrogen abundance gradients in local galaxies". In: *MNRAS* 469, pp. 151–170. DOI: 10.1093/mnras/stx789. arXiv: 1703.03813.

Belfiore, F. et al. (2017b). "SDSS-IV MaNGA - the spatially resolved transition from star formation to quiescence". In: *MNRAS* 466, pp. 2570–2589. DOI: 10.1093/mnras/stw3211. arXiv: 1609.01737.

Bell, E. F. and R. S. de Jong (2001). "Stellar Mass-to-Light Ratios and the Tully-Fisher Relation". In: *ApJ* 550, pp. 212–229. DOI: 10.1086/319728. eprint: astro-ph/0011493.

Bell, E. F. et al. (2004). "Nearly 5000 Distant Early-Type Galaxies in COMBO-17: A Red Sequence and Its Evolution since $z{\sim}1$". In: *ApJ* 608, pp. 752–767. DOI: 10.1086/420778. eprint: astro-ph/0303394.

Bell, E. F. et al. (2012). "What Turns Galaxies Off? The Different Morphologies of Star-forming and Quiescent Galaxies since $z \sim 2$ from CANDELS". In: *ApJ* 753, 167, p. 167. DOI: 10.1088/0004-637X/753/2/167. arXiv: 1110.3786.

Bennett, C. L. et al. (2003). "First-Year Wilkinson Microwave Anisotropy Probe (WMAP) Observations: Preliminary Maps and Basic Results". In: *ApJS* 148, pp. 1–27. DOI: 10.1086/377253. eprint: astro-ph/0302207.

Bernardi, M. et al. (2006). "Evolution and Environment of Early-Type Galaxies". In: *AJ* 131, pp. 1288–1317. DOI: 10.1086/499522. eprint: astro-ph/0509360.

Bigiel, F. et al. (2008). "The Star Formation Law in Nearby Galaxies on Sub-Kpc Scales". In: *AJ* 136, pp. 2846–2871. DOI: 10.1088/0004-6256/136/6/2846. arXiv: 0810.2541.

Blanton, M. R. (2006). "Galaxies in SDSS and DEEP2: A Quiet Life on the Blue Sequence?" In: *ApJ* 648, pp. 268–280. DOI: 10.1086/505628. eprint: astro-ph/0512127.

Blanton, M. R. et al. (2003). "The Broadband Optical Properties of Galaxies with Redshifts 0.02<z<0.22". In: *ApJ* 594, pp. 186–207. DOI: 10.1086/375528. eprint: astro-ph/0209479.

Blanton, M. R. et al. (2011). "Improved Background Subtraction for the Sloan Digital Sky Survey Images". In: *AJ* 142, 31, p. 31. DOI: 10.1088/0004-6256/142/1/31. arXiv: 1105.1960 [astro-ph.IM].

Blanton, M. R. et al. (2017). "Sloan Digital Sky Survey IV: Mapping the Milky Way, Nearby Galaxies, and the Distant Universe". In: *AJ* 154, 28, p. 28. DOI: 10.3847/1538-3881/aa7567. arXiv: 1703.00052.

Block, D. L. and R. J. Wainscoat (1991). "Morphological differences between optical and infrared images of the spiral galaxy NGC309". In: *Nature* 353, pp. 48–50. DOI: 10.1038/353048a0.

Block, D. L. et al. (2001). "The gravitational torque of bars in optically unbarred and barred galaxies". In: *A&A* 375, pp. 761–769. DOI: 10.1051/0004-6361:20010775. eprint: astro-ph/0106019.

Boissier, S. and N. Prantzos (1999). "Chemo-spectrophotometric evolution of spiral galaxies - I. The model and the Milky Way". In: *MNRAS* 307, pp. 857–876. DOI: 10.1046/j.1365-8711.1999.02699.x. eprint: astro-ph/9902148.

– (2000). "Chemo-spectrophotometric evolution of spiral galaxies - II. Main properties of present-day disc galaxies". In: *MNRAS* 312, pp. 398–416. DOI: 10.1046/j.1365-8711.2000.03133.x.

Borch, A. et al. (2006). "The stellar masses of 25 000 galaxies at $0.2 < z < 1.0$ estimated by the COMBO-17 survey". In: *A&A* 453, pp. 869–881. DOI: 10.1051/0004-6361:20054376. eprint: astro-ph/0604405.

Bouché, N. et al. (2007). "Dynamical Properties of $z \sim 2$ Star-forming Galaxies and a Universal Star Formation Relation". In: *ApJ* 671, pp. 303–309. DOI: 10.1086/522221. arXiv: 0706.2656.

Bouché, N. et al. (2010). "The Impact of Cold Gas Accretion Above a Mass Floor on Galaxy Scaling Relations". In: *ApJ* 718, pp. 1001–1018. DOI: 10.1088/0004-637X/718/2/1001. arXiv: 0912.1858.

Bournaud, F. and B. G. Elmegreen (2009). "Unstable Disks at High Redshift: Evidence for Smooth Accretion in Galaxy Formation". In: *ApJ* 694, pp. L158–L161. DOI: 10.1088/0004-637X/694/2/L158. arXiv: 0902.2806 [astro-ph.CO].

Brammer, G. B. et al. (2009). "The Dead Sequence: A Clear Bimodality in Galaxy Colors from $z = 0$ to $z = 2.5$". In: *ApJ* 706, pp. L173–L177. DOI: 10.1088/0004-637X/706/1/L173. arXiv: 0910.2227.

Brinchmann, J. et al. (2004). “The physical properties of star-forming galaxies in the low-redshift Universe”. In: *MNRAS* 351, pp. 1151–1179. DOI: 10.1111/j.1365-2966.2004.07881.x. eprint: astro-ph/0311060.

Brooks, A. M. et al. (2007). “The Origin and Evolution of the Mass-Metallicity Relationship for Galaxies: Results from Cosmological N-Body Simulations”. In: *ApJ* 655, pp. L17–L20. DOI: 10.1086/511765. eprint: astro-ph/0609620.

Brooks, A. M. et al. (2009). “The Role of Cold Flows in the Assembly of Galaxy Disks”. In: *ApJ* 694, pp. 396–410. DOI: 10.1088/0004-637X/694/1/396. arXiv: 0812.0007.

Bruzual, G. and S. Charlot (2003). “Stellar population synthesis at the resolution of 2003”. In: *MNRAS* 344, pp. 1000–1028. DOI: 10.1046/j.1365-8711.2003.06897.x. eprint: astro-ph/0309134.

Bundy, K. et al. (2006). “The Mass Assembly History of Field Galaxies: Detection of an Evolving Mass Limit for Star-Forming Galaxies”. In: *ApJ* 651, pp. 120–141. DOI: 10.1086/507456. eprint: astro-ph/0512465.

Bundy, K. et al. (2015). “Overview of the SDSS-IV MaNGA Survey: Mapping nearby Galaxies at Apache Point Observatory”. In: *ApJ* 798, 7, p. 7. DOI: 10.1088/0004-637X/798/1/7. arXiv: 1412.1482.

Calura, F. et al. (2009). “The evolution of the mass-metallicity relation in galaxies of different morphological types”. In: *A&A* 504, pp. 373–388. DOI: 10.1051/0004-6361/200911756. arXiv: 0904.2180.

Calzetti, D. et al. (2000). “The Dust Content and Opacity of Actively Star-forming Galaxies”. In: *ApJ* 533, pp. 682–695.

Cappellari, M. and Y. Copin (2003). “Adaptive spatial binning of integral-field spectroscopic data using Voronoi tessellations”. In: *MNRAS* 342, pp. 345–354. DOI: 10.1046/j.1365-8711.2003.06541.x. eprint: astro-ph/0302262.

Cappellari, M. and E. Emsellem (2004). “Parametric Recovery of Line-of-Sight Velocity Distributions from Absorption-Line Spectra of Galaxies via Penalized Likelihood”. In: *PASP* 116, pp. 138–147. DOI: 10.1086/381875. eprint: astro-ph/0312201.

Cardiel, N. et al. (1998). “Reliable random error estimation in the measurement of line-strength indices”. In: *A&AS* 127, pp. 597–605. DOI: 10.1051/aas:1998123. eprint: astro-ph/9706116.

Carollo, C. M., I. J. Danziger, and L. Buson (1993). “Metallicity Gradients in Early Type Galaxies”. In: *MNRAS* 265, p. 553. DOI: 10.1093/mnras/265.3.553.

Carollo, C. M. and S. J. Lilly (2001). “The Metallicity of $0.5 < Z < 1$ Field Galaxies”. In: *ApJ* 548, pp. L153–L157. DOI: 10.1086/319104. eprint: astro-ph/0011353.

Carton, D. et al. (2015). “Gas-phase metallicity profiles of the Bluedisk galaxies: Is metallicity in a local star formation regulated equilibrium?” In: *MNRAS* 451, pp. 210–235. DOI: 10.1093/mnras/stv967. arXiv: 1505.02797.

Carton, D. et al. (2018). “First gas-phase metallicity gradients of $0.1 < z < 0.8$ galaxies with MUSE”. In: *MNRAS* 478, pp. 4293–4316. DOI: 10.1093/mnras/sty1343. arXiv: 1805.08131.

Cassata, P. et al. (2008). “GMASS ultradeep spectroscopy of galaxies at z $\sim$2. III. The emergence of the color bimodality at z $\sim$2”. In: *A&A* 483, pp. L39–L42. DOI: 10.1051/0004-6361:200809881. arXiv: 0804.1064.

Cen, R. and J. P. Ostriker (1992). “Galaxy formation and physical bias”. In: *ApJ* 399, pp. L113–L116. DOI: 10.1086/186620.

Chabrier, G. (2003). “Galactic Stellar and Substellar Initial Mass Function”. In: *PASP* 115, pp. 763–795. DOI: 10.1086/376392. eprint: astro-ph/0304382.
Charlot, S. and M. Longhetti (2001). “Nebular emission from star-forming galaxies”. In: *MNRAS* 323, pp. 887–903.
Chiappini, C., F. Matteucci, and D. Romano (2001). “Abundance Gradients and the Formation of the Milky Way”. In: *ApJ* 554, pp. 1044–1058. DOI: 10.1086/321427. eprint: astro-ph/0102134.
Cicone, C. et al. (2014). “Massive molecular outflows and evidence for AGN feedback from CO observations”. In: *A&A* 562, A21, A21. DOI: 10.1051/0004-6361/201322464. arXiv: 1311.2595.
Ciesla, L. et al. (2016). “The imprint of rapid star formation quenching on the spectral energy distributions of galaxies”. In: *A&A* 585, A43, A43. DOI: 10.1051/0004-6361/201527107. arXiv: 1510.07657.
Cimatti, A., E. Daddi, and A. Renzini (2006). “Mass downsizing and top-down assembly of early-type galaxies”. In: *A&A* 453, pp. L29–L33. DOI: 10.1051/0004-6361:20065155. eprint: astro-ph/0605353.
Cimatti, A. et al. (2013). “Active Galactic Nucleus Feedback at $z \sim 2$ and the Mutual Evolution of Active and Inactive Galaxies”. In: *ApJ* 779, L13, p. L13. DOI: 10.1088/2041-8205/779/1/L13. arXiv: 1311.4401.
Cirasuolo, M. and J. S. Dunlop (2008). “Galaxy Formation and Evolution: The Far-IR/Sub-mm View”. In: *Panoramic Views of Galaxy Formation and Evolution*. Ed. by T. Kodama, T. Yamada, and K. Aoki. Vol. 399. Astronomical Society of the Pacific Conference Series, p. 153. arXiv: 0810.1290.
Cirasuolo, M. et al. (2007). “The evolution of the near-infrared galaxy luminosity function and colour bimodality up to $z \sim 2$ from the UKIDSS Ultra Deep Survey Early Data Release”. In: *MNRAS* 380, pp. 585–595. DOI: 10.1111/j.1365-2966.2007.12038.x. eprint: astro-ph/0609287.
Citro, A. et al. (2016). “Inferring the star-formation histories of the most massive and passive early-type galaxies at $z < 0.3$”. In: *A&A* 592, A19, A19. DOI: 10.1051/0004-6361/201527772. arXiv: 1604.07826.
Citro, A. et al. (2017). “A methodology to select galaxies just after the quenching of star formation”. In: *MNRAS* 469, pp. 3108–3124. DOI: 10.1093/mnras/stx932. arXiv: 1704.05462.
Colless, M. et al. (2001). “The 2dF Galaxy Redshift Survey: spectra and redshifts”. In: *MNRAS* 328, pp. 1039–1063. DOI: 10.1046/j.1365-8711.2001.04902.x. eprint: astro-ph/0106498.
Conroy, C. and P. G. van Dokkum (2016). “Pixel Color Magnitude Diagrams for Semi-resolved Stellar Populations: The Star Formation History of Regions within the Disk and Bulge of M31”. In: *ApJ* 827, 9, p. 9. DOI: 10.3847/0004-637X/827/1/9. arXiv: 1602.05580.
Conselice, C. J. et al. (2007). “The properties and evolution of a K-band selected sample of massive galaxies at $z \sim 0.4$-2 in the Palomar/DEEP2 survey”. In: *MNRAS* 381, pp. 962–986. DOI: 10.1111/j.1365-2966.2007.12316.x. arXiv: 0708.1040.
Couch, W. J. and R. M. Sharples (1987). “A spectroscopic study of three rich galaxy clusters at Z = 0.31”. In: *MNRAS* 229, pp. 423–456. DOI: 10.1093/mnras/229.3.423.

Cowie, L. L. et al. (1996). "New Insight on Galaxy Formation and Evolution From Keck Spectroscopy of the Hawaii Deep Fields". In: *AJ* 112, p. 839. DOI: 10.1086/118058. eprint: astro-ph/9606079.

Crosthwaite, L. P. and J. L. Turner (2007). "CO(1-0), CO(2-1), and Neutral Gas in NGC 6946: Molecular Gas in a Late-Type, Gas-Rich, Spiral Galaxy". In: *AJ* 134, pp. 1827–1842. DOI: 10.1086/521645. arXiv: 0707.2636.

Cucciati, O. et al. (2006). "The VIMOS VLT Deep Survey: the build-up of the colour-density relation". In: *A&A* 458, pp. 39–52. DOI: 10.1051/0004-6361:20065161. eprint: astro-ph/0603202.

Cullen, F. et al. (2014). "The mass-metallicity-star formation rate relation at $z > 2$ with 3D Hubble Space Telescope". In: *MNRAS* 440, pp. 2300–2312. DOI: 10.1093/mnras/stu443. arXiv: 1310.0816.

Daddi, E. et al. (2007). "Multiwavelength Study of Massive Galaxies at $z{\sim}2$. I. Star Formation and Galaxy Growth". In: *ApJ* 670, pp. 156–172. DOI: 10.1086/521818. arXiv: 0705.2831.

Daddi, E. et al. (2010). "Different Star Formation Laws for Disks Versus Starbursts at Low and High Redshifts". In: *ApJ* 714, pp. L118–L122. DOI: 10.1088/2041-8205/714/1/L118. arXiv: 1003.3889.

Dalton, G. et al. (2014). "Project overview and update on WEAVE: the next generation wide-field spectroscopy facility for the William Herschel Telescope". In: *Ground-based and Airborne Instrumentation for Astronomy V*. Vol. 9147. Proc. SPIE, p. 91470L. DOI: 10.1117/12.2055132. arXiv: 1412.0843 [astro-ph.IM].

Davé, R., K. Finlator, and B. D. Oppenheimer (2012). "An analytic model for the evolution of the stellar, gas and metal content of galaxies". In: *MNRAS* 421, pp. 98–107. DOI: 10.1111/j.1365-2966.2011.20148.x. arXiv: 1108.0426.

Davé, R. et al. (2010). "The intergalactic medium over the last 10 billion years - I. Lyα absorption and physical conditions". In: *MNRAS* 408, pp. 2051–2070. DOI: 10.1111/j.1365-2966.2010.17279.x. arXiv: 1005.2421.

Davies, R. L., E. M. Sadler, and R. F. Peletier (1993). "Line-strength gradients in elliptical galaxies". In: *MNRAS* 262, pp. 650–680. DOI: 10.1093/mnras/262.3.650.

de Jong, R. S. and C. Lacey (2000). "The Local Space Density of SB-SDM Galaxies as Function of Their Scale Size, Surface Brightness, and Luminosity". In: *ApJ* 545, pp. 781–797. DOI: 10.1086/317840. eprint: astro-ph/0008071.

De Lucia, G. et al. (2006). "The formation history of elliptical galaxies". In: *MNRAS* 366, pp. 499–509. DOI: 10.1111/j.1365-2966.2005.09879.x. eprint: astro-ph/0509725.

Decarli, R. et al. (2016). "ALMA Spectroscopic Survey in the Hubble Ultra Deep Field: CO Luminosity Functions and the Evolution of the Cosmic Density of Molecular Gas". In: *ApJ* 833, 69, p. 69. DOI: 10.3847/1538-4357/833/1/69. arXiv: 1607.06770.

Dekel, A. and Y. Birnboim (2008). "Gravitational quenching in massive galaxies and clusters by clumpy accretion". In: *MNRAS* 383, pp. 119–138. DOI: 10.1111/j.1365-2966.2007.12569.x. arXiv: 0707.1214.

Dekel, A. et al. (2009). "Cold streams in early massive hot haloes as the main mode of galaxy formation". In: *Nature* 457, pp. 451–454. DOI: 10.1038/nature07648. arXiv: 0808.0553.

Dopita, M. A. and R. S. Sutherland (2003). *Astrophysics of the diffuse universe*.

Dopita, M. A. et al. (2000). "A Theoretical Recalibration of the Extragalactic H II Region Sequence". In: *ApJ* 542, pp. 224–234. DOI: 10.1086/309538.

Dopita, M. A. et al. (2006). "Modeling the Pan-Spectral Energy Distribution of Starburst Galaxies. III. Emission Line Diagnostics of Ensembles of Evolving H II Regions". In: *ApJS* 167, pp. 177–200. DOI: 10.1086/508261. eprint: astro-ph/0608062.

Dopita, M. A. et al. (2015). "Probing the Physics of Narrow-line Regions in Active Galaxies. III. Accretion and Cocoon Shocks in the LINER NGC 1052". In: *ApJ* 801, 42, p. 42. DOI: 10.1088/0004-637X/801/1/42. arXiv: 1501.02507.

Draine, B. T. et al. (2007). "Dust Masses, PAH Abundances, and Starlight Intensities in the SINGS Galaxy Sample". In: *ApJ* 663, pp. 866–894. DOI: 10.1086/518306. eprint: astro-ph/0703213.

Drory, N. et al. (2004). "The Munich Near-Infrared Cluster Survey (MUNICS). VI. The Stellar Masses of K-Band-selected Field Galaxies to z ∼1.2". In: *ApJ* 608, pp. 742–751. DOI: 10.1086/420781. eprint: astro-ph/0403041.

Drory, N. et al. (2005). "The Stellar Mass Function of Galaxies to z ∼ 5 in the FORS Deep and GOODS-South Fields". In: *ApJ* 619, pp. L131–L134. DOI: 10.1086/428044. eprint: astro-ph/0412167.

Dutton, A. A., F. C. van den Bosch, and A. Dekel (2010). "On the origin of the galaxy star-formation-rate sequence: evolution and scatter". In: *MNRAS* 405, pp. 1690–1710. DOI: 10.1111/j.1365-2966.2010.16620.x. arXiv: 0912.2169.

Edmunds, M. G. (1990). "General Constraints on the Effect of Gas Flows in the Chemical Evolution of Galaxies". In: *MNRAS* 246, p. 678.

Elbaz, D. et al. (2007). "The reversal of the star formation-density relation in the distant universe". In: *A&A* 468, pp. 33–48. DOI: 10.1051/0004-6361:20077525. eprint: astro-ph/0703653.

Ellison, S. L. et al. (2008). "Clues to the Origin of the Mass-Metallicity Relation: Dependence on Star Formation Rate and Galaxy Size". In: *ApJ* 672, p. L107. DOI: 10.1086/527296. arXiv: 0711.4833.

Erb, D. K. (2008). "A Model for Star Formation, Gas Flows, and Chemical Evolution in Galaxies at High Redshifts". In: *ApJ* 674, pp. 151–156. DOI: 10.1086/524727. arXiv: 0710.4146.

Erb, D. K. et al. (2006). "The Mass-Metallicity Relation at z∼2". In: *ApJ* 644, pp. 813–828. DOI: 10.1086/503623. eprint: astro-ph/0602473.

Eskridge, P. B. et al. (2002). "Near-Infrared and Optical Morphology of Spiral Galaxies". In: *ApJS* 143, pp. 73–111. DOI: 10.1086/342340. eprint: astro-ph/0206320.

Faber, S. M. et al. (2007). "Galaxy Luminosity Functions to z∼1 from DEEP2 and COMBO-17: Implications for Red Galaxy Formation". In: *ApJ* 665, pp. 265–294. DOI: 10.1086/519294. eprint: astro-ph/0506044.

Fabian, A. C. (2012). "Observational Evidence of Active Galactic Nuclei Feedback". In: *ARA&A* 50, pp. 455–489. DOI: 10.1146/annurev-astro-081811-125521. arXiv: 1204.4114.

Fall, S. M. and G. Efstathiou (1980). "Formation and rotation of disc galaxies with haloes". In: *MNRAS* 193, pp. 189–206. DOI: 10.1093/mnras/193.2.189.

Farouki, R. and S. L. Shapiro (1981). "Computer simulations of environmental influences on galaxy evolution in dense clusters. II - Rapid tidal encounters". In: *ApJ* 243, pp. 32–41. DOI: 10.1086/158563.

Ferland, G. J. et al. (1998). "CLOUDY 90: Numerical Simulation of Plasmas and Their Spectra". In: *PASP* 110, pp. 761–778. DOI: 10.1086/316190.

Ferland, G. J. et al. (2013). "The 2013 Release of Cloudy". In: *Rev. Mex. Astron. Astrofis.* 49, pp. 137–163. arXiv: 1302.4485 [astro-ph.GA].

Ferreras, I. et al. (2012). "The Road to the Red Sequence: A Detailed View of the Formation of a Massive Galaxy at z $\sim$ 2". In: *AJ* 144, 47, p. 47. DOI: 10.1088/0004-6256/144/2/47. arXiv: 1109.6323.

Finlator, K. and R. Davé (2008). "The origin of the galaxy mass-metallicity relation and implications for galactic outflows". In: *MNRAS* 385, pp. 2181–2204. DOI: 10.1111/j.1365-2966.2008.12991.x. arXiv: 0704.3100.

Fontana, A. et al. (2006). "The Galaxy mass function up to z 4 in the GOODS-MUSIC sample: into the epoch of formation of massive galaxies". In: *A&A* 459, pp. 745–757. DOI: 10.1051/0004-6361:20065475. eprint: astro-ph/0609068.

Fontanot, F. et al. (2006). "The effect of stellar feedback and quasar winds on the active galactic nucleus population". In: *MNRAS* 373, pp. 1173–1187. DOI: 10.1111/j.1365-2966.2006.11094.x. eprint: astro-ph/0609823.

Fossati, M. et al. (2017). "Galaxy Environment in the 3D-HST Fields: Witnessing the Onset of Satellite Quenching at z $\sim$ 1-2". In: *ApJ* 835, 153, p. 153. DOI: 10.3847/1538-4357/835/2/153. arXiv: 1611.07524.

Foster, C. et al. (2012). "Galaxy And Mass Assembly (GAMA): the mass-metallicity relationship". In: *A&A* 547, A79, A79. DOI: 10.1051/0004-6361/201220050. arXiv: 1209.1636.

Fraternali, F. and J. J. Binney (2006). "A dynamical model for the extraplanar gas in spiral galaxies". In: *MNRAS* 366, pp. 449–466. DOI: 10.1111/j.1365-2966.2005.09816.x. eprint: astro-ph/0511334.

Gallazzi, A. et al. (2005). "The ages and metallicities of galaxies in the local universe". In: *MNRAS* 362, pp. 41–58. DOI: 10.1111/j.1365-2966.2005.09321.x. eprint: astro-ph/0506539.

García-Benito, R. et al. (2015). "CALIFA, the Calar Alto Legacy Integral Field Area survey. III. Second public data release". In: *A&A* 576, A135, A135. DOI: 10.1051/0004-6361/201425080. arXiv: 1409.8302.

Garnett, D. R. (2002). "The Luminosity-Metallicity Relation, Effective Yields, and Metal Loss in Spiral and Irregular Galaxies". In: *ApJ* 581, pp. 1019–1031. DOI: 10.1086/344301. eprint: astro-ph/0209012.

Genzel, R. et al. (2010). "A study of the gas-star formation relation over cosmic time". In: *MNRAS* 407, pp. 2091–2108. DOI: 10.1111/j.1365-2966.2010.16969.x. arXiv: 1003.5180.

Gilbank, D. G. et al. (2010). "The local star formation rate density: assessing calibrations using [OII], H and UV luminosities". In: *MNRAS* 405, pp. 2594–2614. DOI: 10.1111/j.1365-2966.2010.16640.x. arXiv: 1002.3172.

Goddard, D. et al. (2017a). "SDSS-IV MaNGA: Spatially resolved star formation histories in galaxies as a function of galaxy mass and type". In: *MNRAS* 466, pp. 4731–4758. DOI: 10.1093/mnras/stw3371. arXiv: 1612.01546.

Goddard, D. et al. (2017b). "SDSS-IV MaNGA: stellar population gradients as a function of galaxy environment". In: *MNRAS* 465, pp. 688–700. DOI: 10.1093/mnras/stw2719. arXiv: 1612.01545.

Gogarten, S. M. et al. (2010). "The Advanced Camera for Surveys Nearby Galaxy Survey Treasury. V. Radial Star Formation History of NGC 300". In: *ApJ* 712, pp. 858–874. DOI: 10.1088/0004-637X/712/2/858. arXiv: 1002.1743 [astro-ph.GA].

González, V. et al. (2010). "The Stellar Mass Density and Specific Star Formation Rate of the Universe at z ∼ 7". In: *ApJ* 713, pp. 115–130. DOI: 10.1088/0004-637X/713/1/115. arXiv: 0909.3517.

González Delgado, R. M. et al. (2014a). "Insights on the Stellar Mass-Metallicity Relation from the CALIFA Survey". In: *ApJ* 791, L16, p. L16. DOI: 10.1088/2041-8205/791/1/L16. arXiv: 1407.1315.

González Delgado, R. M. et al. (2014b). "The star formation history of CALIFA galaxies: Radial structures". In: *A&A* 562, A47, A47. DOI: 10.1051/0004-6361/201322011. arXiv: 1310.5517.

González Delgado, R. M. et al. (2015). "The CALIFA survey across the Hubble sequence. Spatially resolved stellar population properties in galaxies". In: *A&A* 581, A103, A103. DOI: 10.1051/0004-6361/201525938. arXiv: 1506.04157.

González Delgado, R. M. et al. (2016). "Star formation along the Hubble sequence. Radial structure of the star formation of CALIFA galaxies". In: *A&A* 590, A44, A44. DOI: 10.1051/0004-6361/201628174. arXiv: 1603.00874.

Goto, T. (2005). "266 E+A galaxies selected from the Sloan Digital Sky Survey Data Release 2: the origin of E+A galaxies". In: *MNRAS* 357, pp. 937–944. DOI: 10.1111/j.1365-2966.2005.08701.x. eprint: astro-ph/0503088.

Goto, T. et al. (2003). "The morphology-density relation in the Sloan Digital Sky Survey". In: *MNRAS* 346, pp. 601–614. DOI: 10.1046/j.1365-2966.2003.07114.x. eprint: astro-ph/0312043.

Green, A. W. et al. (2018). "The SAMI Galaxy Survey: Data Release One with emission-line physics value-added products". In: *MNRAS* 475, pp. 716–734. DOI: 10.1093/mnras/stx3135. arXiv: 1707.08402.

Gunawardhana, M. L. P. et al. (2011). "Galaxy and Mass Assembly (GAMA): the star formation rate dependence of the stellar initial mass function". In: *MNRAS* 415, pp. 1647–1662. DOI: 10.1111/j.1365-2966.2011.18800.x. arXiv: 1104.2379.

Gunawardhana, M. L. P. et al. (2015). "Galaxy And Mass Assembly (GAMA): bivariate functions of Hα star-forming galaxies". In: *MNRAS* 447, pp. 875–901. DOI: 10.1093/mnras/stu2232. arXiv: 1411.2557.

Gunn, J. E. and J. R. Gott III (1972). "On the Infall of Matter Into Clusters of Galaxies and Some Effects on Their Evolution". In: *ApJ* 176, p. 1. DOI: 10.1086/151605.

Guth, A. H. (1981). "Inflationary universe: A possible solution to the horizon and flatness problems". In: *Phys. Rev. D* 23, pp. 347–356. DOI: 10.1103/PhysRevD.23.347.

Guth, A. H., D. I. Kaiser, and Y. Nomura (2014). "Inflationary paradigm after Planck 2013". In: *Physics Letters B* 733, pp. 112–119. DOI: 10.1016/j.physletb.2014.03.020. arXiv: 1312.7619.

Guzmán, R. et al. (1997). "The Nature of Compact Galaxies in the Hubble Deep Field. II. Spectroscopic Properties and Implications for the Evolution of the Star Formation Rate Density of the Universe1," in: *ApJ* 489, pp. 559–572. DOI: 10.1086/304797. eprint: astro-ph/9704001.

Hahn, C., J. L. Tinker, and A. Wetzel (2017). "Star Formation Quenching Timescale of Central Galaxies in a Hierarchical Universe". In: *ApJ* 841, 6, p. 6. DOI: 10.3847/1538-4357/aa6d6b. arXiv: 1609.04398.

Heavens, A. et al. (2004). "The star-formation history of the Universe from the stellar populations of nearby galaxies". In: *Nature* 428, pp. 625–627. DOI: 10.1038/nature02474. eprint: astro-ph/0403293.

Henry, A. et al. (2013). "Low Masses and High Redshifts: The Evolution of the Mass-Metallicity Relation". In: *ApJ* 776, L27, p. L27. DOI: 10.1088/2041-8205/776/2/L27. arXiv: 1309.4458.

Higdon, J. L. (1995). "Wheels of Fire. I. Massive Star Formation in the Cartwheel Ring Galaxy". In: *ApJ* 455, p. 524. DOI: 10.1086/176602.

Hinshaw, G. et al. (2003). "First-Year Wilkinson Microwave Anisotropy Probe (WMAP) Observations The Angular Power Spectrum". In: *ApJS* 148, pp. 135–159. DOI: 10.1086/377225. eprint: astro-ph/0302217.

Ho, I.-T. et al. (2015). "Metallicity gradients in local field star-forming galaxies: insights on inflows, outflows, and the coevolution of gas, stars and metals". In: *MNRAS* 448, pp. 2030–2054. DOI: 10.1093/mnras/stv067. arXiv: 1501.02668.

Hogg, D. W. et al. (2003). "The Overdensities of Galaxy Environments as a Function of Luminosity and Color". In: *ApJ* 585, pp. L5–L9. DOI: 10.1086/374238. eprint: astro-ph/0212085.

Holden, B. P. et al. (2012). "A Constant Limiting Mass Scale for Flat Early-type Galaxies from $z \sim 1$ to $z = 0$: Density Evolves but Shapes Do Not". In: *ApJ* 749, 96, p. 96. DOI: 10.1088/0004-637X/749/2/96. arXiv: 1108.6086.

Hopkins, A. M. et al. (2003). "Star Formation Rate Indicators in the Sloan Digital Sky Survey". In: *ApJ* 599, pp. 971–991. DOI: 10.1086/379608. eprint: astro-ph/0306621.

Hopkins, P. F. et al. (2010). "Mergers and Bulge Formation in ΛCDM: Which Mergers Matter?" In: *ApJ* 715, pp. 202–229. DOI: 10.1088/0004-637X/715/1/202. arXiv: 0906.5357 [astro-ph.CO].

Hubble, E. P. (1926). "Extragalactic nebulae." In: *ApJ* 64. DOI: 10.1086/143018.

Huertas-Company, M. et al. (2011). "Revisiting the Hubble sequence in the SDSS DR7 spectroscopic sample: a publicly available Bayesian automated classification". In: *A&A* 525, A157, A157. DOI: 10.1051/0004-6361/201015735. arXiv: 1010.3018.

Hummer, D. G. and P. J. Storey (1987). "Recombination-line intensities for hydrogenic ions. I - Case B calculations for H I and He II". In: *MNRAS* 224, pp. 801–820. DOI: 10.1093/mnras/224.3.801.

Ilbert, O. et al. (2010). "Galaxy Stellar Mass Assembly Between $0.2 < z < 2$ from the S-COSMOS Survey". In: *ApJ* 709, pp. 644–663. DOI: 10.1088/0004-637X/709/2/644. arXiv: 0903.0102 [astro-ph.CO].

Ilbert, O. et al. (2013). "Mass assembly in quiescent and star-forming galaxies since $z \sim 4$ from UltraVISTA". In: *A&A* 556, A55, A55. DOI: 10.1051/0004-6361/201321100. arXiv: 1301.3157.

Inami, H. et al. (2017). "The MUSE Hubble Ultra Deep Field Survey. II. Spectroscopic redshifts and comparisons to color selections of high-redshift galaxies". In: *A&A* 608, A2, A2. DOI: 10.1051/0004-6361/201731195. arXiv: 1710.03773.

Issa, M. R., I. MacLaren, and A. W. Wolfendale (1990). "Dust-to-gas ratio and metallicity variations in nearby galaxies". In: *A&A* 236, pp. 237–241.

Johansson, P. H., T. Naab, and J. P. Ostriker (2012). "Forming Early-type Galaxies in ΛCDM Simulations. I. Assembly Histories". In: *ApJ* 754, 115, p. 115. DOI: 10.1088/0004-637X/754/2/115. arXiv: 1202.3441.

Juneau, S. et al. (2014). "Active Galactic Nuclei Emission Line Diagnostics and the Mass-Metallicity Relation up to Redshift z ∼ 2: The Impact of Selection Effects and Evolution". In: *ApJ* 788, 88, p. 88. DOI: 10.1088/0004-637X/788/1/88. arXiv: 1403.6832.

Karim, A. et al. (2011). "The Star Formation History of Mass-selected Galaxies in the COSMOS Field". In: *ApJ* 730, 61, p. 61. DOI: 10.1088/0004-637X/730/2/61. arXiv: 1011.6370.

Kashino, D. et al. (2017). "The FMOS-COSMOS Survey of Star-forming Galaxies at z ≈ 1.6. IV. Excitation State and Chemical Enrichment of the Interstellar Medium". In: *ApJ* 835, 88, p. 88. DOI: 10.3847/1538-4357/835/1/88. arXiv: 1604.06802.

Kauffmann, G. (1996). "The age of elliptical galaxies and bulges in a merger model". In: *MNRAS* 281, pp. 487–492. DOI: 10.1093/mnras/281.2.487. eprint: astro-ph/9502096.

Kauffmann, G. et al. (2003). "The host galaxies of active galactic nuclei". In: *MNRAS* 346, pp. 1055–1077. DOI: 10.1111/j.1365-2966.2003.07154.x. eprint: astro-ph/0304239.

Kaviraj, S. (2010). "Recent star formation in local, morphologically disturbed spheroidal galaxies on the optical red sequence". In: *MNRAS* 408, pp. 170–180. DOI: 10.1111/j.1365-2966.2010.17139.x. arXiv: 1007.4810.

Kennicutt, R. C. and N. J. Evans (2012). "Star Formation in the Milky Way and Nearby Galaxies". In: *ARA&A* 50, pp. 531–608. DOI: 10.1146/annurev-astro-081811-125610. arXiv: 1204.3552.

Kennicutt Jr., R. C. (1998a). "Star Formation in Galaxies Along the Hubble Sequence". In: *ARA&A* 36, pp. 189–232.

– (1998b). "The Global Schmidt Law in Star-forming Galaxies". In: *ApJ* 498, pp. 541–552. DOI: 10.1086/305588. eprint: astro-ph/9712213.

Kennicutt Jr., R. C. et al. (2007). "Star Formation in NGC 5194 (M51a). II. The Spatially Resolved Star Formation Law". In: *ApJ* 671, pp. 333–348. DOI: 10.1086/522300. arXiv: 0708.0922.

Kewley, L. J. and S. L. Ellison (2008). "Metallicity Calibrations and the Mass Metallicity Relation for Star-forming Galaxies". In: *ApJ* 681, pp. 1183–1204. DOI: 10.1086/587500. arXiv: 0801.1849.

Kewley, L. J., R. A. Jansen, and M. J. Geller (2005). "Aperture Effects on Star Formation Rate, Metallicity, and Reddening". In: *PASP* 117, pp. 227–244. DOI: 10.1086/428303. eprint: astro-ph/0501229.

Kewley, L. J. et al. (2001). "Theoretical Modeling of Starburst Galaxies". In: *ApJ* 556, pp. 121–140. DOI: 10.1086/321545. eprint: astro-ph/0106324.

Kobayashi, C., V. Springel, and S. D. M. White (2007). "Simulations of Cosmic Chemical Enrichment". In: *MNRAS* 376, pp. 1465–1479. DOI: 10.1111/j.1365-2966.2007.11555.x. eprint: astro-ph/0604107.

Kobulnicky, H. A. and L. J. Kewley (2004). "Metallicities of 0.3z1.0 Galaxies in the GOODS-North Field". In: *ApJ* 617, pp. 240–261. DOI: 10.1086/425299. eprint: astro-ph/0408128.

Kodama, T. et al. (2004). "Downsizing in galaxy formation at z ∼ 1 in the Subaru/XMM Newton Deep Survey (SXDS)". In: *MNRAS* 350, pp. 1005–1014. DOI: 10.1111/j.1365-2966.2004.07711.x. eprint: astro-ph/0402276.

Köppen, J., C. Weidner, and P. Kroupa (2007). "A possible origin of the mass metallicity relation of galaxies". In: *MNRAS* 375, pp. 673–684. DOI: 10.1111/j.1365-2966.2006.11328.x. eprint: astro-ph/0611723.

Kormendy, J. and R. C. Kennicutt Jr. (2004). "Secular Evolution and the Formation of Pseudobulges in Disk Galaxies". In: *ARA&A* 42, pp. 603–683. DOI: 10.1146/annurev.astro.42.053102.134024. eprint: astro-ph/0407343.

Kriek, M. et al. (2008). "The Detection of a Red Sequence of Massive Field Galaxies at z $\sim$ 2.3 and Its Evolution to z $\sim$ 0". In: *ApJ* 682, 896-906, pp. 896–906. DOI: 10.1086/589677. arXiv: 0804.4175.

Kriek, M. et al. (2009). "An Ultra-Deep Near-Infrared Spectrum of a Compact Quiescent Galaxy at z = 2.2". In: *ApJ* 700, pp. 221–231. DOI: 10.1088/0004-637X/700/1/221. arXiv: 0905.1692 [astro-ph.CO].

Kroupa, P. (2001). In: *MNRAS* 322, p. 231.

Kuntschner, H. et al. (2001). "On the dependence of spectroscopic indices of early-type galaxies on age, metallicity and velocity dispersion". In: *MNRAS* 323, pp. 615–629. DOI: 10.1046/j.1365-8711.2001.04263.x. eprint: astro-ph/0011234.

Lara-López, M. A. et al. (2009a). "Star-forming galaxies in SDSS: signs of metallicity evolution". In: *A&A* 493, pp. L5–L8. DOI: 10.1051/0004-6361:200811033. arXiv: 0812.2626.

Lara-López, M. A. et al. (2009b). "Study of star-forming galaxies in SDSS up to redshift 0.4. I. Metallicity evolution". In: *A&A* 505, pp. 529–539. DOI: 10.1051/0004-6361/200912214. arXiv: 0907.0450 [astro-ph.CO].

Lara-López, M. A. et al. (2010). "A fundamental plane for field star-forming galaxies". In: *A&A* 521, L53, p. L53. DOI: 10.1051/0004-6361/201014803. arXiv: 1005.0509.

Larson, R. B. (1974). "Dynamical models for the formation and evolution of spherical galaxies". In: *MNRAS* 166, pp. 585–616. DOI: 10.1093/mnras/166.3.585.

– (1976). "Models for the formation of disc galaxies". In: *MNRAS* 176, pp. 31–52. DOI: 10.1093/mnras/176.1.31.

Larson, R. B., B. M. Tinsley, and C. N. Caldwell (1980). "The evolution of disk galaxies and the origin of S0 galaxies". In: *ApJ* 237, pp. 692–707. DOI: 10.1086/157917.

Laskar, T., E. Berger, and R.-R. Chary (2011). "Exploring the Galaxy Mass-metallicity Relation at z $\sim$3-5". In: *ApJ* 739, 1, p. 1. DOI: 10.1088/0004-637X/739/1/1. arXiv: 1102.1019.

Laurikainen, E. and H. Salo (2002). "Bar strengths in spiral galaxies estimated from 2MASS images". In: *MNRAS* 337, pp. 1118–1138. DOI: 10.1046/j.1365-8711.2002.06008.x. eprint: astro-ph/0209214.

Law, D. R. et al. (2016). "The Data Reduction Pipeline for the SDSS-IV MaNGA IFU Galaxy Survey". In: *AJ* 152, 83, p. 83. DOI: 10.3847/0004-6256/152/4/83. arXiv: 1607.08619 [astro-ph.IM].

Le Borgne, D. et al. (2006). "Gemini Deep Deep Survey. VI. Massive Hδ-strong Galaxies at z$\sim$ 1". In: *ApJ* 642, pp. 48–62. DOI: 10.1086/500005. eprint: astro-ph/0503401.

Lee, J. C. et al. (2009). "Comparison of Hα and UV Star Formation Rates in the Local Volume: Systematic Discrepancies for Dwarf Galaxies". In: *ApJ* 706, pp. 599–613. DOI: 10.1088/0004-637X/706/1/599. arXiv: 0909.5205 [astro-ph.CO].

Lee, K.-S. et al. (2012). "How Do Star-forming Galaxies at $z > 3$ Assemble Their Masses?" In: *ApJ* 752, 66, p. 66. DOI: 10.1088/0004-637X/752/1/66. arXiv: 1111.1233.

Lee, N. et al. (2015). "A Turnover in the Galaxy Main Sequence of Star Formation at $M^* \sim 10^{10}\ M_\odot$ for Redshifts $z < 1.3$". In: *ApJ* 801, 80, p. 80. DOI: 10.1088/0004-637X/801/2/80. arXiv: 1501.01080.

Leitherer, C. et al. (1999). "Starburst99: Synthesis Models for Galaxies with Active Star Formation". In: *ApJS* 123, pp. 3–40. DOI: 10.1086/313233. eprint: astro-ph/9902334.

Leitner, S. N. (2012). "On the Last 10 Billion Years of Stellar Mass Growth in Star-forming Galaxies". In: *ApJ* 745, 149, p. 149. DOI: 10.1088/0004-637X/745/2/149.

Lejeune, T., F. Cuisinier, and R. Buser (1997). "Standard stellar library for evolutionary synthesis. I. Calibration of theoretical spectra". In: *A&AS* 125, pp. 229–246. DOI: 10.1051/aas:1997373. eprint: astro-ph/9701019.

Lemaux, B. C. et al. (2017). "Chronos and KAIROS: MOSFIRE observations of post-starburst galaxies in $z \sim 1$ clusters and groups". In: *MNRAS* 472, pp. 419–438. DOI: 10.1093/mnras/stx1579. arXiv: 1608.00973.

Lequeux, J. et al. (1979). "Chemical composition and evolution of irregular and blue compact galaxies". In: *A&A* 80, pp. 155–166.

Leroy, A. K. et al. (2013). "Molecular Gas and Star Formation in nearby Disk Galaxies". In: *AJ* 146, 19, p. 19. DOI: 10.1088/0004-6256/146/2/19. arXiv: 1301.2328.

Levesque, E. M., L. J. Kewley, and K. L. Larson (2010). "Theoretical Modeling of Star-Forming Galaxies. I. Emission-Line Diagnostic Grids for Local and Low-Metallicity Galaxies". In: *AJ* 139, pp. 712–727. DOI: 10.1088/0004-6256/139/2/712. arXiv: 0908.0460.

Levesque, E. M. and C. Leitherer (2013). "Modeling Tracers of Young Stellar Population Age in Star-forming Galaxies". In: *ApJ* 779, 170, p. 170. DOI: 10.1088/0004-637X/779/2/170. arXiv: 1311.1202.

Lilly, S. J. et al. (2013). "Gas Regulation of Galaxies: The Evolution of the Cosmic Specific Star Formation Rate, the Metallicity-Mass-Star-formation Rate Relation, and the Stellar Content of Halos". In: *ApJ* 772, 119, p. 119. DOI: 10.1088/0004-637X/772/2/119. arXiv: 1303.5059.

Lin, L. et al. (2017). "SDSS-IV MaNGA-resolved Star Formation and Molecular Gas Properties of Green Valley Galaxies: A First Look with ALMA and MaNGA". In: *ApJ* 851, 18, p. 18. DOI: 10.3847/1538-4357/aa96ae. arXiv: 1710.08610.

Lisenfeld, U. and A. Ferrara (1998). "Dust-to-Gas Ratio and Metal Abundance in Dwarf Galaxies". In: *ApJ* 496, pp. 145–154. DOI: 10.1086/305354. eprint: astro-ph/9705037.

Lynds, R. and A. Toomre (1976). "On the interpretation of ring galaxies: the binary ring system II Hz 4." In: *ApJ* 209, pp. 382–388. DOI: 10.1086/154730.

Madau, P. and M. Dickinson (2014). "Cosmic Star-Formation History". In: *ARA&A* 52, pp. 415–486. DOI: 10.1146/annurev-astro-081811-125615. arXiv: 1403.0007.

Madau, P. et al. (1996). "High-redshift galaxies in the Hubble Deep Field: colour selection and star formation history to $z{\sim}4$". In: *MNRAS* 283, pp. 1388–1404. DOI: 10.1093/mnras/283.4.1388. eprint: astro-ph/9607172.

Magdis, G. E. et al. (2010). "On the stellar masses of IRAC detected Lyman Break Galaxies at z $\sim$ 3". In: *MNRAS* 401, pp. 1521–1531. DOI: 10.1111/j.1365-2966.2009.15779.x. arXiv: 0909.3950.

Magdis, G. E. et al. (2012). "The Evolving Interstellar Medium of Star-forming Galaxies since z = 2 as Probed by Their Infrared Spectral Energy Distributions". In: *ApJ* 760, 6, p. 6. DOI: 10.1088/0004-637X/760/1/6. arXiv: 1210.1035.

Mahtessian, A. P. (2011). "Luminosity function of the field galaxies". In: *Astrophysics* 54, pp. 162–176. DOI: 10.1007/s10511-011-9169-6. arXiv: 1103.4009.

Maier, C. et al. (2006). "Oxygen Gas Abundances at z $\sim$1.4: Implications for the Chemical Evolution History of Galaxies". In: *ApJ* 639, pp. 858–867. DOI: 10.1086/499518. eprint: astro-ph/0511255.

Maier, C. et al. (2014). "The Mass-Metallicity and Fundamental Metallicity Relations at z $>$ 2 Using Very Large Telescope and Subaru Near-infrared Spectroscopy of zCOSMOS Galaxies". In: *ApJ* 792, 3, p. 3. DOI: 10.1088/0004-637X/792/1/3. arXiv: 1406.6069.

Maier, C. et al. (2015). "Mass-metallicity relation of zCOSMOS galaxies at z $\approx$ 0.7, its dependence on star formation rate, and the existence of massive low-metallicity galaxies". In: *A&A* 577, A14, A14. DOI: 10.1051/0004-6361/201425224. arXiv: 1410.7389.

Maier, C. et al. (2016). "CLASH-VLT: Strangulation of cluster galaxies in MACS J0416.1-2403 as seen from their chemical enrichment". In: *A&A* 590, A108, A108. DOI: 10.1051/0004-6361/201628223. arXiv: 1602.00686.

Maiolino, R. et al. (2008). "AMAZE. I. The evolution of the mass-metallicity relation at z $>$ 3". In: *A&A* 488, pp. 463–479. DOI: 10.1051/0004-6361:200809678. arXiv: 0806.2410.

Mannucci, F. et al. (2009). "LSD: Lyman-break galaxies Stellar populations and Dynamics - I. Mass, metallicity and gas at z $\sim$ 3.1". In: *MNRAS* 398, pp. 1915–1931. DOI: 10.1111/j.1365-2966.2009.15185.x. arXiv: 0902.2398.

Mannucci, F. et al. (2010). "A fundamental relation between mass, star formation rate and metallicity in local and high-redshift galaxies". In: *MNRAS* 408, pp. 2115–2127. DOI: 10.1111/j.1365-2966.2010.17291.x. arXiv: 1005.0006.

Mapelli, M. and L. Mayer (2012). "Ring galaxies from off-centre collisions". In: *MNRAS* 420, pp. 1158–1166. DOI: 10.1111/j.1365-2966.2011.20098.x. arXiv: 1111.0028.

Martig, M. et al. (2009). "Morphological Quenching of Star Formation: Making Early-Type Galaxies Red". In: *ApJ* 707, pp. 250–267. DOI: 10.1088/0004-637X/707/1/250. arXiv: 0905.4669 [astro-ph.CO].

Martin, D. C. et al. (2007). "The UV-Optical Galaxy Color-Magnitude Diagram. III. Constraints on Evolution from the Blue to the Red Sequence". In: *ApJS* 173, pp. 342–356. DOI: 10.1086/516639. eprint: astro-ph/0703281.

McIntosh, D. H. et al. (2014). "A new population of recently quenched elliptical galaxies in the SDSS". In: *MNRAS* 442, pp. 533–557. DOI: 10.1093/mnras/stu808. arXiv: 1308.0054.

Mendel, J. T. et al. (2009). "The anatomy of the NGC5044 group - II. Stellar populations and star formation histories". In: *MNRAS* 396, pp. 2103–2123. DOI: 10.1111/j.1365-2966.2009.14689.x. arXiv: 0903.1092.

Mendel, J. T. et al. (2013). "Towards a physical picture of star formation quenching: the photometric properties of recently quenched galaxies in the Sloan Digital Sky

Survey". In: *MNRAS* 429, pp. 2212–2227. DOI: 10.1093/mnras/sts489. arXiv: 1211.6115.

Mendez, A. J. et al. (2011). "AEGIS: The Morphologies of Green Galaxies at 0.4 < z < 1.2". In: *ApJ* 736, 110, p. 110. DOI: 10.1088/0004-637X/736/2/110. arXiv: 1101.3353.

Meynet, G. et al. (1994). "Grids of massive stars with high mass loss rates. V. From 12 to 120 $M_{sun\_}$ at Z=0.001, 0.004, 0.008, 0.020 and 0.040". In: *A&AS* 103, pp. 97–105.

Mok, A. et al. (2013). "Efficient satellite quenching at z∼1 from the GEEC2 spectroscopic survey of galaxy groups". In: *MNRAS* 431, pp. 1090–1106. DOI: 10.1093/mnras/stt251. arXiv: 1302.2562.

Moore, B. et al. (1998). "Resolving the Structure of Cold Dark Matter Halos". In: *ApJ* 499, pp. L5–L8. DOI: 10.1086/311333. eprint: astro-ph/9709051.

Moran, S. M. et al. (2012). "The GALEX Arecibo SDSS Survey. V. The Relation between the H I Content of Galaxies and Metal Enrichment at Their Outskirts". In: *ApJ* 745, 66, p. 66. DOI: 10.1088/0004-637X/745/1/66. arXiv: 1112.1084 [astro-ph.CO].

Moresco, M. et al. (2012). "Improved constraints on the expansion rate of the Universe up to z ∼ 1.1 from the spectroscopic evolution of cosmic chronometers". In: *J. Cosmology Astropart. Phys.* 8, 006, p. 006. DOI: 10.1088/1475-7516/2012/08/006. arXiv: 1201.3609 [astro-ph.CO].

Mortlock, A. et al. (2011). "A deep probe of the galaxy stellar mass functions at z∼ 1-3 with the GOODS NICMOS Survey". In: *MNRAS* 413, pp. 2845–2859. DOI: 10.1111/j.1365-2966.2011.18357.x. arXiv: 1101.2867.

Mouhcine, M. et al. (2006). "The metallicities of luminous, massive field galaxies at intermediate redshifts". In: *MNRAS* 369, pp. 891–908. DOI: 10.1111/j.1365-2966.2006.10360.x. eprint: astro-ph/0603639.

Mouhcine, M. et al. (2008). "Simulating the mass-metallicity relation from z ∼ 1". In: *A&A* 486, pp. 711–720. DOI: 10.1051/0004-6361:20078190. arXiv: 0801.2476.

Moustakas, J., R. C. Kennicutt Jr., and C. A. Tremonti (2006). "Optical Star Formation Rate Indicators". In: *ApJ* 642, pp. 775–796. DOI: 10.1086/500964. eprint: astro-ph/0511730.

Moustakas, J. et al. (2010). "Optical Spectroscopy and Nebular Oxygen Abundances of the Spitzer/SINGS Galaxies". In: *ApJS* 190, pp. 233–266. DOI: 10.1088/0067-0049/190/2/233. arXiv: 1007.4547.

Moustakas, J. et al. (2013). "PRIMUS: Constraints on Star Formation Quenching and Galaxy Merging, and the Evolution of the Stellar Mass Function from z = 0-1". In: *ApJ* 767, 50, p. 50. DOI: 10.1088/0004-637X/767/1/50. arXiv: 1301.1688 [astro-ph.CO].

Muñoz-Mateos, J. C. et al. (2007). "Specific Star Formation Rate Profiles in Nearby Spiral Galaxies: Quantifying the Inside-Out Formation of Disks". In: *ApJ* 658, pp. 1006–1026. DOI: 10.1086/511812. eprint: astro-ph/0612017.

Muñoz-Mateos, J. C. et al. (2011). "Radial Distribution of Stars, Gas, and Dust in SINGS Galaxies. III. Modeling the Evolution of the Stellar Component in Galaxy Disks". In: *ApJ* 731, 10, p. 10. DOI: 10.1088/0004-637X/731/1/10. arXiv: 1102.1724.

Muzzin, A. et al. (2012). "The Gemini Cluster Astrophysics Spectroscopic Survey (GCLASS): The Role of Environment and Self-regulation in Galaxy Evolution at z∼1”. In: *ApJ* 746, 188, p. 188. DOI: 10.1088/0004-637X/746/2/188. arXiv: 1112.3655.

Muzzin, A. et al. (2013). “A Public K_s -selected Catalog in the COSMOS/ULTRAVISTA Field: Photometry, Photometric Redshifts, and Stellar Population Parameters”. In: *ApJS* 206, 8, p. 8. DOI: 10.1088/0067-0049/206/1/8. arXiv: 1303.4410.

Naab, T., S. Khochfar, and A. Burkert (2006). “Properties of Early-Type, Dry Galaxy Mergers and the Origin of Massive Elliptical Galaxies”. In: *ApJ* 636, pp. L81–L84. DOI: 10.1086/500205. eprint: astro-ph/0509667.

Nagao, T., R. Maiolino, and A. Grazian (2008). “The Evolution of the Galaxy Mass-Metallicity Relation at High Redshift”. In: *Panoramic Views of Galaxy Formation and Evolution*. Ed. by T. Kodama, T. Yamada, and K. Aoki. Vol. 399. Astronomical Society of the Pacific Conference Series, p. 272.

Nagao, T., R. Maiolino, and A. Marconi (2006). “Gas metallicity diagnostics in star-forming galaxies”. In: *A&A* 459, pp. 85–101. DOI: 10.1051/0004-6361:20065216. eprint: astro-ph/0603580.

Nakajima, K. and M. Ouchi (2014). “Ionization state of inter-stellar medium in galaxies: evolution, SFR-M_*-Z dependence, and ionizing photon escape”. In: *MNRAS* 442, pp. 900–916. DOI: 10.1093/mnras/stu902. arXiv: 1309.0207.

Nelan, J. E. et al. (2005). “NOAO Fundamental Plane Survey. II. Age and Metallicity along the Red Sequence from Line Strength Data”. In: *ApJ* 632, pp. 137–156. DOI: 10.1086/431962. eprint: astro-ph/0505301.

Noeske, K. G. et al. (2007a). “Star Formation in AEGIS Field Galaxies since z=1.1: Staged Galaxy Formation and a Model of Mass-dependent Gas Exhaustion”. In: *ApJ* 660, pp. L47–L50. DOI: 10.1086/517927. eprint: astro-ph/0703056.

Noeske, K. G. et al. (2007b). “Star Formation in AEGIS Field Galaxies since z=1.1: The Dominance of Gradually Declining Star Formation, and the Main Sequence of Star-forming Galaxies”. In: *ApJ* 660, pp. L43–L46. DOI: 10.1086/517926. eprint: astro-ph/0701924.

Oliver, S. et al. (2010). “Specific star formation and the relation to stellar mass from $0 < z < 2$ as seen in the far-infrared at 70 and 160 μm”. In: *MNRAS* 405, pp. 2279–2294. DOI: 10.1111/j.1365-2966.2010.16643.x. arXiv: 1003.2446 [astro-ph.CO].

Osterbrock, D. E. (1989). *Astrophysics of gaseous nebulae and active galactic nuclei*.

Paalvast, M. and J. Brinchmann (2017). “Metallicity calibrations of galaxies with low star formation rates: the influence of a stochastic IMF”. In: *MNRAS* 470, pp. 1612–1625. DOI: 10.1093/mnras/stx1271. arXiv: 1705.10309.

Paalvast, M. et al. (2018). “Properties and redshift evolution of star-forming galaxies with high [OIII]/[OII] ratios with MUSE at 0.28<z<0.85”. In: *ArXiv e-prints*. arXiv: 1808.04899.

Pannella, M. et al. (2009). “Star Formation and Dust Obscuration at $z \sim 2$: Galaxies at the Dawn of Downsizing”. In: *ApJ* 698, pp. L116–L120. DOI: 10.1088/0004-637X/698/2/L116. arXiv: 0905.1674 [astro-ph.CO].

Panter, B. et al. (2007). “The star formation histories of galaxies in the Sloan Digital Sky Survey”. In: *MNRAS* 378, pp. 1550–1564. DOI: 10.1111/j.1365-2966.2007.11909.x. eprint: astro-ph/0608531.

Papovich, C. et al. (2011). "The rising star formation histories of distant galaxies and implications for gas accretion with time". In: *MNRAS* 412, pp. 1123–1136. DOI: 10.1111/j.1365-2966.2010.17965.x. arXiv: 1007.4554.

Peebles, P. J. E. (1969). "Origin of the Angular Momentum of Galaxies". In: *ApJ* 155, p. 393. DOI: 10.1086/149876.

Peeples, M. S. and F. Shankar (2011). "Constraints on star formation driven galaxy winds from the mass-metallicity relation at z= 0". In: *MNRAS* 417, pp. 2962–2981. DOI: 10.1111/j.1365-2966.2011.19456.x. arXiv: 1007.3743 [astro-ph.CO].

Peng, Y., R. Maiolino, and R. Cochrane (2015). "Strangulation as the primary mechanism for shutting down star formation in galaxies". In: *Nature* 521, pp. 192–195. DOI: 10.1038/nature14439. arXiv: 1505.03143.

Peng, Y.-j. et al. (2010). "Mass and Environment as Drivers of Galaxy Evolution in SDSS and zCOSMOS and the Origin of the Schechter Function". In: *ApJ* 721, pp. 193–221. DOI: 10.1088/0004-637X/721/1/193. arXiv: 1003.4747 [astro-ph.CO].

Peng, Y.-j. et al. (2012). "Mass and Environment as Drivers of Galaxy Evolution. II. The Quenching of Satellite Galaxies as the Origin of Environmental Effects". In: *ApJ* 757, 4, p. 4. DOI: 10.1088/0004-637X/757/1/4. arXiv: 1106.2546 [astro-ph.CO].

Peng, Ying-jie and Roberto Maiolino (2014). "From haloes to Galaxies I. The dynamics of the gas regulator model and the implied cosmic sSFR history". In: *Monthly Notices of the Royal Astronomical Society* 443.4, pp. 3643–3664. DOI: 10.1093/mnras/stu1288. eprint: /oup/backfile/content_public/journal/mnras/443/4/10.1093_mnras_stu1288/2/stu1288.pdf. URL: http://dx.doi.org/10.1093/mnras/stu1288.

Penzias, A. A. and R. W. Wilson (1965). "A Measurement of Excess Antenna Temperature at 4080 Mc/s." In: *ApJ* 142, pp. 419–421. DOI: 10.1086/148307.

Pérez-González, P. G. et al. (2008). "The Stellar Mass Assembly of Galaxies from z = 0 to z = 4: Analysis of a Sample Selected in the Rest-Frame Near-Infrared with Spitzer". In: *ApJ* 675, pp. 234–261. DOI: 10.1086/523690. arXiv: 0709.1354.

Perlmutter, S. et al. (1999). "Measurements of Ω and Λ from 42 High-Redshift Supernovae". In: *ApJ* 517, pp. 565–586. DOI: 10.1086/307221. eprint: astro-ph/9812133.

Pezzulli, G. and F. Fraternali (2016). "Accretion, radial flows and abundance gradients in spiral galaxies". In: *MNRAS* 455, pp. 2308–2322. DOI: 10.1093/mnras/stv2397. arXiv: 1510.04289.

Pezzulli, G. et al. (2015). "The instantaneous radial growth rate of stellar discs". In: *MNRAS* 451, pp. 2324–2336. DOI: 10.1093/mnras/stv1077. arXiv: 1505.03544.

Pichon, C. et al. (2011). "Rigging dark haloes: why is hierarchical galaxy formation consistent with the inside-out build-up of thin discs?" In: *MNRAS* 418, pp. 2493–2507. DOI: 10.1111/j.1365-2966.2011.19640.x. arXiv: 1105.0210.

Planck Collaboration et al. (2014). "Planck 2013 results. I. Overview of products and scientific results". In: *A&A* 571, A1, A1. DOI: 10.1051/0004-6361/201321529. arXiv: 1303.5062.

Planck Collaboration et al. (2018). "Planck 2018 results. VI. Cosmological parameters". In: *ArXiv e-prints*. arXiv: 1807.06209.

Poggianti, B. M. et al. (2004). "A Comparison of the Galaxy Populations in the Coma and Distant Clusters: The Evolution of k+a Galaxies and the Role of the Intracluster Medium". In: *ApJ* 601, pp. 197–213. DOI: 10.1086/380195. eprint: astro-ph/0309449.

Poggianti, B. M. et al. (2008). "The Relation between Star Formation, Morphology, and Local Density in High-Redshift Clusters and Groups". In: *ApJ* 684, 888-904, pp. 888–904. DOI: 10.1086/589936. arXiv: 0805.1145.

Portinari, L. and C. Chiosi (1999). "On star formation and chemical evolution in the Galactic disc". In: *A&A* 350, pp. 827–839. eprint: astro-ph/9908326.

Pozzetti, L. et al. (2007). "The VIMOS VLT Deep Survey. The assembly history of the stellar mass in galaxies: from the young to the old universe". In: *A&A* 474, pp. 443–459. DOI: 10.1051/0004-6361:20077609. arXiv: 0704.1600.

Pozzetti, L. et al. (2010). "zCOSMOS - 10k-bright spectroscopic sample. The bimodality in the galaxy stellar mass function: exploring its evolution with redshift". In: *A&A* 523, A13, A13. DOI: 10.1051/0004-6361/200913020. arXiv: 0907.5416.

Prantzos, N. and S. Boissier (2000). "Chemo-spectrophotometric evolution of spiral galaxies - III. Abundance and colour gradients in discs". In: *MNRAS* 313, pp. 338–346. DOI: 10.1046/j.1365-8711.2000.03228.x. eprint: astro-ph/9911111.

Prendergast, K. H. (1983). "Theoretical studies of gas flow in barred spirals galaxies". In: *Internal Kinematics and Dynamics of Galaxies*. Ed. by E. Athanassoula. Vol. 100. IAU Symposium, pp. 215–220.

Quai, S. et al. (2018). "Galaxies in the act of quenching star formation". In: *MNRAS*. DOI: 10.1093/mnras/sty1045. arXiv: 1804.08631.

Quilis, V., B. Moore, and R. Bower (2000). "Gone with the Wind: The Origin of S0 Galaxies in Clusters". In: *Science* 288, pp. 1617–1620. DOI: 10.1126/science.288.5471.1617. eprint: astro-ph/0006031.

Quintero, A. D. et al. (2004). "Selection and Photometric Properties of K+A Galaxies". In: *ApJ* 602, pp. 190–199. DOI: 10.1086/380601. eprint: astro-ph/0307074.

Reddy, N. A. et al. (2012). "The Characteristic Star Formation Histories of Galaxies at Redshifts z $\sim$ 2-7". In: *ApJ* 754, 25, p. 25. DOI: 10.1088/0004-637X/754/1/25. arXiv: 1205.0555.

Regan, M. W. and P. Teuben (2003). "The Formation of Nuclear Rings in Barred Spiral Galaxies". In: *ApJ* 582, pp. 723–742. DOI: 10.1086/344721. eprint: astro-ph/0210244.

Riess, A. G. et al. (1998). "Observational Evidence from Supernovae for an Accelerating Universe and a Cosmological Constant". In: *AJ* 116, pp. 1009–1038. DOI: 10.1086/300499. eprint: astro-ph/9805201.

Rigby, J. R. and G. H. Rieke (2004). "Missing Massive Stars in Starbursts: Stellar Temperature Diagnostics and the Initial Mass Function". In: *ApJ* 606, pp. 237–257. DOI: 10.1086/382776. eprint: astro-ph/0401239.

Roberts, M. S. and A. H. Rots (1973). "Comparison of Rotation Curves of Different Galaxy Types". In: *A&A* 26, pp. 483–485.

Rodighiero, G. et al. (2010). "The first Herschel view of the mass-SFR link in high-z galaxies". In: *A&A* 518, L25, p. L25. DOI: 10.1051/0004-6361/201014624. arXiv: 1005.1089.

Rodighiero, G. et al. (2011). “The Lesser Role of Starbursts in Star Formation at z = 2”. In: *ApJ* 739, L40, p. L40. DOI: 10.1088/2041-8205/739/2/L40. arXiv: 1108.0933.

Rodighiero, G. et al. (2014). “A multiwavelength consensus on the main sequence of star-forming galaxies at z ∼ 2”. In: *MNRAS* 443, pp. 19–30. DOI: 10.1093/mnras/stu1110. arXiv: 1406.1189.

Rodrigues, M. et al. (2008). “IMAGES IV: strong evolution of the oxygen abundance in gaseous phases of intermediate mass galaxies from z ∼ 0.8”. In: *A&A* 492, pp. 371–388. DOI: 10.1051/0004-6361:200810435. arXiv: 0810.0272.

Rodrigues, M. et al. (2012). “A decrease of the gas exchanges between galaxies and the intergalactic medium, from 12 to 6 billion years ago”. In: *MNRAS* 421, pp. 2888–2903. DOI: 10.1111/j.1365-2966.2012.20518.x. arXiv: 1203.6248 [astro-ph.CO].

Rosales-Ortega, F. F. et al. (2011). “PPAK wide-field Integral Field Spectroscopy of NGC 628 - II. Emission line abundance analysis”. In: *MNRAS* 415, pp. 2439–2474. DOI: 10.1111/j.1365-2966.2011.18870.x. arXiv: 1104.1136.

Rosales-Ortega, F. F. et al. (2012). “A New Scaling Relation for H II Regions in Spiral Galaxies: Unveiling the True Nature of the Mass-Metallicity Relation”. In: *ApJ* 756, L31, p. L31. DOI: 10.1088/2041-8205/756/2/L31. arXiv: 1207.6216.

Rubin, V. C., W. K. Ford Jr., and N. Thonnard (1978). “Extended rotation curves of high-luminosity spiral galaxies. IV - Systematic dynamical properties, SA through SC”. In: *ApJ* 225, pp. L107–L111. DOI: 10.1086/182804.

– (1980). “Rotational properties of 21 SC galaxies with a large range of luminosities and radii, from NGC 4605 /R = 4kpc/ to UGC 2885 /R = 122 kpc/”. In: *ApJ* 238, pp. 471–487. DOI: 10.1086/158003.

Salim, S. (2014). “Green Valley Galaxies”. In: *Serbian Astronomical Journal* 189, pp. 1–14. DOI: 10.2298/SAJ1489001S. arXiv: 1501.01963.

Salim, S. et al. (2007). “UV Star Formation Rates in the Local Universe”. In: *ApJS* 173, pp. 267–292.

Salim, S. et al. (2009). “Mid-IR Luminosities and UV/Optical Star Formation Rates at z < 1.4”. In: *ApJ* 700, pp. 161–182. DOI: 10.1088/0004-637X/700/1/161. arXiv: 0905.0162 [astro-ph.CO].

Salim, S. et al. (2015). “On the Mass-Metallicity-Star Formation Rate Relation for Galaxies at z∼2”. In: *ApJ* 808, 25, p. 25. DOI: 10.1088/0004-637X/808/1/25. arXiv: 1506.03080.

Salmi, F. et al. (2012). “Dissecting the Stellar-mass-SFR Correlation in z = 1 Star-forming Disk Galaxies”. In: *ApJ* 754, L14, p. L14. DOI: 10.1088/2041-8205/754/1/L14. arXiv: 1206.1704.

Salmon, B. et al. (2015). “The Relation between Star Formation Rate and Stellar Mass for Galaxies at 3.5 <= z <= 6.5 in CANDELS”. In: *ApJ* 799, 183, p. 183. DOI: 10.1088/0004-637X/799/2/183. arXiv: 1407.6012.

Sánchez, S. F. et al. (2012). “Integral field spectroscopy of a sample of nearby galaxies. II. Properties of the H ii regions”. In: *A&A* 546, A2, A2. DOI: 10.1051/0004-6361/201219578. arXiv: 1208.1117.

Sánchez, S. F. et al. (2013). “Mass-metallicity relation explored with CALIFA. I. Is there a dependence on the star-formation rate?” In: *A&A* 554, A58, A58. DOI: 10.1051/0004-6361/201220669. arXiv: 1304.2158.

Sánchez, S. F. et al. (2014). "A characteristic oxygen abundance gradient in galaxy disks unveiled with CALIFA". In: *A&A* 563, A49, A49. DOI: 10.1051/0004-6361/201322343. arXiv: 1311.7052.
Sánchez, S. F. et al. (2017). "The mass-metallicity relation revisited with CALIFA". In: *MNRAS* 469, pp. 2121–2140. DOI: 10.1093/mnras/stx808. arXiv: 1703.09769.
Sánchez-Blázquez, P. et al. (2014). "PPAK Wide field Integral Field Spectroscopy of NGC 628 - III. Stellar population properties". In: *MNRAS* 437, pp. 1534–1548. DOI: 10.1093/mnras/stt1984. arXiv: 1310.4804.
Sargent, M. T. et al. (2012). "The Contribution of Starbursts and Normal Galaxies to Infrared Luminosity Functions at z < 2". In: *ApJ* 747, L31, p. L31. DOI: 10.1088/2041-8205/747/2/L31. arXiv: 1202.0290.
Sargent, M. T. et al. (2014). "Regularity Underlying Complexity: A Redshift-independent Description of the Continuous Variation of Galaxy-scale Molecular Gas Properties in the Mass-star Formation Rate Plane". In: *ApJ* 793, 19, p. 19. DOI: 10.1088/0004-637X/793/1/19. arXiv: 1303.4392.
Sarzi, M. et al. (2006). "The SAURON project - V. Integral-field emission-line kinematics of 48 elliptical and lenticular galaxies". In: *MNRAS* 366, pp. 1151–1200. DOI: 10.1111/j.1365-2966.2005.09839.x. eprint: astro-ph/0511307.
Savaglio, S. et al. (2005). "The Gemini Deep Deep Survey. VII. The Redshift Evolution of the Mass-Metallicity Relation". In: *ApJ* 635, pp. 260–279. DOI: 10.1086/497331. eprint: astro-ph/0508407.
Scannapieco, C. et al. (2008). "Effects of supernova feedback on the formation of galaxy discs". In: *MNRAS* 389, pp. 1137–1149. DOI: 10.1111/j.1365-2966.2008.13678.x. arXiv: 0804.3795.
Schaefer, A. L. et al. (2017). "The SAMI Galaxy Survey: spatially resolving the environmental quenching of star formation in GAMA galaxies". In: *MNRAS* 464, pp. 121–142. DOI: 10.1093/mnras/stw2289. arXiv: 1609.02635.
Schawinski, K. et al. (2010). "Galaxy Zoo: The Fundamentally Different Co-Evolution of Supermassive Black Holes and Their Early- and Late-Type Host Galaxies". In: *ApJ* 711, pp. 284–302. DOI: 10.1088/0004-637X/711/1/284. arXiv: 1001.3141.
Schawinski, K. et al. (2014). "The green valley is a red herring: Galaxy Zoo reveals two evolutionary pathways towards quenching of star formation in early- and late-type galaxies". In: *MNRAS* 440, pp. 889–907. DOI: 10.1093/mnras/stu327. arXiv: 1402.4814.
Schiminovich, D. et al. (2007). "The UV-Optical Color Magnitude Diagram. II. Physical Properties and Morphological Evolution On and Off of a Star-forming Sequence". In: *ApJS* 173, pp. 315–341. DOI: 10.1086/524659. arXiv: 0711.4823.
Schmidt, M. (1959). "The Rate of Star Formation." In: *ApJ* 129, p. 243. DOI: 10.1086/146614.
– (1968). "Space Distribution and Luminosity Functions of Quasi-Stellar Radio Sources". In: *ApJ* 151, p. 393. DOI: 10.1086/149446.
Schmutz, W., C. Leitherer, and R. Gruenwald (1992). "Theoretical continuum energy distributions for Wolf-Rayet stars". In: *PASP* 104, pp. 1164–1172. DOI: 10.1086/133104.

Schreiber, C. et al. (2015). "The Herschel view of the dominant mode of galaxy growth from z = 4 to the present day". In: *A&A* 575, A74, A74. DOI: 10.1051/0004-6361/201425017. arXiv: 1409.5433.

Schuster, K. F. et al. (2007). "A complete ^{12}CO 2-1 map of M 51 with HERA. I. Radial averages of CO, HI, and radio continuum". In: *A&A* 461, pp. 143–151. DOI: 10.1051/0004-6361:20065579. eprint: astro-ph/0609670.

Seaton, M. J. (1979). "Interstellar extinction in the UV". In: *MNRAS* 187, 73P–76P. DOI: 10.1093/mnras/187.1.73P.

Sellwood, J. A. and A. Wilkinson (1993). "Dynamics of barred galaxies". In: *Reports on Progress in Physics* 56, pp. 173–256. DOI: 10.1088/0034-4885/56/2/001. eprint: astro-ph/0608665.

Shapiro, P. R. and G. B. Field (1976). "Consequences of a New Hot Component of the Interstellar Medium". In: *ApJ* 205, pp. 762–765. DOI: 10.1086/154332.

Smethurst, R. J. et al. (2016). "Galaxy Zoo: evidence for rapid, recent quenching within a population of AGN host galaxies". In: *MNRAS* 463, pp. 2986–2996. DOI: 10.1093/mnras/stw2204. arXiv: 1609.00023.

Smoot, G. F., M. V. Gorenstein, and R. A. Muller (1977). "Detection of anisotropy in the cosmic blackbody radiation". In: *Physical Review Letters* 39, pp. 898–901. DOI: 10.1103/PhysRevLett.39.898.

Smoot, G. F. et al. (1992). "Structure in the COBE differential microwave radiometer first-year maps". In: *ApJ* 396, pp. L1–L5. DOI: 10.1086/186504.

Sokołowska, A. et al. (2016). "Diffuse Coronae in Cosmological Simulations of Milky Way-sized Galaxies". In: *ApJ* 819, 21, p. 21. DOI: 10.3847/0004-637X/819/1/21. arXiv: 1504.04620.

Somerville, R. S. and R. Davé (2015). "Physical Models of Galaxy Formation in a Cosmological Framework". In: *ARA&A* 53, pp. 51–113. DOI: 10.1146/annurev-astro-082812-140951. arXiv: 1412.2712.

Spergel, D. N. et al. (2003). "First-Year Wilkinson Microwave Anisotropy Probe (WMAP) Observations Determination of Cosmological Parameters". In: *ApJS* 148, pp. 175–194. DOI: 10.1086/377226. eprint: astro-ph/0302209.

Spindler, A. et al. (2018). "SDSS-IV MaNGA: the spatial distribution of star formation and its dependence on mass, structure, and environment". In: *MNRAS* 476, pp. 580–600. DOI: 10.1093/mnras/sty247. arXiv: 1710.05049.

Spitoni, E. et al. (2010). "The origin of the mass-metallicity relation: an analytical approach". In: *A&A* 514, A73, A73. DOI: 10.1051/0004-6361/200913799. arXiv: 1001.4374 [astro-ph.CO].

Stark, D. P. et al. (2009). "The Evolutionary History of Lyman Break Galaxies Between Redshift 4 and 6: Observing Successive Generations of Massive Galaxies in Formation". In: *ApJ* 697, pp. 1493–1511. DOI: 10.1088/0004-637X/697/2/1493. arXiv: 0902.2907 [astro-ph.CO].

Stasińska, G. et al. (2006). "Semi-empirical analysis of Sloan Digital Sky Survey galaxies - III. How to distinguish AGN hosts". In: *MNRAS* 371, pp. 972–982. DOI: 10.1111/j.1365-2966.2006.10732.x. eprint: astro-ph/0606724.

Steinhauser, D., S. Schindler, and V. Springel (2016). "Simulations of ram-pressure stripping in galaxy-cluster interactions". In: *A&A* 591, A51, A51. DOI: 10.1051/0004-6361/201527705. arXiv: 1604.05193.

Stewart, K. R. et al. (2013). "Angular Momentum Acquisition in Galaxy Halos". In: *ApJ* 769, 74, p. 74. DOI: 10.1088/0004-637X/769/1/74. arXiv: 1301.3143 [astro-ph.CO].
Strateva, I. et al. (2001). "Color Separation of Galaxy Types in the Sloan Digital Sky Survey Imaging Data". In: *AJ* 122, pp. 1861–1874. DOI: 10.1086/323301. eprint: astro-ph/0107201.
Strauss, M. A. et al. (2002). "Spectroscopic Target Selection in the Sloan Digital Sky Survey: The Main Galaxy Sample". In: *AJ* 124, pp. 1810–1824. DOI: 10.1086/342343. eprint: astro-ph/0206225.
Stringer, M. et al. (2011). "Star formation trends in high-redshift galaxy surveys: the elephant or the tail?" In: *MNRAS* 414, pp. 1927–1936. DOI: 10.1111/j.1365-2966.2011.18533.x. arXiv: 1011.2745.
Tacchella, S. et al. (2015). "Evidence for mature bulges and an inside-out quenching phase 3 billion years after the Big Bang". In: *Science* 348, pp. 314–317. DOI: 10.1126/science.1261094. arXiv: 1504.04021.
Tacconi, L. J. et al. (2013). "Phibss: Molecular Gas Content and Scaling Relations in z $\sim$ 1-3 Massive, Main-sequence Star-forming Galaxies". In: *ApJ* 768, 74, p. 74. DOI: 10.1088/0004-637X/768/1/74. arXiv: 1211.5743.
Tempel, E. et al. (2014). "Flux- and volume-limited groups/clusters for the SDSS galaxies: catalogues and mass estimation". In: *A&A* 566, A1, A1. DOI: 10.1051/0004-6361/201423585. arXiv: 1402.1350.
Thomas, D. et al. (2005). "The Epochs of Early-Type Galaxy Formation as a Function of Environment". In: *ApJ* 621, pp. 673–694. DOI: 10.1086/426932. eprint: astro-ph/0410209.
Thomas, D. et al. (2010). "Environment and self-regulation in galaxy formation". In: *MNRAS* 404, pp. 1775–1789. DOI: 10.1111/j.1365-2966.2010.16427.x. arXiv: 0912.0259.
Tielens, A. G. G. M. (2010). *The Physics and Chemistry of the Interstellar Medium*.
Trager, S. C. et al. (2000). "The Stellar Population Histories of Local Early-Type Galaxies. I. Population Parameters". In: *AJ* 119, pp. 1645–1676. DOI: 10.1086/301299. eprint: astro-ph/0001072.
Trayford, J. W. et al. (2017). "Optical colours and spectral indices of z = 0.1 eagle galaxies with the 3D dust radiative transfer code skirt". In: *MNRAS* 470, pp. 771–799. DOI: 10.1093/mnras/stx1051. arXiv: 1705.02331.
Tremonti, C. A. et al. (2004). "The Origin of the Mass-Metallicity Relation: Insights from 53,000 Star-forming Galaxies in the Sloan Digital Sky Survey". In: *ApJ* 613, pp. 898–913. DOI: 10.1086/423264. eprint: astro-ph/0405537.
Treu, T. et al. (2003). "A Wide-Field Hubble Space Telescope Study of the Cluster Cl 0024+16 at z = 0.4. I. Morphological Distributions to 5 Mpc Radius". In: *ApJ* 591, pp. 53–78. DOI: 10.1086/375314. eprint: astro-ph/0303267.
Vale Asari, N. et al. (2009). "The evolution of the mass-metallicity relation in SDSS galaxies uncovered by astropaleontology". In: *MNRAS* 396, pp. L71–L75. DOI: 10.1111/j.1745-3933.2009.00664.x. arXiv: 0903.4167 [astro-ph.GA].
van den Bosch, F. C. et al. (2008). "The importance of satellite quenching for the build-up of the red sequence of present-day galaxies". In: *MNRAS* 387, pp. 79–91. DOI: 10.1111/j.1365-2966.2008.13230.x. arXiv: 0710.3164.

Vazdekis, A. et al. (2012). “MIUSCAT: extended MILES spectral coverage - I. Stellar population synthesis models”. In: *MNRAS* 424, pp. 157–171. DOI: 10.1111/j.1365-2966.2012.21179.x. arXiv: 1205.5496.

Veilleux, S., G. Cecil, and J. Bland-Hawthorn (2005). “Galactic Winds”. In: *ARA&A* 43, pp. 769–826. DOI: 10.1146/annurev.astro.43.072103.150610. eprint: astro-ph/0504435.

Vila-Costas, M. B. and M. G. Edmunds (1992). “The relation between abundance gradients and the physical properties of spiral galaxies”. In: *MNRAS* 259, pp. 121–145. DOI: 10.1093/mnras/259.1.121.

Wang, Jing et al. (2011). “The GALEX Arecibo SDSS survey ? III. Evidence for the inside-out formation of Galactic discs”. In: *Monthly Notices of the Royal Astronomical Society* 412.2, pp. 1081–1097. DOI: 10.1111/j.1365-2966.2010.17962.x. eprint: /oup/backfile/content_public/journal/mnras/412/2/10.1111/j.1365-2966.2010.17962.x/2/mnras0412-1081.pdf. URL: http://dx.doi.org/10.1111/j.1365-2966.2010.17962.x.

Wang, L. et al. (2007). “Modelling and interpreting the dependence of clustering on the spectral energy distributions of galaxies”. In: *MNRAS* 377, pp. 1419–1430. DOI: 10.1111/j.1365-2966.2007.11737.x. eprint: astro-ph/0701682.

Wetzel, A. R. et al. (2013). “Galaxy evolution in groups and clusters: satellite star formation histories and quenching time-scales in a hierarchical Universe”. In: *MNRAS* 432, pp. 336–358. DOI: 10.1093/mnras/stt469. arXiv: 1206.3571.

Whitaker, K. E. et al. (2012). “The Star Formation Mass Sequence Out to z = 2.5”. In: *ApJ* 754, L29, p. L29. DOI: 10.1088/2041-8205/754/2/L29. arXiv: 1205.0547.

Whitaker, K. E. et al. (2014). “Constraining the Low-mass Slope of the Star Formation Sequence at $0.5 < z < 2.5$”. In: *ApJ* 795, 104, p. 104. DOI: 10.1088/0004-637X/795/2/104. arXiv: 1407.1843.

White, S. D. M. and M. J. Rees (1978). “Core condensation in heavy halos - A two-stage theory for galaxy formation and clustering”. In: *MNRAS* 183, pp. 341–358. DOI: 10.1093/mnras/183.3.341.

Wild, V. et al. (2007). “Bursty stellar populations and obscured active galactic nuclei in galaxy bulges”. In: *MNRAS* 381, pp. 543–572. DOI: 10.1111/j.1365-2966.2007.12256.x. arXiv: 0706.3113.

Wild, V. et al. (2009). “Post-starburst galaxies: more than just an interesting curiosity”. In: *MNRAS* 395, pp. 144–159. DOI: 10.1111/j.1365-2966.2009.14537.x. arXiv: 0810.5122.

Wild, V. et al. (2016). “The evolution of post-starburst galaxies from z=2 to 0.5”. In: *MNRAS* 463, pp. 832–844. DOI: 10.1093/mnras/stw1996. arXiv: 1608.00588.

Wilkins, S. M., N. Trentham, and A. M. Hopkins (2008). “The evolution of stellar mass and the implied star formation history”. In: *MNRAS* 385, pp. 687–694. DOI: 10.1111/j.1365-2966.2008.12885.x. arXiv: 0801.1594.

Williams, R. J. et al. (2009). “Detection of Quiescent Galaxies in a Bicolor Sequence from Z = 0-2”. In: *ApJ* 691, pp. 1879–1895. DOI: 10.1088/0004-637X/691/2/1879. arXiv: 0806.0625.

Willmer, C. N. A. et al. (2006). “The Deep Evolutionary Exploratory Probe 2 Galaxy Redshift Survey: The Galaxy Luminosity Function to $z{\sim}1$”. In: *ApJ* 647, pp. 853–873. DOI: 10.1086/505455. eprint: astro-ph/0506041.

Wong, T. and L. Blitz (2002). "The Relationship between Gas Content and Star Formation in Molecule-rich Spiral Galaxies". In: *ApJ* 569, pp. 157–183. DOI: 10.1086/339287. eprint: astro-ph/0112204.

Worthey, G. and D. L. Ottaviani (1997). "Hγ and Hδ Absorption Features in Stars and Stellar Populations". In: *ApJS* 111, pp. 377–386. DOI: 10.1086/313021.

Wu, P.-F. et al. (2014). "Star Formation Quenching in High-redshift Large-scale Structure: Post-starburst Galaxies in the Cl 1604 Supercluster at z $\sim$ 0.9". In: *ApJ* 792, 16, p. 16. DOI: 10.1088/0004-637X/792/1/16. arXiv: 1311.0586.

Wuyts, S. et al. (2011). "On Star Formation Rates and Star Formation Histories of Galaxies Out to z $\sim$ 3". In: *ApJ* 738, 106, p. 106. DOI: 10.1088/0004-637X/738/1/106. arXiv: 1106.5502.

Wyder, T. K. et al. (2007). "The UV-Optical Galaxy Color-Magnitude Diagram. I. Basic Properties". In: *ApJS* 173, pp. 293–314. DOI: 10.1086/521402. arXiv: 0706.3938.

Wyder, T. K. et al. (2009). "The Star Formation Law at Low Surface Density". In: *ApJ* 696, pp. 1834–1853. DOI: 10.1088/0004-637X/696/2/1834. arXiv: 0903.3015 [astro-ph.CO].

Yan, R. et al. (2006). "On the Origin of [O II] Emission in Red-Sequence and Poststarburst Galaxies". In: *ApJ* 648, pp. 281–298. DOI: 10.1086/505629. eprint: astro-ph/0512446.

Yates, R. M., G. Kauffmann, and Q. Guo (2012). "The relation between metallicity, stellar mass and star formation in galaxies: an analysis of observational and model data". In: *MNRAS* 422, pp. 215–231. DOI: 10.1111/j.1365-2966.2012.20595.x. arXiv: 1107.3145.

Yeh, S. C. C. and C. D. Matzner (2012). "Ionization Parameter as a Diagnostic of Radiation and Wind Pressures in H II Regions and Starburst Galaxies". In: *ApJ* 757, 108, p. 108. DOI: 10.1088/0004-637X/757/2/108. arXiv: 1206.6493 [astro-ph.GA].

York, D. G. et al. (2000). "The Sloan Digital Sky Survey: Technical Summary". In: *AJ* 120, pp. 1579–1587. DOI: 10.1086/301513. eprint: astro-ph/0006396.

Zahid, H. J., L. J. Kewley, and F. Bresolin (2011). "The Mass-Metallicity and Luminosity-Metallicity Relations from DEEP2 at z $\sim$ 0.8". In: *ApJ* 730, 137, p. 137. DOI: 10.1088/0004-637X/730/2/137. arXiv: 1006.4877.

Zahid, H. J. et al. (2014). "The FMOS-COSMOS Survey of Star-forming Galaxies at z $\sim$ 1.6. II. The Mass-Metallicity Relation and the Dependence on Star Formation Rate and Dust Extinction". In: *ApJ* 792, 75, p. 75. DOI: 10.1088/0004-637X/792/1/75. arXiv: 1310.4950.

Zaritsky, D., R. C. Kennicutt Jr., and J. P. Huchra (1994). "H II regions and the abundance properties of spiral galaxies". In: *ApJ* 420, pp. 87–109. DOI: 10.1086/173544.

Zwicky, F. (1933). "Die Rotverschiebung von extragalaktischen Nebeln". In: *Helvetica Physica Acta* 6, pp. 110–127.